

# Fluorescence fluctuation methods in biophysical sciences

Habilitationsschrift

vorgelegt  
der Fakultät Mathematik und Naturwissenschaften  
der Technischen Universität Dresden

von

Zdeněk Petrášek, PhD  
geboren am 3. September 1973 in Prachatice

Eingereicht am: 30. 5. 2012

Die Habilitationsschrift wurde in der Zeit von Januar 2006  
bis Mai 2012 im Biotechnologischen Zentrum der TU Dresden angefertigt.

Gutachter: Prof. Dr. Petra Schwille, Technische Universität Dresden  
Prof. Dr. Jörg Enderlein, Georg-August-Universität Göttingen  
Prof. Dr. Markus Sauer, Julius-Maximilians-Universität Würzburg

Wissenschaftlicher Vortrag und Probevorlesung am: 11. 4. 2013

# Contents

<b>1</b>	<b>Summary</b>	<b>3</b>
<b>2</b>	<b>Fluctuation methods</b>	<b>5</b>
2.1	Introduction . . . . .	5
2.2	Fluorescence fluctuation methods, FCS . . . . .	6
2.2.1	Principle and experimental realization . . . . .	6
2.2.2	Theory . . . . .	8
2.2.3	Extensions of FCS and combination with other techniques . . . . .	11
2.2.4	Practical aspects . . . . .	11
<b>3</b>	<b>Spatio-temporal correlations</b>	<b>13</b>
3.1	Fixed configuration . . . . .	13
3.2	Scanning FCS . . . . .	14
<b>4</b>	<b>Two-photon excitation</b>	<b>19</b>
4.1	Principle . . . . .	19
4.2	Two-photon excitation in fluorescence microscopy . . . . .	19
4.2.1	Two-photon excitation in FCS . . . . .	20
4.2.2	Saturation . . . . .	20
4.3	Photobleaching . . . . .	22
4.3.1	Photobleaching mechanisms . . . . .	24
4.3.2	Reduction of photobleaching . . . . .	25
<b>5</b>	<b>Biophysical applications of fluctuation methods</b>	<b>27</b>
<b>6</b>	<b>Perspectives</b>	<b>29</b>
<b>7</b>	<b>References</b>	<b>32</b>
<b>8</b>	<b>Included articles</b>	<b>41</b>
A1	Fluctuations as a source of information in fluorescence microscopy . . . . .	41
A2	Scanning fluorescence correlation spectroscopy . . . . .	55
A3	Simultaneous two-photon fluorescence correlation spectroscopy and lifetime imaging of dye molecules in submicrometer fluidic structures . . . . .	81
A4	Precise measurement of diffusion coefficients using scanning fluorescence correlation spectroscopy . . . . .	91
A5	Circular scanning fluorescence correlation spectroscopy on membranes . . . . .	105

A6	Photobleaching in two-photon scanning fluorescence correlation spectroscopy . . . . .	123
A7	Independence of maximum single molecule fluorescence count rate on the temporal and spectral laser pulse width in two-photon FCS . . . . .	137
A8	Characterization of protein dynamics in asymmetric cell division by scanning fluorescence correlation spectroscopy . . . . .	145
<b>9</b>	<b>Erklärung</b>	<b>159</b>

# 1 Summary

The subject of this work is the development of experimental methods based on detection and analysis of fluorescence fluctuations, and their application to the investigation of biophysical phenomena.

The analysis of fluorescence fluctuations within a femtoliter-sized volume by temporal autocorrelation of the measured signal is the basis of Fluorescence Correlation Spectroscopy (FCS). Since its appearance, many variations and extensions of this now standard fluorescence fluctuation method have been introduced. Here, two lines of further development are followed. The first extends the temporal analysis by adding spatial dimension, leading to spatio-temporal fluctuation methods. This has been realized here by scanning the measurement volume within the sample along a circular path, thus detecting the fluorescence from a range of different locations. We have applied this method to study diffusion in bulk as well as in two-dimensional membrane systems, and show that it is more robust to sample non-idealities than standard FCS, a feature particularly important for biological applications.

The second focus of this work is on the combination of fluorescence fluctuation analysis with two-photon excitation. Two-photon excitation has many attractive properties, often exploited in fluorescence microscopy in life sciences, but results in lower performance of fluctuation methods in comparison with common one-photon excitation. The principal limiting factor is the maximum fluorescence signal detectable from any single molecule. As the main cause, the photobleaching of the fluorescent molecules has been identified. The presented work aims at understanding the mechanisms by which photobleaching limits the performance of the fluctuation analysis when two-photon excitation is employed, and explores the ways of optimizing the excitation to reduce these negative effects.

The combination of two-photon excitation and scanning FCS has been applied to study the protein dynamics in a developing one-cell embryo, showing that fluorescence fluctuation analysis is applicable even under the challenging experimental conditions encountered in living biological samples.



## 2 Fluctuation methods

### 2.1 Introduction

Fluctuations, or noise, accompany practically any physical experiment. It has been, however, recognized that fluctuations in a measurement of a physical quantity are not necessarily only disturbing noise degrading the experimental results, but they can carry useful information. This fact has been utilized in experimental methods that analyze fluctuations in small systems, both in equilibrium and outside equilibrium, to obtain important microscopic system parameters.

Large systems in equilibrium are described by thermodynamic state parameters, which assume constant values. Considering the detailed structure of the system, the dynamics and the interactions of its microscopic constituents lead to fluctuations of the macroscopic parameters. In the thermodynamic limit these fluctuations are, however, vanishingly small. For example, the fluctuations of the internal energy and other parameters of ideal gas scale as  $1/\sqrt{N}$  with the number  $N$  of particles. On the other hand, when the investigated system is sufficiently small, the fluctuations of thermodynamic parameters around their mean values become significant and can be detected with sensitive experimental methods.

In order to study the dynamics of the microscopic constituents of a large system, one can induce a macroscopic perturbation, and observe the reaction of the system, for example, relaxation to the equilibrium. When the system is small so that the fluctuations around equilibrium are detectable, the analysis of these fluctuations can yield principally the same information as the relaxation methods, without the need to bring the system out of equilibrium. The parameters obtained by these two different types of methods are linked by fluctuation-dissipation theorems. For example, the friction coefficient  $\zeta$ , describing the dissipation of energy by friction force when a sphere is pulled through a viscous medium (non-equilibrium process), and the diffusion coefficient  $D$ , describing the random fluctuations in particle position in equilibrium, are connected by the Einstein relation  $D = k_B T / \zeta$ .

In experimental fluctuation methods, fluctuations of a chosen physical quantity are measured and analyzed to obtain relevant microscopic parameters. Examples include: measurement of conductivity fluctuations in electrolyte, where the number of ions fluctuates as a result of a chemical reaction, to determine the rate of the chemical reaction [44]; analysis of resistance/conductance fluctuations to study charge carrier dynamics in organic charge-transfer materials [87], measurement of fluctuations of electrical current through membrane to study molecular transport through a membrane channel [110], analysis of thermal fluctuations of an atomic force microscope (AFM) cantilever to study fluid microrheology near interface [80], and measurement of fluctuations of scattered or emitted light (fluorescence) as a consequence of particle diffusion and interactions [11, 81, 128].

This work is concerned with the development and application of methods that measure and analyze fluctuations of fluorescence of individual molecules. The fluorescence fluctuations can reflect a host of microscopic physical processes ranging from light absorption and emission (manifested as photon antibunching), dye photophysics and photochemistry, conformational changes of molecules, intermolecular interactions, and molecular transport. Fluorescence thus ‘reports’ on another physical parameter which fluctuates around

its equilibrium or stationary value, be it population of electronic states of the molecule, population of different conformational states, concentration of chemically reacting species, or simply concentration of molecules in a small volume. The rates of the underlying processes and the numbers of fluorescing molecules are the main parameters that can be obtained with these methods.

The methods within this work are developed with the intention to be applicable to biologically relevant systems and phenomena. The samples include aqueous solutions of fluorescent or fluorescently labelled molecules, artificial two-dimensional membrane systems mimicking biological membranes, and parts of actual living organisms, such as cellular cytoplasm and cell membrane. The main physical processes of interest are molecular transport (diffusion and flow), and intra- and intermolecular interactions (binding and dissociation). The quantitative parameters characterizing these processes can then be used to construct quantitative physical models of the biological systems and their function.

Fluctuation methods are suitable for studying biological systems on sub-cellular to molecular level because the fluctuations on the relevant micrometer and sub-micrometer scales are often non-negligible, and it is therefore natural to exploit them, rather than to try to eliminate them in experimental data by averaging. Furthermore, it may not always be possible to use relaxation methods because of the small dimensions and the difficulty to induce a controlled perturbation, the possibility of a complex biological response, and the potential difference between the final relaxed state and the initial state. Optical methods have the additional advantage of minimum interference with life processes, and the high sensitivity of fluorescence techniques makes them ideal for combination with fluctuation analysis applied to biological samples.

In a broader context, the role of fluctuations in living systems is interesting also for other reasons. While it is intuitively clear that noise, realized for example as fluctuation in the number of molecules, can disturb biochemical reaction networks and steer the evolution of the system into undesirable direction, there is evidence that stochastic behaviour induced by molecular fluctuations can be of biological advantage that goes beyond the obvious evolutionary advantage in giving rise to variability necessary for natural selection [39, 55]. The effects of fluctuations in living systems are also related to an important concept of biological robustness, that is, the ability to maintain the original function and to develop along a pre-determined path ('to remain alive') under the influence of both external and internal fluctuations and disturbances [68]. The availability of methods able to experimentally quantify fluctuations in complex living systems on molecular level is therefore important for developing a better understanding of these properties of living matter.

## **2.2 Fluorescence fluctuation methods, FCS**

### **2.2.1 Principle and experimental realization**

The principle of fluorescence fluctuation methods lies in detecting and analyzing a fluctuating fluorescence signal from a small number of molecules, derived from fluctuation of some, directly unobservable, physical parameter [40, 81, 128]. The number of molecules should be small, so that the fluctuations are sufficiently large relative to the average signal to be experimentally detectable. The molecules are either in bulk liquid phase, diffusing or being actively transported in solution, or confined within a surface, where they may diffuse

freely, or are immobilized. The measurement on a small number of molecules (of the order 0.1–100, on average) is usually achieved by a combination of low concentration (nanomolar range,  $1 \text{ nM} = 0.6 \text{ molecule} \cdot \mu\text{m}^{-3}$ ) and a small measurement volume ( $\leq 1 \mu\text{m}^3$ ).

The information is obtained from the raw data by evaluation along two lines, which can be combined: the analysis of the distribution of fluctuating fluorescence values yields, for example, the mean particle number and the mean state populations; the temporal characteristics of fluctuations reflect the dynamics of the underlying physical process. The range of the accessible time scales is large, from tens of picoseconds, limited by the timing accuracy of fast detectors and electronics, to seconds and more, limited by the overall sample and instrument stability. Any processes that give rise to changes in fluorescence within this time range can in principle be probed.

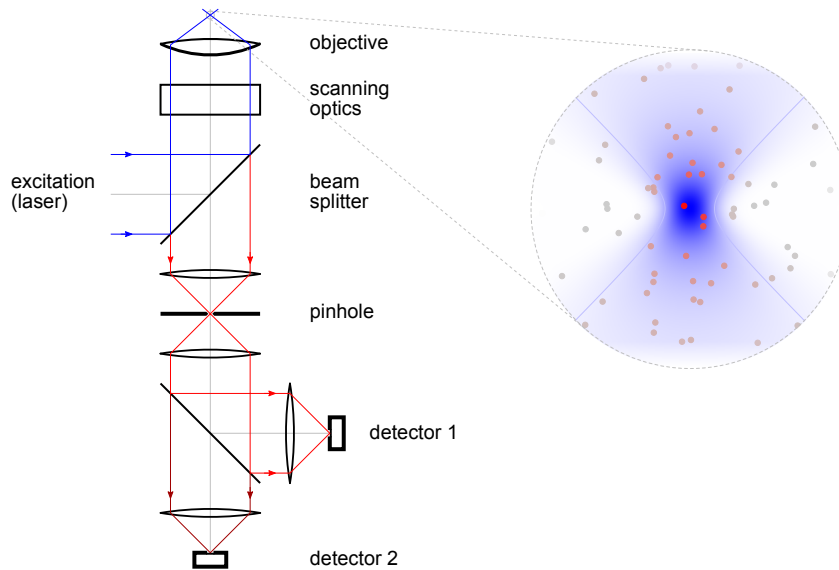


**Figure 1:** A scheme of a confocal setup for fluorescence fluctuation measurements. The excitation light from a laser is focused by the objective into a well-defined diffraction-limited volume; the geometrical objective focus is imaged onto a pinhole which spatially limits the volume for fluorescence detection. The focused excitation and spatially restricted detection together define the measurement volume. The scanning optics allows for confocal imaging and scanning FCS experiments. The detection can be divided into more channels, depending on emission wavelength, polarization, etc.

The small detection volume is typically realized by focusing excitation light into a diffraction-limited focal spot and restricting the detection of the generated fluorescence to the approximately same volume. The experimental setup is practically identical to a confocal laser scanning microscope (Fig. 1). An important aspect is the confocal alignment of the pinhole with the objective focal point. This defines the shape and size of the measurement volume. The pinhole need not be used in connection with two-photon excitation.

Although this is the most common experimental arrangement, specialized setups are used, for example, when smaller measurement volumes are required, or measurements on surface are performed. Measurement volumes smaller than in the confocal setup (Fig. 1) can be achieved by excitation with evanescent fields, created, for example, by total internal

reflection on the glass-liquid interface [122], or their combination with volume physically confined by subwavelength apertures [77]. Alternatively, stimulated depletion of emission (STED) principle, employed in superresolution microscopy, can be used to restrict the measurement volume [36, 65].

### 2.2.2 Theory

Some basic elements of the theoretical description of fluorescence fluctuation experiments are presented here.

The spatial distribution of the excitation and detection efficiencies near the objective focus are important for correct data interpretation. The relationship between the spatial illumination intensity profile  $W(\mathbf{r})$  and the excitation profile  $E(\mathbf{r})$  depend on the mode of excitation: for one-photon excitation  $E(\mathbf{r}) = W(\mathbf{r})$ , for two-photon excitation  $E(\mathbf{r}) = W^2(\mathbf{r})$ . However, this relationship becomes more complex if optical saturation or other effects are present. The detection via pinhole is described by the collection efficiency function  $CEF(\mathbf{r})$ . The combination of excitation and detection leads to the overall measurement profile  $S(\mathbf{r}) = E(\mathbf{r})CEF(\mathbf{r})$ . All profiles are scaled so that the maximum value is 1 at the geometrical focus positioned into the origin ( $\mathbf{r} = 0$ ).

The average detected fluorescence  $F(\mathbf{r})$  originating from position  $\mathbf{r}$  is proportional to the combined excitation and detection efficiency  $S(\mathbf{r})$ :  $F(\mathbf{r}) = \eta_0 c S(\mathbf{r})$ , where  $\eta_0$  is the molecular brightness (photon counts per molecule per second) in the centre of the volume. Defining the measurement volume  $V$  as  $V = \int S(\mathbf{r}) d\mathbf{r}$ , the average fluorescence can be expressed as  $F = \eta_0 c V$ , where  $c$  is the concentration of fluorescent species.

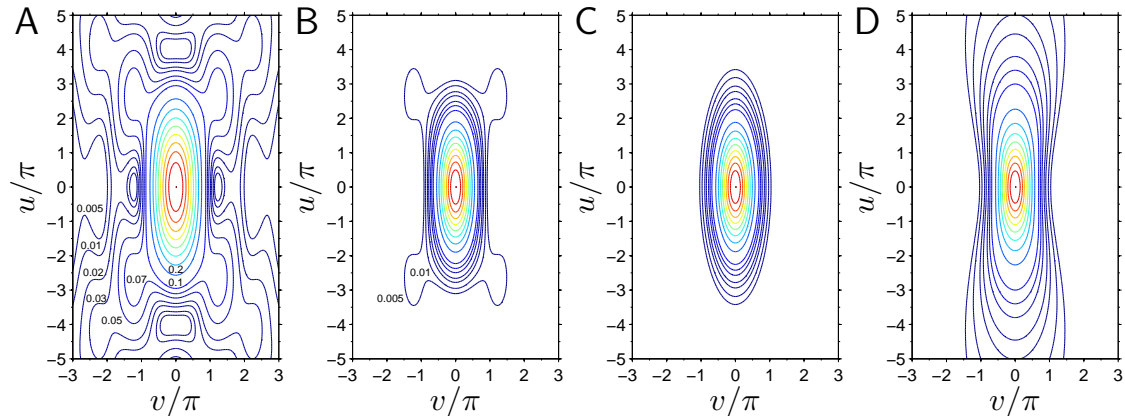


**Figure 2:** Several descriptions of excitation efficiency near the objective focus. A: Fresnel diffraction of a spherical wave at a circular aperture (after M. Born and E. Wolf [17], p. 486), B: the second power of A, applicable for two-photon excitation, C: three-dimensional Gaussian approximation (Eq. 1), D: Gaussian-Lorentzian approximation (Eq. 2). (reduced cylindrical coordinates:  $u = 2\pi/\lambda(a/f)^2 z$ ,  $v = 2\pi/\lambda(a/f)r$ )

The measurement profile  $S(\mathbf{r})$  is usually approximated by a three-dimensional Gaussian function (Fig.2C):

$$S(\mathbf{r}) = e^{-\frac{x^2+y^2}{2a^2}} e^{-\frac{z^2}{2(wa)^2}}, \quad (1)$$

with the size parameter  $a$  and an axial elongation factor  $w$ . This model is often sufficient

to describe a standard FCS experiment, and has the advantage of leading to a fully analytical description of the experimental data. In certain situations where more accurate approximation is required, for example, when two-photon excitation is used [10], or when measurements are performed on surfaces, the Gaussian-Lorentzian model is employed (Fig.2D):

$$S(\mathbf{r}) = \frac{a_0^2}{a^2(z)} e^{-\frac{x^2+y^2}{2a^2(z)}}, \quad a^2(z) = a_0^2 + b^2 z^2, \quad b = \frac{\lambda}{4\pi n a_0}. \quad (2)$$

More accurate descriptions include the effect of pinhole separately [28, 42], or are based on exact (numerical) calculation [43].

There are many ways the fluctuating fluorescence signal can be processed to obtain the desired information, resulting in methods denoted by various acronyms.

The most common procedure is to evaluate the normalized temporal autocorrelation  $g(\tau)$  of the fluorescence intensity  $F(t)$ :

$$g(\tau) = \frac{\langle F(t)F(t+\tau) \rangle}{\langle F(t) \rangle^2} - 1. \quad (3)$$

The method where the data interpretation proceeds by analyzing the autocorrelation function  $g(\tau)$  is called Fluorescence Correlation Spectroscopy (FCS) [40, 74, 81, 105, 128].

The function  $g(\tau)$  reflects the temporal decay of fluctuations; its limit to zero time  $\lim_{\tau \rightarrow 0} g(\tau)$  yields the relative variance of fluctuations:

$$g(\tau)_{\tau \rightarrow 0} = \frac{\sigma_F^2}{\langle F(t) \rangle^2} = \frac{\gamma}{cV} = \frac{1}{cV_{eff}}. \quad (4)$$

When the source of fluctuations is the variable number of molecules in the focus, and if this can be described by the Poisson distribution, as assumed in Eq. 4, then the amplitude of the autocorrelation is inversely proportional to number of particles in the effective volume  $V_{eff}$ . Eq. 4 is the basis for determining absolute concentrations from fluorescence fluctuations.

The  $\gamma$  parameter in Eq. 4, defined as:

$$\gamma = \frac{\int S^2(\mathbf{r}) d\mathbf{r}}{\int S(\mathbf{r}) d\mathbf{r}}, \quad (5)$$

describes the confinement of the measurement volume, and is related to the distribution of the brightness values with which molecules near the focus contribute to the total fluorescence. The  $\gamma$  factor is important for correct interpretation of the autocorrelation amplitude  $g(0)$ , and therefore determination of concentration (Eq. 4). It is sensitive to optical distortions and saturation, and plays a crucial role in description of photobleaching effects, as described in a later section.

The position of a particle performing simple Brownian diffusion is described by a probability distribution function (pdf)  $p(\mathbf{r}, t)$ :

$$p(\mathbf{r}, t) = \frac{1}{(4\pi Dt)^{3/2}} e^{-\frac{r^2}{4Dt}}, \quad (6)$$

where  $\mathbf{r}$  is the particle position relative to its location at time  $t = 0$ , and  $D$  is the particle diffusion coefficient. It is a Gaussian function with a square width (mean square displacement)  $\sigma^2$  increasing linearly with time:  $\sigma^2 = 2Dt$ .

Combining Eq. 6 with the model of the measurement volume  $S(\mathbf{r})$  (Eq. 1) in Eq. 3 by calculating the ensemble average leads to the commonly used model for the autocorrelation function in FCS:

$$g(\tau) = \frac{1}{cV_{eff}} \frac{1}{\left(1 + \frac{\tau}{\tau_D}\right) \sqrt{1 + \frac{\tau}{w^2\tau_D}}}, \quad (7)$$

where the diffusion time  $\tau_D$  is typically obtained from the data by fitting, and is used to determine the unknown diffusion coefficient  $D$ :

$$\tau_D = \frac{a^2}{D}. \quad (8)$$

The volume size parameter  $a$  must be known, and is usually determined by a reference measurement, assuming constant volume size and shape. Eq. 7 represents the simplest form of autocorrelation model, and is often supplemented by factors accounting for fast photophysical processes, such as singlet-triplet transitions [131].

The value of the diffusion coefficient may be interesting on its own, or it may serve as an indicator of changes of parameters that it depends on: the viscosity  $\eta$  of the environment, or the size and shape of the diffusing particle. Observed change of the diffusion coefficient upon controlled variation of external parameters may then reflect binding to or dissociation from a particle of different size, or conformational changes of macromolecules.

In addition to concentrations and diffusion coefficients, practically any process that leads to changes of fluorescence intensity can be monitored by fluctuation analysis and FCS. Examples include photon antibunching as a consequence of finite excitation and emission rates, photophysical transitions between triplet and other electronic excited states, resonance energy transfer, photochemical reactions, redox reactions and conformational changes affecting the spectral properties of the molecules, etc. Details on these applications can be found in several review articles [74, 105].

In addition to analyzing the fluctuating fluorescence signal by means of the autocorrelation function (Eq. 3), a range of other methods have been developed. The distribution of experimental fluorescence values can be quantified not only by the mean value and the variance as in FCS, but by higher-order moments and cumulants [88, 107], or the full distribution can be fitted to an appropriate model (Fluorescence Intensity Distribution Analysis — FIDA [64], Photon Counting Histogram — PCH [21]).

The temporal characteristics of fluctuations can be analyzed, among others, by higher-order correlations of the form  $\langle F^n(t)F^m(t + \tau) \rangle$  [95, 96], or, in case of a single molecule, by a detailed analysis of the full fluorescence trajectory consisting of photon arrival times, identifying discrete states, residence times and transition rates [1].

The attached article A1 [104] discusses a range of other methods that obtain useful information about the system by analyzing fluctuations of fluorescence signals in microscopy experiments.

### 2.2.3 Extensions of FCS and combination with other techniques

The possibility to separate the emitted fluorescence according to different parameters, such as wavelength and polarization (Fig. 1), and to detect the photons with high temporal resolution following pulsed excitation, leads to a range of extensions of the basic fluorescence correlation method.

Detection in different wavelength ranges enables monitoring of two or more different types of molecules and their interactions. This is the basis of Fluorescence Cross-Correlation Spectroscopy (FCCS), a powerful way to quantify molecular associations and obtain reaction rates [3, 116]. Polarization-resolved detection combined with resolution in the nanosecond time range is useful for detection of molecular rotation [18, 106] even when the rotational correlation times significantly exceed the fluorescence lifetime and the standard technique of fluorescence anisotropy decay [75] cannot be used. Time resolution on the scale of fluorescence decay can be used to separate signal from molecules with similar or overlapping emission spectra but with different fluorescence lifetimes (Fluorescence Lifetime Correlation Spectroscopy — FLCS) [15], or fast scattering from fluorescence [63].

The attached article A3 [100] explores the effects of confinement of fluorescent molecules in microfluidic channels on their dynamics and emission properties. The detection of fluorescence with temporal resolution ranging from picoseconds to seconds enables combination of two different techniques, FCS and Fluorescence Lifetime Imaging (FLIM) [120], in one instrument, the laser scanning microscope (Fig. 1)

The restriction on the molecular motion imposed by the confinement is reflected in the fluorescence fluctuation analysis. In thin (thinner than the axial volume dimension), broad channels, the observed motion is effectively described by two-dimensional diffusion. In narrow channels which have their width comparable to the lateral volume size, or near the channel boundary, the description requires more complex models, as the influence of boundaries cannot be neglected. These effects are relevant for FCS applications in micro- and nano-fluidic systems, as well as in biological samples where confinement, excluded volumes and boundaries are common [45, 125].

The location of a molecule near an interface between environments with different refractive indices, for example, near the glass channel surface within a thin solvent layer, influences the molecule’s emission properties, such as the fluorescence intensity and lifetime, and the directional distribution of emission [41, 79]. FLIM is a suitable technique to visualize the surface effects on the decay kinetics of the fluorophore.

### 2.2.4 Practical aspects

The performance of fluorescence fluctuation methods depends on the signal-to-noise ratio in the data that are eventually fitted to a theoretical model; most commonly in the correlation function  $g(\tau)$  (Eq. 3). The main source of noise is the photon shot noise. A small molecule with diffusion coefficient  $D = 400 \mu\text{m}^2\text{s}^{-1}$  spends typically the time  $\tau_D = 0.1$  ms in the measurement volume characterized by  $a = 0.2 \mu\text{m}$  (Eq. 8). The typical number of photons detected from a single molecule during this short time is on the order of 1 to 10, and will therefore exhibit large fluctuations. The more photons the molecule emits during this short time, the more information it leaves about its transit time and its diffusion

coefficient, and the higher will the signal-to-noise ratio be. That the molecular brightness  $\eta$ , that is, the number of photons detected from a single molecule on average per unit time, is the most important parameter for signal-to-noise ratio in fluorescence correlation experiments has also been shown theoretically [71]. Efforts to maximize the molecular brightness by increasing the excitation intensity are limited by photophysical and photochemical effects, a particularly important aspect when using two-photon excitation, as discussed in more detail in a later section.

Other important factors that influence the performance of the fluorescence fluctuation methods are those affecting the shape of the measurement volume [43]: the optical properties of the sample, most importantly the variations of the refractive index; the adjustment of the focusing optics and pinhole; and photophysical effects, such as saturation and photobleaching, most likely to occur at high excitation intensities employed to maximize the molecular brightness  $\eta$ .

There is therefore need for modifying the existing or developing new fluorescence fluctuations techniques where the sensitivity to the above mentioned effects would be reduced. The more robust approaches are particularly important for applications in biological samples, where the optical heterogeneity and continual development due to living processes pose additional challenges. The development of the sample with time leads to low long-term stability, and reduces the available time for a single measurement. The limited control over the state of the biological sample and processes therein means that additional fluctuations, possibly on any time scale, interfering with the investigated process and hard to account for can be present. Another potential difficulties are caused by fragility of the investigated sample, reflected by possible phototoxicity as a consequence of high excitation intensities.

In the following section, spatio-temporal correlation methods are introduced. One of the important features of some of these methods is higher robustness to many of the disturbing effects mentioned here.

### 3 Spatio-temporal correlations

Traditional fluctuation methods (FCS) analyze fluctuations at a fixed location; the distinction between different processes is solely on the bases of their temporal characteristics. For example, in case of diffusion, the experiment essentially tells us how fast the molecules disappear from the measurement volume, but not where they are going.

The difference in the shape of the temporal decay of correlations is sufficient to distinguish between, for example, simple diffusion and flow, but difficulties may arise when more processes take place together on comparable time scales: two diffusion components, additional fast kinetics, or chemical reactions. The difficulty to resolve these processes stems to a large extent from the fact that correlation curves are rather featureless and slowly decaying.

The addition of extra dimension — space — to the design of the experiment increases the possibility to distinguish between processes that involve translational motion and therefore generate spatial correlations (diffusion, flow), and processes involving only change of state (conformational change, FRET change, binding to or detachment from a surface, when measurement limited to within the surface).

Perhaps the technically easiest way to probe transport on different spatial scales is to apply the standard FCS with different volume sizes  $a$  (Fig. 3E). The method has been employed to detect deviations from simple diffusion characterized by a single diffusion coefficient  $D$ , as a consequence of the presence of domains and obstacles to diffusion on spatial scales smaller than the measurement volume size (i. e., below the optical resolution limit), both on surfaces and in bulk solution [82, 127].

Another important motivation for introducing the spatial dimension into fluctuation methods is the gain in robustness. Spatio-temporal correlation models have typically clearer features compared to standard FCS (compare Figs. 4B and C), leading to higher sensitivity. The known spatial geometry of the experimental arrangement additionally reduces the dependence on the accurate knowledge of the size of the measurement volume. This is especially important with measurements under non-ideal conditions, as is often the case with biological samples.

The spatio-temporal correlation measurements can be realized either by using fixed spatial configuration of measurement volumes, or a flexible arrangement, realized by scanning the excitation beam in a desired pattern.

#### 3.1 Fixed configuration

An early example of spatio-temporal correlation experiment is the measurement of flow velocity in a microchannel [19, 33]. Two foci are positioned along the flow lines in a channel at a known distance  $d$  (Fig. 3D), and the corresponding signals are cross-correlated resulting in a sharp peak at the flow time between the two foci  $\tau_c = d/v$ . This allows the determination of the velocity  $v$  in a more robust way than determining the flow time through a single focus  $\tau_a$ , which is more sensitive to alterations of the volume size and shape, and other fluctuations in the system. Figure 4 illustrates the reduced sensitivity of the flow time  $\tau_c$  determined from spatial cross-correlation between two foci to the presence of additional fast and slow dynamics and variations in the volume size  $a$ . A similar principle is the reason for high robustness of spatial cross-correlation methods discussed below.

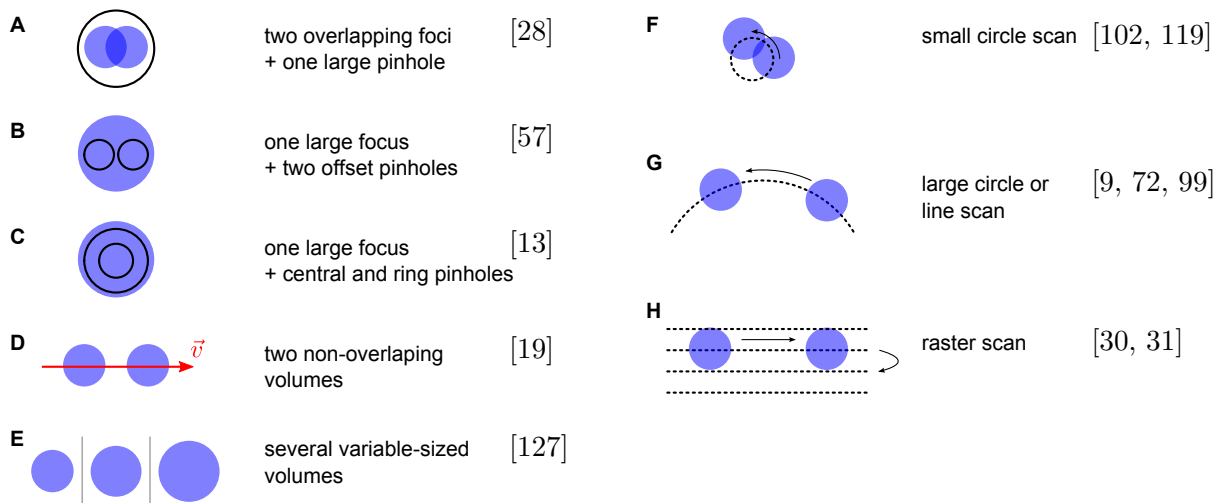


**Figure 3:** Various arrangements of measurement volumes for probing spatio-temporal fluorescence correlations. A-C: two closely located static volumes; D: two non-overlapping volumes for flow detection; E: volumes of different sizes subsequently probing different spatial scales; F-H: single volumes scanned in a periodic pattern (scanning FCS).

Dual-focus FCS [28] is a well-characterized method that quantifies correlation between two overlapping volumes (Fig. 3A). These are realized by using two pulsed lasers (40 MHz) with interleaved excitation, orthogonal polarizations and time-resolved detection to excite only molecules in one volume at a time, and to assign the detected fluorescence to the respective volume. The distance between the volumes plays the role of the volume size in standard FCS in the sense that it provides the length scale needed to convert the measured temporal correlation characteristics into the diffusion coefficient  $D$ . Contrary to the measurement volume size  $a$ , the distance between the two volumes is practically unaffected by the optical properties of the sample and can be accurately calibrated. Consequently, the method is robust against optical saturation [78] and other disturbing effects [27].

A similar spatio-temporal scheme uses a single laser beam combined with two pinholes to create two overlapping volumes [57] (Fig. 3B), and applies thresholding of the raw fluorescence data to effectively diminish the size of the measurement volume. Another method creates a central and a surrounding annular volumes by means of a central and a ring pinholes [13] (Fig. 3C).

### 3.2 Scanning FCS

Static realization of two overlapping volumes requires a relatively complex excitation and detection arrangement (pulsed lasers with time-resolved detection in case of dual-focus FCS), and typically does not allow flexible adjustment of the distance between the foci. Scanning FCS is a modification of FCS where a single measurement volume, realized in a standard way by a laser focus combined with a detection pinhole, is moved through the sample in a controlled way (Fig. 3F-H). The correlation of the detected fluorescence at the lag time  $\tau$  is in fact a spatio-temporal correlation  $g(\xi, \tau)$  at the distance  $\xi(\tau)$ , as defined by the scanned pattern. While scanning FCS does not provide the full spatio-temporal correlation  $g(\xi, \tau)$  (Fig. 8E), or the spatial correlation at a single distance  $\xi$  at all lag times

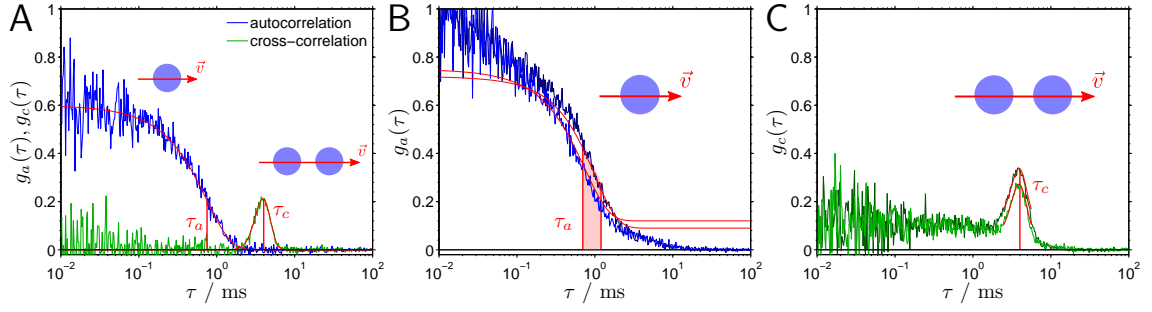


**Figure 4:** Illustration of the robustness of the spatial cross-correlation compared to the standard autocorrelation on the example of measurement of the flow velocity  $v$ . A: In the absence of additional fluctuations and optical distortions the flow velocity can be determined either from the autocorrelation flow time  $\tau_a = 2a/v$  (single focus) or from the cross-correlation flow time  $\tau_c = d/v$  (two foci at a distance  $d$ ); B, C: in the presence of additional fluctuations at short or long times, or unaccounted-for changes of the volume size  $a$ , the autocorrelation flow time  $\tau_a$  can be determined only with a large uncertainty (B), while the cross-correlation flow time  $\tau_c$  is minimally influenced by these effects, and allows accurate determination of the velocity  $v$  (C). The parameters used in the simulated correlation curves  $g_a(\tau) = g_0 \exp(-(v\tau)^2/(4a^2(1 + \tau/\tau_D)))/\sqrt{1 + \tau/\tau_D}$  and  $g_c(\tau) = g_0 \exp(-(d - v\tau)^2/(4a^2(1 + \tau/\tau_D)))/\sqrt{1 + \tau/\tau_D}$  are:  $a_1 = 0.15 \mu\text{m}$ ,  $a_2 = 0.2 \mu\text{m}$ ,  $d = 1.6 \mu\text{m}$ ,  $v = 0.4 \mu\text{m ms}^{-1}$  and  $D = 40 \mu\text{m}^2\text{s}^{-1}$ .

$\tau$  as the dual-focus methods, the spatial correlation at variable distances  $\xi(\tau)$ , defined by a suitably chosen scan pattern, leads to similar advantages over the standard single-focus FCS.

An important practical advantage of scanning FCS over the spatio-temporal correlation methods with a fixed foci pattern is that it can be realized in a standard confocal laser scanning microscope (Fig. 1) by driving the scanners in the desired pattern. Furthermore, the scan pattern (scan radius, frequency, etc.) can be adapted to the geometry and dynamics of the investigated system, making the method flexible.

Many versions of scanning FCS have been exploited in the past. The initial motivation was to improve the statistical accuracy of concentration measurements on slowly moving molecules, or to enable measurements on immobile molecules. Later implementations and applications quantified also the diffusion and flow of fluorescent molecules or scattering particles, and took advantage of the reduced photobleaching artefacts.

The attached article A2 [103] discusses scanning FCS in relation to its standard counterpart and other fluorescence correlation techniques, and reviews early applications of scanning FCS. It further describes a construction of a two-photon laser scanning microscope optimized for fluorescence fluctuation measurements. The instrument allows for programming arbitrary scan pattern, a feature usually not available with commercial systems. It has been used in the work presented here in the attached articles whenever two-photon excitation was employed.

Two of the attached articles (A4 [102] and A5 [98]) describe implementation and application of scanning FCS where the measurement volume is scanned in a circle of a radius on the scale of  $1 \mu\text{m}$ , that is, comparable to the volume size (Fig. 3F). This configuration has been introduced by Berland *et al.* [9] for improving the signal-to-noise ratio for slowly

diffusing species, and later refined by Skinner *et al.* [119], who used it to differentiate between diffusion, flow and immobilization of fluorescent species, and to determine the orientation of the flow velocity vector.

In the work described in the attached article A4 an advantage is taken of the fact that the size of the measurement volume  $a$  can be obtained from the data by fitting, together with the diffusion coefficient  $D$ . This is possible because the autocorrelation  $g(\tau)$  in the presence of circular scanning with radius  $R$  and frequency  $f$  depends independently on  $a$  and  $D$ :

$$g(\tau) = \frac{g_0}{\left(1 + \frac{D\tau}{a^2}\right) \sqrt{1 + \frac{D\tau}{w^2 a^2}}} e^{-\frac{R^2 \sin^2(\pi f \tau)}{a^2 + D\tau}}, \quad (9)$$

and not only via their combination in the diffusion time  $\tau_D$  (Eq. 8), as in standard FCS with stationary measurement volume (Eq. 7). Rather than calibrating the volume size  $a$ , the scan radius  $R$  has to be determined. This can, however, be done accurately, and is much less sensitive to the optical complexity of the sample, resulting in the observed robustness of the scanning method.

As a result, diffusion coefficients in bulk (3D) can be determined precisely, even when optical properties of the sample distort the measurement volume or change its size. Furthermore, reduction of photobleaching compared to stationary volume is achieved, as already reported previously [119]. The small-circle scanning FCS exhibits similar performance features as dual-focus FCS [28], is however more flexible (variable  $R$  and  $f$ ), and potentially easier to implement. The method is shown to yield reliable results even in cytoplasm of living cells, an optically complex environment.

dye	this work		literature values
	3DG	GL	$D$ [ $\mu\text{m}^2\text{s}^{-1}$ ]
Alexa 488	435	405	393
Alexa 546	341	317	—
eGFP	95	87	$88 \pm 4$
fluorescein	436	398	401 – 415
rhodamine 6G	426	389	$393 \pm 1$

**Table 1:** Diffusion coefficients of several commonly used fluorescent dyes determined as described in the article A4. The values obtained using the Gaussian (3DG) and Gaussian-Lorentzian (GL) models of the measurement volumes are compared with literature values. The literature values, as quoted in the article A4, were adjusted for the temperature  $T=22.5^\circ\text{C}$ , at which the measurements were performed. The relative errors of the measurements are 2–5%.

In the work presented in the article A4, the shape of the measurement volume has been described by a 3D Gaussian function (Fig. 2, Eq. 9). However, as argued below, the volume shape in case of two-photon excitation is more accurately described by a function the lateral extent of which is increasing with the distance from the focal plane. Using Gaussian-Lorentzian function (Eq. 2) as a more accurate approximation of the volume leads to slightly lower diffusion coefficients, which are, however, closer to the values reported in the literature (Table 1).

In a subsequent study (attached article A5), the same scanning FCS principle has been implemented for more commonly employed one-photon excitation, and applied to the study of molecular diffusion confined to a two-dimensional surface — phospholipid membranes.

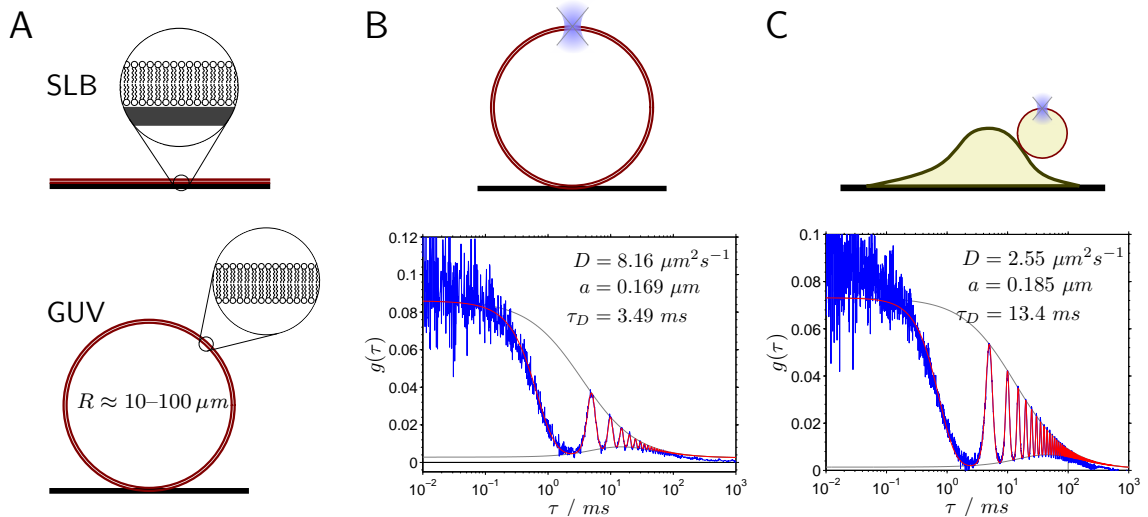


**Figure 5:** A: Two model systems for biological membranes: Supported Lipid Bilayers (SLB) prepared on a glass or mica surface, and Giant Unilamellar Vesicles (GUV), spherical membrane structures with aqueous solution both inside and outside; B: an example of diffusion measurement of fluorescence membrane probe DiO in a vesicle composed of DOPC lipid with scanning FCS; the measurement volume was positioned on the top pole of the vesicle; C: measurement of the same membrane probe in a giant plasma membrane vesicle induced on the surface of a cell (collaboration with R. Worch and T. Weidemann).

The membrane was either flat, supported by a smooth mica surface, or spherical, realized by giant unilamellar vesicles (GUV) of diameter on the scale of  $10-100 \mu m$  (Fig. 5A). Both supported membranes and GUVs serve as model systems for cellular membranes [73, 109, 111, 115], and are commonly applied to study phase behaviour of membranes composed of various lipid mixtures [4, 5], and interactions between membranes and proteins, and other biologically relevant molecules [59]. Dynamics and interactions of molecules within membrane are important for understanding and quantification of kinetics of chemical reactions and their coupling to physical processes, such as force generation, membrane deformation, tubulation, vesicle budding, etc.

On surfaces, the measurement volume (or rather the area) is determined by the cross-section between the surface and the focused beam, and therefore depends on the relative position of the two. Therefore, in contrast to the bulk applications, the volume size may vary not only as a result of possible optical distortions, but strongly depends on the focus positioning. The accurate determination of the diffusion coefficient  $D$  (Eq. 8) and concentration  $c$  (Eq. 4) from one standard FCS measurement is therefore not straightforward.

Assuming Gaussian-Lorentzian shape of the excitation beam, reliable results can be obtained from a series of measurements at different axial positions  $z$  ( $z$ -scan method [7]). This requires, however, sample stability for the time needed to acquire the whole set of measurements, and relies on the accuracy of the description of the volume shape. In the ar-

article A5 [98], it is shown that the circle-scan approach yields reliable results with a single measurement. Similarly to the principle introduced in the article A4 [102], the spatio-temporal correlation realized by a circle scan allows the volume size  $a$ , and therefore the diffusion coefficient  $D$  and concentration  $c$ , to be determined from a single measurement, without knowing the precise position of the surface with respect to the focal plane. Additionally, the method was shown to be largely insensitive to processes faster or slower than diffusion, such as membrane fluctuations or drift, which would normally disturb standard FCS measurements.

It is the robustness to disturbing processes on time scales other than that of diffusion, which makes the method particularly attractive for applications to biological systems, where the control over the sample stability is often limited. Fig. 5 shows an example: giant plasma membrane vesicles (GPMV) were induced chemically on the surface of a living cell. The lipid and protein membrane composition of GPMV is thought to be identical to that of the cellular membrane with the exception of the missing cytoskeleton. The diffusion of a fluorescent lipid analogue DiO, used as a probe for the fluidity of the membrane, is slower in GPMV ( $D = 2.6 \mu\text{m}^2\text{s}^{-1}$ ) than in a GUV composed of a single type of a lipid and containing no proteins ( $D = 8.2 \mu\text{m}^2\text{s}^{-1}$ ); but is faster than in a cell membrane, where the cytoskeleton is present ( $D \approx 1.0 \mu\text{m}^2\text{s}^{-1}$ ). In a similar way, the concentration and the diffusion coefficient of fluorescently labelled membrane proteins can be determined.

### Other implementations

As an alternative to circular scanning, spatio-temporal correlation measurements can be realized by a linear scan (Fig. 3H). A practical advantage of this is that linear and raster scans are already implemented in commercial laser scanning microscopes. However, in contrast to circular scan methods, careful attention has to be paid to correct raw data processing, since the fly-back, acceleration and deceleration periods have to be handled properly in correlation analysis. Both line [22] and raster [30] scan correlation measurements have been applied to studies of molecular diffusion in bulk, as well as in membranes.

Another direction of development of spatio-temporal fluorescence fluctuation methods is based on parallel measurement from a large number of volumes, and applying (cross-)correlation analysis to the obtained fluorescence signal. This requires spatially-resolved detectors, such as fast emCCD cameras with low read-out noise [20, 62], or, alternatively, APD arrays [47]. The detection volume can be flexibly defined by extracting signal only from the selected pixels. Focusing the excitation laser beam into an arbitrary arrangement of spots can be achieved by use of spatial light modulators based on liquid crystals [14]. Excitation by focused beams is necessary for measurements in three dimensions, since the measurement volume must be well confined in space. On surfaces (membranes), the confinement is achieved by detection alone (pixel selection), therefore the whole probed area can be illuminated [61]. However, photostability of molecules confined within the surface may become an issue in this case. Currently, the read-out speed (emCCD) and noise (CMOS) of imaging detectors is the principal restricting factor of parallel fluctuation analysis, limiting its application to rather slow processes.

## 4 Two-photon excitation

### 4.1 Principle

Two-photon absorption is a process whereby two photons are absorbed almost simultaneously (<fs) producing an excited state of energy  $\hbar\omega_0$ , equal to the sum of the energies of the two photons. The probability  $p_{g \rightarrow f}$  of the transition from the ground state to the excited state as a result of interaction with the electric field  $E(t)$  can be approximated as follows [85]:

$$p_{g \rightarrow f} = \left| \int E^2(t) e^{i\omega_0 t} dt \right|^2 = \left| \int \tilde{E}(\omega_0/2 - \Omega) \tilde{E}(\omega_0/2 + \Omega) d\Omega \right|^2, \quad (10)$$

where  $\tilde{E}(\omega)$  is the Fourier transform of the field  $E(t)$ , and the second integral is over the spectral width of the excitation pulse. The transition probability depends not only on the amplitudes  $|\tilde{E}(\omega)|$  of the spectral components, but also on their relative phases. For a given pulse energy and spectrum, the transition probability reaches a maximum when the phase differences between all spectral components are zero (transform-limited pulse). By changing the spectral phases, the probability of optical transitions can be selectively controlled [84, 85].

For a given spectrum and relative phases of a short pulse the rate of the excitation process  $k_{2p}$  is proportional to the square of the excitation intensity  $I$ :

$$k_{2p} \sim \sigma_{2p} I^2, \quad (11)$$

where  $\sigma_{2p}$  is the two-photon cross-section (typically on the order of  $10^{-50}$ – $10^{-48}$  cm<sup>4</sup>s for fluorescent dyes, but several orders of magnitude larger for quantum dots [76, 136]).

As the cross-section of the two-photon absorption is generally low, extremely high excitation intensities compared to one-photon absorption are required. These are commonly realized by using short laser pulses ( $\sim 100$  fs) of high peak power ( $\sim 1$  kW) delivered at high frequency ( $\sim 80$  MHz) focused onto a small area ( $\sim 0.1$   $\mu\text{m}^2$ ). The selection rules for two-photon absorption are different from those for one-photon absorption. Consequently, the two-photon absorption spectra often differ from one-photon absorption spectra, when compared at the double of the wavelength of single-photon absorption [133, 134].

### 4.2 Two-photon excitation in fluorescence microscopy

Two-photon excitation has several advantages compared to single-photon excitation, which led to its combination with confocal laser scanning microscopy [26, 52, 70, 136], and later also with fluorescence fluctuation analysis [10, 50, 113].

When a laser beam is tightly focused by an objective with high numerical aperture, the quadratic dependence of two-photon absorption on the excitation intensity ensures that the excitation of fluorescent molecules is restricted to a well-confined volume near the objective focus (Fig. 2). This effect alone is sufficient to achieve optical sectioning in imaging, and the use of the confocal pinhole in the detection path is therefore not necessary (Fig. 1), simplifying the microscope design and alignment [26].

Many of the features of two-photon excitation in laser scanning microscopy are particularly advantageous in applications on biological specimens. The restriction of excitation

to a small volume around the focus greatly reduces cumulative photobleaching of the fluorescent label. This becomes very important when the total pool of fluorescent molecules is limited (enclosed volume), when the same area is imaged repeatedly, or when large sample volumes are imaged by successively scanning horizontal sections. Related to this is the issue of phototoxicity: the production of potentially toxic species by photoinduced reactions is reduced because of the spatially limited excitation.

The spectral separation between the excitation and emission with two-photon excitation is considerably larger than with one-photon excitation. This not only simplifies the choice of beamsplitters and emission filters, but, with the typically broad shape of two-photon excitation spectra [133], makes it possible to excite two spectrally distinct fluorophores with one excitation wavelength [50].

Currently the most widespread application of two-photon microscopy in biological field is deep tissue imaging [52]. Imaging in depths up to one millimetre has been demonstrated [121]. This is possible mainly due to two features of two-photon excitation: first, the long-wavelength light (near-IR) is scattered less than visible wavelengths, meaning that focusing deeper into the sample is possible, and, second, the localized excitation means that the emitted fluorescence does not have to be imaged, but simply detected, making it possible to take advantage of the scattered fluorescence by non-descanned detection with a large-area detector, and thus to increase the signal.

#### 4.2.1 Two-photon excitation in FCS

Several of the described aspects of two-photon excitation are particularly attractive for fluctuation experiments, in addition to the reasons given above. The alignment of the instrument is greatly simplified, as no detection pinhole is needed. The potential benefit is even greater in experiments with two different fluorescent dyes, for example, investigating molecular associations/dissociations with two-colour fluorescence cross-correlation spectroscopy [50]. With one-photon excitation this generally requires perfect alignment of two excitation sources, with sub-diffraction precision of the overlap of the two foci, and alignment of two detection pinholes. If both dyes can be efficiently excited by two-photon process at one wavelength, the excitation volumes coincide by default, and no additional alignment is necessary [114].

Although it might appear that two-photon excitation is superior to one-photon excitation, there is a major limiting factor affecting the performance of fluctuation methods: the maximum value of the molecular brightness  $\eta_{\max}$ , the parameter largely determining the signal-to-noise ratio of FCS experiments, that can be reached with two-photon excitation is usually considerably smaller than that reachable with one-photon excitation [32, 37, 113]. Differences of 5–10 $\times$  have been determined experimentally. The reasons for this difference have been linked to processes occurring at high excitation intensities: optical saturation and photobleaching.

#### 4.2.2 Saturation

At high excitation intensities the emissive excited state or other states (triplet) may become significantly populated due to their finite lifetimes, and the ground state partially depleted, leading to sub-linear (one-photon excitation) or sub-quadratic (two-photon ex-

citation), that is, saturated, dependence of observed fluorescence on the excitation intensity. Similar effect can occur with pulsed excitation, where the emission rate is limited by the excitation rate, assuming at most one excitation event per pulse per molecule. This effect and its influence on FCS experiments has been studied in the context of both one-photon [48, 91] and two-photon [8, 92] excitation.

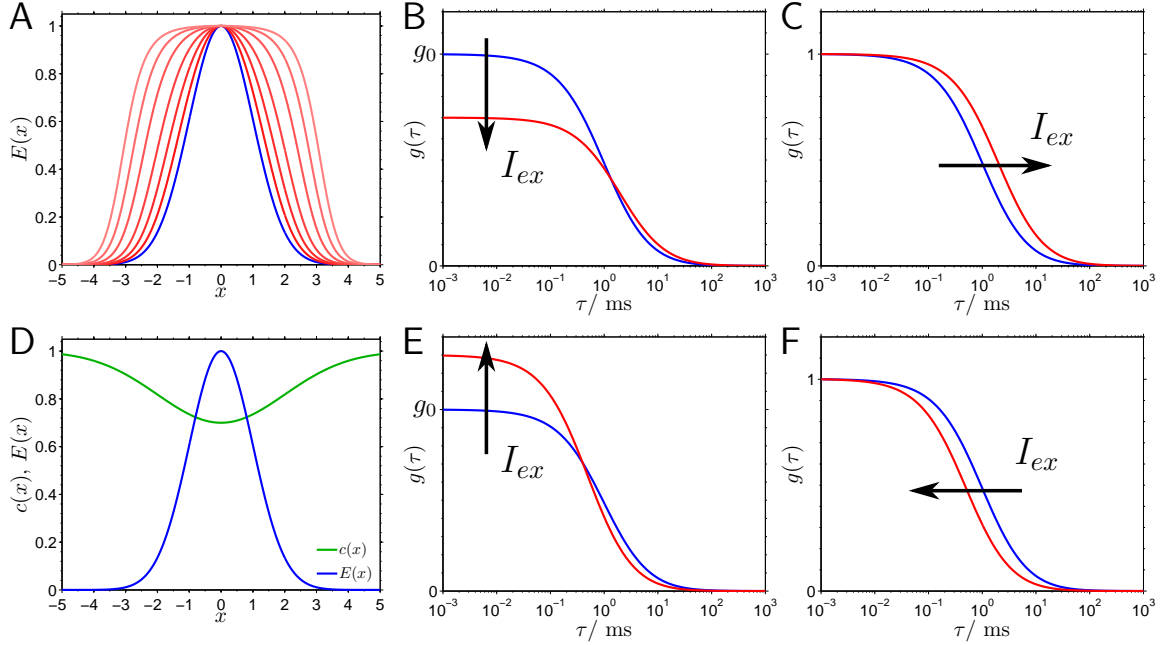


**Figure 6:** Simplified view of the expected effects of optical saturation and photobleaching on fluorescence autocorrelation curves. A: saturation increases the size of the excitation volume; more molecules contribute to the emission, therefore the autocorrelation amplitude decreases (B, Eq. 4); and the diffusion time increases (C). D: Photobleaching leads to partial depletion of fluorescent molecules in the focus, therefore an increase of the autocorrelation amplitude might be expected (E); photobleaching within the measurement volume reduces the apparent diffusion time (F).

As a result of these studies, the qualitative effects of saturation can be briefly summarized as follows. The saturation is stronger in the center of the illuminated volume, where the excitation intensity is higher, than at the edges. This leads to a modified shape of the excitation profile  $S(\mathbf{r})$ , and consequently different shape factor  $\gamma$  and volume size  $V_0$ . The volume  $V_0$  becomes larger (Fig. 6A), leading to longer diffusion times  $\tau_D$  and apparently slower diffusion (Fig. 6C), and a larger number of molecules contributing to emission. The volume becomes more confined, which is expressed by higher  $\gamma$  values, however, the increase of the volume  $V_0$  is typically stronger than that of  $\gamma$ , resulting in lower correlation amplitudes  $g(0)$  (Eq. 4, Fig. 6B). If the effect of enlarged volume is not taken into account, apparently higher concentration is determined.

It is important to note, however, that in order to match the theory with the experimental data an exponential term accounting for photobleaching with two-photon excitation usually has to be included in the autocorrelation model [92]. This is enforced by an observed decrease of diffusion times, in contradiction to the expectations of a purely saturation-based model [8, 92].

### 4.3 Photobleaching

While saturation limits the signal from individual molecules, causing non-linear (or non-quadratic, in case of two-photon excitation) dependence on the excitation intensity, photobleaching eliminates the emission of a molecule altogether. Intuitive and simplifying explanation of the influence of photobleaching on FCS predicts two effects (Fig. 6D-F): shortening of apparent diffusion times as a consequence of the molecule being photobleached (with certain probability) on its diffusion path within the measurement volume, and reduction of the number of non-bleached molecules within the volume, leading to higher correlation amplitude  $g(0)$ , therefore apparently lower concentration. The first effect motivated modeling of photobleaching in two-photon FCS by an exponential term, similar to that describing fast kinetics [8, 130]. As an approximate solution, it describes experimental data well in situations of weak bleaching. The second effect has been justified by a relatively uniform concentration profile in the focus (Fig. 6D), obtained from theoretical steady-state solutions of diffusion equation with the bleaching term [83]. The photobleaching effects in FCS have been experimentally investigated with both one-photon [25, 32, 37, 38, 129, 130] and two-photon [32, 37] excitation.

Based on this simplifying view, the predicted effects of photobleaching are exactly opposite to those of saturation (Fig. 6). Observing the onset of deviation from the ideal behaviour as the excitation intensity is increased, it should be possible to determine which of the two effects appears first. The commonly reported decrease of the autocorrelation amplitude  $g(0)$  with intensity has led to recognizing saturation as the dominant process [8, 92]. However, saturation is expected to have the same effect on generated fluorescence and molecular brightness irrespective of the mode of excitation (one- or two- photon, if both pulsed). The same degree of saturation at a given emission rate is expected, as the emission rate is independent of the process by which the emissive state  $S_1$  is reached. The several times lower maximum brightness values  $\eta_{\max}$  reached with two-photon excitation contradict the notion that saturation is the principal limiting factor. The additional saturation effect due to pulsed excitation with two-photon excitation (typically  $\sim 80$  MHz) is not strong enough to explain the observations.

The major drawback of two-photon excitation compared to one-photon excitation is that considerably lower molecular brightness  $\eta_{\max}$  can be experimentally reached, negatively influencing the signal-to-noise ratio. Therefore it is important to understand the mechanisms by which large deviations from the ideal behaviour appear already at brightness levels at which minimum deviations are observed with one-photon excitation.

The intuitive explanation of the effect of photobleaching on the correlation amplitude  $g(0)$  presented above is rather oversimplifying, since photobleaching not only lowers the average concentration of fluorescent molecules in the focus (Fig. 6D), but also affects the spatial distribution of generated fluorescence, and therefore the factor  $\gamma$  and  $g(0)$ , as follows from Eq. 4. In the attached article A6 [101], we therefore studied in more detail by what mechanism photobleaching affects the FCS measurements, to which extend photobleaching alone could explain the effects observed at high excitation intensities, and how these effects could be reduced.

We considered the spatial distribution of the excitation efficiency  $S(\mathbf{r})$  and the bleaching efficiency  $B(\mathbf{r})$ , with the bleaching rate in the maximum  $k_b$ , and by numerically solving

the diffusion equation with the bleaching term:

$$\frac{\partial c(\mathbf{r}, t)}{\partial t} = D\Delta c(\mathbf{r}, t) - k_b B(\mathbf{r})c(\mathbf{r}, t), \quad (12)$$

obtained steady state distributions of the molecular concentration  $c(\mathbf{r})$  and emitted fluorescence  $F(\mathbf{r})$  (Fig. 7). Introducing the generalized volume contrast  $\gamma$ :

$$\gamma = \frac{\int c(\mathbf{r})S^2(\mathbf{r})d\mathbf{r}}{\int c(\mathbf{r})S(\mathbf{r})d\mathbf{r}} \quad (13)$$

provided the way to describe the combined effects of the measurement profile  $S(\mathbf{r})$  and the concentration profile  $c(\mathbf{r})$  on the correlation amplitude  $g(0)$ . Comparison with the experimental data showed that the Gaussian-Lorentzian illumination profile (Fig. 2) is the more appropriate model for two-photon excitation when photobleaching effects need to be accounted for. Notably, the diffuse distribution of the generated fluorescence largely around the edges of the illuminated area (Fig. 7) leads to a strong decrease of the volume contrast  $\gamma$  (Eq. 13), and therefore causes decreases of the autocorrelation amplitude (Eq. 4), an effect usually thought to indicate saturation. The spatial distribution of fluorescence also offers a qualitative explanation of the changes of the autocorrelation decay profile with excitation intensity.

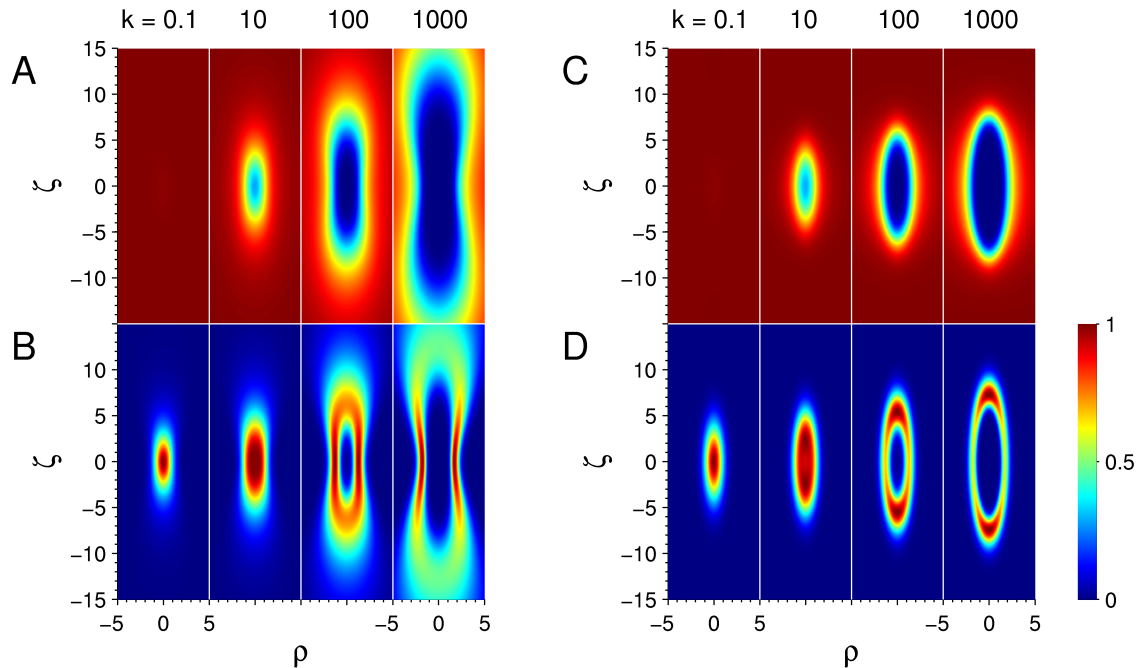


**Figure 7:** Contour plots of the calculated concentration profiles  $c(\rho)$  (A, C), and fluorescence profiles  $F(\rho) = \eta_0 c_0 c(\rho)S(\rho)$  scaled to 1 at their maximum (B, D) for GL (A, B) and 3DG (C, D) models in normalized cylindrical coordinates  $(\rho, \zeta) = (r, z)/a$ , for four values of the bleaching parameter  $k = k_b a^2/D$ :  $k = 0.1, 10, 100, 1000$ . (Figure 1 from supporting information to article A6 [101])

Scanning the measurement volume in a circle of a small radius ( $\sim 12 \mu\text{m}$ ) resulted in weaker depletion of fluorescent molecules in the measurement region, and clearly showed

that photobleaching is the dominant cause of the distortions at high intensities. Since weaker depletion of fluorescent molecules reduces the effects of photobleaching on the measurement, scanning the excitation beam is an attractive way to reduce photobleaching artefacts. This has been further exploited in an application of scanning FCS described in the attached article A8 [99], and is described in more detail below.

### 4.3.1 Photobleaching mechanisms

The term photobleaching describes a process whereby a molecule, as a result of excitation by light, undergoes a chemical reaction with the product being non-fluorescent. Alternatively, the emitter can enter a long-lived dark state, and return non-radiatively to the original ground state  $S_0$  only after a time much longer than the time scale of the investigated processes (transient photobleaching, photoswitching).

The photochemical reaction, leading to non-fluorescent products, is often initiated from higher excited states, which are more prone to ionization, radical formation, or are in general more reactive. These states can be either the higher singlet states  $S_{n>1}$  reached by absorption from the  $S_1$  state, or the higher triplet states  $T_{n>1}$ , reached by absorption from the triplet state  $T_1$ , after the molecule has undergone intersystem crossing  $S_1 \rightarrow T_1$ . As the whole process requires absorption of two or more photons within a short time (the lifetime of the excited states  $S_1$  or  $T_1$ ), photobleaching becomes usually relevant at high excitation intensities, and its dependence on excitation intensity is typically higher than linear [83, 97].

Photobleaching within the objective focus is significantly more severe with two-photon excitation than with one-photon excitation [32, 97]. One of the reasons is, that the high intensities needed for the initial two-photon absorption step ( $S_0 \rightarrow S_1$ ) are sufficient for any subsequent one-photon absorption into higher levels to occur with significant probability [112]. This may be the reason why triplet states are not observed in FCS experiments — intersystem crossing to  $T_1$  is followed by absorption to higher triplet states and photobleaching. Absorption of three or more photons leads to cubic or higher dependence of photobleaching on the excitation power. However, partial saturation of any of the involved one-photon transitions may render the dependence more complex [38].

The control over photobleaching is very important not only in fluorescence fluctuation methods employing two-photon excitation, but in general for application of fluorescent molecules as labels in microscopy. Especially in situations where the concentration of labelled molecules is low, and therefore maximum signal from every individual molecule is desirable; in single molecule imaging and tracking; or in recently developed superresolution fluorescence microscopy methods relying on saturation of absorption or stimulated emission [51]. All these methods require application of high excitation intensities, with a high risk of photobleaching reactions. An exception is the photoactivated localization microscopy [12], where controllable photobleaching is a desirable step in the photoactivation-detection-photobleaching cycle applied to each molecule and repeated many times on the whole sample to gradually build up a sub-diffraction image of the labelled structures.

### 4.3.2 Reduction of photobleaching

Recognizing photobleaching as the principal factor affecting the performance of fluorescence fluctuation measurements with two-photon excitation raises an obvious question: how could photobleaching or its effects be avoided or reduced?

One possible solution is the addition of chemicals preventing formation of reactive dye species, or promoting their regeneration into the original dye molecule. The photobleaching pathway via the triplet state is influenced by the presence of oxygen, with deoxygenation of the solution efficiently reducing photobleaching rate. Radical scavengers, antioxidants, such as ascorbic acid, and triplet state quenchers (mercaptoethylamine), were shown to diminish photobleaching, indicating the role of radical ion formation and triplet states in the process [32, 129]. However, the effect of additives depends on the mode of excitation (one- or two-photon excitation) and on the dye molecule [32]. Combination of two additives, such as enzymatic oxygen-scavenging system and reducing agent Trolox [108], or of reducing and oxidizing agents (ROXS) [124], has been shown to be particularly effective in suppressing photobleaching. A potential disadvantage of this approach is that in some situations the addition of chemicals or deoxygenation may interfere with other chemical or biological processes in the sample, or may not be possible at all.

Other strategies to reduce photobleaching, this time physical rather than chemical, are based on optimizing the mode of excitation.

It has been shown that changing the excitation frequency with pulsed excitation may reduce photobleaching in fluorescence microscopy imaging. Reducing the excitation frequency allows the long-lived states, such as triplet, to relax before the next excitation pulse is applied, thus reducing the cumulative photobleaching via the triplet pathway [35]. On the other hand, increasing the excitation frequency with passive beam splitter, while reducing the peak pulse intensity to keep the average excitation efficiency constant, reduces the relative yield of higher-than-second order processes. This also led to reduced photobleaching in fluorescence microscopy [58], and in fluorescence fluctuation analysis [89]. Whether increase or decrease of excitation frequency will lead to reduction of photobleaching depends on the molecule and its dominant photobleaching pathway.

Potentially more efficient could be the advanced methods of tailoring short pulses, such as those controlling the phase delay between different spectral components of the pulse [23, 84, 85, 93, 118]. A relatively high bandwidth is required to produce short pulses (several tens of nm for near-IR pulses of few tens of fs). In the shortest, bandwidth-limited pulse, all spectral component have the same phase. The relative phases of spectral pulse components can be adjusted by an LCD-based spatial light modulator (SLM) positioned into a spectrally dispersed beam. This generally results in a longer pulse, often of complex temporal shape. However, by adaptively optimizing the spectral phases, an enhancement of certain two-photon absorption transitions relative to others can be achieved [24, 94]. Similar pulse optimization can be used to control the yield of different product pathways in a photochemical reaction [2], and to control Raman transitions. Pulse shaping based on this principle could be used to optimize the ratio between the emission yield and yield of the photochemical bleaching reaction. As a result, higher molecular brightness values in FCS could possibly be reached.

There are, however, potential difficulties with applying this method to reduce photo-

bleaching: the absorption lines (bands) of organic molecules are rather broad, while the phase-control method performs best for narrow absorption lines; and there may be more possible photobleaching pathways. Nevertheless, iterative optimization of spectral phases has been successfully applied to organic fluorescent molecules [24, 94], and was even shown to reduce photobleaching relative to fluorescence [66].

The laser source available for the work presented here produced pulses with narrower spectral width than usually employed in the pulse shaping methods described above ( $\Delta\lambda \leq 10 \text{ nm}$ ), and we had no possibility of such detailed control over the spectral phases of the pulse. However, we could control several parameters of the pulse: the pulse length by a prism-based pre-stretcher introducing negative group velocity dispersion (GVD); the spectral pulse width by adjusting the position of an intracavity prism in the commercial Ti:Sapph laser; and the central wavelength  $\lambda$  of the pulse.

The results of a study of the effects of these pulse parameters on the performance of two-photon FCS with a common fluorescent dye tetramethylrhodamine (TMR) are presented in the attached article A7 [90]. The main conclusions are that the maximum achievable molecular brightness  $\eta_{\text{max}}$  does not significantly depend on the pulse length or spectral width. However, with shorter or spectrally brighter pulses the emission intensity is higher at the same excitation intensity. While this is naturally expected for shorter pulses (= higher peak power), it is an interesting result in case of spectrally broader pulses. A possible explanation is a larger range of accessible excitation pathways with higher spectral pulse content.

Furthermore, the maximum achievable brightness  $\eta_{\text{max}}$  shows strong variations with respect to the excitation wavelength, and a clear maximum approximately coinciding with the maximum two-photon cross-section. This maximum appears at wavelength where the yield of emission relative to the yield of bleaching is highest, and is therefore the optimal wavelength for excitation. Finally, the spectral variations of  $\eta_{\text{max}}$  confirm presence of higher-than-second order processes, such as photobleaching, since optical saturation alone would lead to a flat spectrum of  $\eta_{\text{max}}$ .

Several practical recommendations follow from this study: The wavelength at which  $\eta_{\text{max}}$  reaches its maximum is the optimal excitation wavelength. The other two parameters that can be relatively easily controlled with some commercial Ti:Sapph lasers, the pulse spectral width and length, are not critical, since they can be compensated for by increasing the excitation intensity. However, if it is desirable to keep the average excitation intensity at minimum, spectrally broad pulses should be used. The pulse duration within the sample is then to be minimized by an appropriate GVD pre-compensation, taking into account all the dispersive optical elements stretching the pulse, especially the objective.

Following the result of this work, a range of fluorescence probes was characterized for two-photon excitation by determining their two-photon action cross-section spectra ( $\sigma_2(\lambda)\Phi_F$ , two-photon absorption cross-section  $\times$  fluorescence quantum yield), and peak brightness spectra  $\eta_{\text{max}}(\lambda)$  [89]. Similarly to TMR, a high degree of correlation between the two types of spectra was observed, with the  $\eta_{\text{max}}(\lambda)$  spectra providing important practical information concerning optimal excitation wavelength and performance with respect to molecular brightness and photobleaching. Additionally, increase of molecular brightness by a factor of two at the same mean excitation power was achieved by increasing the excitation frequency with a pulse splitter.

## 5 Biophysical applications of fluctuation methods

Fluorescence techniques have the great advantage for biological applications in that they are fully compatible with experiments on living samples, interfere minimally with live processes, and are extremely sensitive, down to a single molecule level.

The importance of fluorescence methods has increased in the last couple of decades in connection with technical development in fluorescence microscopy (confocal microscopy, superresolution, multiparameter detection), and with the development in fluorescent labelling of biomolecules, especially using fluorescent proteins [117]. While in most cases the fluorophore is used only as a label, identifying the location and concentration of the molecule of interest, on a more advanced level the fluorophore serves as a sensor, with its fluorescence properties (spectrum, lifetime, polarization, etc.) responding to the environment and to molecular dynamics and interactions. In some situations, native fluorescence can be used to study natural photophysical and photochemical processes, as in photosynthesis.

Fluorescence fluctuation methods complement the imaging methods by providing information that cannot be obtained with conventional fluorescence imaging [67].

In the attached article A8 [99], the combined benefits of two-photon excitation and scanning FCS, as discussed above, are exploited to characterize dynamics of fluorescently labeled proteins in a living system — a developing one-cell embryo of a widely studied model organism, a 1 mm-long nematode *Caenorhabditis elegans*.

An interesting process preceding the first division of the one-cell embryo is its polarization — development of asymmetry in protein distribution between the two halves of the embryo, in final effect leading to asymmetric division, important for cell diversity (Fig. 8A). Although the proteins involved in polarity establishment have been identified by biochemical methods, their detailed dynamics, mutual interactions, and interactions with other cellular components *in vivo* still need to be quantitatively characterized. The ultimate goal is to construct and verify quantitative physical models of polarity establishment and cellular division.

While fluorescence imaging of living embryo is commonly used to study the localization of the labelled proteins and their dynamics on the scale of seconds, the dynamics on shorter scales is not accessible. Fluorescence fluctuation methods yield information about shorter time scales, allowing conclusions about interactions within the cell to be drawn.

Here, we focused on mainly two proteins, PAR-2 and NMY-2, genetically labeled with the enhanced green fluorescent protein eGFP. NMY-2, non-muscle myosin, is a motor protein localized mainly in the embryo cortex (cytoskeletal layer below the embryo surface shell and the membrane), and its function is related to the mechanical properties of the cortex, such as force generation and contractility. PAR-2 is a protein initially homogeneously distributed in cytoplasm. As the cell begins to polarize, PAR-2 localizes at the posterior cortex and eventually, after division, is present on the cortex of only one of the daughter cells. It is necessary for the asymmetric division, but the exact mechanism of its function is unknown.

An important question is how PAR-2 interacts with the cortex. The study using two-photon scanning FCS, presented in the attached article A8, has shown that PAR-2 is not

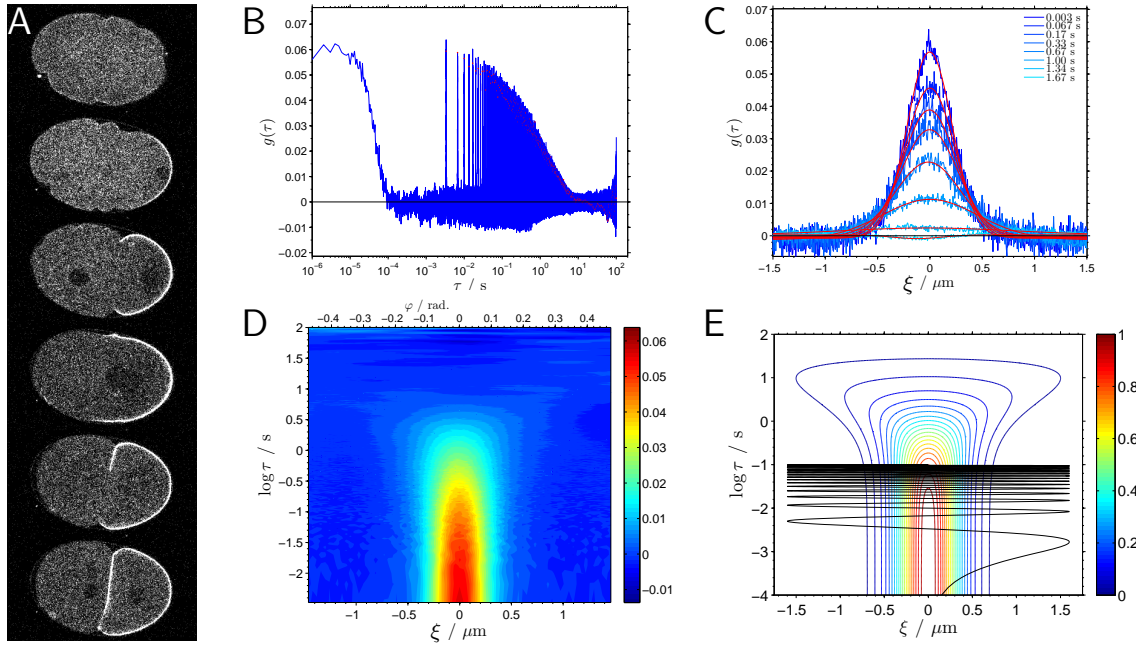


**Figure 8:** A: Polarization of *C. elegans* embryo during the first division visualized by the redistribution of the protein PAR-2 (total time period:  $\sim 20$  min., horizontal embryo size:  $\sim 50 \mu\text{m}$ ); B: an example of fluorescence autocorrelation of cortical PAR-2 obtained with circular scanning FCS; C: the evolution of the shape of selected correlation peaks from B with lag time  $\tau$ ; D: the correlation peaks from B replotted as a spatio-temporal fluorescence correlation  $g(\xi, \tau)$ ; E: the solid black line shows the subspace  $(\xi, \tau)$  of the spatio-temporal correlation probed by circular scan:  $\xi = 2R \sin(\pi f \tau)$  (plotted for  $R = 0.8 \mu\text{m}$ ,  $f = 300$  Hz, for clarity shown only for  $\tau < 0.1$  s).

rigidly bound to the cortex, but moves within it on timescales significantly shorter than NMY-2. Its motion has diffusive, or even subdiffusive, character (Fig. 8B-D), which might reflect heterogeneous population, also indicated by non-uniform fluorescence intensity of the images of the cortex. The motion of NMY-2, an integral part of the cortex, is slower and has a flow-like, directed rather than diffusive character, which could be attributed to the contractility of the cortex. The larger fraction, if not all, of PAR-2 in the cortex is therefore not rigidly bound to the cortex, and could possibly be located within the cellular membrane attached to the cortex from the outside.

The dynamics of the cortex proteins has been probed by scanning FCS with the scan radius much larger than the laser focus size, and with the focus positioned within the flattened part of the embryo cortex. The obtained fluorescence autocorrelation can be plotted in a standard way, as a function of the lag time  $\tau$ , consisting of narrow correlation peaks with their height decaying on the time-scale of the protein dynamics (Fig. 8B). Additional information is contained in the shape of the correlation peaks, which is related to the pdf of the molecular motion (Eq. 6) and the shape of the measurement volume  $S(\mathbf{r})$  (Fig. 8C). This can be replotted in a form of a spatio-temporal correlation  $g(\xi, \tau)$  (Fig. 8D).

The use of two-photon excitation and circular scanning in this study were of particular importance. The relatively slow motion of the proteins on the cortex precludes standard FCS measurements: the long residence time of the molecules in the focus leads to photobleaching, and to poor statistics during the short measurement time limited by the

sample stability and embryo development. Scanning the beam over a larger area means that more statistically independent locations are sampled, permitting shorter acquisition times. Additionally, the possible bleaching dose is distributed over a larger area leading to a negligible photobleaching effect. Furthermore, two-photon excitation significantly reduces cumulative photobleaching and phototoxicity, making prolonged observation of the embryo and the selection of the measurement time-point at the desired development stage possible.

The applications of fluorescence fluctuation methods, as exemplified by this work, have the potential to provide new quantitative information that can be used as input for models of polarity establishment [46], and in this way bring new insights into the function of complex systems, such as living cell.

## 6 Perspectives

Two main advantages of spatio-temporal fluorescence fluctuation analysis, realized by scanning FCS in this work, has been exploited here: the robustness to optical distortions affecting the measurement volume size or to the focus positioning with respect to the membrane, and the reduction of the effects of photobleaching, most relevant with slow transport processes, such as protein diffusion in the embryo cortex.

There is, however, a greater potential in spatio-temporal correlation methods, which has not been fully explored yet. In contrast to standard FCS, which probes motion only on the scale of the measurement volume, the spatio-temporal correlation can access dynamics on different spatial scales. It can therefore provide more information, which might help to distinguish between different, more complex, models, for example, combination of diffusion and attachment/detachment, diffusion affected by the complex environment or chemical reactions, etc.

In complex, heterogeneous environments, often encountered in biological context, the diffusion may differ from simple Brownian diffusion in that the particle probability distribution function  $p(\mathbf{r}, t)$  is not necessarily Gaussian (Eq. 6), and the mean square displacement does not increase linearly with time in the whole time range observed [49]. Such dynamics of diffusers are usually called anomalous diffusion. It has been observed in environments with high volume density of proteins or other large molecules, both in bulk [6] and in membranes [53], and in actin networks [132]. However, the crowding effects depend on the relative size of the ‘crowding’ molecules and diffusing molecules, and do not necessarily lead to anomalous diffusion [34], or only at certain time scales. The diffusion with modified diffusion coefficient can then be described by effective size-dependent viscosity [60].

A simple form of FCS probing different spatial scales — variable-spot size FCS (Fig. 3E) — has been employed to study diffusion in two distinct types of heterogeneous media [127]. In the first case, the molecules were thought to be confined to sub-resolution domains within which they diffuse relatively slowly. Occasionally, they could cross from one domain to another and thus overcome a large distance in a short time, effectively leading to faster diffusion on long time scales. The slower diffusion on the short time scales could not be observed directly due to the limitations by optical resolution, but could be inferred from the data measured at different volume sizes. In the second case, the molecules were

partially confined to spaces within a cytoskeleton network. On the short time scales the diffusion was faster, unaffected by the network; on the long time scales the diffusion was slowed down by the limited probability of crossing the cytoskeleton barrier. Since the standard FCS with several different volume sizes was shown to distinguish between these different situations and normal diffusion [82, 127], it is expected that spatio-temporal correlation experiments could contribute to better characterization and understanding of these complex diffusion processes.

The diffusion of molecules can deviate from normal diffusion also as a result of chemical reactions changing the molecule's diffusion coefficient. A simple example of such a reaction is the conversion between two forms, each with a different diffusion coefficient:  $D_1$  and  $D_2$ . The concentrations  $c_1$  and  $c_2$  of the two species obey the following reaction-diffusion equation:

$$\begin{aligned}\frac{\partial c_1(\mathbf{r}, t)}{\partial t} &= D_1 \Delta c_1 + a_{11} c_1 + a_{12} c_2 \\ \frac{\partial c_2(\mathbf{r}, t)}{\partial t} &= D_2 \Delta c_2 + a_{21} c_1 + a_{22} c_2,\end{aligned}\tag{14}$$

where the coefficients  $a_{ij}$  describe the interconversion rates. This model applies to, for example, binding to a larger molecule with the rate  $k_1 = -a_{11} = a_{21}$ , and detachment with the rate  $k_2 = a_{12} = -a_{22}$ . If the molecules become immobilized upon binding,  $D_2$  is set to zero [29, 86].

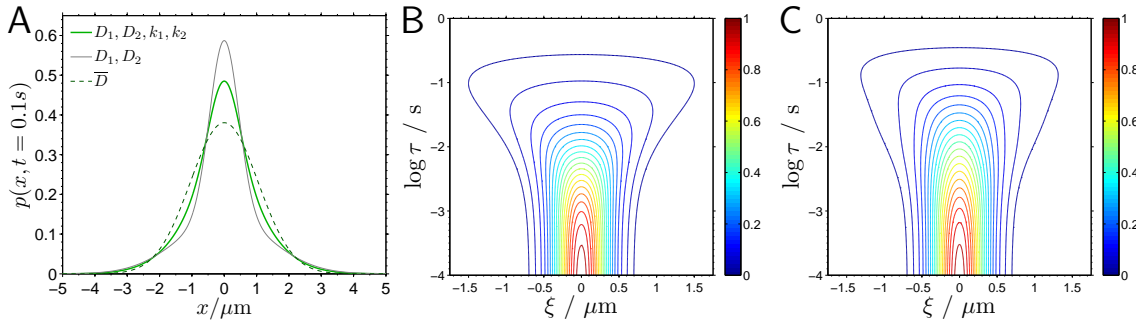


**Figure 9:** A: The probability density function  $p(x, t)$  of diffusing molecules switching between two diffusion coefficients as described by Eq. 14 at time  $t = 0.1 \text{ s}$  (thick green line) is different from the pdf of two types of molecules that do not interconvert (thin grey line) and also from the pdf of molecules diffusing with the average diffusion coefficient  $\bar{D}$  (dashed green line). B, C: this difference is preserved between the calculated spatio-temporal correlations of dynamics with the average diffusion coefficient  $\bar{D}$  (B) and dynamics with switching between  $D_1$  and  $D_2$  (C). ( $D_1 = 1 \mu\text{m}^2\text{s}^{-1}$ ,  $D_2 = 10 \mu\text{m}^2\text{s}^{-1}$ ,  $k_1 = k_2 = 10 \text{ s}^{-1}$ )

Although the mean square displacement in this model increases linearly with time, characterized by the weighted mean diffusion coefficient  $\bar{D}$ , the probability distribution function (pdf) for one particle is non-Gaussian, and deviates from both the pdf of normal diffusion (Eq. 6) with the mean diffusion coefficient  $\bar{D}$  and from the pdf of two independent components with  $D_1$  and  $D_2$  (Fig. 9A). Simply monitoring the mean square displacement therefore may not be sufficient to distinguish this process from simple Brownian diffusion. The situation where the mean square displacement is linear with time, but the distribution is non-Gaussian has been experimentally observed: diffusion of colloidal particles along lipid tubes and in actin network [126].

Spatio-temporal correlation measurement is sensitive to the shape of the probability density distribution of the diffusing particle. Although the spatial resolution is limited by the size of the measurement volume, the difference between simple diffusion and diffusion with change of diffusivity (Eq. 14) might be sufficiently large and should be experimentally observable (Fig. 9B-C). Spatio-temporal correlation could therefore be an alternative to particle tracking methods used to study diffusion in complex environments.

Simple biological and biochemical processes can be described by reaction-diffusion models of molecular interactions and dynamics in geometries derived from the shapes of cells and tissues. An early example of such a model is the description by A. Turing [123] of the formation and maintenance of a stationary non-uniform concentration profile of biologically active molecules ('concentration gradient'), as a consequence of localized production, diffusional spreading, and distributed degradation. Models of this kind are used to describe, for example, oscillations of protein concentration in bacteria [56], formation of concentration gradients affecting the development of tissues [16, 135], cell polarization [46], spatial pattern formation [69], etc.

Future models of biological processes can be expected to encompass a broader range of physical phenomena. The coupling of chemical reactions to the mechanics of macromolecules and molecular assemblies can give rise to force generation (for example, motor proteins interacting with microfilaments), directed motion and flows on larger than molecular scales, stress and strain on the level of cells and tissues [54]. The mechanical processes can then affect back the chemical reactions, by changing the geometry of the reaction environment (boundary conditions), and possibly the concentrations of the reacting species.

The construction and verification of such models requires experimental determination of a range of quantitative physical parameters — among them also diffusion coefficients, concentrations and rate constants. Fluorescence fluctuation methods have potential to provide these values with sufficient accuracy and under undisturbed, biologically relevant conditions.

## 7 References

- [1] M. Andrec, R. M. Levy, and D. S. Talaga. Direct determination of kinetic rates from single-molecule photon arrival trajectories using hidden Markov models. *J. Phys. Chem. A*, 107(38):7454–7464, September 2003.
- [2] A. Assion, T. Baumert, M. Bergt, T. Brixner, B. Kiefer, V. Seyfried, M. Strehle, and G. Gerber. Control of chemical reactions by feedback-optimized phase-shaped femtosecond laser pulses. *Science*, 282(5390):919–922, October 1998.
- [3] K. Bacia, S. A. Kim, and P. Schwille. Fluorescence cross-correlation spectroscopy in living cells. *Nat. Methods*, 3(2):83–89, Feb 2006.
- [4] K. Bacia, D. Scherfeld, N. Kahya, and P. Schwille. Fluorescence correlation spectroscopy relates rafts in model and native membranes. *Biophys. J.*, 87(2):1034–1043, August 2004.
- [5] K. Bacia, P. Schwille, and T. Kurzchalia. Sterol structure determines the separation of phases and the curvature of the liquid-ordered phase in model membranes. *Proc. Natl. Acad. Sci. U. S. A.*, 102(9):3272–3277, March 2005.
- [6] D. S. Banks and C. Fradin. Anomalous diffusion of proteins due to molecular crowding. *Biophys. J.*, 89(5):2960–2971, November 2005.
- [7] A. Benda, M. Beneš, V. Mareček, A. Lhotský, W. T. Hermens, and M. Hof. How to determine diffusion coefficients in planar phospholipid systems by confocal fluorescence correlation spectroscopy. *Langmuir*, 19(10):4120–4126, May 2003.
- [8] K. Berland and G. Q. Shen. Excitation saturation in two-photon fluorescence correlation spectroscopy. *Appl. Opt.*, 42(27):5566–5576, September 2003.
- [9] K. M. Berland, P. T. C. So, Y. Chen, W. W. Mantulin, and E. Gratton. Scanning two-photon fluctuation correlation spectroscopy: Particle counting measurements for detection of molecular aggregation. *Biophys. J.*, 71(1):410–420, 1996.
- [10] K. M. Berland, P. T. C. So, and E. Gratton. Two-photon fluorescence correlation spectroscopy: Method and application to the intracellular environment. *Biophys. J.*, 68(2):694–701, February 1995.
- [11] B. J. Berne and R. Pecora. *Dynamic Light Scattering*. Dover Publications Inc., 2003.
- [12] E. Betzig, G. H. Patterson, R. Sougrat, O. W. Lindwasser, S. Olenych, J. S. Bonifacino, M. W. Davidson, J. Lippincott-Schwartz, and H. F. Hess. Imaging intracellular fluorescent proteins at nanometer resolution. *Science*, 313(5793):1642–1645, Sep 2006.
- [13] Y. Blancquaert, A. Delon, J. Derouard, and R. Jaffiol. Spatial fluorescence cross-correlation spectroscopy between core and ring pinholes. *Proc. of SPIE*, 6191:61910B, 2006.
- [14] Y. Blancquaert, J. Gao, J. Derouard, and A. Delon. Spatial fluorescence cross-correlation spectroscopy by means of a spatial light modulator. *Journal Of Biophotonics*, 1(5):408–418, October 2008.
- [15] M. Bohmer, M. Wahl, H. J. Rahn, R. Erdmann, and J. Enderlein. Time-resolved fluorescence correlation spectroscopy. *Chem. Phys. Lett.*, 353(5-6):439–445, February 2002.
- [16] T. Bollenbach, K. Kruse, P. Pantazis, M. González-Gaitán, and F. Jülicher. Robust formation of morphogen gradients. *Phys. Rev. Lett.*, 94(1):018103, January 2005.
- [17] M. Born and E. Wolf. *Principles of Optics*. Cambridge University Press, 7th edition, 1999.
- [18] J. W. Borst, S. P. Laptanok, A. H. Westphal, R. Kuhnemuth, H. Hornen, N. V. Visser, S. Kalinin, J. Aker, A. van Hoek, C. A. M. Seidel, and A. J. W. G. Visser. Structural changes of yellow cameleon domains observed by quantitative fret analysis and polarized fluorescence correlation spectroscopy. *Biophys. J.*, 95(11):5399–5411, December 2008.

- [19] M. Brinkmeier, K. Dörre, K. Riebeseel, and R. Rigler. Confocal spectroscopy in microstructures. *Biophys. Chem.*, 66(2-3):229–239, June 1997.
- [20] M. Burkhardt and P. Schwille. Electron multiplying ccd based detection for spatially resolved fluorescence correlation spectroscopy. *Opt. Express*, 14(12):5013–5020, June 2006.
- [21] Y. Chen, J. D. Müller, P. T. So, and E. Gratton. The photon counting histogram in fluorescence fluctuation spectroscopy. *Biophys. J.*, 77(1):553–567, Jul 1999.
- [22] S. Chiantia, J. Ries, N. Kahya, and P. Schwille. Combined AFM and two-focus SFCS study of raft-exhibiting model membranes. *ChemPhysChem*, 7(11):2409–2418, November 2006.
- [23] M. Dantus and V. V. Lozovoy. Experimental coherent laser control of physicochemical processes. *Chem. Rev.*, 104(4):1813–1859, April 2004.
- [24] J. M. Dela Cruz, I. Pastirk, V. V. Lozovoy, K. A. Walowicz, and M. Dantus. Multiphoton intrapulse interference 3: Probing microscopic chemical environments. *J. Phys. Chem. A*, 108(1):53–58, January 2004.
- [25] A. Delon, Y. Usson, J. Derouard, T. Biben, and C. Souchier. Photobleaching, mobility, and compartmentalisation: Inferences in fluorescence correlation spectroscopy. *J. Fluoresc.*, 14(3):255–267, May 2004.
- [26] W. Denk, J. H. Strickler, and W. W. Webb. 2-photon laser scanning fluorescence microscopy. *Science*, 248(4951):73–76, April 1990.
- [27] T. Dertinger, A. Loman, B. Ewers, C. B. Müller, B. Krämer, and J. Enderlein. The optics and performance of dual-focus fluorescence correlation spectroscopy. *Opt. Express*, 16(19):14353–14368, September 2008.
- [28] T. Dertinger, V. Pacheco, I. von der Hocht, R. Hartmann, I. Gregor, and J. Enderlein. Two-focus fluorescence correlation spectroscopy: A new tool for accurate and absolute diffusion measurements. *ChemPhysChem*, 8:433–443, 2007.
- [29] T. Dertinger, I. von der Hocht, A. Benda, M. Hof, and J. Enderlein. Surface sticking and lateral diffusion of lipids in supported bilayers. *Langmuir*, 22(22):9339–9344, October 2006.
- [30] M. A. Digman, C. M. Brown, P. Sengupta, P. W. Wiseman, A. R. Horwitz, and E. Gratton. Measuring fast dynamics in solutions and cells with a laser scanning microscope. *Biophys. J.*, 89(2):1317–1327, 2005.
- [31] M. A. Digman, P. Sengupta, P. W. Wiseman, C. M. Brown, A. R. Horwitz, and E. Gratton. Fluctuation correlation spectroscopy with a laser-scanning microscope: Exploiting the hidden time structure. *Biophys. J.*, 88(5):L33–L36, 2005.
- [32] P. S. Dittrich and P. Schwille. Photobleaching and stabilization of fluorophores used for single-molecule analysis with one- and two-photon excitation. *Appl. Phys. B: Lasers Opt.*, 73(8):829–837, December 2001.
- [33] P. S. Dittrich and P. Schwille. Spatial two-photon fluorescence cross-correlation spectroscopy for controlling molecular transport in microfluidic structures. *Anal. Chem.*, 74(17):4472–4479, September 2002.
- [34] J. A. Dix and A. S. Verkman. Crowding effects on diffusion in solutions and cells. *Annu. Rev. Biophys.*, 37:247–263, 2008.
- [35] G. Donnert, C. Eggeling, and S. W. Hell. Major signal increase in fluorescence microscopy through dark-state relaxation. *Nat. Methods*, 4(1):81–86, Jan 2007.
- [36] C. Eggeling, C. Ringemann, R. Medda, G. Schwarzmann, K. Sandhoff, S. Polyakova, V. N. Belov, B. Hein, C. von Middendorff, A. Schönle, and S. W. Hell. Direct observation of the nanoscale dynamics of membrane lipids in a living cell. *Nature*, 457(7233):1159–1162, February 2009.

- [37] C. Eggeling, A. Volkmer, and C. A. M. Seidel. Molecular photobleaching kinetics of rhodamine 6G by one- and two-photon induced confocal fluorescence microscopy. *ChemPhysChem*, 6(5):791–804, May 2005.
- [38] C. Eggeling, J. Widengren, R. Rigler, and C. A. M. Seidel. Photobleaching of fluorescent dyes under conditions used for single-molecule detection: Evidence of two-step photolysis. *Anal. Chem.*, 70(13):2651–2659, July 1998.
- [39] A. Eldar and M. B. Elowitz. Functional roles for noise in genetic circuits. *Nature*, 467(7312):167–173, September 2010.
- [40] E. L. Elson and D. Magde. Fluorescence correlation spectroscopy. I. Conceptual basis and theory. *Biopolymers*, 13(1):1–27, 1974.
- [41] J. Enderlein. Fluorescence detection of single molecules near a solution/glass interfacean electrodynamic analysis. *Chem. Phys. Lett.*, 308(3-4):263–266, July 1999.
- [42] J. Enderlein. Theoretical study of detection of a dipole emitter through an objective with high numerical aperture. *Opt. Lett.*, 25(9):634–636, May 2000.
- [43] J. Enderlein, I. Gregor, D. Patra, T. Dertinger, and U. B. Kaupp. Performance of fluorescence correlation spectroscopy for measuring diffusion and concentration. *ChemPhysChem*, 6(11):2324–2336, November 2005.
- [44] G. Feher and M. Weissman. Fluctuation spectroscopy: Determination of chemical reaction kinetics from frequency spectrum of fluctuations. *Proc. Natl. Acad. Sci. U. S. A.*, 70(3):870–875, 1973.
- [45] A. Gennerich and D. Schild. Fluorescence correlation spectroscopy in small cytosolic compartments depends critically on the diffusion model used. *Biophys. J.*, 79(6):3294–3306, 2000.
- [46] N. W. Goehring, P. K. Trong, J. S. Bois, D. Chowdhury, E. M. Nicola, A. A. Hyman, and S. W. Grill. Polarization of PAR proteins by advective triggering of a pattern-forming system. *Science*, 334(6059):1137–1141, November 2011.
- [47] M. Gösch, A. Serov, T. Anhut, T. Lasser, A. Rochas, P. A. Besse, R. S. Popovic, H. Blom, and R. Rigler. Parallel single molecule detection with a fully integrated single-photon 2x2 CMOS detector array. *J. Biomed. Opt.*, 9(5):913–921, September 2004.
- [48] I. Gregor, D. Patra, and J. Enderlein. Optical saturation in fluorescence correlation spectroscopy under continuous-wave and pulsed excitation. *ChemPhysChem*, 6(1):164–170, January 2005.
- [49] S. Havlin and D. Ben-Avraham. Diffusion in disordered media. *Adv. Phys.*, 36(6):695–798, November 1987.
- [50] K. G. Heinze, A. Koltermann, and P. Schwille. Simultaneous two-photon excitation of distinct labels for dual-color fluorescence crosscorrelation analysis. *Proc. Natl. Acad. Sci. U. S. A.*, 97(19):10377–10382, September 2000.
- [51] S. W. Hell. Far-field optical nanoscopy. *Science*, 316(5828):1153–1158, May 2007.
- [52] F. Helmchen and W. Denk. Deep tissue two-photon microscopy. *Nat. Methods*, 2(12):932–940, December 2005.
- [53] M. R. Horton, F. Höfling, J. O. Rädler, and T. Franosch. Development of anomalous diffusion among crowding proteins. *Soft Matter*, 6(12):2648–2656, 2010.
- [54] J. Howard, S. W. Grill, and J. S. Bois. Turing’s next steps: the mechanochemical basis of morphogenesis. *Nat. Rev. Mol. Cell Biol.*, 12(6):392–398, June 2011.
- [55] M. Howard and A. D. Rutenberg. Pattern formation inside bacteria: Fluctuations due to the low copy number of proteins. *Phys. Rev. Lett.*, 90(12):128102, March 2003.

- [56] M. Howard, A. D. Rutenberg, and S. de Vet. Dynamic compartmentalization of bacteria: Accurate division in E-coli. *Phys. Rev. Lett.*, 87(27):278102, December 2001.
- [57] R. Jaffiol, Y. Blancquaert, A. Delon, and J. Derouard. Spatial fluorescence cross-correlation spectroscopy. *Appl. Opt.*, 45(6):1225–1235, February 2006.
- [58] N. Ji, J. C. Magee, and E. Betzig. High-speed, low-photodamage nonlinear imaging using passive pulse splitters. *Nat. Methods*, 5(2):197–202, February 2008.
- [59] N. Kahya. Protein-protein and protein-lipid interactions in domain-assembly: Lessons from giant unilamellar vesicles. *Biochim. Biophys. Acta Biomembr.*, 1798(7):1392–1398, July 2010.
- [60] T. Kalwarczyk, N. Ziębacz, A. Bielejewska, E. Zaboklicka, K. Koynov, J. Szymański, A. Wilk, A. Patkowski, J. Gapiński, H. J. Butt, and R. Hołyst. Comparative analysis of viscosity of complex liquids and cytoplasm of mammalian cells at the nanoscale. *Nano Lett.*, 11(5):2157–2163, May 2011.
- [61] B. Kannan, L. Guo, T. Sudhakaran, S. Ahmed, I. Maruyama, and T. Wohland. Spatially resolved total internal reflection fluorescence correlation microscopy using an electron multiplying charge-coupled device camera. *Anal. Chem.*, 79(12):4463–4470, June 2007.
- [62] B. Kannan, J. Y. Har, P. Liu, I. Maruyama, J. L. Ding, and T. Wohland. Electron multiplying charge-coupled device camera based fluorescence correlation spectroscopy. *Anal. Chem.*, 78(10):3444–3451, May 2006.
- [63] P. Kapusta, M. Wahl, A. Benda, M. Hof, and J. Enderlein. Fluorescence lifetime correlation spectroscopy. *J. Fluoresc.*, 17(1):43–48, January 2007.
- [64] P. Kask, K. Palo, D. Ullmann, and K. Gall. Fluorescence-intensity distribution analysis and its application in biomolecular detection technology. *Proc. Natl. Acad. Sci. U. S. A.*, 96(24):13756–13761, Nov 1999.
- [65] L. Kastrup, H. Blom, C. Eggeling, and S. W. Hell. Fluorescence fluctuation spectroscopy in sub-diffraction focal volumes. *Phys. Rev. Lett.*, 94(17):178104, May 2005.
- [66] H. Kawano, Y. Nabekawa, A. Suda, Y. Oishi, H. Mizuno, A. Miyawaki, and K. Midorikawa. Attenuation of photobleaching in two-photon excitation fluorescence from green fluorescent protein with shaped excitation pulses. *Biochem. Biophys. Res. Commun.*, 311(3):592–596, November 2003.
- [67] S. A. Kim, K. G. Heinze, and P. Schwille. Fluorescence correlation spectroscopy in living cells. *Nat. Methods*, 4(11):963–973, November 2007.
- [68] H. Kitano. Towards a theory of biological robustness. *Mol. Syst. Biol.*, 3:137, September 2007.
- [69] S. Kondo and T. Miura. Reaction-diffusion model as a framework for understanding biological pattern formation. *Science*, 329(5999):1616–1620, September 2010.
- [70] K. König. Multiphoton microscopy in life sciences. *J. Microsc.*, 200:83–104, 2000.
- [71] D. E. Koppel. Statistical accuracy in fluorescence correlation spectroscopy. *Phys. Rev. A: At., Mol., Opt. Phys.*, 10(6):1938–1945, 1974.
- [72] D. E. Koppel, F. Morgan, A. E. Cowan, and J. H. Carson. Scanning concentration correlation spectroscopy using the confocal laser microscope. *Biophys. J.*, 66(2):502–507, 1994.
- [73] J. Korlach, P. Schwille, W. W. Webb, and G. W. Feigenson. Characterization of lipid bilayer phases by confocal microscopy and fluorescence correlation spectroscopy. *Proc. Natl. Acad. Sci. U. S. A.*, 96(15):8461–8466, July 1999.
- [74] O. Krichevsky and G. Bonnet. Fluorescence correlation spectroscopy: the technique and its applications. *Rep. Prog. Phys.*, 65(2):251–297, 2002.
- [75] J. R. Lakowicz. *Principles of Fluorescence Spectroscopy*. Springer, 3rd edition, 2006.

- [76] D. R. Larson, W. R. Zipfel, R. M. Williams, S. W. Clark, M. P. Bruchez, F. W. Wise, and W. W. Webb. Water-soluble quantum dots for multiphoton fluorescence imaging in vivo. *Science*, 300(5624):1434–1436, May 2003.
- [77] M. J. Levene, J. Korlach, S. W. Turner, M. Foquet, H. G. Craighead, and W. W. Webb. Zero-mode waveguides for single-molecule analysis at high concentrations. *Science*, 299(5607):682–686, January 2003.
- [78] A. Loman, T. Dertinger, F. Koberling, and J. Enderlein. Comparison of optical saturation effects in conventional and dual-focus fluorescence correlation spectroscopy. *Chem. Phys. Lett.*, 459(1-6):18–21, June 2008.
- [79] W. Lukosz. Light-emission by magnetic and electric dipoles close to a plane dielectric interface. 3. Radiation-patterns of dipoles with arbitrary orientation. *J. Opt. Soc. Am.*, 69(11):1495–1503, 1979.
- [80] H. L. Ma, J. Jimenez, and R. Rajagopalan. Brownian fluctuation spectroscopy using atomic force microscopes. *Langmuir*, 16(5):2254–2261, March 2000.
- [81] D. Magde, W. W. Webb, and E. Elson. Thermodynamic fluctuations in a reacting system — measurement by fluorescence correlation spectroscopy. *Phys. Rev. Lett.*, 29(11):705–708, 1972.
- [82] A. Masuda, K. Ushida, and T. Okamoto. Direct observation of spatiotemporal dependence of anomalous diffusion in inhomogeneous fluid by sampling-volume-controlled fluorescence correlation spectroscopy. *Physical Review E*, 72(6):060101, December 2005.
- [83] J. Mertz. Molecular photodynamics involved in multi-photon excitation fluorescence microscopy. *Eur. Phys. J. D*, 3(1):53–66, 1998.
- [84] D. Meshulach and Y. Silberberg. Coherent quantum control of two-photon transitions by a femtosecond laser pulse. *Nature*, 396(6708):239–242, November 1998.
- [85] D. Meshulach and Y. Silberberg. Coherent quantum control of multiphoton transitions by shaped ultrashort optical pulses. *Phys. Rev. A: At., Mol., Opt. Phys.*, 60(2):1287–1292, August 1999.
- [86] A. Michelman-Ribeiro, D. Mazza, T. Rosales, T. J. Stasevich, H. Boukari, V. Rishi, C. Vinson, J. R. Knutson, and J. G. McNally. Direct measurement of association and dissociation rates of DNA binding in live cells by fluorescence correlation spectroscopy. *Biophys. J.*, 97(1):337–346, July 2009.
- [87] J. Müller. Fluctuation spectroscopy: A new approach for studying low-dimensional molecular metals. *ChemPhysChem*, 12(7):1222–1245, May 2011.
- [88] J. D. Müller. Cumulant analysis in fluorescence fluctuation spectroscopy. *Biophys. J.*, 86(6):3981–3992, June 2004.
- [89] J. Mütze, V. Iyer, J. J. Macklin, J. Colonell, B. Karsh, Z. Petrášek, P. Schwille, L. L. Looger, L. D. Lavis, and T. D. Harris. Excitation spectra and brightness optimization of two-photon excited probes. *Biophys. J.*, 102(4):934–944, February 2012.
- [90] J. Mütze, Z. Petrášek, and P. Schwille. Independence of maximum single molecule fluorescence count rate on the temporal and spectral laser pulse width in two-photon FCS. *J. Fluoresc.*, 17:805–810, 2007.
- [91] A. Nagy, J. R. Wu, and K. M. Berland. Characterizing observation volumes and the role of excitation saturation in one-photon fluorescence fluctuation spectroscopy. *J. Biomed. Opt.*, 10(4):044015, 2005.
- [92] A. Nagy, J. R. Wu, and K. M. Berland. Observation volumes and  $\gamma$ -factors in two-photon fluorescence fluctuation spectroscopy. *Biophys. J.*, 89(3):2077–2090, September 2005.
- [93] P. Nuernberger, G. Vogt, T. Brixner, and G. Gerber. Femtosecond quantum control of molecular dynamics in the condensed phase. *Phys. Chem. Chem. Phys.*, 9(20):2470–2497, 2007.
- [94] J. P. Ogilvie, D. Debarre, X. Solinas, J. L. Martin, E. Beaurepaire, and M. Joffre. Use of coherent control for selective two-photon fluorescence microscopy in live organisms. *Opt. Express*, 14(2):759–766, January 2006.

- [95] A. G. Palmer and N. L. Thompson. Molecular aggregation characterized by high order autocorrelation in fluorescence correlation spectroscopy. *Biophys. J.*, 52(2):257–270, Aug 1987.
- [96] A. G. Palmer and N. L. Thompson. High-order fluorescence fluctuation analysis of model protein clusters. *Proc. Natl. Acad. Sci. U.S.A.*, 86(16):6148–6152, 1989.
- [97] G. H. Patterson and D. W. Piston. Photobleaching in two-photon excitation microscopy. *Biophys. J.*, 78(4):2159–2162, April 2000.
- [98] Z. Petrášek, S. Derenko, and P. Schwille. Circular scanning fluorescence correlation spectroscopy on membranes. *Opt. Express*, 19(25):25006–25021, December 2011.
- [99] Z. Petrášek, C. Hoegel, A. Mashaghi, T. Ohrt, A. A. Hyman, and P. Schwille. Characterization of protein dynamics in asymmetric cell division by scanning fluorescence correlation spectroscopy. *Biophys. J.*, 95(11):5476–5486, December 2008.
- [100] Z. Petrášek, M. Krishnan, I. Mönch, and P. Schwille. Simultaneous two-photon fluorescence correlation spectroscopy and lifetime imaging of dye molecules in submicrometer fluidic structures. *Microsc. Res. Tech.*, 70(5):459–466, May 2007.
- [101] Z. Petrášek and P. Schwille. Photobleaching in two-photon scanning fluorescence correlation spectroscopy. *ChemPhysChem*, 9:147–158, 2008.
- [102] Z. Petrášek and P. Schwille. Precise measurement of diffusion coefficients using scanning fluorescence correlation spectroscopy. *Biophys. J.*, 94:1437–1448, 2008.
- [103] Z. Petrášek and P. Schwille. *Single Molecules and Nanotechnology*, volume 12 of *Springer Series in Biophysics*, chapter Scanning fluorescence correlation spectroscopy, pages 83–105. Springer, 2008. Chapter 4.
- [104] Z. Petrášek and P. Schwille. Fluctuations as a source of information in fluorescence microscopy. *J. R. Soc. Interface*, 6:S15–S25, February 2009.
- [105] E. P. Petrov and P. Schwille. *Standardization and Quality Assurance in Fluorescence Measurements II: Bioanalytical and Biomedical Applications*, volume 6 of *Springer Series on Fluorescence*, chapter State of the Art and Novel Trends in Fluorescence Correlation Spectroscopy, pages 145–197. Springer, Berlin, Heidelberg, New York, 2008.
- [106] C. M. Pieper and J. Enderlein. Fluorescence correlation spectroscopy as a tool for measuring the rotational diffusion of macromolecules. *Chem. Phys. Lett.*, 516(1-3):1–11, November 2011.
- [107] H. Qian and E. L. Elson. On the analysis of high order moments of fluorescence fluctuations. *Biophys. J.*, 57(2):375–380, Feb 1990.
- [108] I. Rasnik, S. A. McKinney, and T. Ha. Nonblinking and longlasting single-molecule fluorescence imaging. *Nat. Methods*, 3(11):891–893, November 2006.
- [109] R. P. Richter, R. Berat, and A. R. Brisson. Formation of solid-supported lipid bilayers: An integrated view. *Langmuir*, 22(8):3497–3505, April 2006.
- [110] T. K. Rostovtseva and S. M. Bezrukov. ATP transport through a single mitochondrial channel, VDAC, studied by current fluctuation analysis. *Biophys. J.*, 74(5):2365–2373, May 1998.
- [111] E. Sackmann. Supported membranes: Scientific and practical applications. *Science*, 271(5245):43–48, January 1996.
- [112] E. J. Sánchez, L. Novotny, G. R. Holtom, and X. S. Xie. Room-temperature fluorescence imaging and spectroscopy of single molecules by two-photon excitation. *J. Phys. Chem. A*, 101(38):7019–7023, September 1997.
- [113] P. Schwille, U. Haupts, S. Maiti, and W. W. Webb. Molecular dynamics in living cells observed by fluorescence correlation spectroscopy with one- and two-photon excitation. *Biophys. J.*, 77(4):2251–2265, October 1999.

- [114] P. Schwille and K. G. Heinze. Two-photon fluorescence cross-correlation spectroscopy. *ChemPhysChem*, 2(5):269–272, May 2001.
- [115] P. Schwille, J. Korfach, and W. W. Webb. Fluorescence correlation spectroscopy with single-molecule sensitivity on cell and model membranes. *Cytometry*, 36(3):176–182, July 1999.
- [116] P. Schwille, F. J. Meyer-Almes, and R. Rigler. Dual-color fluorescence cross-correlation spectroscopy for multicomponent diffusional analysis in solution. *Biophys. J.*, 72(4):1878–1886, 1997.
- [117] N. C. Shaner, P. A. Steinbach, and R. Y. Tsien. A guide to choosing fluorescent proteins. *Nat. Methods*, 2(12):905–909, December 2005.
- [118] Y. Silberberg. Quantum coherent control for nonlinear spectroscopy and microscopy. *Annu. Rev. Phys. Chem.*, 60:277–292, 2009.
- [119] J. P. Skinner, Y. Chen, and J. D. Müller. Position-sensitive scanning fluorescence correlation spectroscopy. *Biophys. J.*, 89(2):1288–1301, 2005.
- [120] K. Suhling, P. M. W. French, and D. Phillips. Time-resolved fluorescence microscopy. *Photochem. Photobiol. Sci.*, 4(1):13–22, 2005.
- [121] P. Theer, M. T. Hasan, and W. Denk. Two-photon imaging to a depth of 1000  $\mu\text{m}$  in living brains by use of a  $\text{Ti:Al}_2\text{O}_3$  regenerative amplifier. *Opt. Lett.*, 28(12):1022–1024, June 2003.
- [122] N. L. Thompson, T. P. Burghardt, and D. Axelrod. Measuring surface dynamics of biomolecules by total internal-reflection fluorescence with photobleaching recovery or correlation spectroscopy. *Biophys. J.*, 33(3):435–454, 1981.
- [123] A. M. Turing. The chemical basis of morphogenesis. *Philos. Trans. R. Soc. Lond. B. Biol. Sci.*, 237(641):37–72, 1952.
- [124] J. Vogelsang, R. Kasper, C. Steinhauer, B. Person, M. Heilemann, M. Sauer, and P. Tinnefeld. A reducing and oxidizing system minimizes photobleaching and blinking of fluorescent dyes. *Angew. Chem., Int. Ed.*, 47(29):5465–5469, 2008.
- [125] I. von der Hocht and J. Enderlein. Fluorescence correlation spectroscopy in cells: Confinement and excluded volume effects. *Exp. Mol. Pathol.*, 82(2):142–146, April 2007.
- [126] B. Wang, S. M. Anthony, S. C. Bae, and S. Granick. Anomalous yet brownian. *Proc. Natl. Acad. Sci. U. S. A.*, 106(36):15160–15164, September 2009.
- [127] L. Wawrezynieck, H. Rigneault, D. Marguet, and P. F. Lenne. Fluorescence correlation spectroscopy diffusion laws to probe the submicron cell membrane organization. *Biophys. J.*, 89(6):4029–4042, December 2005.
- [128] M. B. Weissman. Fluctuation spectroscopy. *Annu. Rev. Phys. Chem.*, 32:205–232, 1981.
- [129] J. Widengren, A. Chmyrov, C. Eggeling, P. A. Lofdahl, and C. A. M. Seidel. Strategies to improve photostabilities in ultrasensitive fluorescence spectroscopy. *J. Phys. Chem. A*, 111(3):429–440, January 2007.
- [130] J. Widengren and R. Rigler. Mechanisms of photobleaching investigated by fluorescence correlation spectroscopy. *Bioimaging*, 4:149–157, 1996.
- [131] J. Widengren, R. Rigler, and Ü. Mets. Triplet-state monitoring by fluorescence correlation spectroscopy. *J. Fluoresc.*, 4(3):255–258, 1994.
- [132] I. Y. Wong, M. L. Gardel, D. R. Reichman, E. R. Weeks, M. T. Valentine, A. R. Bausch, and D. A. Weitz. Anomalous diffusion probes microstructure dynamics of entangled F-actin networks. *Phys. Rev. Lett.*, 92(17):178101, April 2004.
- [133] C. Xu, R. M. Williams, W. Zipfel, and W. W. Webb. Multiphoton excitation cross-sections of molecular fluorophores. *Bioimaging*, 4:198–207, 1996.

- [134] C. Xu, W. Zipfel, J. B. Shear, R. M. Williams, and W. W. Webb. Multiphoton fluorescence excitation: New spectral windows for biological nonlinear microscopy. *Proc. Natl. Acad. Sci. U. S. A.*, 93(20):10763–10768, October 1996.
- [135] S. R. Yu, M. Burkhardt, M. Nowak, J. Ries, Z. Petrášek, S. Scholpp, P. Schwille, and M. Brand. Fgf8 morphogen gradient forms by a source-sink mechanism with freely diffusing molecules. *Nature*, 461(7263):533–536, September 2009.
- [136] W. R. Zipfel, R. M. Williams, and W. W. Webb. Nonlinear magic: multiphoton microscopy in the biosciences. *Nat. Biotechnol.*, 21(11):1369–1376, November 2003.



## 8 Included articles

### A1

#### **Fluctuations as a source of information in fluorescence microscopy**

Z. Petrášek and P. Schwille

*J. R. Soc. Interface*, 6:S15–S25, 2009.



## REVIEW

# Fluctuations as a source of information in fluorescence microscopy

Zdeněk Petrášek\* and Petra Schwille

*Biophysics group, Biotechnologisches Zentrum, Technische Universität Dresden,  
Tatzberg 47-51, 01307 Dresden, Germany*

Fluctuations in fluorescence spectroscopy and microscopy have traditionally been regarded as noise—they lower the resolution and contrast and do not permit high acquisition rates. However, fluctuations can also be used to gain additional information about a system. This fact has been exploited in single-point microscopic techniques, such as fluorescence correlation spectroscopy and analysis of single molecule trajectories, and also in the imaging field, e.g. in spatio-temporal image correlation spectroscopy. Here, we discuss how fluctuations are used to obtain more quantitative information from the data than that given by average values, while minimizing the effects of noise due to stochastic photon detection.

**Keywords:** fluorescence spectroscopy; imaging; single molecule

## 1. INTRODUCTION

Fluorescence spectroscopy and microscopy techniques use the sensitivity of fluorescence to the environment of the probe to gain important information about the investigated system. The temporal variation of fluorescence parameters, such as intensity, lifetime, anisotropy or spectral properties, reflects the dynamic behaviour, while the spatial variation of these quantities provides contrast in imaging. The effects of fluorescence resonance energy transfer (FRET) or electron transfer on fluorescence allow spatial resolution far above the optical diffraction limit.

When studying samples with low concentration of fluorescent species or individual molecules, or when operating at high temporal resolution, the measured signal is typically weak and fluctuating. Often only the mean value of the signal is considered relevant, while the fluctuations are regarded as noise. This apparent noise does not, however, have its origin only in the imperfections of the experimental procedure, but the observable fluctuations are an inherent property of the thermodynamic system due to its small size. The presence of equilibrium fluctuations of an observable physical parameter has been exploited in various non-fluorescence fluctuation techniques, such as quasi-elastic light scattering (Berne & Pecora 1976), conductivity fluctuations in solutions (Feher & Weissman 1973) or through channels in a membrane (Neher & Stevens 1977), etc. (Weissman 1981). The high sensitivity combined with high temporal and spatial resolution that can be

achieved experimentally by detecting fluorescence is the reason why the techniques where the fluctuations of physical quantities of a system are reflected by fluctuations in fluorescence have become the most widespread. Fluorescence fluctuation techniques have been extensively applied in chemistry, biophysics, biology and related fields in studies of photochemistry, diffusion properties, chemical kinetics, binding equilibria, aggregation, conformational fluctuations, to name a few (Rigler & Elson 2001; Krichevsky & Bonnet 2002; Petrov & Schwille 2008), both *in vitro* (Kahya & Schwille 2006) and in living cells (Bacia & Schwille 2003; Bacia *et al.* 2006), on small molecular ensembles as well as on single molecules (Edman & Rigler 2000).

The observed fluorescence fluctuations have usually several different sources. First, the signal fluctuations originate from varying number of emitters in the probed volume, or from variations of the emission properties of the emitting species due to interactions (lifetime and spectrum), reorientation (anisotropy) or internal dynamics. These fluctuations reflect an underlying physical evolution of the system, and are therefore of high interest. A second source of fluctuations, particularly relevant at low light levels or short integration times, is the variation of the number of detected photons due to the stochastic nature of light emission and detection. Also referred to as shot noise, these fluctuations do not carry useful information, but rather obscure the investigated physical process. Other fluctuation sources are those linked to background fluorescence, impurities or scattered light, and noise associated with the detection device (read-out noise, etc.).

While the relevance of the latter fluctuation sources can be reduced by eliminating background signals,

\*Author for correspondence (zdenek.petrasek@biotec.tu-dresden.de).

One contribution of 9 to a Theme Supplement 'Quantitative fluorescence microscopy: The 1st international Theodor Förster lecture series'.

improvement of the optical design, development in detection technology and the use of photon-counting detectors, the first two sources will always be present. The aim of fluctuation-oriented techniques is to use the fluctuations of an observable fluorescence parameter to gain better insight into the physics of the system. Shot noise fluctuations present an obstacle on the way to this goal. Proper data treatment is required to eliminate the shot noise effects, while preserving the relevant information during the data reduction process, without introducing biases and at the same time keeping the precision as high as possible. The data analysis, usually involving averaging, should ideally return enough information to allow discrimination between different models.

The great importance of equilibrium fluctuations in physics stems from their connection to the macroscopic properties of the system. This is expressed by the fluctuation–dissipation theorem, which relates the fluctuations of a system in thermal equilibrium to the system response to external forces when brought out of equilibrium (Kubo 1966). Since the microscopic origins of equilibrium fluctuations and the macroscopic response are the same, analysis of fluctuations provides important parameters describing the macroscopic behaviour, and vice versa. For example, the fluctuation–dissipation theorem provides a relation between frictional coefficient (force dissipation) and the fluctuations in particle velocity in the case of Brownian motion; and the relation between thermal noise in a resistor and impedance in the electric circuit. The applications of fluorescence fluctuation methods as described here aim not only at obtaining the macroscopic response parameters (e.g. diffusion coefficient) but also at elucidating directly the microscopic properties of the system (e.g. rate and equilibrium constants).

The majority of the techniques described in this paper study fluctuations in a steady state, as opposed to relaxation techniques, where the system is perturbed and the relaxation back to the steady state is monitored. The exceptions are the correlation analysis of singlet–triplet transitions and antibunching (Widengren *et al.* 1995), where the processes of interest are the excitation to a higher energy state (perturbation of equilibrium) and subsequent relaxation back to the ground state.

We would like to discuss here how current fluorescence microscopic techniques use fluorescence fluctuations to obtain more information about the investigated system than by considering only simple mean fluorescence values, and how knowledge about the photon statistics is incorporated into the analysis, in order to reduce or eliminate bias and extract maximum information. By fluorescence microscopy we mean not only imaging, but also techniques where measurement is performed at one microscopic location: single-point measurements. It is the size of the volume, in combination with low concentration, which results in a relatively low number of emitting species, and therefore gives the relevance to fluctuations. In an extreme case, measurement on a single molecule can be performed to investigate the internal dynamics. Imaging can be viewed as many point measurements in (semi-)parallel, and many considerations for point measurements can also be applied there.

The division of the techniques into single-point measurements and imaging is based on the differences in the information content of the data typically obtained with these two techniques, calling for different analysis methods and therefore providing somewhat different information. In comparison with single-point measurements, imaging has usually lower temporal resolution and suffers from stronger shot noise contributions. On the other hand, it has the advantage of parallelism and offers the possibility of spatial correlation between different locations.

## 2. SINGLE-POINT MEASUREMENTS

With single-point measurements, we understand measurements on a small sample volume containing on average few or only one molecule. A small number of molecules is necessary for the amplitude of fluctuations to be large relative to the mean value, making fluctuation analysis experimentally possible (figure 1).

The experimental techniques can be divided into two groups, based on the number of molecules observed. In measurements performed on small numbers of molecules, without attempting to separate the signal from individual molecules, the fluctuations reflect the motion of molecules and intermolecular interactions, as well as the intramolecular dynamics. These techniques are suitable for the investigation of diffusion properties, association/dissociation reactions, aggregation, etc. Measurements performed strictly on one molecule are particularly suited for studying the intramolecular dynamics. There are two main reasons for that: the fluctuations due to changing number of molecules observed simultaneously are not present, and consequently, the data complexity is reduced because one does not have to deal with molecules in different phases on their internal state trajectory.

How can we extract meaningful physical information from a fluctuating signal? The simplest analysis involves the calculation of the mean of the observables from the measurement, e.g. fluorescence intensities in two polarization channels, and deduction of the value of the relevant parameter of the system from these mean values, in this case fluorescence anisotropy. In this analysis, however, no use is made of the fluctuations.

In one of the most widely used fluctuation techniques, fluorescence correlation spectroscopy (FCS; Elson & Magde 1974; Krichevsky & Bonnet 2002; Petrov & Schwille 2008), temporal correlations  $g(\tau) = \langle F(t + \tau)F(t) \rangle$  of the signal  $F(t)$  between different times  $\tau$  are calculated in addition to the mean  $\langle F(t) \rangle$  (figure 2). This procedure allows us to decide whether the fluctuating signal originates from a few diffusing molecules or continuous fluorescent mass. The correlation values and their decay with time are a rich source of information on concentration, diffusion properties, chemical reactions, internal dynamics, photophysics, etc., on temporal scales from below nanoseconds to seconds and longer. Correlation analysis between different detection channels (spatial, spectral and polarization) widens the range of accessible system parameters even further (Bacia *et al.* 2006). FCS has been applied not only to *in vitro* or model systems,

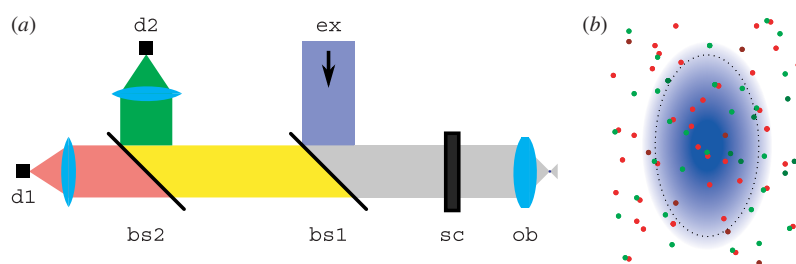


Figure 1. (a) A schematic of a generic experimental set-up for single-point and scanning fluorescence measurements. The parallel excitation beam (ex) is deflected by the scanning optics (sc) and focused by a high numerical aperture objective (ob) into a desired diffraction-limited focal spot, where the fluorescent molecules are excited. The fluorescence is collected and collimated by the same objective, descanned, and separated from the excitation path by a wavelength-selective beam splitter (bs1). The following beam splitter(s) (bs2) divide the fluorescence into two or more channels, based on the differences in wavelength or polarization. The separated fluorescence is optionally spatially filtered by a confocal pinhole to ensure a well-confined measurement volume with small effective number of molecules (not shown), and may be further filtered by additional emission filters to suppress unwanted background, before being detected by point detectors, such as avalanche photodiodes or photomultiplier tubes (d1, d2). (b) Freely diffusing fluorescent molecules enter the measurement volume randomly, where they are excited and from which the fluorescence is detected. The number of molecules in the volume fluctuates; the relative amplitude and duration of fluctuations can be evaluated to provide concentration and diffusion coefficients. Independently diffusing molecules with different emission characteristics (light red circles, light green circles) can be distinguished from the bound species (joined light green and light red circles) by cross-correlation analysis. In addition to number fluctuations, fluctuations in intensity or other fluorescence parameter (light red circles ↔ dark red circles, light green circles ↔ dark green circles) can be detected, reflecting the intramolecular dynamics or intermolecular interactions.

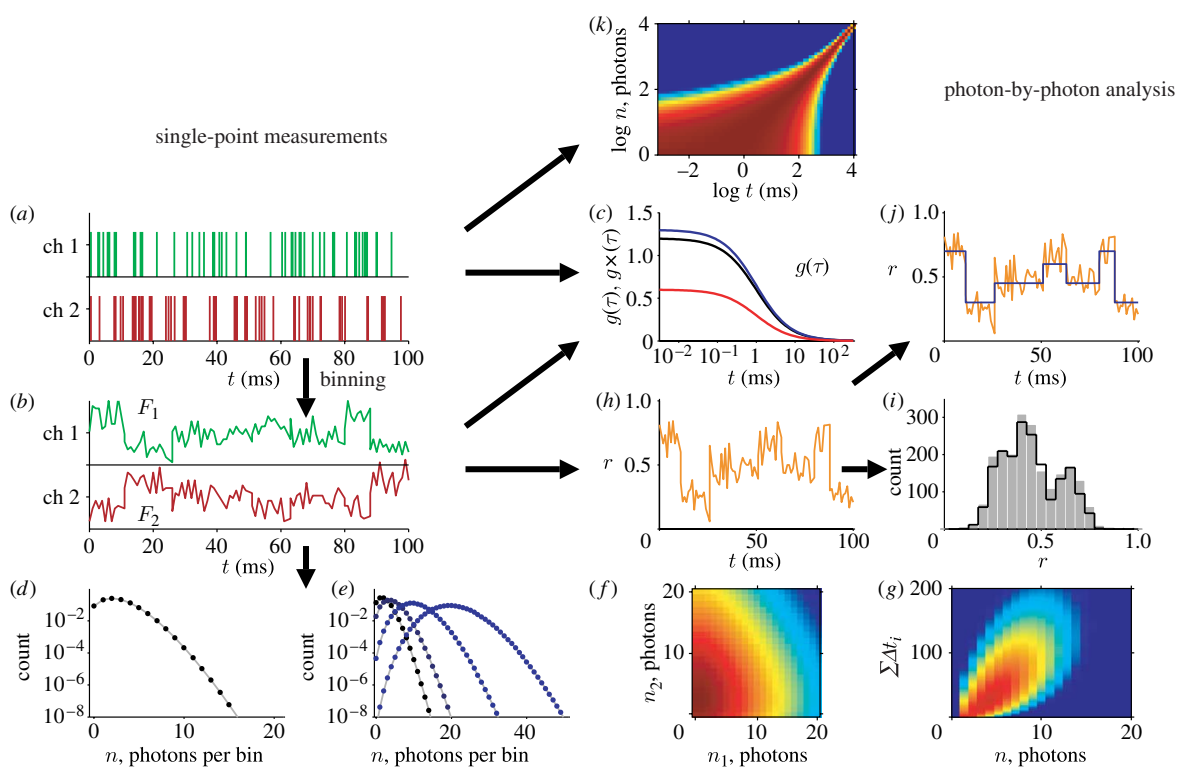


Figure 2. Fluctuation analysis in single-point measurements. The (a) photon sequences recorded in multiple detection channels are (b) typically binned before (c) the correlation analysis or various types of intensity distribution analysis: (d) FIDA/PCH, (e) fluorescence intensity multiple distributions analysis (FIMDA), (f) two-dimensional FIDA, and (g) fluorescence intensity and lifetime distribution analysis (FILDA). The binned data from different channels can be combined to yield another parameter, for example, (h) the proximity ratio  $r$  ( $r = F_1 / (F_1 + F_3)$ ). The histograms of proximity ratios are analysed by (i) probability distribution analysis. The states can be identified from the trace of  $r$  revealing (j) the state trajectory. Alternatively, the raw photon sequences can be (c) directly correlated without binning, analysed by means of (k) photon arrival-time interval distribution (PAID), or by other methods operating directly on the photon-by-photon basis.

such as molecules diffusing and interacting in phospholipid membranes (Kahya & Schuille 2006), but also directly in living cells, for example, to monitor endocytosis of cholera toxin followed by separation of its subunits (Bacia *et al.* 2002), and to study binding of calmodulin to protein kinase II in cytoplasm (Kim *et al.* 2004).

Since the correlation is calculated between different time channels, and photon detection events are uncorrelated, the contribution due to photon-counting statistics to the correlation value is eliminated. The photon-counting noise affects only the variance of the correlation value.

It is worth noting that in FCS we are still performing ensemble averaging, assumed equivalent to temporal averaging, but extract additional observables (correlations) from the data in addition to the mean. Even in a true single molecule experiment we seek to perform an ensemble average, in a sense that the extracted parameters should be representative of a class of molecules (ensemble), not only of one particular molecule on which the experiment has been performed. The crucial question is how to perform the data reduction ('averaging' in a sense) in order to retain the maximum amount of relevant information and to eliminate the superfluous fluctuations due to the photon-counting noise without biasing the results.

With all its benefits, classical FCS does not exploit all the information contained in the data. A natural question is: what other observables can we calculate from the data to learn even more about the system?

One way is to consider correlations of higher order, such as  $g_{mn}(\tau) = \langle F^m(t + \tau)F^n(t) \rangle$ . Analysis of higher order correlations of the fluctuating signal, or higher order moments, allows characterization of distribution of aggregate sizes (Palmer & Thompson 1987). Considering multiple time correlations  $g(\tau_1, \dots, \tau_{n-1}) = \langle F(t)F(t + \tau_1) \dots F(t + \tau_{n-1}) \rangle$  with  $\tau_i \rightarrow 0$  instead of higher order moments  $\langle F(t)^n \rangle$  eliminate the contributions of shot noise (Qian & Elson 1990), because the shot noise between different channels is uncorrelated.

Higher order correlation functions, together with dual-colour cross-correlations, were shown to allow differentiation between systems in equilibrium and non-equilibrium steady state (Qian & Elson 2004). The non-equilibrium steady state of an open system is characterized by the presence of externally controlled fluxes (exchange of material), non-zero gradients in chemical potential and time irreversibility of fluctuations. It may exhibit concentration oscillations, but the average concentrations of reacting species may also be constant, as in a system in thermodynamic equilibrium (Qian *et al.* 2002). Living systems, or their parts, such as distinct reaction networks, are often in a non-equilibrium steady state, rather than in equilibrium. It is, therefore, important to be able to recognize and characterize the non-equilibrium steady state, for example, by determining the fluxes. Experimental approaches employing fluctuation analysis have been proposed for this task, and are expected to play an important role in the studies of reaction networks in living cells (Qian 2006, 2007).

Going one step further, one can sort the detected photons in bins of a fixed temporal width shorter than

the diffusion time (diffusion can then be neglected), and analyse the full distribution of the number of photons per bin instead of calculating only the moments of the distribution (fluorescence intensity distribution analysis (FIDA; Kask *et al.* 1999), photon counting histogram (PCH; Chen *et al.* 1999)). The distribution is determined by both the fluctuation of the number of molecules in the observed volume and the photon-counting statistics. Assuming essentially Poisson statistics of these two sources of fluctuations allows one to determine the mean number of molecules (concentration) and the molecular brightness (mean number of photons detected from one molecule per unit time). Contrary to FCS, this method is sensitive to the presence of more species of different brightness, regardless of their diffusion properties (Müller *et al.* 2000). FCS can resolve two species only if their diffusion times differ significantly, implying large difference in size, and even then provides only product of concentration and square of the brightness of each species. FIDA was applied to study hybridization and cleavage of labelled oligonucleotides, with resolution of all cleavage products based on molecular brightness (Kask *et al.* 1999).

Sorting photons into bins shorter than the diffusion time and analysing the histogram of photon counts means that all dynamic information due to diffusion contained in the correlations between different bins is lost. However, if a series of histograms is constructed where the bin width increases from one histogram to another, in the range of bin widths from shorter than longer than the diffusion time, the motion of molecules will affect the distributions (Palo *et al.* 2000; Gopich & Szabo 2005b). Then, in addition to brightness and concentration, the temporal characteristics of fluctuations can be extracted, as done by evaluating correlations in FCS. The technique has been demonstrated by determining the binding constant of a protein–ligand interaction (Palo *et al.* 2000). A similar way to extract information about molecular diffusion from photon count histograms with a range of bin widths is to analyse the cumulants of the resulting photon count distributions (Wu & Müller 2005).

As in FCS, dividing the fluorescence signal into two channels on the basis of different polarization, emission wavelength, etc., with selectively higher sensitivity for one or the other species to be resolved, leads to significantly higher accuracy compared with the one-channel technique. Both photon streams are binned and a joint photon count number distribution (two-dimensional histogram) is constructed and fitted to a model (Kask *et al.* 2000). This approach was shown to be suitable for studying the antibody–antigen binding and ligand–receptor interactions (Kask *et al.* 2000). Adding nanosecond resolution and pulsed excitation introduces the ability to distinguish fluorescence species by the differences in their fluorescence lifetime, in addition to brightness. The raw data are reduced and analysed by constructing two-dimensional histograms, where the second axis is determined by the sum of the delay times from the excitation pulse of all photons in the bin. Binding of peptide to calmodulin could be monitored with this method, owing to the change of fluorescence lifetime upon complex formation (Palo *et al.* 2002).

Another analysis approach, bringing together the benefits of FCS and photon count distribution analysis, avoids binning the photon counts and involves construction of a two-dimensional histogram of photon pairs instead (photon arrival-time interval distribution (PAID; Laurence *et al.* 2004)). One histogram dimension is defined by the temporal separation of the two photons (analogous to FCS correlation) and the other dimension corresponds to the number of photons detected within the time interval defined by the detection of the two photons. The analysis of the histogram allows simultaneous determination of the mean number of molecules, molecular brightness and characterization of diffusion. The technique was shown to resolve and characterize different species involved in the RNA–polymerase–DNA interaction (Laurence *et al.* 2004). As with the other methods, PAID can be extended by combining photon streams from different detection channels.

The methods discussed so far use correlation or photon count distribution analysis to analyse signal from a small number of molecules. When the interest is in the intramolecular dynamics, e.g. conformation fluctuations and the related fluctuations in enzymatic activity (Xie 2002), observation of one molecule at a time allows even more detailed data analysis. This can be realized by immobilizing the molecule, confining it into a volume smaller than the probed volume, or diluting the sample so that statistically at most one molecule is present in the observation volume.

When freely diffusing, the molecule passing through the probed volume generates a photon burst, with its size limited by the time spent in the volume. Consequently, only a limited number of photons is available for analysis, and any observable quantity determined from the information carried by these photons, such as FRET efficiency (or alternatively, proximity ratio (Antonik *et al.* 2006)) or fluorescence anisotropy (Kalinin *et al.* 2007), is affected by the stochasticity of photon detection. With an elaborate analysis, the photon-counting statistics can be fully accounted for, and discrete probability distributions of the observables can be constructed that accurately describe the shot noise broadening of not only the experimental histograms, but also the step-like histogram structure due to the discrete nature of the photon-counting data. As a result, probability distribution analysis is very sensitive to histogram broadening due to a distribution of the values of the observable quantity, i.e. to the sample heterogeneity. When applied to FRET in donor–acceptor labelled DNA, motion inhomogeneities in the range of 0.5 nm could be resolved (Antonik *et al.* 2006). The method can be implemented either for the data binned into equally sized bins (Antonik *et al.* 2006; Kalinin *et al.* 2007) or for histograms of values obtained from whole bursts of varying size (Nir *et al.* 2006).

The probability distribution analysis reveals state heterogeneity, but not the interconversion rates between the states. These can be obtained by calculating the observable value (fluorescence lifetime, FRET efficiency, etc.) in channels of the binned signal, identifying the states and constructing histograms of dwell times, as demonstrated by identifying different conformational states of a fluctuating DNA oligonucleotide (Eggeling

*et al.* 1998). Alternatively, temporal autocorrelation of the calculated fluctuating observable can be used.

Identification of states from the trajectory of the observable becomes difficult when the number of states, the transition rates or the photon-counting noise increase. Then, it is advantageous to view the molecular evolution through an unknown sequence of states as a Markov process, meaning that the next molecular state depends only on the previous state and not on earlier history. The state trajectory can be reconstructed and the transition rates can be determined from the fluctuating data using hidden Markov models (HMM; Talaga 2007). This procedure uses directly the raw photon sequence defined by the photon arrival times (Andrec *et al.* 2003). HMM were shown to be applicable to the identification of rotational steps of ATP synthase from the FRET data (Zarrabi *et al.* 2007), and to protein–DNA interaction studies (McKinney *et al.* 2006). Since the experimental observables reflecting the state of the molecule are not necessarily unique to each state, the measured sequence of the observable need not be a Markov process anymore. Non-Markovian property of the data, experimentally manifested by non-exponential relaxations, can be identified not only by HMM, but also by higher order correlation analysis (Edman & Rigler 2000).

Binning the data into channels prior to further processing may appear to have the advantage of reducing the photon-counting noise. However, binning causes loss of information contained in the precise timing of the photon. In order to avoid this information loss, photon-by-photon analysis algorithms requiring no binning have been developed. They allow calculation of correlation functions, or other type of analysis, directly from the photon sequence, without having to determine the relevant observable, such as lifetime or FRET distance, at every instance beforehand (Yang & Xie 2002; Gopich & Szabo 2005a). The benefit is a higher time resolution and a broader temporal correlation range. Photon-by-photon analysis of FRET distance trajectory using a maximum-likelihood approach additionally provides rigorous error estimates (Schroder & Grubmuller 2003). A photon-by-photon analysis using a Bayesian estimator has been developed for identification of a fluorescent molecule diffusing through a laser focus from a known set of possible species, based on the differences in diffusion coefficient or brightness (McHale *et al.* 2004).

Considering the various analysis methods (Lippitz *et al.* 2005) yielding often different types of information, an obvious question arises: is a particular method analysing the data efficiently, and what is the limit on the amount of information that can be extracted from given data with certain noise level? The answers are being sought using the concepts of information theory, such as Shannon information, entropy, mutual information or Fisher information (Watkins & Yang 2004; Talaga 2006). The information theory analysis of the data processing method can tell us, for example, whether it is possible to reconstruct a hidden molecular state trajectory from the given photon stream. The optimal methods use photon-by-photon approach, often in combination with maximum-likelihood estimators fully incorporating the Poisson statistics of photon detection.

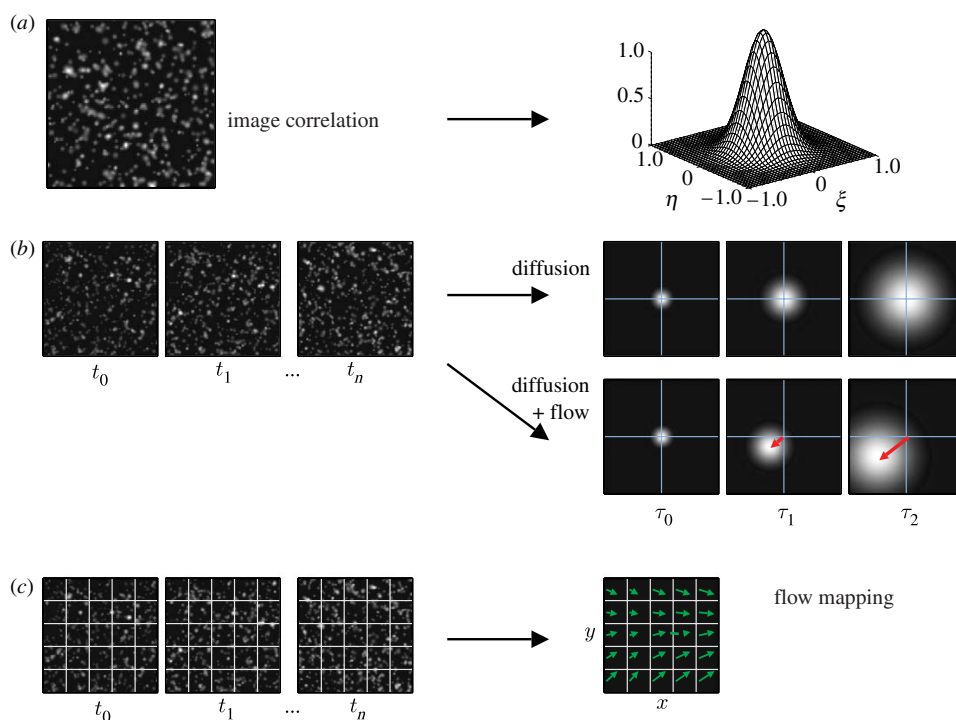


Figure 3. Spatial correlation analysis. (a) Spatial correlation of a fluorescence image produces a peak centred at the origin; the correlation value at  $(\xi, \eta) \rightarrow (0, 0)$  is inversely proportional to the density of fluorescent species, and the width of the correlation peak is related to the instrument point spread function and the size of the fluorescent features in the image. (b) Spatio-temporal correlation spectroscopy (STICS): performing additional temporal correlation across a sequence of images enables the determination of diffusion coefficients by quantifying the broadening of the correlation peak at increasing correlation times  $\tau_i$ . The shift of the correlation peak maximum away from the origin corresponds to the mean displacement vector (red arrows) and can be used to determine the magnitude and direction of the average flow. (c) Dividing the image into segments and performing spatio-temporal correlation analysis in each segment separately allows mapping of the flow field (green arrows).

### 3. BEYOND POINT MEASUREMENTS

In many cases of intermolecular interactions the fluctuations due to molecular motion are very slow. Consequently, the measurement at one location would require prohibitively long time for the system to sample sufficiently well the space of its allowed states, i.e. to approximate well enough the ensemble average. A solution to this problem is to perform the measurement on many systems in parallel.

In image correlation spectroscopy (Petersen *et al.* 1993), the image  $F(x, y)$  containing many copies of the investigated system (e.g. aggregating membrane receptor) is autocorrelated (figure 3). The autocorrelation amplitude  $g(0, 0)$  of the spatial image correlation  $g(\xi, \eta)$  is related to the receptor density in the image. If an assumption can be made about the distribution of the number of the fluorescent subunits of the receptor, the autocorrelation amplitude can yield information about the parameters of this distribution, such as the mean number of subunits. In this way, molecular aggregation on immobile or slowly moving complexes can be studied. As other correlation techniques, image correlation can be extended to work with more detection channels (Petersen *et al.* 1998), or to use higher order correlations in order to better characterize aggregation. Applications of image correlation include quantification of the aggregation state of plasma membrane receptors

revealing their preclustering before ligand binding (Wiseman & Petersen 1999).

If higher temporal resolution is required than that available with fast imaging, but the motion of fluorescent species is still too slow for measurement at one location, combination of standard FCS with scanning the measurement volume across the sample may help (Petrášek & Schwille 2008b), as was shown in the measurements of slow motion of GFP-labelled proteins in the cortex of developing *C. elegans* embryos (Petrášek *et al.* 2008). In this way, a large total volume can be sampled allowing good averaging. The motion of the measurement volume has to be taken into account in the correlation analysis. Scanning can provide additional benefits: reduction of photobleaching (Petrášek & Schwille 2008a), elimination of slow membrane fluctuations (Ries & Schwille 2006), or simultaneous measurement of flows, diffusion and immobilization (Skinner *et al.* 2005).

Since scanning FCS obtains signal from different locations, autocorrelation of the detected photon stream represents a subset of the full spatio-temporal correlation  $g(\xi, \eta, \tau)$ , sampled only at certain coordinates  $(\xi, \tau)$  determined by the scan path, however with considerably higher temporal resolution. Owing to its relation to the probability density function  $p(\mathbf{r}, t)$  describing the particle motion, the spatio-temporal correlation provides more detailed characterization of

the particle dynamics than, for example, the commonly investigated dependence of the mean square displacement on time (Petrášek *et al.* 2008).

One of the motivations behind scanning described so far was to obtain statistically significant data for correlation analysis by measuring many particles at different locations. A different application uses circular scanning with a feedback loop to follow the motion of one fluorescent particle in three dimensions without disturbing it (Berglund & Mabuchi 2005; Levi *et al.* 2005). In this way, the particle trajectory is obtained, and at the same time the fluorescence stream can be analysed for the internal dynamics on a temporal scale as long as the tracking period (McHale *et al.* 2007). This approach enables measurement on one particle without immobilizing or confining it, thereby minimally affecting its behaviour. The technique has been applied to the study of phagocytosis of protein-coated beads (Levi *et al.* 2005) and to the fluctuation analysis of freely diffusing quantum dots from nanosecond time scales, permitting monitoring of antibunching, to the time scale of seconds, where bright/dark state transitions are observed (McHale *et al.* 2007). The limits of tracking accuracy and maximum trackable speed are set by the bandwidth of the feedback loop and especially by the photon-counting statistics (Enderlein 2000; Berglund & Mabuchi 2006). Shot noise is, in this case, a source of two negative effects: it obscures the useful information in the detected signal, and prevents fast diffusing particles from being tracked.

#### 4. MICROSCOPY IMAGING

Fluorescence microscopy imaging techniques are usually employed to gain different information from that obtained in single-point measurements: two- or three-dimensional spatial distribution of fluorescent molecules, particles or larger structures, or distribution of any parameter reflected by their fluorescence, and the changes of these distributions in time. However, the situation is similar regarding the useful signal and noise: the fluctuations of the sample carrying interesting information are mixed with the fluctuations due to photon-counting statistics, or the detection process in general. The relevance of detection-associated fluctuations is exacerbated by typically shorter acquisition times per pixel than in single-point measurements. For this reason, the elimination of fluctuations in imaging has been more in focus than the exploitation of fluctuations as a source of new information.

The general problem of noise reduction has been extensively researched in different fields reaching from astrophysics to biomedical imaging (Verveer *et al.* 1999; Bonnet 2004; Puetter *et al.* 2005). Many of these approaches are applicable also to fluorescence microscopy imaging, as can be seen in examples of three-dimensional image reconstruction and deconvolution techniques. The image restoration algorithms are able to deal with different noise distributions, and can therefore be optimized for images obtained with analogue detectors or the increasingly popular photon-counting devices.

Proper treatment of detection noise is especially important in fluorescence microscopy techniques where the contrast is not formed directly by variations in fluorescence intensity, but by variations in another parameter calculated from the data, such as in ratio imaging or lifetime imaging. Low pixel intensities imply high noise necessitating the use of unbiased estimators of these quantities.

In ratio imaging, the signal is separated into two detection channels on the basis of different polarization or emission wavelength. The signal ratio can be used to monitor rotational mobility, resonance energy transfer, spectral fluctuations, etc. The presence of noise in the two signals  $x$  and  $y$  causes not only a spread of values of calculated ratio  $x/y$ , but also deviation (bias) from its true value (Wang 2007). The estimated ratio  $x/y$  can then be falsely found to depend on the total intensity  $x+y$ . The knowledge of the noise statistics allows estimation of the bias and construction of less biased or unbiased estimators (van Kempen & van Vliet 2000). For example, the ratio estimator  $E(x/y) = x(1/y + (1-y)/(y(y^2-2)))$  has almost no bias and equal or smaller variance than  $E(x/y) = x/y$  for practically useful values of  $x$  and  $y$ , if  $x$  and  $y$  are Poisson distributed with uncorrelated noise.

In fluorescence lifetime imaging, the lifetime (or decay rate) is calculated by fitting the fluorescence decay in one pixel to a model function, in the simplest case a single exponential (Suhling *et al.* 2005). Using the criterion of minimum  $\chi_r^2$  for finding the estimate of fluorescence lifetime implicitly assumes Gaussian-distributed noise. However, in imaging applications the photon counts per pixel are often low, and the Poisson distribution of the number of photons in individual channels is no longer well approximated by the Gaussian distribution. The  $\chi_r^2$  minimization then results in biased decay rate values. Maximum-likelihood estimators assuming Poisson photon-counting statistics are known to produce smaller bias that can be easily corrected for (Tellinghuisen & Wilkerson 1993).

Photon-counting noise is the fundamental factor determining the accuracy limit in recently introduced super-resolution imaging techniques (Betzig *et al.* 2006; Sharonov & Hochstrasser 2006; Toprak & Selvin 2007; Huang *et al.* 2008) and in high-accuracy particle-tracking experiments (Yildiz & Selvin 2005). Both classes of techniques rely on the calculation of the centre position of a pixelized diffraction-limited image of a much smaller emitter, built up from a limited number of photon counts. The accuracy limit has been shown to lie at approximately 1–2 nm under realistic conditions (Thompson *et al.* 2002). Relevant analysis methods of photon-counting data, including the centroid calculation (Suhling *et al.* 1999), have been previously developed in the field of astrophysics, where similar limitations and problems are encountered—weak signals combined with the need of high spatial resolution.

The previous examples illustrate how fluctuations limit the imaging techniques and how they are dealt with. But can the fluctuations of the physical properties of the sample be used to obtain additional information, as in single-point techniques?

Conceptually simpler are the methods attempting to perform the previously discussed point measurements at many locations in parallel. In addition to the above-mentioned lifetime and ratio imaging, new techniques are appearing that aim at producing maps of physical parameters derived from the signal fluctuations. For example, temporal correlation of a sequence of images  $g(0, 0, \tau)$  provides information about diffusion (Wiseman *et al.* 2000; Burkhardt & Schwille 2006), and, if performed pixel wise, can be used to generate maps of diffusion coefficients and concentrations, as demonstrated in an example of lipid molecules diffusing in a lipid bilayer, and receptor proteins diffusing on cell membranes (Kannan *et al.* 2007). Analysis of the mean and variance of a fluctuating fluorescence signal in individual pixels of an image sequence can be used to produce maps of average molecular brightness and average particle number (Digman *et al.* 2008).

The fluctuation analysis can, however, use also the spatial information contained in images. When investigating the dynamics of a fluorescently labelled microscopic sample, the motion of structures or even individual particles is identified in a sequence of images, and can be further evaluated to yield quantitative information. However, it is often desirable, or dictated by the biological system, that the concentration of fluorescent molecules is low. Additionally, fast dynamics necessitates short integration times. Both these requirements lead to low signal per image pixel, and therefore strong contribution of photon-counting noise, often preventing direct identification and tracking of distinct labelled structures. Still, correlation analysis of an image sequence makes it possible to identify a pattern in the fluctuating signal affected by photon-counting statistics. Images are divided into small segments  $F(x, y, t)$  for which three-dimensional correlation  $g(\xi, \eta, \tau)$  is calculated. The temporal decay and the location of the correlation maximum in  $(\xi, \eta)$  are used to determine the average diffusion coefficient and flow vector (Hebert *et al.* 2005). Assembling the results from all image segments produces a map of diffusion coefficients and a flow map (figure 3). It is also possible to eliminate immobile image features and thus focus only on the dynamic (fluctuating) constituents of the system. The flow mapping via correlation analysis has been used, for example, to study the motion of adhesion-related proteins and actin in migrating cells (Brown *et al.* 2006).

The amplitude, and therefore detectability, of physical fluctuations in images can be enhanced by optimized labelling, as used in the technique called speckle microscopy (Danuser & Waterman-Storer 2006). Speckle microscopy is suitable for studying the assembly dynamics, subunit turnover and movement of biological structures, consisting of a large number of subunits of one or several types, such as microtubules or actin filaments. A small fraction of the subunits (0.5%) is fluorescently labelled, resulting in a speckled pattern on the otherwise invisible structure. Appearance, disappearance and motion of the pattern reflect the dynamics of the structure, without the need to identify (resolve), localize or track individual molecules (Waterman-Storer *et al.* 1998). Correlation analysis of

image segments between subsequent frames provides an average displacement vector, describing the motion even in the presence of high noise and low speckle contrast. Consequently, flow maps can be constructed, with resolution determined by the size of correlated image segment only slightly lower than the diffraction limit (Ji & Danuser 2005). The calculated flow map can subsequently assist tracking of individual speckles in the image sequence. With sufficient contrast, the speckles can also be identified and analysed individually, without the preceding correlation step.

The spatio-temporal correlation analysis is typically performed on the data obtained from highly sensitive CCD cameras where the whole frame is exposed simultaneously, and the temporal resolution is limited by the frame transfer rate. Higher temporal resolution than in frame-based image correlation can be achieved in correlation analysis of images from a confocal laser scanning microscope (Digman *et al.* 2005). Since the laser beam is scanned across the sample in a well-defined fashion to create an image, correlation of the fluorescence separately along the fast and slow axis, and across the frames, gives access to three different time scales on which the molecular dynamics can be measured. This approach combines the features of imaging with scanning FCS.

## 5. CONCLUSION

Perhaps not surprisingly, the extraction and analysis of useful information carried by fluctuating fluorescence signal has advanced most in the field of single molecule spectroscopy. The reasons can be related to the facts that when observing only one molecule no additional fluctuations due to the occupation number or trajectory phase differences are present, the shot noise fluctuations are well defined, and background contributions to the signal can be efficiently eliminated. FCS on a small number of molecules is well established and exists in many variations, some of them optimized to determine one parameter precisely, others to measure many parameters simultaneously. In imaging applications, the focus has traditionally been on removing fluctuations regarded as noise. Nevertheless, correlation approaches can use physical fluctuations in the sample to image quantities, such as flow directions, that appear lost in noise to a human eye.

Concerning the technology development, detectors and optics have approached their limits in sensitivity, and significant further development can be expected perhaps in parallel detection (avalanche photodiode arrays). A transfer of technology is occurring from astrophysics, where position-sensitive detectors with high temporal resolution are being developed, such as quadrant anode, wedge-and-strip, or delay line multi-channel plate detectors (Michalet *et al.* 2007). Similarly, although fluorescent probes are improving in photostability and brightness, the limitations on photon yield due to finite lifetime and the total energy dose deposited in biological sample will persist.

Therefore, it has become increasingly important to find ways to extract the maximum possible information from the available data. Some of the experience with

the advanced analysis methods in the single molecule field is expected to be transferred to imaging. Instrumentation is available that can record the whole photon stream from which the images are built up with picosecond resolution (Emiliani *et al.* 2003; Becker *et al.* 2006; Wahl *et al.* 2007), in principle allowing a similar type of analysis as in single-point techniques. Implementation of multiparameter fluorescence detection (Widengren *et al.* 2006), i.e. separating the signal into many detection channels, is particularly important in order to resolve heterogeneities typical for complex samples typically investigated with imaging.

Additionally, new analysis methods will have to be developed that will take into account the complexity of living organisms, reflected, for example, by the fact that the investigated system is often in a non-equilibrium steady state rather than in thermodynamic equilibrium.

## REFERENCES

- Andrec, M., Levy, R. M. & Talaga, D. S. 2003 Direct determination of kinetic rates from single-molecule photon arrival trajectories using hidden Markov models. *J. Phys. Chem. A* **107**, 7454–7464. (doi:10.1021/jp035514+)
- Antonik, M., Felekyan, S., Gaiduk, A. & Seidel, C. A. M. 2006 Separating structural heterogeneities from stochastic variations in fluorescence resonance energy transfer distributions via photon distribution analysis. *J. Phys. Chem. B* **110**, 6970–6978. (doi:10.1021/jp057257+)
- Bacia, K. & Schuille, P. 2003 A dynamic view of cellular processes by *in vivo* fluorescence auto- and cross-correlation spectroscopy. *Methods* **29**, 74–85. (doi:10.1016/S1046-2023(02)00291-8)
- Bacia, K., Majoul, I. V. & Schuille, P. 2002 Probing the endocytic pathway in live cells using dual-color fluorescence cross-correlation analysis. *Biophys. J.* **83**, 1184–1193.
- Bacia, K., Kim, S. A. & Schuille, P. 2006 Fluorescence cross-correlation spectroscopy in living cells. *Nat. Methods* **3**, 83–89. (doi:10.1038/nmeth822)
- Becker, W. *et al.* 2006 Fluorescence lifetime images and correlation spectra obtained by multidimensional time-correlated single photon counting. *Microsc. Res. Tech.* **69**, 186–195. (doi:10.1002/jemt.20251)
- Berglund, A. J. & Mabuchi, H. 2005 Tracking-FCS: fluorescence correlation spectroscopy of individual particles. *Opt. Express* **13**, 8069–8082. (doi:10.1364/OPEX.13.008069)
- Berglund, A. J. & Mabuchi, H. 2006 Performance bounds on single-particle tracking by fluorescence modulation. *Appl. Phys. B Lasers Opt.* **83**, 127–133. (doi:10.1007/s00340-005-2111-z)
- Berne, B. J. & Pecora, R. 1976 *Dynamic light scattering*. New York, NY: Dover Publications, Inc.
- Betzig, E., Patterson, G. H., Sougrat, R., Lindwasser, O. W., Olenych, S., Bonifacino, J. S., Davidson, M. W., Lippincott-Schwartz, J. & Hess, H. F. 2006 Imaging intracellular fluorescent proteins at nanometer resolution. *Science* **313**, 1642–1645. (doi:10.1126/science.1127344)
- Bonnet, N. 2004 Some trends in microscope image processing. *Micron* **35**, 635–653. (doi:10.1016/j.micron.2004.04.006)
- Brown, C. M., Hebert, B., Kolin, D. L., Zareno, J., Whitmore, L., Horwitz, A. R. & Wiseman, P. W. 2006 Probing the integrin-actin linkage using high-resolution protein velocity mapping. *J. Cell Sci.* **119**(Pt 24), 5204–5214. (doi:10.1242/jcs.03321)
- Burkhardt, M. & Schuille, P. 2006 Electron multiplying CCD based detection for spatially resolved fluorescence correlation spectroscopy. *Opt. Express* **14**, 5013–5020. (doi:10.1364/OE.14.005013)
- Chen, Y., Müller, J. D., So, P. T. & Gratton, E. 1999 The photon counting histogram in fluorescence fluctuation spectroscopy. *Biophys. J.* **77**, 553–567.
- Danuser, G. & Waterman-Storer, C. M. 2006 Quantitative fluorescent speckle microscopy of cytoskeleton dynamics. *Annu. Rev. Biophys. Biomol. Struct.* **35**, 361–387. (doi:10.1146/annurev.biophys.35.040405.102114)
- Digman, M. A., Brown, C. M., Sengupta, P., Wiseman, P. W., Horwitz, A. R. & Gratton, E. 2005 Measuring fast dynamics in solutions and cells with a laser scanning microscope. *Biophys. J.* **89**, 1317–1327. (doi:10.1529/biophysj.105.062836)
- Digman, M. A., Dalal, R., Horwitz, A. F. & Gratton, E. 2008 Mapping the number of molecules and brightness in the laser scanning microscope. *Biophys. J.* **94**, 2320–2332. (doi:10.1529/biophysj.107.114645)
- Edman, L. & Rigler, R. 2000 Memory landscapes of single-enzyme molecules. *Proc. Natl Acad. Sci. USA* **97**, 8266–8271. (doi:10.1073/pnas.130589397)
- Eggeling, C., Fries, J. R., Brand, L., Günther, R. & Seidel, C. A. 1998 Monitoring conformational dynamics of a single molecule by selective fluorescence spectroscopy. *Proc. Natl Acad. Sci. USA* **95**, 1556–1561. (doi:10.1073/pnas.95.4.1556)
- Elson, E. L. & Magde, D. 1974 Fluorescence correlation spectroscopy. I. Conceptual basis and theory. *Biopolymers* **13**, 1–27. (doi:10.1002/bip.1974.360130102)
- Emiliani, V., Sanvitto, D., Tramier, M., Piolot, T., Petrášek, Z., Kemnitz, K., Durieux, C. & Coppey-Moisand, M. 2003 Low-intensity two-dimensional imaging of fluorescence lifetimes in living cells. *Appl. Phys. Lett.* **83**, 2471–2473. (doi:10.1063/1.1604938)
- Enderlein, J. 2000 Positional and temporal accuracy of single molecule tracking. *Single Mol.* **1**, 225–230. (doi:10.1002/1438-5171(200009)1:3<225::AID-SIMO225>3.0.CO;2-O)
- Feher, G. & Weissman, M. 1973 Fluctuation spectroscopy: determination of chemical reaction kinetics from frequency spectrum of fluctuations. *Proc. Natl Acad. Sci. USA* **70**, 870–875. (doi:10.1073/pnas.70.3.870)
- Gopich, I. & Szabo, A. 2005a Fluorophore-quencher distance correlation functions from single-molecule photon arrival trajectories. *J. Phys. Chem. B* **109**, 6845–6848. (doi:10.1021/jp045398q)
- Gopich, I. V. & Szabo, A. 2005b Photon counting histograms for diffusing fluorophores. *J. Phys. Chem. B* **109**, 17 683–17 688. (doi:10.1021/jp052345f)
- Hebert, B., Costantino, S. & Wiseman, P. W. 2005 Spatiotemporal image correlation spectroscopy (STICS) theory, verification, and application to protein velocity mapping in living CHO cells. *Biophys. J.* **88**, 3601–3614. (doi:10.1529/biophysj.104.054874)
- Huang, B., Wang, W., Bates, M. & Zhuang, X. 2008 Three-dimensional super-resolution imaging by stochastic optical reconstruction microscopy. *Science* **319**, 810–813. (doi:10.1126/science.1153529)
- Ji, L. & Danuser, G. 2005 Tracking quasi-stationary flow of weak fluorescent signals by adaptive multi-frame correlation. *J. Microsc.* **220**, 150–167. (doi:10.1111/j.1365-2818.2005.01522.x)
- Kahya, N. & Schuille, P. 2006 Fluorescence correlation studies of lipid domains in model membranes (review). *Mol. Membr. Biol.* **23**, 29–39. (doi:10.1080/09687860500489099)

- Kalinin, S., Felekyan, S., Antonik, M. & Seidel, C. A. M. 2007 Probability distribution analysis of single-molecule fluorescence anisotropy and resonance energy transfer. *J. Phys. Chem. B* **111**, 10 253–10 262. (doi:10.1021/jp072293p)
- Kannan, B., Guo, L., Sudhaharan, T., Ahmed, S., Maruyama, I. & Wohland, T. 2007 Spatially resolved total internal reflection fluorescence correlation microscopy using an electron multiplying charge-coupled device camera. *Anal. Chem.* **79**, 4463–4470. (doi:10.1021/ac0624546)
- Kask, P., Palo, K., Ullmann, D. & Gall, K. 1999 Fluorescence-intensity distribution analysis and its application in biomolecular detection technology. *Proc. Natl Acad. Sci. USA* **96**, 13 756–13 761. (doi:10.1073/pnas.96.24.13756)
- Kask, P., Palo, K., Fay, N., Brand, L., Mets, U., Ullmann, D., Jungmann, J., Pschorr, J. & Gall, K. 2000 Two-dimensional fluorescence intensity distribution analysis: theory and applications. *Biophys. J.* **78**, 1703–1713.
- Kim, S. A., Heinze, K. G., Waxham, M. N. & Schwille, P. 2004 Intracellular calmodulin availability accessed with two-photon cross-correlation. *Proc. Natl Acad. Sci. USA* **101**, 105–110. (doi:10.1073/pnas.2436461100)
- Krichevsky, O. & Bonnet, G. 2002 Fluorescence correlation spectroscopy: the technique and its applications. *Rep. Prog. Phys.* **65**, 251–297. (doi:10.1088/0034-4885/65/2/203)
- Kubo, R. 1966 Fluctuation-dissipation theorem. *Rep. Prog. Phys.* **29**, 255–284. (doi:10.1088/0034-4885/29/1/306)
- Laurence, T. A., Kapanidis, A. N., Kong, X. X., Chemla, D. S. & Weiss, S. 2004 Photon arrival-time interval distribution (PAID): a novel tool for analyzing molecular interactions. *J. Phys. Chem. B* **108**, 3051–3067. (doi:10.1021/jp036499b)
- Levi, V., Ruan, Q. & Gratton, E. 2005 3-D particle tracking in a two-photon microscope: application to the study of molecular dynamics in cells. *Biophys. J.* **88**, 2919–2928. (doi:10.1529/biophysj.104.044230)
- Lippitz, M., Kulzer, F. & Orrit, M. 2005 Statistical evaluation of single nano-object fluorescence. *ChemPhysChem* **6**, 770–789. (doi:10.1002/cphc.200400560)
- McHale, K., Berghlund, A. J. & Mabuchi, H. 2004 Bayesian estimation for species identification in single-molecule fluorescence microscopy. *Biophys. J.* **86**, 3409–3422. (doi:10.1529/biophysj.103.038414)
- McHale, K., Berghlund, A. J. & Mabuchi, H. 2007 Quantum dot photon statistics measured by three-dimensional particle tracking. *Nano Lett.* **7**, 3535–3539. (doi:10.1021/nl0723376)
- McKinney, S. A., Joo, C. & Ha, T. 2006 Analysis of single-molecule FRET trajectories using hidden Markov modeling. *Biophys. J.* **91**, 1941–1951. (doi:10.1529/biophysj.106.082487)
- Michalet, X., Siegmund, O. H. W., Vallerga, J. V., Jelinsky, P., Millaud, J. E. & Weiss, S. 2007 Detectors for single-molecule fluorescence imaging and spectroscopy. *J. Mod. Opt.* **54**, 239–281. (doi:10.1080/09500340600769067)
- Müller, J. D., Chen, Y. & Gratton, E. 2000 Resolving heterogeneity on the single molecular level with the photon-counting histogram. *Biophys. J.* **78**, 474–486.
- Neher, E. & Stevens, C. F. 1977 Conductance fluctuations and ionic pores in membranes. *Annu. Rev. Biophys. Bioeng.* **6**, 345–381. (doi:10.1146/annurev.bb.06.060177.002021)
- Nir, E., Michalet, X., Hamadani, K. M., Laurence, T. A., Neuhauser, D., Kovchegov, Y. & Weiss, S. 2006 Shot-noise limited single-molecule FRET histograms: comparison between theory and experiments. *J. Phys. Chem. B* **110**, 22 103–22 124. (doi:10.1021/jp063483n)
- Palmer, A. G. & Thompson, N. L. 1987 Molecular aggregation characterized by high order autocorrelation in fluorescence correlation spectroscopy. *Biophys. J.* **52**, 257–270.
- Palo, K., Mets, U., Jäger, S., Kask, P. & Gall, K. 2000 Fluorescence intensity multiple distributions analysis: concurrent determination of diffusion times and molecular brightness. *Biophys. J.* **79**, 2858–2866.
- Palo, K., Brand, L., Eggeling, C., Jäger, S., Kask, P. & Gall, K. 2002 Fluorescence intensity and lifetime distribution analysis: toward higher accuracy in fluorescence fluctuation spectroscopy. *Biophys. J.* **83**, 605–618.
- Petrášek, Z. & Schwille, P. 2008a Photobleaching in two-photon scanning fluorescence correlation spectroscopy. *ChemPhysChem* **9**, 147–158. (doi:10.1002/cphc.200700579)
- Petrášek, Z. & Schwille, P. 2008b Scanning fluorescence correlation spectroscopy. In *Single molecules and nanotechnology*, ch. 4. Springer Series in Biophysics, vol. 12, pp. 83–105. Berlin, Germany: Springer.
- Petrášek, Z., Hoegge, C., Hyman, A. A. & Schwille, P. 2008 Two-photon fluorescence imaging and correlation analysis applied to protein dynamics in *C. elegans* embryo. *Proc. SPIE* **6860**, 686 01L.
- Petersen, N. O., Höddelius, P. L., Wiseman, P. W., Seger, O. & Magnusson, K. E. 1993 Quantitation of membrane receptor distributions by image correlation spectroscopy: concept and application. *Biophys. J.* **65**, 1135–1146.
- Petersen, N. O., Brown, C., Kaminski, A., Rocheleau, J., Srivastava, M. & Wiseman, P. W. 1998 Analysis of membrane protein cluster densities and sizes *in situ* by image correlation spectroscopy. *Faraday Discuss.* **111**, 289–305. (doi:10.1039/a806677i)
- Petrov, E. P. & Schwille, P. 2008 State of the art and novel trends in fluorescence correlation spectroscopy. In *Standardization and quality assurance in fluorescence measurements II: bioanalytical and biomedical applications*. Springer Series on Fluorescence, vol. 6, pp. 145–197. Berlin, Germany: Springer.
- Puetter, R. C., Gosnell, T. R. & Yeh, A. 2005 Digital image reconstruction: deblurring and denoising. *Annu. Rev. Astron. Astrophys.* **43**, 139–194. (doi:10.1146/annurev.astro.43.112904.104850)
- Qian, H. 2006 Open-system nonequilibrium steady state: statistical thermodynamics, fluctuations, and chemical oscillations. *J. Phys. Chem. B* **110**, 15 063–15 074. (doi:10.1021/jp061858z)
- Qian, H. 2007 Phosphorylation energy hypothesis: open chemical systems and their biological functions. *Annu. Rev. Phys. Chem.* **58**, 113–142. (doi:10.1146/annurev.physchem.58.032806.104550)
- Qian, H. & Elson, E. L. 1990 On the analysis of high order moments of fluorescence fluctuations. *Biophys. J.* **57**, 375–380.
- Qian, H. & Elson, E. L. 2004 Fluorescence correlation spectroscopy with high-order and dual-color correlation to probe nonequilibrium steady states. *Proc. Natl Acad. Sci. USA* **101**, 2828–2833. (doi:10.1073/pnas.0305962101)
- Qian, H., Saffarian, S. & Elson, E. L. 2002 Concentration fluctuations in a mesoscopic oscillating chemical reaction system. *Proc. Natl Acad. Sci. USA* **99**, 10 376–10 381. (doi:10.1073/pnas.152007599)
- Ries, J. & Schwille, P. 2006 Studying slow membrane dynamics with continuous wave scanning fluorescence correlation spectroscopy. *Biophys. J.* **91**, 1915–1924. (doi:10.1529/biophysj.106.082297)
- Rigler, R. & Elson, E. S. (eds) 2001 *Fluorescence correlation spectroscopy. Theory and application*, 1st edn. Chemical Physics Series. Berlin, Germany: Springer.
- Schroder, G. F. & Grubmüller, H. 2003 Maximum likelihood trajectories from single molecule fluorescence resonance energy transfer experiments. *J. Chem. Phys.* **119**, 9920–9924. (doi:10.1063/1.1616511)

- Sharonov, A. & Hochstrasser, R. M. 2006 Wide-field subdiffraction imaging by accumulated binding of diffusing probes. *Proc. Natl Acad. Sci. USA* **103**, 18 911–18 916. (doi:10.1073/pnas.0609643104)
- Skinner, J. P., Chen, Y. & Müller, J. D. 2005 Position-sensitive scanning fluorescence correlation spectroscopy. *Biophys. J.* **89**, 1288–1301. (doi:10.1529/biophysj.105.060749)
- Suhling, K., Airey, R. & Morgan, B. 1999 Optimisation of centroiding algorithms for photon event counting imaging. *Nucl. Instrum. Methods Phys. Res. Sect. A* **437**, 393–418. (doi:10.1016/S0168-9002(99)00770-6)
- Suhling, K., French, P. M. W. & Phillips, D. 2005 Time-resolved fluorescence microscopy. *Photochem. Photobiol. Sci.* **4**, 13–22. (doi:10.1039/b412924p)
- Talaga, D. S. 2006 Information theoretical approach to single-molecule experimental design and interpretation. *J. Phys. Chem. A* **110**, 9743–9757. (doi:10.1021/jp062192b)
- Talaga, D. S. 2007 Markov processes in single molecule fluorescence. *Curr. Opin. Colloid Interface Sci.* **12**, 285–296. (doi:10.1016/j.cocis.2007.08.014)
- Tellinghuisen, J. & Wilkerson, C. W. 1993 Bias and precision in the estimation of exponential decay parameters from sparse data. *Anal. Chem.* **65**, 1240–1246. (doi:10.1021/ac00057a022)
- Thompson, R. E., Larson, D. R. & Webb, W. W. 2002 Precise nanometer localization analysis for individual fluorescent probes. *Biophys. J.* **82**, 2775–2783.
- Toprak, E. & Selvin, P. R. 2007 New fluorescent tools for watching nanometer-scale conformational changes of single molecules. *Annu. Rev. Biophys. Biomol. Struct.* **36**, 349–369. (doi:10.1146/annurev.biophys.36.040306.132700)
- van Kempen, G. M. & van Vliet, L. J. 2000 Mean and variance of ratio estimators used in fluorescence ratio imaging. *Cytometry* **39**, 300–305. (doi:10.1002/(SICI)1097-0320(20000401)39:4<300::AID-CYTO8>3.0.CO;2-O)
- Verveer, P. J., Gemkow, M. J. & Jovin, T. M. 1999 A comparison of image restoration approaches applied to three-dimensional confocal and wide-field fluorescence microscopy. *J. Microsc.* **193**, 50–61. (doi:10.1046/j.1365-2818.1999.00421.x)
- Wahl, M., Rahn, H.-J., Gregor, I., Erdmann, R. & Enderlein, J. 2007 Dead-time optimized time-correlated photon counting instrument with synchronized, independent timing channels. *Rev. Sci. Instrum.* **78**, 033 106. (doi:10.1063/1.2715948)
- Wang, Y.-L. 2007 Noise-induced systematic errors in ratio imaging: serious artefacts and correction with multi-resolution denoising. *J. Microsc.* **228**(Pt 2), 123–131. (doi:10.1111/j.1365-2818.2007.01834.x)
- Waterman-Storer, C. M., Desai, A., Bulinski, J. C. & Salmon, E. D. 1998 Fluorescent speckle microscopy, a method to visualize the dynamics of protein assemblies in living cells. *Curr. Biol.* **8**, 1227–1230. (doi:10.1016/S0960-9822(07)00515-5)
- Watkins, L. P. & Yang, H. 2004 Information bounds and optimal analysis of dynamic single molecule measurements. *Biophys. J.* **86**, 4015–4029. (doi:10.1529/biophysj.103.037739)
- Weissman, M. B. 1981 Fluctuation spectroscopy. *Annu. Rev. Phys. Chem.* **32**, 205–232. (doi:10.1146/annurev.pc.32.100181.001225)
- Widengren, J., Mets, U. & Rigler, R. 1995 Fluorescence correlation spectroscopy of triplet states in solution: a theoretical and experimental study. *J. Phys. Chem.* **99**, 13 368–13 379. (doi:10.1021/j100036a009)
- Widengren, J., Kudryavtsev, V., Antonik, M., Berger, S., Gerken, M. & Seidel, C. A. M. 2006 Single-molecule detection and identification of multiple species by multi-parameter fluorescence detection. *Anal. Chem.* **78**, 2039–2050. (doi:10.1021/ac0522759)
- Wiseman, P. W. & Petersen, N. O. 1999 Image correlation spectroscopy. II. Optimization for ultrasensitive detection of preexisting platelet-derived growth factor-beta receptor oligomers on intact cells. *Biophys. J.* **76**, 963–977.
- Wiseman, P. W., Squier, J. A., Ellisman, M. H. & Wilson, K. R. 2000 Two-photon image correlation spectroscopy and image cross-correlation spectroscopy. *J. Microsc.* **200**, 14–25. (doi:10.1046/j.1365-2818.2000.00736.x)
- Wu, B. & Müller, J. D. 2005 Time-integrated fluorescence cumulant analysis in fluorescence fluctuation spectroscopy. *Biophys. J.* **89**, 2721–2735. (doi:10.1529/biophysj.105.063685)
- Xie, X. S. 2002 Single-molecule approach to dispersed kinetics and dynamic disorder: probing conformational fluctuation and enzymatic dynamics. *J. Chem. Phys.* **117**, 11 024–11 032. (doi:10.1063/1.1521159)
- Yang, H. & Xie, X. S. 2002 Probing single-molecule dynamics photon by photon. *J. Chem. Phys.* **117**, 10 965–10 979. (doi:10.1063/1.1521154)
- Yildiz, A. & Selvin, P. R. 2005 Fluorescence imaging with one nanometer accuracy: application to molecular motors. *Acc. Chem. Res.* **38**, 574–582. (doi:10.1021/ar040136s)
- Zarrabi, N., Düser, M. G., Reuter, R., Dunn, S. D., Wrachtrup, J. & Börsch, M. 2007 Detecting substeps in the rotary motors of F<sub>0</sub>F<sub>1</sub>-ATP synthase by hidden Markov models. *Proc. SPIE* **6444**, 64440E. (doi:10.1117/12.701001)



## A2

### **Scanning fluorescence correlation spectroscopy**

Z. Petrášek and P. Schwille

Single Molecules and Nanotechnology, volume 12 of *Springer Series in Biophysics*,  
Chapter 4, pages 83–105, 2008.



# Chapter 4

## Scanning Fluorescence Correlation Spectroscopy

Zdeněk Petrášek and Petra Schwille(✉)

4.1	Introduction.....	84
4.2	Theory.....	85
4.2.1	Fluorescence Correlation Methods.....	85
4.2.2	Fluorescence Correlation Spectroscopy.....	85
4.2.3	Image Correlation Spectroscopy.....	87
4.2.4	Spatiotemporal Image Correlation Spectroscopy.....	87
4.2.5	Scanning Fluorescence Correlation Spectroscopy.....	88
4.3	Applications.....	94
4.4	Implementation.....	97
4.4.1	Light Source.....	98
4.4.2	Optical Part.....	98
4.4.3	Electronics.....	99
4.4.4	Software.....	100
4.4.5	Data analysis.....	101
4.5	Conclusion.....	102
	References.....	103

**Abstract** Fluorescence correlation techniques are used to investigate photophysical, photochemical, interaction and transport properties of fluorescent or fluorescently labelled molecules at extremely low concentrations by analyzing the fluctuations of the measured fluorescence signal. Since their introduction more than thirty years ago, many variations of fluorescence correlation techniques have been developed. They range from the original and the most widely applied Fluorescence Correlation Spectroscopy analyzing temporal fluctuations at a fixed position and suitable for the investigation of molecules in motion to Image Correlation Spectroscopy analyzing spatial correlations of immobile species. Scanning Fluorescence Correlation Spectroscopy is a group of correlation techniques where the measurement volume is moved across the sample in a defined way, resulting in a spatiotemporal correlation of the detected fluorescence. Scanning improves the accuracy of measurements on slowly moving molecules, diminishes the negative effects of photobleaching, and allows measurements on systems where other fluorescence correlation approaches

---

Petra Schwille  
Institut für Biophysik, Technische Universität Dresden, Tatzberg 47–51, 01307 Dresden, Germany  
petra.schwille@biotec.tu-dresden.de

R. Rigler and H. Vogel (eds.), *Single Molecules and Nanotechnology*. 83  
*Springer Series in Biophysics 12*.  
© Springer-Verlag Berlin Heidelberg 2008

perform poorly or are not possible. This chapter discusses scanning FCS in its relation to other fluorescence correlation methods, describes different variations of scanning FCS, summarizes some of the applications, and finally presents an example of experimental setup designed for two-photon scanning FCS.

## 4.1 Introduction

Fluorescence correlation techniques obtain information about the investigated system by measuring the magnitude of spontaneous microscopic fluctuations and their relaxation while the system is in equilibrium from the macroscopic point of view. The actually measured quantity reflecting the fluctuations of the parameter of interest (e.g., the mean number of particles) is the fluorescence intensity. In other fluctuation methods this “reporting” quantity can be, for example, scattered light or conductivity (Weissman 1981).

Fluorescence fluctuations typically encountered in fluorescence correlation methods arise due to Brownian translational and rotational particle diffusion, particle interactions (such as association/dissociation in chemical reactions in equilibrium), as well as intramolecular processes, for example, transitions between singlet and triplet energy states, radical ion formation, and the like. All these processes giving rise to fluorescence fluctuations can therefore be studied with fluorescence correlation methods.

The most widely used fluorescence fluctuation method is fluorescence correlation spectroscopy (FCS) (Rigler and Elson 2001; Krichevsky and Bonnet 2002; Thompson et al. 2002) which measures the signal fluctuations in one stationary volume with a size usually limited by light diffraction. Fluorescence correlation spectroscopy has been applied to studies of many biological processes involving single molecules (Schwille 2001; Hess et al. 2002; Bacia and Schwille 2003). The suitability of FCS for applications in biology can be linked to its high sensitivity, noninvasiveness, high spatial resolution, and the fact that the investigated system is not disturbed from equilibrium as in some other methods, such as fluorescence recovery after photobleaching (FRAP).

In many cases the investigated molecules are immobile or diffuse too slowly to cause sufficient temporal fluorescence fluctuations needed for FCS analysis. Still, fluctuation analysis can be performed on such systems. In this case the spatial rather than the temporal fluctuations provide information on molecular concentrations, aggregation, association, and so on. The method analyzing spatial fluorescence distributions is known as image correlation spectroscopy (ICS) (Petersen et al. 1993).

Scanning fluorescence correlation spectroscopy (SFCS), presented in this contribution, could be broadly defined as FCS with relative movement of the sample and the measurement volume. It combines the high temporal resolution of FCS with the measurement in many locations encountered in ICS, therefore it can be logically grouped somewhere between these two methods. Combining the advantages of both, SFCS expands the range of the systems that can be studied with fluorescence fluctuation analysis.

## 4.2 Theory

### 4.2.1 Fluorescence Correlation Methods

A typical fluorescence correlation experiment constitutes the measurement of a fluorescence signal  $F(p)$  as a function of some parameter  $p$ . The fluctuations of the fluorescence signal reflect fluctuations of some quantity of interest; for example, the average number of molecules in the measurement volume, and their proper evaluation yields the desired quantity values. The parameter  $p$  can be any combination of the spatial coordinates  $x$ ,  $y$ ,  $z$  and time  $t$ . The fluorescence correlation methods can be classified on the basis of the choice of the parameter  $p$ .

The fluctuations are quantified by means of the autocorrelation function  $G(\Delta p)$  of the measured signal  $F(p)$ :

$$G(\Delta p) = \langle F(p)F(p + \Delta p) \rangle, \quad (4.1)$$

or the normalized autocorrelation function  $g(\Delta p)$ :

$$g(\Delta p) = \frac{\langle F(p)F(p + \Delta p) \rangle}{\langle F(p) \rangle^2} - 1, \quad (4.2)$$

which can be understood as an autocorrelation of the fluctuations  $\delta F(p)$  of  $F(p)$ :  $\delta F(p) = F(p) - \langle F(p) \rangle$ . The averaging  $\langle \cdot \rangle$  in the above equations is performed over the set or subset of the experimental values  $F(p)$ . The calculated correlation function is then fitted to a model function based on the theoretical model of the investigated system. The average  $\langle \cdot \rangle$  in the derivation of the model correlation function is calculated as an ensemble average.

One can imagine an idealized experiment where  $F(p)$  is measured as a function of all spatial coordinates and time ( $p = x, y, z, t$ ) with high resolution in all four dimensions. The four-dimensional autocorrelation function would then reflect correlations over all possible combinations of dimensions. However, such a measurement is not yet technically possible and even not necessary due to high information redundancy in such a hypothetical dataset in a typical investigated system. In practice, the parameter  $p$  corresponds to one or two (max. three) coordinates out of  $x$ ,  $y$ ,  $z$ , and  $t$ .

### 4.2.2 Fluorescence Correlation Spectroscopy

The most common choice of the parameter  $p$  in  $F(p)$  is the time  $t$  and the method is then called fluorescence correlation spectroscopy. Although FCS is sometimes used to denote the whole family of fluorescence correlation techniques, it is used here in a narrower sense, as a method where temporal correlation of the fluorescence from one location is calculated. The correlation function depends on one parameter: the correlation (lag) time  $\tau = \Delta t$ .

In the simplest case a FCS experiment provides two parameters describing the investigated system: the average number of independently diffusing fluorescent particles  $\bar{n}$ . in the measurement volume, and the diffusion coefficient of the particles. The average number of particles  $\bar{n}$ . can be obtained directly from the value of the autocorrelation function at  $\tau = 0$ , assuming proportionality between the number of particles  $n$  and the fluorescence intensity  $F(t)$  at any time:  $F = kn$ , and a Poisson distribution of the number of particles  $n$ , namely the fact that the variance of particle number is equal to the mean:  $\sigma_n^2 = \bar{n}$ . From Equation 4.2 then follows,

$$g(0) = \frac{\langle F(t)^2 \rangle}{\langle F(t) \rangle^2} - 1 = \frac{\sigma_F^2}{\langle F \rangle^2} = \frac{\sigma_n^2}{\langle n \rangle^2} = \frac{1}{\bar{n}}. \quad (4.3)$$

The above expression represents a comparison between the size of the fluctuations of the fluorescence signal  $\sigma_F^2$  and the mean signal size itself  $\langle F \rangle$ . The inverse dependence of the amplitude  $g(0)$  on the average number of particles  $\bar{n}$ . is a mathematical representation of the intuitive fact that the relative magnitude of fluctuations decreases with increasing number of particles.

The diffusion coefficient can be obtained by fitting the experimentally determined autocorrelation (Equation 4.2) to the appropriate model function (see, e.g., Krichevsky and Bonnet 2002). A more realistic model taking into account the excitation intensity profile results in an additional proportionality factor in Equation 4.3.

In a practical realization of a FCS experiment the fluorescence intensity  $F(t)$  is measured in a small (diffraction-limited) stationary sample volume with high temporal resolution going down to the nanosecond time range. In combination with time-correlated single photon counting (TCSPC) technique the temporal resolution can be extended to the picosecond time range (Felekyan et al. 2005). The other end of the useful measurement range, the long correlation times, is limited only by the possibility/ability to maintain the investigated system and the experimental setup stationary and undisturbed over a long time period. The practically attainable time range spans many orders of magnitude which makes FCS applicable to the studies of a large range of diffusional and inter- and intramolecular processes.

Inasmuch as the fluorescence  $F(t)$  in FCS is measured as a function of time, the averaging in the definition of the autocorrelation (Eq. 2) is a time average. The averaging has to be performed over a sufficient number of independent “fluctuation events” in order to provide a reasonably precise estimate of the desired parameters (number of particles, diffusion time) by comparison with the model function calculated using ensemble average. If the particles are immobile and the average number of particles is the parameter of interest, time-averaging in Equation 4.2 does not lead to an accurate estimate because the fluctuations of the number of particles in the measurement volume are practically nonexistent ( $\sigma_n^2 \rightarrow 0$ ; see Equation 4.3). One solution to this problem is offered by image correlation spectroscopy.

### 4.2.3 *Image Correlation Spectroscopy*

In many biologically relevant applications the molecules of interest bind to membranes and other cellular structures that may significantly reduce their mobility. Although in some cases of slow diffusion FCS measurements are possible by extending the measurement time, in other cases photobleaching of the labels prevents measurements over longer periods of time.

As a solution to this problem image correlation spectroscopy has been introduced (Petersen et al. 1993). In ICS the fluorescence image of the sample is recorded; that is, the measured fluorescence  $F(p)$  is a function of spatial coordinates:  $p = x, y$ . The image is autocorrelated according to Equation 4.2. Similarly to FCS, the amplitude of the autocorrelation function  $g(0,0)$  reflects the average number of independent fluorescent particles (Equation 4.3). The average number of particles together with fluorescence intensity per particle can be used to characterize aggregation (Brown and Petersen 1998). The shape of the autocorrelation function reflects the excitation beam profile and the particle size, if the particles are comparable to or larger than the beam waist diameter, and may also be affected by the particle diffusion if this cannot be neglected during the used exposure time.

The average in the definition of the autocorrelation function (Equation 4.2) is calculated over the pixels of the acquired image and can be thus regarded as an approximation of an ensemble average. The number of independent sample volumes, corresponding to the number of independent fluctuation events in FCS, can be estimated as the image size divided by the size of the measurement volume.

In ICS, the spatial correlation is performed to assure sufficient averaging in estimation of  $g(0, 0)$ , and not to obtain autocorrelation of fixed features in the image. On the contrary, the image has to be uniform on the scale larger than the measurement volume size to avoid artefacts. This prerequisite is equivalent to the requirement that the fluorescence signal be stationary in a FCS measurement. Methods dealing with analysis of ICS data containing unwanted features were introduced (Rocheleau et al. 2003). An exception is applications where ICS is used to characterize changes in image structures, for example, the measurement of extension fluctuations of a stretched DNA molecule (Reisner et al. 2005).

### 4.2.4 *Spatiotemporal Image Correlation Spectroscopy*

Image correlation spectroscopy as described above does not provide any temporal information. If dynamic information is required, ICS can be extended by acquiring a series of images in rapid succession. In the formalism introduced above this corresponds to measuring the fluorescence  $F(p)$  as a function of space and time:  $p = x, y, t$ . The correlation analysis can then be performed separately on spatial and temporal coordinates (Wiseman et al. 2000; Srivastava and Petersen 1996; Wiseman et al. 2004) or fully as defined by Equations 4.1 and 4.2. The latter approach has been called spatiotemporal image correlation spectroscopy (STICS) (Hebert et al. 2005). Spatiotemporal

ICS allows, in addition to concentration and aggregation measurements, the measurements of slow diffusion and magnitude and directions of flows. If parts of the image are analyzed separately, diffusion coefficient- or velocity-mapping are possible. The spatial–temporal correlation offers more than a simple combination of FCS and ICS. For example, the direction and magnitude of flow cannot be determined by FCS or ICS alone, but a spatial cross-correlation analysis among at least three measurement volumes is necessary (Brinkmeier et al. 1999; Gosch and Rigler 2005).

Compared with FCS, STICS suffers from lower temporal resolution which is determined by the maximum rate of image acquisition. Thus, only relatively slow dynamics can be studied.

#### 4.2.5 Scanning Fluorescence Correlation Spectroscopy

In scanning fluorescence correlation spectroscopy the fluorescence is recorded from a small measurement volume defined by the focused illuminating beam as in FCS, and this measurement volume is moved relative to the sample in a controlled way. Because the movement of the measurement volume in the sample is the only principal difference from FCS, all other features of FCS are preserved in SFCS, most importantly the high temporal resolution. The fluorescence signal  $F(t)$  is measured as a function of spatial and temporal coordinates:  $p = x, y, t$ , however, contrary to STICS, not the whole  $xyt$  space is sampled. At any time  $t$  only one point in  $xy$  is probed. Consequently, the correlation function calculated according to Equation 4.2 cannot be evaluated in the whole correlation space  $\xi, \theta, \tau (= \Delta x, \Delta y, \Delta t)$  but only at some points. This is schematically illustrated in Figure 4.1.

The diagram in Figure 4.1A describes a line-scan SFCS where the measurement volume is moved repeatedly along the  $x$ -axis in the positive direction (the flyback period is neglected in the figure). The bold lines represent the sampled points in the

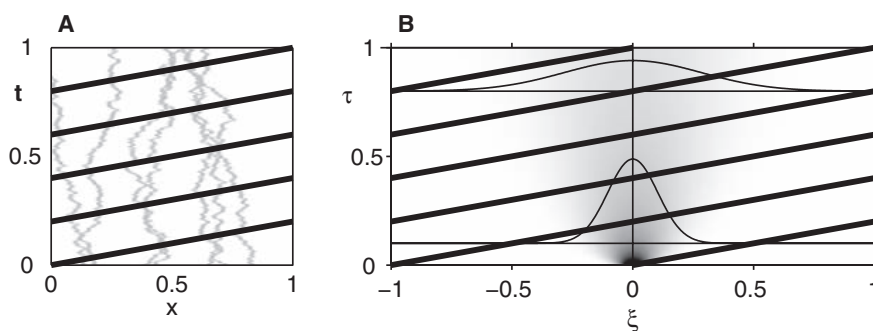


**Figure 4.1** A schematic description of the line scan. **A**: the measurement volume position along the  $x$  axis in time is marked by bold lines; traces of several diffusing particles are shown in grey; **B**: the correlation coordinates  $\xi$  and  $\tau$  at which the autocorrelation can be calculated from the measurement depicted in A are marked by bold lines; the full two-dimensional autocorrelation is shown in gray together with two profiles at early and late correlation times  $\tau$

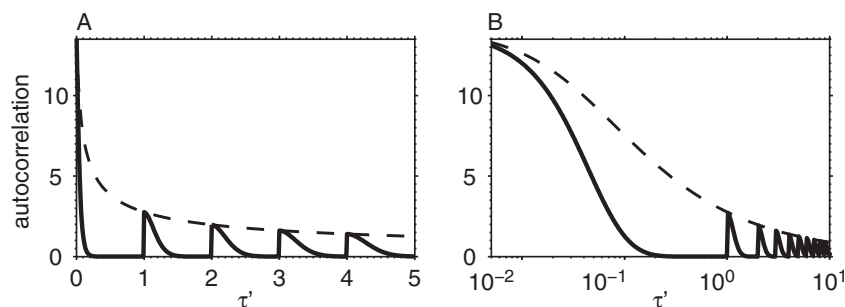


**Figure 4.2** The theoretical autocorrelation function from the line scan depicted in Figure 4.1A; the bold curve corresponds to the profile along the bold lines in Figure 4.1B for  $\xi > 0$ ; the dashed curve is a profile for  $\xi = 0$  and represents a point-FCS measurement: **A**: linear time axis, **B**: logarithmic time axis

$xy$  space. The gray curves symbolize the positions of several diffusing particles. The diagram in Figure 4.1B shows the corresponding spatiotemporal autocorrelation  $g(\xi, \tau)$ . The gray values correspond to the theoretical autocorrelation function. Two profiles of the autocorrelation along the spatial axis at early and late times are shown. They are of Gaussian shape with the width increasing with time due to diffusion. The bold lines show the parts of the two-dimensional autocorrelation function obtainable from the line scan measurement. The autocorrelation profile along the bold lines (for positive  $\xi$  values), which is the actual result of the depicted line-scan SFCS measurement, is shown in Figure 4.2. The Figures 4.1 and 4.2 essentially describe the experiment of Koppel et al. (1994).

It can be seen from Figures 4.1 and 4.2 that although SFCS does not yield the full two-dimensional autocorrelation, a suitable choice of the measured profiles of the  $g(\xi, \tau)$  (determined by the scan amplitude and period) provides a large amount of information about the autocorrelation. The high spatiotemporal resolution of SFCS may be preferable to the full, albeit lower-resolution, two-dimensional autocorrelation obtainable with STICS because of high information redundancy in  $g(\xi, \tau)$ . This redundancy is most apparent in case of pure diffusion, where the temporal profile at  $\xi = 0$  (a standard FCS curve) contains full information about the particle concentration and diffusion process. The redundancy is also present in more complex processes, for example, diffusion combined with flow.

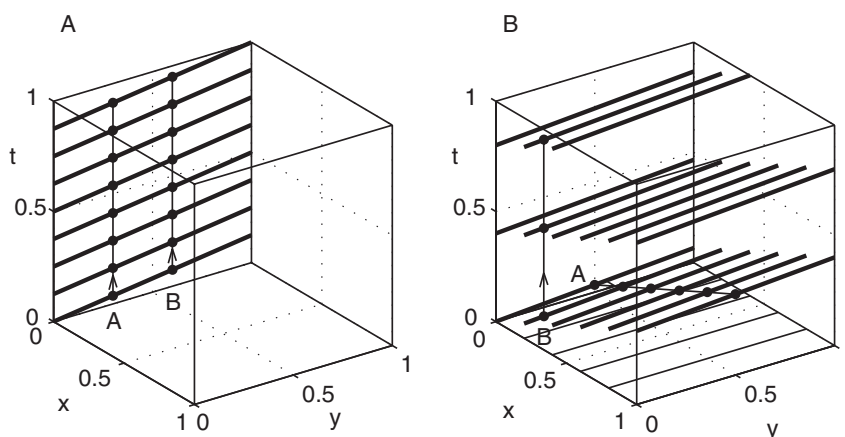
A usual FCS experiment would be represented in Figure 4.1A by a vertical line at a selected location  $x$ , and the obtained autocorrelation would correspond to a temporal profile at  $\xi = 0$  in Figure 4.1B and the dashed curve envelope in Figure 4.2. In some sense SFCS suffers from lower temporal resolution because only the points separated by the scan period ( $\tau = nT$ ) are sampled from the full FCS curve. This does not pose a problem when the diffusion is slow and when the sampling of the correlation function by the scan period  $T$  is sufficiently fine. Additionally, the missing information is partially contained in the shape (width) of the peaks of the SFCS curve (Figure 4.2).

Figure 4.1 also shows that the moving beam collects the signal from all particles along the scan path, whereas a stationary beam (FCS) would detect only the

particles that happen to diffuse to its position. There are even some positions in the shown example where no particle would be detected. This demonstrates how SFCS increases the number of independent sampling volumes which determines the effective number of independent points over which the averaging in Equation (4.2) takes place. In this way SFCS can increase the statistical accuracy of the averaging process. The scanned area (amplitude) and the scan speed (period) and their relation to the diffusion time determine the gain in accuracy due to the increase of the number of independent sample volumes and the loss of time resolution due to the probe volume “escaping” the particles before they can diffuse out and thus leave a trace about their diffusion time. The experimental parameters have to be carefully chosen depending on the diffusion characteristics and the expectations placed on the recovered parameters: whereas for slowly diffusing particles the scanned area will be large, leading to reduction in time resolution (which is not a problem for slowly diffusing or stationary particles), for fast diffusion the scanned area can be smaller allowing for the necessary higher temporal resolution, or the scanning can be abandoned altogether.

Figures 4.3 and 4.4 show several examples of scanning patterns in two spatial dimensions: a line scan, a raster scan, a circle scan, and a spiral scan. The line scan (Figure 4.3A) represents the same scenario as shown in Figure 4.1. In addition to the already discussed motivation for employing SFCS, scanning provides a way of measuring fluorescence signal autocorrelation from multiple locations simultaneously. This is done by dividing the acquired data to parts based on spatial location (points A and B in Figure 4.3A) and autocorrelating them separately. The reduced temporal resolution given by the line scan period then determines the range of measurable diffusional processes. In addition, the signals from different locations can be cross-correlated, allowing, for example, detection of uniform flows.

The raster scan (Figure 4.3B) extends the probed space to two dimensions. The signal can then be correlated along three different directions giving in principle access to three different time scales on which diffusion can be studied. Autocorrelation



**Figure 4.3** Two examples of scanning patterns: **A**: line scan, **B**: raster scan

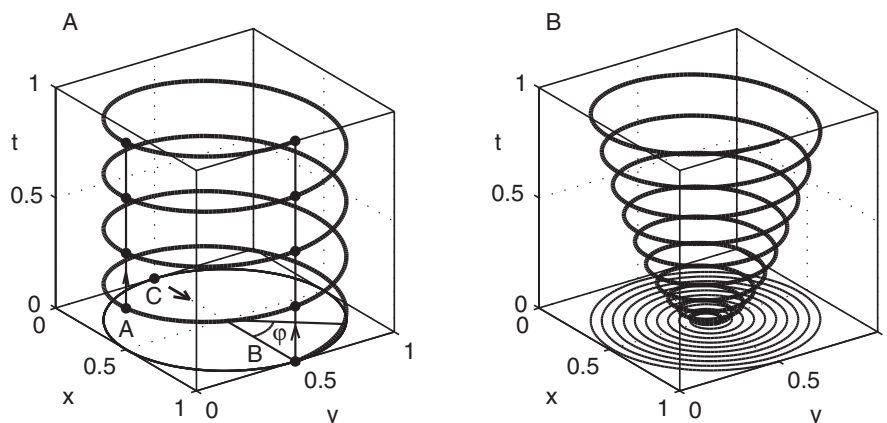


**Figure 4.4** Two examples of scanning patterns: **A**: circle scan, **B**: spiral scan

along the scanned line monitors the diffusion and other processes causing fluctuations that are faster than the scan speed. Slower diffusion will be reflected in the autocorrelation across the scan lines (line A in Figure 4.3B) and very slow diffusion can be monitored by correlating the signal across the frames (line B in Figure 4.3B). Neglecting the temporal differences between different points within one frame and performing spatiotemporal correlation across the frames reduces the raster scan SFCS to STICS.

As in line scan SFCS, individual correlation analysis of parts of the data corresponding to different spatial locations produces a map monitoring slow diffusion. This may however be problematic to realize in practice because of poor signal-to-noise ratio. Spatial mapping of flow vectors has been achieved using STICS (Hebert et al. 2005), and a similar approach is used in particle imaging velocimetry (PIV) where, however, the signal quality is better due to the far larger than molecular scales (Adrian 1991).

The line scan and raster scan modes or their variations can be easily implemented on a commercial confocal laser scanning microscope (CLSM). The presence of turning points in line and raster scan modes, and of the return period in one-directional scan means that accurate synchronization between the measurement volume position and data acquisition is necessary for correct calculation of the autocorrelation because parts of the signal stream have to be excluded from the analysis. This synchronization is to some extent implemented in CLSMs as it is the basis of the image formation.

Circle scan SFCS (Figure 4.4A) has the advantage that no turning points or dead times are present. Therefore, in the simplest case, no synchronization is necessary and the data stream can be correlated as in a usual FCS experiment. However, if circle scan SFCS is used to obtain spatially resolved information, for example, diffusion coefficients along the perimeter of the circle, accurate synchronization is obviously needed.

The knowledge of the scanning beam position at all times opens up a possibility for the measurement of magnitudes and directions of uniform flows across the

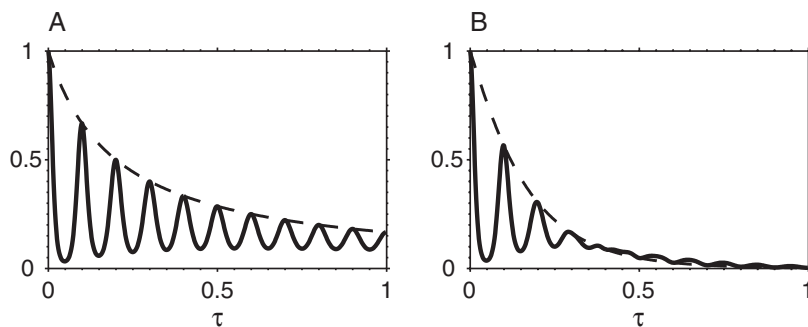
scanned region, as demonstrated by Skinner et al. (2005). The fluorescence signal is recorded as a function of time that uniquely determines the phase angle  $\varphi(t)$  of the focal point position. The fluorescence signal can then be autocorrelated with respect to a particular angle  $\varphi_0 \in (0, 2\pi)$  producing a phase angle-dependent autocorrelation function  $g(\varphi_0, \tau)$ . The autocorrelation of the data is calculated according to a modified Equation (4.2):

$$g(\varphi_0, \tau) = \frac{\langle F(t)F(t+\tau) \rangle_{\varphi_0}}{\langle F(t) \rangle^2} - 1, \quad (4.4)$$

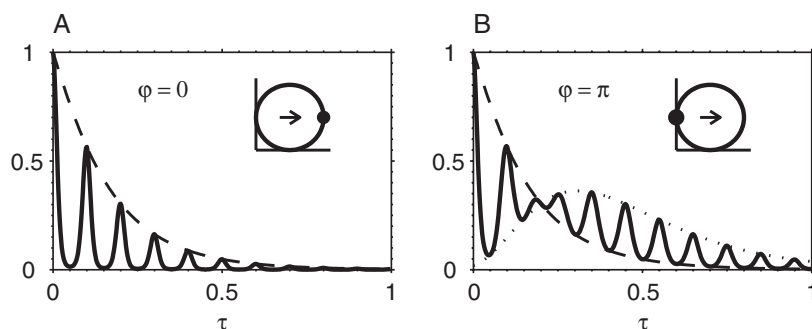
where the calculation of the average  $\langle \tau \rangle_{\varphi}$  is restricted to angles  $\varphi = \varphi_0 + 2\pi m$ ; that is, the averaging is done only over times  $t$  at which the focal point was at the position determined by the phase  $\varphi_0$ .

Figure 4.5 shows the theoretical autocorrelation functions of circle scan SFCS in the presence of only diffusion (Figure 4.5A) and in the presence of diffusion and directional flow (Figure 4.5B) together with usual FCS curves (dashed envelopes). Although the existence of flow can be seen in Figure 4.5B, the autocorrelation curve contains only information about its magnitude but not its direction.

Figure 4.6 shows position-sensitive autocorrelation curves calculated for angles  $\varphi_0 = 0$  (Figure 4.6A) and  $\varphi_0 = \pi$  (Figure 4.6B), for diffusion and flow in the positive  $x$ -axis direction (bold arrow in Figure 4.4A). The angle  $\varphi_0 = 0$  corresponds to the point B in Figure 4.4A and the angle  $\varphi_0 = \pi$  to the point C. The particles detected at the point B are flowing away from the scanned region, therefore they do not contribute to the autocorrelation at later times due to their flow, and the autocorrelation is fully enveloped by a standard point FCS curve (Figure 4.6A). The particles detected at position C cross the scanning path again after flowing across the circle diameter, which results in a higher correlation values at corresponding times compared to a point FCS (Figure 4.6B). The dotted envelope represents a correlation curve that would be obtained in a spatial cross-correlation experiment with the two measurement volumes positioned at points C and B. This experiment, however,



**Figure 4.5** Theoretical autocorrelation functions obtained with a circle scan: **A**: in the presence of diffusion only; **B**: in the presence of diffusion and uniform flow; this curve represents the average of the position-sensitive autocorrelation (Figure 4.6) over all angles  $\varphi$



**Figure 4.6** Theoretical position-sensitive autocorrelation functions obtained with a circle scan in the presence of diffusion and uniform flow: **A**: autocorrelation for  $\varphi = 0$ , that is, for the point where the flowing molecules leave the scanned region; **B**: autocorrelation for  $\varphi = \pi$ , that is, for the point where the flowing molecules enter the scanned region

allows one to determine only the projection of the velocity vector onto the line connecting the two points, not the flow direction in the  $xy$ -plane. The advantage of the circle scan SFCS lies in the fact that one measurement dataset is used to calculate autocorrelation for all phase angles  $\varphi_0$  allowing accurate determination of the direction of flow without any a priori knowledge.

Scanning FCS has the potential to diminish the negative effects of photobleaching, which is an important limiting factor in FCS, especially when two-photon excitation is employed. The local depletion of fluorescent molecules and apparent shortening of diffusion times due to photodestruction are encountered when high excitation powers are used. The use of high excitation powers is motivated by the fact that the signal-to-noise ratio in the experimental curves increases with the fluorescence count rate per molecule.

In SFCS the total excitation light dose is distributed over the scanned region. In addition, the depleted concentration of fluorescent molecules at one location can be partially recovered due to the diffusional influx of intact molecules before the same spot is revisited by the excitation beam in the next scan cycle. Scanning FCS does not reduce the total photobleaching (if linear dependence between excitation dose and photobleaching yield is assumed) but alleviates its effects on the autocorrelation by “escaping” the regions containing photobleached molecules and spreading the photobleached molecules over a larger area. The circle scan lowers the excitation dose at any position by a factor equal to the ratio between the circle circumference and the measurement spot diameter. Alternatively, the spiral scan with a constant speed (Figure 4.4B) can be applied to further decrease the excitation dose at any location. This approach then comes close to ICS if the molecules are immobile.

An interesting question is whether photobleaching itself could be reduced, not only its negative consequences. If photobleaching is mediated by the triplet states, as shown in some cases (Widengren and Rigler 1996; Dittrich and Schwille 2001), exciting one location for a time shorter than the time needed for a significant build-up of the triplet state population (determined by the rates of transitions between the molecular energy

states) and revisiting the same location after all the triplet states have decayed back to the ground state would lower the possibility of triplet–triplet absorption, and therefore photobleaching. However, rather high scanning speeds, possibly achievable with acousto-optical deflectors, would be necessary to explore this possibility.

Scanning FCS can be combined with all variations of FCS. For example, the cross-correlation analysis of fluorescence fluctuations in two detection channels defined by different emission wavelengths (Schwille et al. 1997) or emission polarizations (Barcellona et al. 2004) could benefit from the combination with scanning. The applications of cross-correlation analysis often focus on the relative amplitudes of the autocorrelation and cross-correlation of the signal rather than on the diffusion kinetics, therefore a partial loss of the information on diffusion kinetics present in some SFCS implementations is not a problem. Scanning FCS can be also combined with the analysis of distribution of photocounts in the binned fluorescence signal  $F(p)$  (photon counting histogram (Chen et al. 1999), fluorescence intensity distribution analysis (Kask et al. 1999)), or higher-order auto/cross-correlation analysis (Palmer and Thompson 1987, 1989; Thompson 1991).

### 4.3 Applications

The early applications of SFCS aimed mainly at the determination of the concentration and the diffusion of the molecules was considered negligible. The reason for scanning was the need to record the fluorescence signal from a sufficient number of statistically independent volumes in systems where the diffusion of the molecules was too slow to guarantee fast turnover of the molecules in the measurement volume. Initially, the sample rather than the excitation beam was moved.

In 1976 Weissman et al. (1976) used a technique that could be regarded as the first application of SFCS to measure molecular weights of DNA molecules stained with ethidium bromide. Because of the relatively large measurement volume and slow diffusion of DNA molecules the sample was placed in a cylindrical cell and rotated with a period of 4 s while the measurement volume was stationary. In this way sampling from approximately 400 independent volumes was achieved and proved to be sufficient for the calculation of the average magnitude of fluctuations necessary to obtain the DNA concentration and subsequently the molecular weight.

The technique of Weissman et al. was modified by Nicoli et al. (1980) who moved the sample placed in a thin cylindrical tube linearly up and down by mounting it on a loudspeaker. The goal of the measurement was to investigate the binding between antibody and antigen attached to a bead of 3–5  $\mu\text{m}$  diameter. The two populations of fluorescently labeled antibodies—free in solution and bound to the antigen on the bead—are then distinguished on basis of their different diffusion times. After a suitably chosen scan period  $T$  the correlation of unbound antibodies disappears and the correlation of slowly diffusing bound molecules is still present.

A line scan SFCS was introduced by Petersen in 1984 (Petersen 1984, 1986; Petersen et al. 1986) as a modification of FCS for slowly diffusing species in cell

membranes. The goal was to measure aggregation, that is, to estimate the number of monomers per aggregate, or to obtain information about the distribution of aggregate sizes. The fluorescence signal was recorded while translating the sample linearly with a constant velocity, and then autocorrelated. In the theoretical treatment (Petersen 1986) a formula is presented relating the amplitude of the autocorrelation to the mean number and variance of the number of monomers per aggregate. Several special cases of multimodal distributions (sums of unimodal distributions characterized by the mean and the variance) are discussed, for example, the simple aggregation reaction  $nA \rightarrow A_n$  where only monomers and aggregates of degree  $n$  are present, or the situation with monomers and aggregates with Poisson-distributed sizes. The line-scanning SFCS was applied to measure the mean number of aggregates of Sindbis virus and vesicular stomatitis virus glycoproteins on the membrane of fibroblasts. The same SFCS implementation was used by St-Pierre and Petersen (1990) to study ligand binding to aggregated receptors, or more precisely, to find the relationship between the degree of ligand binding and the state of receptor aggregation. Another application involved the measurement of epidermal growth factor receptor distribution on A431 cells (St-Pierre and Petersen 1992).

The applications of SFCS described so far were concerned only with the amplitude of the correlation function and did not attempt to obtain any information about the diffusion of the fluorescent species. Meyer and Schindler (1988) used circular scanning to measure particle concentration and diffusion coefficient. The circular path was achieved by rotating an optical unit holding a tilted objective. The autocorrelation of the measured fluorescence exhibited periodic peaks at times corresponding to the period  $T$  of rotation. The amplitude of the peak at time  $\tau = 0$  provided the particle number, and the decrease of the amplitude and the broadening of the peaks at longer lag times  $\tau = nT$  was used to determine the diffusion coefficient. The method was applied to study concentration- and calcium-dependent aggregation of lipid vesicles, and the time course of aggregation of a membrane matrix protein from *E. coli* in lipid monolayer. The range of diffusion coefficients  $D$  that can be determined with the used setup is  $10^{-7}$ – $10^{-10}$   $\text{cm}^2\text{s}^{-1}$ .

Koppel et al. (1994) used a commercial confocal laser scanning microscope (CLSM) to perform SFCS by repeatedly scanning a single line across the sample. The major advantage of using a CLSM compared to the above-described techniques is a smaller detection volume and the possibility of faster scanning. The correlation curves were fitted to a model of two-dimensional diffusion plus uniform flow (representing in this case the moving excitation beam) which yielded the particle number and the diffusion coefficient. The method has been applied to the measurement of the diffusion coefficient of ethidium bromide-stained DNA of different sizes in solution, and to the analysis of diffusion of colloidal gold particles in suspension and bound to PE in supported planar bilayers. In case of the gold particles scattered light rather than fluorescence was used to detect the particles. The maximum diffusion coefficient measurable with this method is on the order of  $10^{-7}$   $\text{cm}^2\text{s}^{-1}$ . Separate analysis of parts of the recorded data was demonstrated, allowing the detection of variations in particle concentrations or diffusion coefficients at different regions along the scanned line.

Berland et al. (1996) demonstrated the use of two-photon excitation with a circle scan SFCS on a home-built CLSM for the measurement of particle concentrations. The method was applied to studying protein aggregation and dissociation in solution. Measuring the dependence of the number of independent particles (dimers and tetramers) on the total protein concentration and assuming equilibrium between dimers and tetramers dissociation constant was determined. Kinetic measurements of dissociation upon dilution and measurements of pH-dependent dissociation were also performed.

An approach similar to SFCS has been applied by Winkler et al. (1999) to confocal fluorescence coincidence analysis, where association between two molecular fragments labeled with different fluorophores is identified by coincident detection of photons in two spectral detection channels. The results demonstrate that moving the sample with frequencies as low as 3 Hz significantly improves the S/N ratio, thus allowing shorter measurement times required for high-throughput screening applications.

Amediék et al. (2002) combined dual-color cross-correlation analysis with scanning. The authors used piezo-driven sample stage moving in several scanning patterns: line, spiral, and a random scan, and investigated their effects on the auto- and cross-correlation curves recorded from immobile samples. The investigated systems were GFP-DsRed fusion proteins immobilized in a gel and double-labeled cholera holotoxin bound to immobile receptors on a cell membrane. Scanning the sample allowed autocorrelation and cross-correlation curves to be recorded and to identify co-localization on basis of the cross-correlation amplitude, a task practically impossible with a standard FCS because of photobleaching of very slowly diffusing or immobile molecules. Among the employed scanning patterns the random scan proved to be most suitable, possibly due to the absence of artefacts arising from the periodicity in the other patterns.

Ruan et al. (2004) applied circle scan SFCS to study slow diffusion of membrane proteins in giant unilamellar vesicles (GUV). The geometry of the experiment was such that the circular path of the measurement volume intersected the surface of the GUV twice, one half of the scan path laid outside the GUV and one half inside. The detected fluorescence signal was processed in such a way that autocorrelation curve for every point along the circular path was obtained. With this approach fast diffusion of the labeled antibody in the outer solution and slow diffusion of the antibody bound to the membrane protein were measured. The application of SFCS in this case does not increase the number of independently sampled volumes on the membrane (only two locations are measured) but allows simultaneous measurement of autocorrelation in different locations, the points along the circular path. Additionally, small movements of the GUV which can prevent point FCS measurements on moving membrane can be compensated for by shifting the signal records from subsequent scans relative to each other, before the data are correlated.

Xiao et al. (2005) used a sample-scanning CLSM to image fluorescent molecules immobilized on a surface and in polystyrene films, and to measure autocorrelation of their fluorescence via line scan SFCS. The authors were interested in the bright/dark state transitions (triplet or radical ion state) on the microsecond time scale. It was

suggested that this method could be applied to determination of the rates of association and dissociation of freely diffusing molecules with immobilized molecules, for example in screening of surface-patterned peptide and nucleic acid microarrays.

Digman et al. (2005a,b) performed autocorrelation analysis on images obtained with a commercial CLSM and a home-built two-photon scanning microscope. The two-dimensional autocorrelation of the raster-scan images provided information about fast diffusion (or scan speed and measurement volume size) along the fast scan axis, as in the line scan SFCS. The autocorrelation decay along the slow scan axis reflects diffusion on a longer time scale. Raster- and line-scan SFCS were demonstrated on paxillin-EGFP diffusing in cytosol of CHOK1 cells.

The most detailed and comprehensive analysis of the possibilities of circular-scan SFCS so far has been presented by Skinner et al. (2005). Taking advantage of synchronization between the beam position along the circular path characterized by the phase angle  $\varphi$  and the data acquisition the authors introduce position-sensitive SFCS (PSFCS). This variation of SFCS allows calculation of the autocorrelation as a function of the phase  $\varphi$  and lag time  $\tau$  which can be used to measure, in addition to diffusion, the direction and speed of flow and the position of immobile particles (see Figures 4.5 and 4.6). If required, an appropriate normalization procedure eliminates unwanted effects in autocorrelation caused by immobile particles. The circular-scan SFCS was shown to be less sensitive to photobleaching than standard FCS. The method has been demonstrated on freely diffusing and uniformly flowing dye in solution and EGFP diffusing in cells.

## 4.4 Implementation

The first applications of SFCS used special experimental setups designed and suitable only for a particular type of experiment (Weissman et al. 1976; Nicoli et al. 1980; Meyer and Schindler 1988). The disadvantages of most of these setups are inflexibility, relatively large measurement volume, and the need to move the sample, which could lead to sample distortions due to its inertia and elastic properties.

With the development of laser scanning microscopy a home-built or a commercial multipurpose CLSM has become the most common instrument used for SFCS. Although a line or a raster scan is easily realizable with a commercial CLSM, the inaccessibility of the control software source code makes the implementation of other scan modes practically impossible. The advantage of a home-built system is the full control over the scanner movement. Furthermore, the emission collection efficiency and the profile of the excitation laser beam at the objective back aperture are perhaps more crucial parameters in fluorescence correlation measurements than in imaging applications. A custom-built setup allows for optimization of these parameters.

We present here a two-photon laser scanning setup built in our laboratory as an example of a versatile instrument for two-photon imaging and SFCS applications.

#### 4.4.1 Light Source

A tunable Ti:Sapph laser Mira 900-F (Coherent, Santa Clara, USA; 76 MHz, 700–1000 nm, 100–150 fs pulse length) pumped by frequency doubled 10 W Nd:YVO<sub>4</sub> laser Verdi V10 (Coherent; 532 nm) is used as the excitation source. Two-photon excitation has certain advantages over one-photon excitation: the excitation is limited to a well-confined volume, therefore no additional volume reduction with the help of a pinhole is needed, and, for the same reason, the total photobleaching in the sample is lower. This fact, together with weaker scattering of light of longer wavelengths makes two-photon excitation particularly suitable for measurements in deeper tissue (König 2000).

The drawback of two-photon excitation is stronger photobleaching in the focal point with the consequence that significantly lower count rates per molecule, and therefore a lower signal-to-noise ratio, can be achieved compared to one-photon excitation.

The described setup could in principle be modified to a one-photon excitation mode by exchanging the laser, using an appropriate beamsplitter and emission filters, and installing a pinhole in the emission path. This could be realized, for example, by coupling the avalanche photodiodes (APD) with an optical fiber of selected core diameter, and placing the entry of the fiber, playing the role of the pinhole, to the present position of APDs.

#### 4.4.2 Optical Part

The optical path of the excitation and emitted light in the microscope is shown in Figure 4.7. The laser beam is initially expanded by the combination of lenses L1 and L2 in order to overfill the entrance aperture of the objective after having passed through

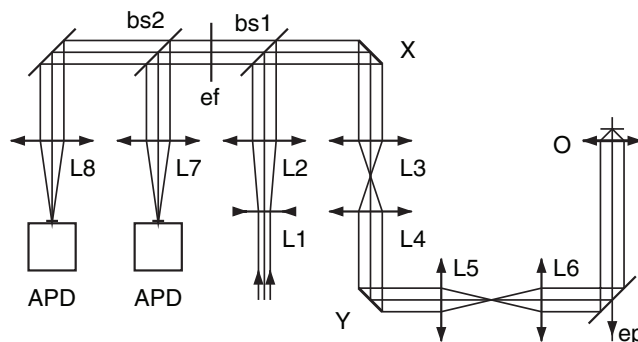


**Figure 4.7** Optical part of the two-photon laser scanning microscope: L1–L8: lenses; bs1, bs2: beam splitters; ef: emission filter; X, Y: scanners with mounted mirrors; O: objective; ep: eyepieces; APD: avalanche photodiode

the rest of the scanning optics. Optionally, the laser beam can be passed through a prism group velocity dispersion compensator before expansion if the pulse duration in the focal point of the objective needs to be optimized (Müller et al. 1998).

The beamsplitter bs1 reflects the infrared excitation beam and transmits the fluorescence collected by the objective. The lenses L3 and L4 image the fast scanner X onto the slow scanner Y and the lenses L5 and L6 image the slow scanner onto the back objective aperture while collimating the beam. The objective then focuses the excitation beam into a diffraction-limited spot and collects the fluorescence which is descanned by following the same path as the excitation beam in the opposite direction. After having been transmitted by the beamsplitter bs1 the fluorescence can be divided into two spectral channels by the beamsplitter bs2 or, alternatively, divided by a polarizing beamsplitter into two polarization components. With the help of the lenses L7 and L8 the fluorescence is focused onto the active area of the avalanche photodiodes (APD; type SPCM-CD2801, PerkinElmer, Wellesley, USA).

The scanning optics is built around an inverted IX 71 microscope (Olympus, Tokyo, Japan). The light enters via a side hole in the revolver holding the filter cubes and is reflected upwards by a mirror mounted in a custom-made filter cube. The light therefore does not pass through the microscope tube lens.

The beam is steered by two mirrors mounted on shafts of closed-loop galvanometer scanners (VM2000, GSI Lumonics GmbH, Unterschleißheim, Germany). The maximum scan frequency is limited to 50–500 Hz, depending on the amplitude of the scan. Faster scanning could be achieved by resonant scanners, however, at the cost of losing the flexibility of choosing the scan pattern. As an alternative to mechanical scanners, much faster acousto-optical deflectors (AOD) can be used to steer the beam (Roodra et al. 2004).

### 4.4.3 *Electronics*

A diagram depicting the electronic components of the experimental setup and their connections is shown in Figure 4.8. The central part of the microscope electronics is formed by the ADWin Gold system (Jäger GmbH, Lorsch, Germany), a general-purpose microprocessor-controlled unit containing several analog and digital inputs and outputs, and counters. The ADWin module generates an arbitrary voltage waveform which, via the scanner drivers (MiniSax, GSI Lumonics), determines the angular deflection of the scanners. The scanners contain a position sensor generating a signal that is provided to the user by the MiniSax drivers. This signal can be recorded by the ADWin module to monitor the real scanner position.

In the imaging mode, the fast scanner X is driven with a voltage waveform of a sawlike shape with rounded turning points formed by fragments of a parabola. The waveform shape has been optimized to maximize the linearity of the scan and to minimize the time needed for changing the direction. The sample is illuminated for the whole time of the scanning cycle (no beam blocking takes place) and the signal is recorded while scanning in both directions (bidirectional scan). The slow scanner Y is moved stepwise during the reversal period of the fast mirror.

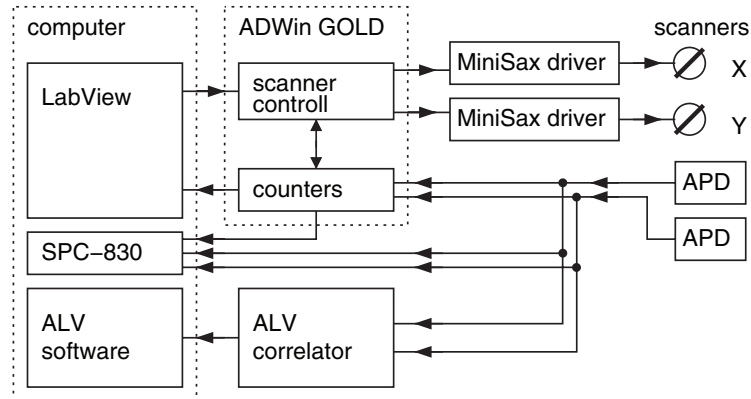


**Figure 4.8** Electronical part of the two-photon laser scanning microscope

The output signal of the APD detectors consists of a sequence of 40 ns TTL pulses, each corresponding to a detected photon. The pulses are counted by the counters in the ADWin module and arranged accordingly into pixels of the image

The APD outputs are also passed to a hardware correlator ALV-6000 (ALV GmbH, Langen, Germany). This correlator is able to process two input signals and calculate their autocorrelations or a cross-correlation, although not both simultaneously. Alternatively, the APD outputs can be processed by a SPC-830 photon counting module (Becker & Hickl GmbH, Berlin, Germany). The SPC-830 module measures the photon arrival time of every photon and stores the data stream into a file. The complete fluorescence intensity trace is then available for offline analysis.

With the help of pixel, line, and frame clock signals generated by the ADWin module and a laser synchronization signal, the SPC-830 can construct fluorescence images, and thanks to precise picosecond timing provided by the time-correlated single photon counting (TCSPC) method fluorescence lifetime imaging (FLIM) can be performed.

The position of the observed section of the sample along the optical axis (z-section) is controlled by a piezo nano-positioning device PIFOC P-721.10 (Physik Instrumente GmbH, Waldbronn, Germany) on which the objective is mounted.

#### 4.4.4 Software

The user interface and the control of the ADWin module and the PIFOC device is provided by a program written in the LabView environment (National Instruments, Austin, USA). Based on the user-defined parameters the waveforms for either the image acquisition or for the SFCS measurement are calculated and passed as an array of values from LabView to ADWin Gold which then generates the actual driving voltage signal. LabView reads the pixel count values from ADWin when they become available, and uses them to create the fluorescence image.

The processor in the ADWin module is capable of running several processes (programs) in a real-time mode. In the presented application four processes are used: one low-priority process checking the status of the scanners and three high-priority processes: one for image acquisition, one for waveform generation for the SFCS measurements and one for positioning the laser beam to any location selected by the user. The execution of these processes is again controlled by LabView.

Due to the finite time response of the mechanical scanners there is a time lag between the driving voltage signal and the actual scanner position. This time lag can lead to synchronization artefacts between the lines scanned in opposite directions which are manifested as a relative shift of the odd and even lines in the image. The time lag occurring with the particular waveform used in the described scanning design varies only slightly with the scan speed and amplitude and is largely taken into account during the image reconstruction. However, a small residual variation of the time lag may still be apparent in the image. The remaining line shift can be easily corrected for by maximizing the overlap between the neighboring lines by finding an optimal value of the line shift  $d$ . Expressed mathematically, the following function has to be minimized by varying  $d$ :

$$f(d) = \frac{1}{\lfloor n/2 \rfloor (n-d)} \sum_{j=0}^{\lfloor n/2 \rfloor - 1} \sum_{i=n-d-1}^{j} (c(i, 2j) - c(i+d, 2j+1))^2, \quad (4.5)$$

where  $c(i, j)$  is the number of counts in the image pixel  $(i, j)$ ,  $i$  and  $j$  are the column and row indices, respectively, and the size of the image is  $n \times n$ .

The synchronization problem is not immediately apparent in a one-directional scan system, because all lines are shifted in the same direction resulting in the shift of the whole image. Although this does not pose a problem in purely imaging applications, in our case, where we want to perform measurement in a well-defined location, be it a point-FCS or a more complex SFCS experiment, exact synchronization between the image on the screen and the beam position within the sample is necessary. From this point of view the one-directional scan is not easier to implement, and because it involves more dead time, the bidirectional scan was chosen for the described device. Figure 4.9 demonstrates the measurement of the fluorescence autocorrelation at a defined location within a cell.

Both the ALV autocorrelator and the SPC-830 photon counting module are supplied with software fully controlling the instruments. The two devices are operating independently, without any interface to the main LabView program.

#### 4.4.5 Data analysis

The ALV autocorrelator provides directly the autocorrelation and cross-correlation functions but not a full photon sequence with high temporal resolution making a more advanced analysis needed in some SFCS applications impossible. The SPC-830

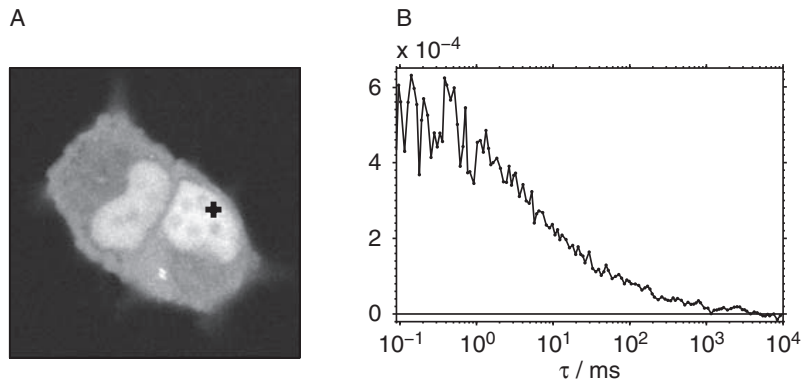


**Figure 4.9** Two-photon excitation fluorescence image of a GFP-expressing cell (A) and the fluorescence autocorrelation curve measured at the point indicated by the cross (B)

module provides a full photon sequence that is correlated offline with a custom-written software (C++) using the multiple-tau approach (Magatti and Ferri 2001). Because the complete fluorescence intensity signal  $F(p)$  is available, various ways of data processing as described above can be implemented.

## 4.5 Conclusion

Scanning FCS is not a single technique but rather a whole family of techniques spanning the gap between the most widely used one-point FCS on one side and ICS on the other side. We have tried to present here various SFCS approaches in relation to FCS and ICS, and to identify the reasons why they are preferable to other fluorescence correlation methods in certain situations. The choice of a particular SFCS implementation is governed by two factors: the information we want to obtain about the sample and the sample properties limiting the range of applicable techniques.

The main reasons that can make SFCS the method of choice instead of FCS or other correlation techniques can be summarized as follows.

- Improve signal-to-noise ratio by increasing the number of statistically independent samples where time averaging is not satisfactory (immobile or slowly diffusing molecules)
- Diminish or avoid the effects of photobleaching (mainly with two-photon excitation)
- Measure correlation at more locations (pseudo-) simultaneously; measure diffusion and flows simultaneously (position-sensitive SFCS)

There are certainly limits to the applicability of SFCS. For example, the scanned region should be homogeneous on a large scale, otherwise a fixed pattern in the detected fluorescence intensity gives rise to unwanted correlations. These effects can

perhaps be eliminated by procedures similar to those dealing with background in ICS (Wiseman and Petersen 1999). Alternatively, they can be taken advantage of in determining the position of immobile molecules (Skinner et al. 2005). Another limitation is the partial loss of diffusion information. This is not likely to be a major hindrance inasmuch as slow diffusion is reflected in the autocorrelation obtained by scanning with a periodic pattern, and other applications may not be interested in diffusion at all, such as cross-correlation binding studies or measurements on immobile molecules.

## References

- R. J. Adrian. Particle-imaging techniques for experimental fluid-mechanics. *Annu. Rev. Fluid Mech.*, 23:261–304, 1991.
- A. Amediek, E. Haustein, D. Scherfeld, and P. Schwille. Scanning dual-color cross-correlation analysis for dynamic co-localization studies of immobile molecules. *Single Molecules*, 3(4):201–210, 2002.
- K. Bacia and P. Schwille. A dynamic view of cellular processes by in vivo fluorescence auto- and cross-correlation spectroscopy. *Methods*, 29(1):74–85, 2003.
- M. L. Barcellona, S. Gammon, T. Hazlett, M. A. Digman, and E. Gratton. Polarized fluorescence correlation spectroscopy of DNA-DAPI complexes. *Microsc. Res. Tech.*, 65(4–5):205–217, 2004.
- K. M. Berland, P. T. C. So, Y. Chen, W. W. Mantulin, and E. Gratton. Scanning two-photon fluctuation correlation spectroscopy: Particle counting measurements for detection of molecular aggregation. *Biophys. J.*, 71(1):410–420, 1996.
- M. Brinkmeier, K. Dorre, J. Stephan, and M. Eigen. Two beam cross correlation: A method to characterize transport phenomena in micrometer-sized structures. *Anal. Chem.*, 71(3):609–616, 1999.
- C. M. Brown and N. O. Petersen. An image correlation analysis of the distribution of clathrin associated adaptor protein (AP-2) at the plasma membrane. *J. Cell Sci.*, 111:271–281, 1998.
- Y. Chen, J. D. Müller, P. T. C. So, and E. Gratton. The photon counting histogram in fluorescence fluctuation spectroscopy. *Biophys. J.*, 77(1):553–567, 1999.
- M. A. Digman, C. M. Brown, P. Sengupta, P. W. Wiseman, A. R. Horwitz, and E. Gratton. Measuring fast dynamics in solutions and cells with a laser scanning microscope. *Biophys. J.*, 89(2):1317–1327, 2005a.
- M. A. Digman, P. Sengupta, P. W. Wiseman, C. M. Brown, A. R. Horwitz, and E. Gratton. Fluctuation correlation spectroscopy with a laser-scanning microscope: Exploiting the hidden time structure. *Biophys. J.*, 88(5):L33–L36, 2005b.
- P. S. Dittrich and P. Schwille. Photobleaching and stabilization of fluorophores used for single-molecule analysis with one- and two-photon excitation. *Appl. Phys. B*, 73(8):829–837, 2001.
- S. Felekyan, R. Kuhnemuth, V. Kudryavtsev, C. Sandhagen, W. Becker, and C. A. M. Seidel. Full correlation from picoseconds to seconds by time-resolved and time-correlated single photon detection. *Rev. Sci. Instrum.*, 76(8):083104, 2005.
- M. Gosch and R. Rigler. Fluorescence correlation spectroscopy of molecular motions and kinetics. *Adv. Drug Deliv. Rev.*, 57(1):169–190, 2005.
- B. Hebert, S. Costantino, and P. W. Wiseman. Spatiotemporal image correlation spectroscopy (STICS) theory, verification, and application to protein velocity mapping in living CHO cells. *Biophys. J.*, 88(5):3601–3614, 2005.
- S. T. Hess, S. H. Huang, A. A. Heikal, and W. W. Webb. Biological and chemical applications of fluorescence correlation spectroscopy: A review. *Biochemistry*, 41(3):697–705, 2002.
- P. Kask, K. Palo, D. Ullmann, and K. Gall. Fluorescence-intensity distribution analysis and its application in biomolecular detection technology. *Proc. Natl. Acad. Sci. U.S.A.*, 96(24):13756–13761, 1999.
- K. König. Multiphoton microscopy in life sciences. *J. Microsc.*, 200:83–104, 2000.

- D. E. Koppel, F. Morgan, A. E. Cowan, and J. H. Carson. Scanning concentration correlation spectroscopy using the confocal laser microscope. *Biophys. J.*, 66(2):502–507, 1994.
- O. Krichevsky and G. Bonnet. Fluorescence correlation spectroscopy: The technique and its applications. *Rep. Prog. Phys.*, 65(2):251–297, 2002.
- D. Magatti and F. Ferri. Fast multi-tau real-time software correlator for dynamic light scattering. *Appl. Opt.*, 40(24):4011–4021, 2001.
- T. Meyer and H. Schindler. Particle counting by fluorescence correlation spectroscopy - simultaneous measurement of aggregation and diffusion of molecules in solutions and in membranes. *Biophys. J.*, 54(6):983–993, 1988.
- M. Müller, J. Squier, R. Wolleschensky, U. Simon, and G. J. Brakenhoff. Dispersion precompensation of 15 femtosecond optical pulses for high-numerical-aperture objectives. *J. Microsc.*, 191:141–150, 1998.
- D. F. Nicoli, J. Briggs, and V. B. Elings. Fluorescence immunoassay based on long-time correlations of number fluctuations. *Proc. Natl. Acad. Sci. U.S.A.*, 77(8):4904–4908, 1980.
- A. G. Palmer and N. L. Thompson. Molecular aggregation characterized by high-order auto-correlation in fluorescence correlation spectroscopy. *Biophys. J.*, 52(2):257–270, 1987.
- A. G. Palmer and N. L. Thompson. High-order fluorescence fluctuation analysis of model protein clusters. *Proc. Natl. Acad. Sci. U.S.A.*, 86(16):6148–6152, 1989.
- N. O. Petersen. Diffusion and aggregation in biological membranes. *Can. J. Biochem. Cell Biol.*, 62(11):1158–1166, 1984.
- N. O. Petersen. Scanning fluorescence correlation spectroscopy 1. Theory and simulation of aggregation measurements. *Biophys. J.*, 49(4):809–815, 1986.
- N. O. Petersen, D. C. Johnson, and M. J. Schlesinger. Scanning fluorescence correlation spectroscopy 2. Application to virus glycoprotein aggregation. *Biophys. J.*, 49(4):817–820, 1986.
- N. O. Petersen, P. L. Hoddellius, P. W. Wiseman, O. Seger, and K. E. Magnusson. Quantitation of membrane-receptor distributions by image correlation spectroscopy—Concept and application. *Biophys. J.*, 65(3):1135–1146, 1993.
- W. Reisner, K. J. Morton, R. Riehn, Y. M. Wang, Z. N. Yu, M. Rosen, J. C. Sturm, S. Y. Chou, E. Frey, and R. H. Austin. Statics and dynamics of single DNA molecules confined in nanochannels. *Phys. Rev. Lett.*, 94(19):196101, 2005.
- R. Rigler and E. S. Elson, editors. *Fluorescence Correlation Spectroscopy. Theory and Application*. Chemical Physics Series. Springer Verlag, Berlin, 1st edition, 2001.
- J. V. Rocheleau, P. W. Wiseman, and N. O. Petersen. Isolation of bright aggregate fluctuations in a multipopulation image correlation spectroscopy system using intensity subtraction. *Biophys. J.*, 84(6):4011–4022, 2003.
- R. D. Roorda, T. M. Hohl, R. Toledo-Crow, and G. Miesenbock. Video-rate nonlinear microscopy of neuronal membrane dynamics with genetically encoded probes. *J. Neurophysiol.*, 92(1):609–621, 2004.
- Q. Q. Ruan, M. A. Cheng, M. Levi, E. Gratton, and W. W. Mantulin. Spatial-temporal studies of membrane dynamics: Scanning fluorescence correlation spectroscopy (SFCS). *Biophys. J.*, 87(2):1260–1267, 2004.
- P. Schwille. Fluorescence correlation spectroscopy and its potential for intracellular applications. *Cell Biochem. Biophys.*, 34(3):383–408, 2001.
- P. Schwille, F. J. Meyer-Almes, and R. Rigler. Dual-color fluorescence cross-correlation spectroscopy for multicomponent diffusional analysis in solution. *Biophys. J.*, 72(4):1878–1886, 1997.
- J. P. Skinner, Y. Chen, and J. D. Muller. Position-sensitive scanning fluorescence correlation spectroscopy. *Biophys. J.*, 89(2):1288–1301, 2005.
- M. Srivastava and N. O. Petersen. Image cross-correlation spectroscopy: A new experimental biophysical approach to measurement of slow diffusion of fluorescent molecules. *Methods Cell Sci.*, 18:47–54, 1996.
- P. R. St-Pierre and N. O. Petersen. Relative ligand-binding to small or large aggregates measured by scanning correlation spectroscopy. *Biophys. J.*, 58(2):503–511, 1990.

- P. R. St-Pierre and N. O. Petersen. Average density and size of microclusters of epidermal growth-factor receptors on A431 cells. *Biochemistry*, 31(9):2459–2463, 1992.
- N. L. Thompson. Fluorescence correlation spectroscopy. In J. R. Lakowicz, editor, *Topics in Fluorescence Spectroscopy, Volume I: Techniques*, pages 337–378. Plenum Press, New York, 1991.
- N. L. Thompson, A. M. Lieto, and N. W. Allen. Recent advances in fluorescence correlation spectroscopy. *Curr. Opin. Struct. Biol.*, 12(5):634–641, 2002.
- M. B. Weissman. Fluctuation spectroscopy. *Annu. Rev. Phys. Chem.*, 32:205–232, 1981.
- M. Weissman, H. Schindler, and G. Feher. Determination of molecular-weights by fluctuation spectroscopy - application to DNA. *Proc. Natl. Acad. Sci. U.S.A.*, 73(8):2776–2780, 1976.
- J. Widengren and R. Rigler. Mechanisms of photobleaching investigated by fluorescence correlation spectroscopy. *Bioimaging*, 4:149–157, 1996.
- T. Winkler, U. Kettling, A. Koltermann, and M. Eigen. Confocal fluorescence coincidence analysis: An approach to ultra high-throughput screening. *Proc. Natl. Acad. Sci. U.S.A.*, 96(4):1375–1378, 1999.
- P. W. Wiseman and N. O. Petersen. Image correlation spectroscopy. II. Optimization for ultrasensitive detection of preexisting platelet-derived growth factor-beta receptor oligomers on intact cells. *Biophys. J.*, 76(2):963–977, 1999.
- P. W. Wiseman, J. A. Squier, M. H. Ellisman, and K. R. Wilson. Two-photon image correlation spectroscopy and image cross-correlation spectroscopy. *J. Microsc.*, 200:14–25, 2000.
- P. W. Wiseman, C. M. Brown, D. J. Webb, B. Hebert, N. L. Johnson, J. A. Squier, M. H. Ellisman, and A. F. Horwitz. Spatial mapping of integrin interactions and dynamics during cell migration by image correlation microscopy. *J. Cell Sci.*, 117(23):5521–5534, 2004.
- Y. Xiao, V. Buschmann, and K. D. Weston. Scanning fluorescence correlation spectroscopy: A tool for probing microsecond dynamics of surface-bound fluorescent species. *Anal. Chem.*, 77(1):36–46, 2005.



## A3

### **Simultaneous two-photon fluorescence correlation spectroscopy and lifetime imaging of dye molecules in submicrometer fluidic structures**

Z. Petrášek, M. Krishnan, I. Mönch and P. Schwille

*Microsc. Res. Tech.* 70:459–466, 2007.



# Simultaneous Two-Photon Fluorescence Correlation Spectroscopy and Lifetime Imaging of Dye Molecules in Submicrometer Fluidic Structures

ZDENĚK PETRÁŠEK,<sup>1\*</sup> MADHAVI KRISHNAN,<sup>1</sup> INGOLF MÖNCH,<sup>2</sup> AND PETRA SCHWILLE<sup>1</sup>

<sup>1</sup>*Institut für Biophysik / BIOTEC, TU Dresden, Dresden, Germany*

<sup>2</sup>*Leibniz Institute for Solid State and Materials Research (IFW), Dresden, Germany*

**KEY WORDS** fluorescence correlation spectroscopy (FCS); fluorescence lifetime imaging (FLIM); microfluidics; diffusion; photophysics

**ABSTRACT** Fluorescence correlation spectroscopy (FCS) is a very sensitive technique that can be used, e.g., for the measurement of low concentrations and for the investigation of transport of fluorescent molecules. Fluorescence lifetime imaging (FLIM) provides spatially resolved information about molecular fluorescence lifetimes reflecting the interactions of the molecules with their environment. We have applied simultaneous two-photon FCS and FLIM to probe the behavior of fluorescent molecules diffusing in submicrometer silicon oxide channels. Our measurements reveal differences in fluorescence lifetimes compared to bulk solution that result from the effects of confinement and the presence of interfaces. Confinement also affects diffusional characteristics of fluorophores as reflected in fluorescence autocorrelation functions. These possible consequences of both spatial confinement and the presence of interfaces between media with different refractive indices on the diffusion and fluorescence lifetime of molecules in nanostructures are discussed in general. *Microsc. Res. Tech.* 70:459–466, 2007. © 2007 Wiley-Liss, Inc.

## INTRODUCTION

Micrometer and submicrometer fluidic devices are being developed to study chemical reactions and biologically relevant molecular interactions in small amounts and ultimately at the single molecule level (Dittrich et al., 2004; Stavis et al., 2005). Some important advantages of this approach over experiments in bulk solutions are lower amounts of reactants, shorter diffusion times, and smaller reaction volumes, resulting in increased signal-to-noise ratios. Most studies on biomolecules in micro- and nanofluidic systems use fluorescence for the detection of molecules because of the high sensitivity of fluorescence detection and the ability to achieve high *S/N* ratios. It is therefore important to know how spatial confinement and location near interfaces between optically different media can influence fluorescence properties of the labels alone.

Fluorescence lifetime imaging (FLIM) is a technique where the image contrast is formed by the spatial variation of the fluorescence lifetimes of the fluorophores (Suhling et al., 2005). It can be used to determine the spatial distribution of molecules with different lifetimes that cannot be distinguished on basis of their fluorescence intensity alone. Alternatively, lifetime imaging detects changes of lifetimes caused by variations in the local environment of the fluorescing molecules, e.g., polarity, ion concentrations, viscosity, etc. Fluorescence lifetime thus not only reflects the local nanoenvironment and photochemistry, but is also influenced by the geometry of the surrounding dielectric media that leads to dependence of fluorescence lifetime on refrac-

tive index (Toptygin, 2003) and its discontinuities (Barnes, 1998; Danz et al., 2002). The dependence of fluorescence lifetime on the orientation of the fluorophore and its distance from the interface has been demonstrated experimentally (Macklin et al., 1996; Vallée et al., 2001; Kreiter et al., 2002).

Fluorescence correlation spectroscopy (FCS) is capable of determining molecular concentrations and diffusion coefficients in small sample volumes and at low concentrations (Rigler and Elson, 2001; Krichevsky and Bonnet, 2002; Bacia and Schwille, 2003). Although usually applied to freely diffusing molecules with their motion unrestricted by external boundaries, FCS was also used to measure diffusion and flow of molecules in microcapillaries and submicrometer structures (Dittrich and Schwille, 2002; Lenne et al., 2002; Foquet et al., 2004). The size reduction and better confinement of the measurement volume improves the signal-to-noise ratio and permits measurements at higher biochemically and physiologically relevant concentrations. However, impenetrable boundaries near the measurement volume affect the diffusion of the molecules and the theoretical description of the autocorrelation curve subsequently becomes more complicated (Gennerich and Schild, 2000).

\*Correspondence to: Zdeněk Petrášek, Institut für Biophysik/BIOTEC, TU Dresden, Tatzberg 47-51, 01307 Dresden, Germany.

E-mail: zdenek.petrasek@biotec.tu.dresden.de

Received 7 July 2006; accepted in revised form 1 September 2006

DOI 10.1002/jemt.20428

Published online 28 March 2007 in Wiley InterScience (www.interscience.wiley.com).

In this article we introduce an experimental setup combining the two techniques, FLIM and FCS, in one instrument. Both techniques are applied to study the fluorescence and diffusion properties of freely diffusing dye molecules confined to silicon oxide channels of 100-nm height. The detected fluorescence intensity and lifetime are shown to be influenced by the proximity of the molecules to the water/glass and water/air interfaces. The confinement of the diffusing molecules and the location of the measurement volume relative to the channel walls determines the shape of the measured fluorescence autocorrelation.

## MATERIALS AND METHODS

### Microscope

The fluorescence measurements were performed on a home-built two-photon laser scanning microscope. A more detailed description of the instrument can be found in Petrášek and Schwille (2007). A tunable Ti:Sapph laser (Mira 900 F, Coherent, Santa Clara, USA) was used as the excitation source. The excitation wavelength was set to 820 nm, and the pulse frequency was 76 MHz. The beam was linearly polarized.

The optical path of the excitation and emitted light in the microscope is shown in Figure 1. The laser beam (red), after having been sufficiently expanded, is reflected from a dichroic beamsplitter (bs, 725-DCSPXR, AHF, Tübingen, Germany) separating the excitation and emitted light. The beam is steered by two mirrors mounted on shafts of closed-loop galvanometer scanners (VM2000, GSI Lumonics GmbH, Unterschleißheim, Germany). The lenses L3 and L4 image the scanning mirrors on each other, and the lenses L1 and L2 image the Y mirror on the back aperture of the objective while collimating the beam. The objective then focuses the excitation beam into a diffraction limited spot whose position within the sample depends on the deflection of the scanners, and collects the emitted light. The fluorescence is descanned by following the same path as the excitation beam in the opposite direction. After having been transmitted by the beamsplitter (bs) and the emission filter (em, HQ600/200M, AHF), the fluorescence is focused by the lens L5 onto the active area of the avalanche photodiode (APD; type SPCM-CD2801, PerkinElmer, Wellesley, USA). Prior to detection the fluorescence can be divided into two spectral channels by an additional beamsplitter. The descanned detection is used because of the need to focus the emitted light onto the small active area of the APDs ( $175 \mu\text{m}^2$ ). The scanning optics is built around an inverted IX 71 microscope (Olympus, Tokyo, Japan). The position of the observed section of the sample along the optical axis ( $z$ -section) is controlled by a piezo nanopositioning device PIFOC P-721.10 (Physik Instrumente GmbH, Waldbronn, Germany) on which the objective is mounted.

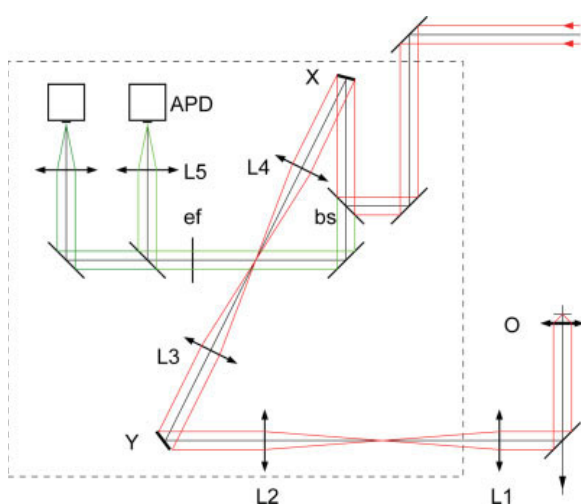


Fig. 1. The optical part of the laser scanning microscope. Red: the excitation beam, green: the emitted light, X, Y: galvanometer scanners with mounted mirrors, bs: dichroic beamsplitter, O: objective, ef: emission filter, L1–L5: lenses, APD: avalanche photodiode. [Color figure can be viewed in the online issue, which is available at [www.interscience.wiley.com](http://www.interscience.wiley.com).]

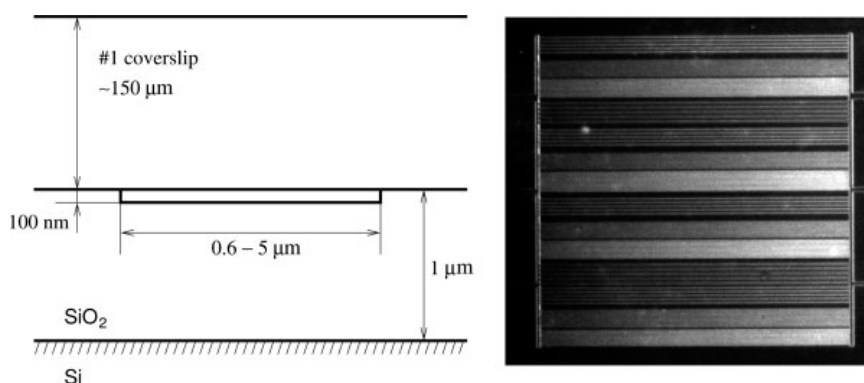


Fig. 2. Scheme of the nanochannel device (left, not to scale) and the image of the channel network (right, size: 1 mm). The channels are etched into a  $1.00 \pm 0.05 \mu\text{m}$  thick  $\text{SiO}_2$  layer on Si; the top of the channel is formed

by a #1 coverslip anodic-bonded to the silicon oxide; the channels are 100-nm deep and their width ranges from 0.6 to 5  $\mu\text{m}$ .

The scanning optics is controlled by the ADWin Gold system (Jäger GmbH, Lorsch, Germany), a general purpose microprocessor-controlled unit generating the voltage waveform driving the scanners and synchronously acquiring the signal from the detector. The user interface and the control of the ADWin module and the PIFOC device is provided by a program written in the LabView environment (National Instruments, Austin, USA).

Fluorescence autocorrelation curves were recorded by positioning the excitation laser beam into a desired location and passing the output signal of the APD to a hardware correlator ALV-6000 (ALV GmbH, Langen, Germany). Accurate synchronization between the signal driving the scanner and the detected signal provided by the ADWin Gold ensures that the actual measurement location within the sample exactly coincides with the position selected via the software on the computer screen.

The time-resolved data for FLIM are acquired with the SPC-830 photon counting module (Becker & Hickl GmbH, Berlin, Germany). The SPC-830 module constructs the fluorescence image from the detector signal and synchronization signals (pixel, line, and frame clock) provided by the ADWin Gold system. By using a laser synchronization signal and the time correlated single photon counting (TCSPC) method precise picosecond timing of the detected photons is achieved. Fluorescence lifetime images are subsequently calculated using SPCImage software (Becker & Hickl GmbH).

The images were acquired typically with size  $256 \times 256$  or  $512 \times 512$  pixels and the pixel dwell time 20–100  $\mu\text{s}$ . For lifetime imaging 25–50 image frames with resolution  $256 \times 256$  pixels and pixel dwell time 100  $\mu\text{s}$  were accumulated. The FLIM measurement thus lasted approx. 5–10 min. The time window of the resulting data set was 12.5 ns wide, i.e. slightly narrower than the excitation period of 13.1 ns, and was divided into 256 channels.

### Fluidic Structures

p-Type silicon with approximately 1000-nm thermal oxide served as substrate for fabrication of channel structure in silicon oxide. Cr/Pd (20/100 nm) was evaporated onto the substrate and patterned using a combination of laser lithography and Ar ion beam etching of metal layers in the exposed regions. The patterned Pd layer served as an etch mask during reactive ion etching (RIE) of exposed silicon oxide in a CF<sub>4</sub> plasma. Substrates were then diced to expose feed structures on the inlet and outlet ends of the channel layout after which the metal mask was removed wet-chemically. The oxide surface was then cleaned and bonded to #1 coverglass using anodic bonding to yield functional fluidic channels compatible with high NA microscopy. The cross-section and top view of the resulting fluidic structure are shown in Figure 2. The channel network consists of a set of parallel channels of nominal widths 0.6–5  $\mu\text{m}$  connected by two perpendicular 10  $\mu\text{m}$  wide channels, each of which is connected to the outside on the opposite sides of the device by three broad feed channels.

The empty channels were filled with a solution of Alexa 546 in water by applying a small drop at the inlets to the channel structure. Due to the capillary forces the

channels were filled almost instantaneously. Channels thus filled were dried to deposit the dye on the channel wall and were refilled with water. Fluid flow in the channel is arrested by equalizing the hydrostatic pressure at the inlet and outlet side of the channel. This was achieved by covering the inlet and outlet sides of the channels with water. If both sides of the structure were covered before the channels were completely filled, air bubbles occupying mostly the entire width and of variable length were trapped within the channel. Bubble sizes occasionally varied during the experiment.

### THEORY

The normalized autocorrelation function  $g(\tau)$  of the fluorescence signal  $F(t)$  is defined in the following way (Bacia and Schwille, 2003):

$$g(\tau) = \frac{\langle F(t)F(t+\tau) \rangle}{\langle F(t) \rangle^2} - 1. \quad (1)$$

Assuming the measurement volume is approximated by a gaussian function  $W(x,y) = \exp(-(x^2 + y^2)/(2a^2))$ , and provided the projections of the molecular motion into the individual coordinate axes are independent of each other, the theoretical model of the autocorrelation function can be factored into terms corresponding to motion along these axes:

$$g(\tau) = \frac{1}{cV} g_x(\tau) g_y(\tau) g_z(\tau), \quad (2)$$

where  $c$  is the concentration of the fluorescent molecules and  $V$  is the size of the measurement volume determined by the excitation and emission profiles. The depth of the channels used here (100 nm) is considerably smaller than the size of the focused laser beam in the vertical ( $z$ ) direction. Therefore no motion in the  $z$  direction can be resolved and the corresponding autocorrelation term is equal to 1:  $g_z(\tau) = 1$ . Free diffusion in an infinite two-dimensional space leads to fluorescence autocorrelation with equal terms for both the  $x$  and  $y$  axes (Bacia and Schwille, 2003):

$$g_x(\tau) = g_y(\tau) = \frac{1}{\sqrt{2}} \frac{1}{\sqrt{1 + \tau/\tau_D}}, \quad (3)$$

where  $\tau_D \equiv a^2/D$  is the diffusion time,  $a$  the parameter describing the shape of the measurement volume, and  $D$  is the diffusion coefficient. The value of the parameter  $a$  in the setup used here is  $135 \pm 5$  nm.

Diffusion along the channel axis (direction along the  $x$  axis) is however unrestricted and the corresponding autocorrelation is described by the term in Eq. (3). In a channel with the width similar to or several times larger than the horizontal width of the measurement volume, the effects of the channel walls on the autocorrelation cannot be neglected; the diffusion in the perpendicular direction (along the  $y$  axis) is confined by the channel walls. Gennerich and Schild (2000) derived a model taking into account the confinement by the walls, and calculated an approximation of this model

useful for data analysis:

$$g'_y(\tau) = g_y(\tau) \frac{2\sqrt{\pi}}{d} \left( 1 + \left( \frac{d \operatorname{erf}(d/2)}{2\sqrt{\pi} \operatorname{erf}^2(d/(2\sqrt{2}))} - 1 \right) \times \frac{e^{-k(d/2)(2\pi/d)^2(\tau/\tau_D)}}{\sqrt{1 + \tau/\tau_D}} \right), \quad (4)$$

where  $k(x) = 0.689 + 0.34e^{-0.37(x-0.5)^2}$ ,

and  $d = d_0/a$  is the normalized width of the channel  $d_0$ . The approximation is valid for channel widths with  $d \leq 16$ , and assumes that the measurement volume is positioned in the centre of the channel.

In a situation where the excitation beam is moving uniformly along a line, the fluorescence autocorrelation is naturally affected by this movement. The description is equivalent to a uniform flow of molecules in addition to diffusion (Kuricheti et al., 2004). The following equation describes the autocorrelation in case of free diffusion in two dimensions and additional flow:

$$g(\tau) = \frac{1}{2cV} \frac{1}{1 + \tau/\tau_D} e^{-\frac{v^2\tau^2}{4a^2(1+\tau/\tau_D)}}. \quad (5)$$

The parameter  $v$  is the velocity of the moving measurement volume (flow velocity).

The triplet “blinking” kinetics are not considered here since it does not usually appear in two-photon excited fluorescence autocorrelation curves when excitation powers below the photobleaching threshold are employed (Schwille et al., 1999).

## RESULTS

### Fluorescence Imaging, FLIM

Filled channels were imaged using two-photon excitation (wavelength 820 nm) and detection of the dye fluorescence (Figs. 3 and 4). When air bubbles were trapped in the channels during the filling process, the fluorescence originating from the air bubble region was always higher than that from liquid-filled regions in the channel. The ratio between the fluorescence intensity in the bubbles and in liquid-filled regions varied between  $1.5\times$  and  $30\times$  and was generally larger when smaller dye concentrations were used.

In order to probe the origin of the fluorescence intensity variations, FLIM was performed on the channels originally filled with dye solutions of different concentrations. Fig. 3A shows fluorescence intensity and lifetime images of  $2.5\ \mu\text{m}$  wide channels filled with 10-nM dye solution. The gradual change in the shape and dimensions of a bubble is reflected in the blurred edges of the bubbles. In the intensity images the bubbles appear approx.  $15\text{--}30\times$  times brighter than the liquid-filled regions in the channels. The FLIM image and the histogram of lifetime values show that the fluorescence lifetime in the liquid-filled channels is constant within the precision of the measurement and has a mean value of  $3.7 \pm 0.3$  ns, which is comparable with the value of  $3.72 \pm 0.1$  ns obtained in the bulk solution. The lifetime in bubble regions is longer:  $\tau_F = 4.2 \pm 0.2$  ns. The errors of the lifetime values were estimated from the histogram of the pixel lifetime values also shown in Fig. 3A.

Figure 3B shows fluorescence intensity and fluorescence lifetime images of  $5\text{-}\mu\text{m}$  wide channels filled originally with 10- $\mu\text{M}$  Alexa 546 solution. The brighter portions of the channels are bubble regions while the darker zones are filled with liquid. The intensity ratio of bubble to liquid filled region is approximately 3 in the vertical channel and 1.5 in the horizontal feed channel. The fluorescence lifetime in the liquid is  $3.6 \pm 0.1$  ns, in agreement with the bulk value. The lifetime in the bubble region is  $4.0 \pm 0.1$  ns and is independent of the bubble brightness. After drying the device so as to eliminate water from the channel a lifetime image of the same area showed a constant lifetime of  $4.0 \pm 0.1$  ns (not shown). Similar lifetime of  $3.9 \pm 0.1$  ns was observed when dye was deposited on glass by drying a drop of dye solution.

The difference in intensity ratios between bubble and liquid regions in the vertical channel compared to the feedlines could be attributed to differences in water film thickness in the bubble region. The different lifetime of the molecules in bubble regions could indicate the influence of the interface on the emission properties of the dye.

### FCS in Channels and Bubbles

In order to determine whether the fluorescence in the bubble region originated from fluorophores immobilized on the channel walls or diffusing fluorophores in the thin liquid film surrounding the bubble, fluorescence signals from locations within liquid-filled channels and bubbles were recorded and autocorrelated. Figure 4 shows the fluorescence image of  $2.5\text{-}$  and  $5\text{-}\mu\text{m}$  wide channels filled with 10-nM Alexa 546 water solution and two autocorrelation curves recorded in the centers of a liquid-filled channel and a channel with an air bubble, as indicated by crosses.

The autocorrelation curve from the bubble could be well fitted with the two-dimensional model of free diffusion (Eqs. (2) and (3)). The recovered diffusion time  $\tau_D = 0.093$  ms was somewhat larger than the value obtained in a drop of bulk solution:  $\tau_D = 0.065$  ms. The autocorrelation curve from the liquid is rather noisy due to the very weak signal, and a poorer fit is obtained with the 2D model. A slightly better fit is achieved with the model taking into account the finite width of the channel ( $2.5\ \mu\text{m}$  in this case) (Eq. (4)), yielding a diffusion time  $\tau_D = 0.13$  ms. We note, however, that the channel width of  $2.5\ \mu\text{m}$  means that the physical situation is beyond the limit of validity of the approximation used in Eq. (4) (Gennerich and Schild, 2000).

The nonzero autocorrelation amplitude of the fluorescence signal from the bubbles and its general agreement with the 2D diffusion model suggests the presence of a thin layer of liquid on the channel walls within which the molecule are free to diffuse. The lower amplitude of the autocorrelation in the bubble, compared with that in the liquid, indicates by definition higher concentration of molecules in the thin liquid layer. The actual concentration difference is expected to be larger than what one might expect from mere comparison of the amplitudes of the autocorrelation curves. This is due to the fact that the amplitude of the curve from liquid region is reduced by the presence of a background signal, comparable in magnitude

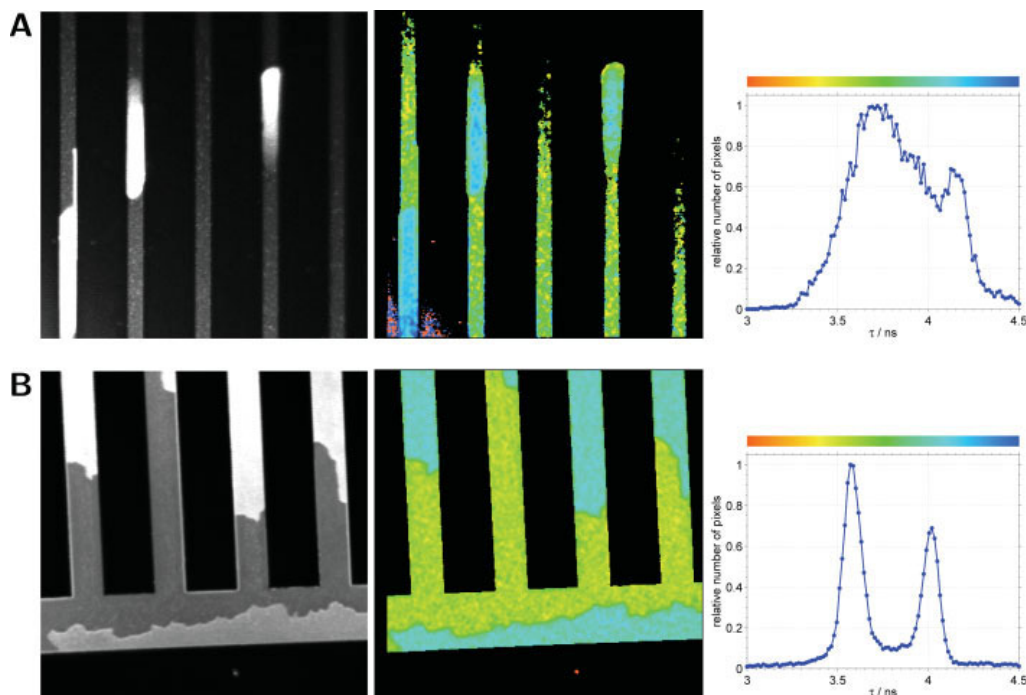


Fig. 3. Fluorescence intensity (left) and lifetime (middle) images of 2.5- $\mu\text{m}$  wide channels filled with 10 nM (A) and 10  $\mu\text{M}$  (B) solution of Alexa 546 in water; right: lifetime distribution in the lifetime image; field of view: 58  $\mu\text{m}$ .

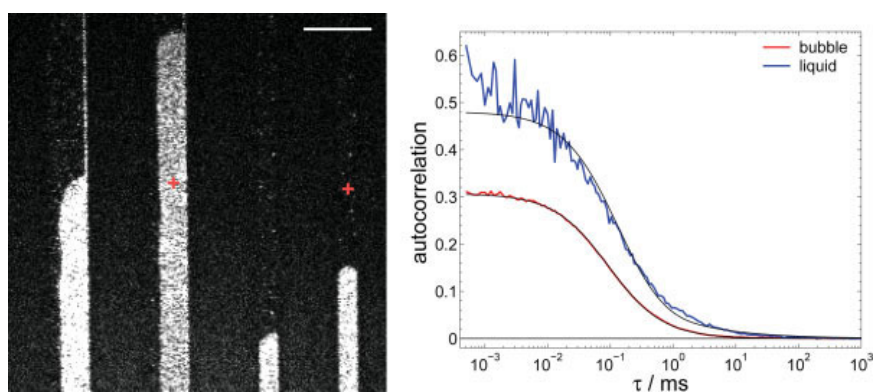


Fig. 4. Left: fluorescence image of 2.5- and 5- $\mu\text{m}$  wide channels filled with 10 nM solution of Alexa 546 in water with trapped air bubbles; right: fluorescence autocorrelation curves measured in a liquid-filled channel (blue) and in a bubble (red); the positions of the measurements are indicated by crosses; scale bar: 10  $\mu\text{m}$ .

to the intensity of the fluorescence signal (Fig. 4). However, the putative higher background-adjusted dye concentration ratio alone does not substantiate the much higher fluorescence intensity observed suggesting an additional fluorescence enhancement mechanism may be present. The FCS measurements in the channels filled with 10- $\mu\text{M}$  solution did not show any autocorrelation because of the too high number of molecules in the measurement volume.

Figure 5 shows autocorrelation curves recorded in the centers of channels 0.6- and 10- $\mu\text{m}$  wide. While the curve from the 10- $\mu\text{m}$  wide channel can be described by unrestricted 2D diffusion with  $\tau_D = 0.077$  ms, the curve from the 0.6- $\mu\text{m}$  wide channel exhibits significantly slower decay of correlation and is much better described by a one-dimensional model. However, the extracted diffusion time of 0.024 ms is much shorter than the value obtained in bulk, implying, faster diffu-

sion that is not readily physically substantiable. In fact, the 1D model is not appropriate in this situation, since the channel is still considerably wider than the beam waist and the diffusion in direction perpendicular to the channel length causes non-negligible fluctuations. The 2D model with confinement in one dimension (Eq. (4)) yields slightly better fit with the diffusion time of 0.09 ms and the parameter  $d$  equal to 6.3, which corresponds to the channel width 0.85  $\mu\text{m}$ . The larger width of the channel obtained from the fit is plausible, since the actual width of the channel could be expected to deviate from the nominal value of 0.6  $\mu\text{m}$  due to process variations.

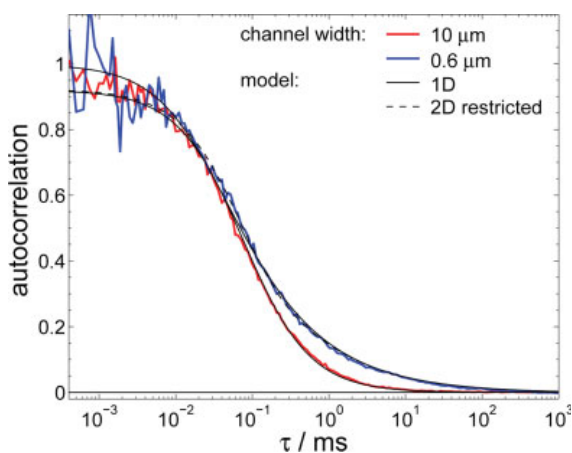


Fig. 5. Fluorescence autocorrelation curves measured in the center of 10- $\mu\text{m}$  (red) and 0.6- $\mu\text{m}$  (blue) wide channels filled with 10 nM solution of Alexa 546 in water; the autocorrelation from the 10  $\mu\text{m}$  wide channel (red) was fit to a 2D model (solid black line); the autocorrelation from the 0.6  $\mu\text{m}$  wide channel (blue) was fit to a 1D model (solid black line) and a 2D model with confinement in one dimension (Eq. (4), dashed black line). [Color figure can be viewed in the online issue, which is available at [www.interscience.wiley.com](http://www.interscience.wiley.com).]

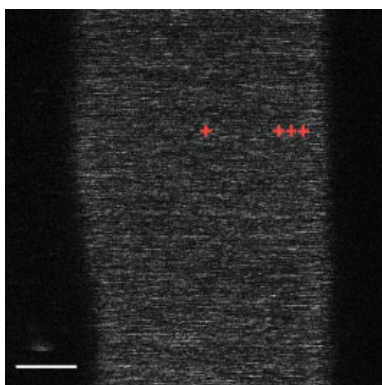
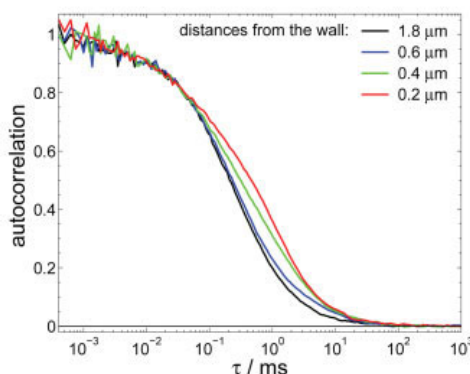


Fig. 6. Left: fluorescence image of a 5- $\mu\text{m}$  wide channel filled with 10 nM solution of Alexa 546 in water, partially filled with an air bubble; right: fluorescence autocorrelation curves measured at different dis-

Figure 6 shows a magnified view of a section of a 5- $\mu\text{m}$  wide channel occupied largely by a bubble. Four autocorrelation functions were recorded in the channel at different distances from the channel wall, estimated from the image to be 0.2, 0.4, 0.6, and 1.8  $\mu\text{m}$ . Only the curve measured near the center of the bubble can be fitted with the 2D model, yielding diffusion time of 0.26 ms. The other three curves display stronger correlation at longer lag times, increasing as the measurement location get closer to the wall. The increased correlation can be explained by molecules diffusing from the measurement volume towards the wall, being reflected and diffusing back to the measurement volume. The smaller distance from the wall increases the probability that the molecule re-enters the measurement volume due to the reflection from the wall, in addition to the reentry due to random change of the diffusion direction, as in unrestricted space.

### Scanning FCS

Closer inspection of Figure 6 reveals that the intensity image is composed of one pixel wide bright streaks along the horizontal direction, i. e. the direction of the fast scan. In order to verify that the streaks correspond to individual diffusing molecules crossing the moving measurement volume we imaged a magnified central part of the channel in Figure 6 with higher scanning speed of 20  $\mu\text{s}$  pixel and autocorrelated the pixel intensity along the lines (Fig. 7). The resulting autocorrelation averaged over all lines of the image was fitted to the model assuming 2D diffusion and a uniform flow, corresponding here to the scanner movement with a known speed (Eq. (5)). Although the temporal resolution of this type of analysis is limited by the pixel dwell time, and the maximum lag times are limited by the time per one scan line, the diffusion time  $\tau_D = 0.27$  ms recovered from the fit agrees with the value obtained by a standard point FCS measurement from the center of the same channel (Fig. 6). The longer diffusion time compared with values obtained in the bulk solution, liquid-filled channels, and some bubbles could be re-



tances from the right channel wall; the positions of the measurements are indicated by crosses; scale bar: 1  $\mu\text{m}$ . [Color figure can be viewed in the online issue, which is available at [www.interscience.wiley.com](http://www.interscience.wiley.com).]

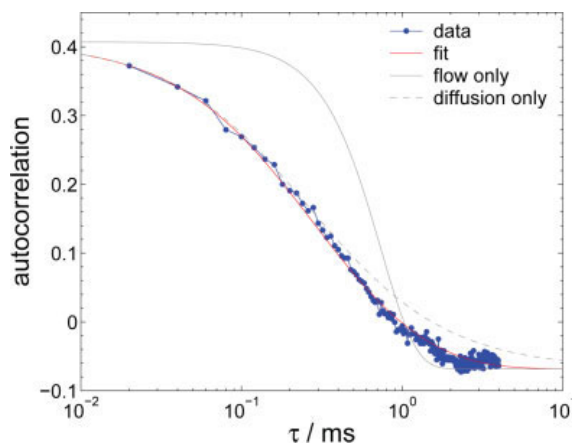


Fig. 7. Fluorescence autocorrelation calculated from the lines of the image of the magnified central part of the channel shown in Figure 6; the curve was fit to the Eq. (5) using known speed of scanning (red curve); the parts of the model function corresponding to diffusion only (dashed gray) and flow/scanner movement only (solid gray) are also shown. [Color figure can be viewed in the online issue, which is available at [www.interscience.wiley.com](http://www.interscience.wiley.com).]

lated to the variable thickness of the liquid layer around the bubble, with very thin liquid layers possibly resulting in slower diffusion. A similar approach to measure diffusion of molecules by analyzing images from a scanning microscope has been demonstrated before (Digman et al., 2005).

## DISCUSSION

Fluorescence imaging of submicron depth fluidic channels containing dye shows higher fluorescence intensity in regions occupied by air bubbles compared to liquid-filled regions. This fluorescence originates at least partially from diffusing molecules as follows from the nonzero autocorrelation of the fluorescence (Fig. 4). Therefore, we assume the molecules diffuse within a thin liquid layer between the bubble and the channel wall, rather than being immobilized on the channel surface.

One reason for the higher fluorescence intensity in bubble region is higher molecular concentration, as inferred from the lower autocorrelation amplitude (Fig. 4). The accumulation of molecules could be caused by preferential location at the air/water interface. However, the difference in the autocorrelation amplitudes does not seem to be sufficient to fully explain the large intensity differences. A possible explanation is an enhancement of fluorescence detection in bubbles due to the changes of emission properties of the molecules located near the interfaces with different refractive indices.

It is known that the angular distribution of fluorescence of molecules located near interface between media with two different refractive indices differs from that of molecules in homogeneous environment (Lukosz, 1979; Enderlein et al., 1999). Molecules located at the interface are more likely to emit into the higher refractive index medium, and a part of this emission even into angles larger than the critical angle. Since the objective collects only light emitted into a certain angle determined by the numerical aper-

ture, modification of the angular distribution of emission due to the presence of interfaces can change the detected fluorescence intensity (Enderlein et al., 1999).

In our case, three media with different refractive indices affect the emission of the molecules: glass (and optically similar  $\text{SiO}_2$ ), water, and air. It is conceivable that the confinement of the fluorescent molecules to a thin aqueous layer between the glass on one side and air on the other side results in different angular distribution of fluorescence than that of molecules in a completely water-filled channel. It is expected that due to the small channel thickness (100 nm) the interfaces on the other side of the channel also influence the emission, i.e. the system consists of five layers in the following order: glass, water, air, water, glass ( $\text{SiO}_2$ ). It would therefore be interesting to investigate the fluorescence in channels of different thickness. The presence of partially reflecting Si approximately  $1 \mu\text{m}$  below the channel may also play a role, although its effects could be expected to be small because of the rather large distance, unknown (possibly random) molecular orientation, and a high NA of fluorescence collection (Lambacher and Fromherz, 2002).

Fluorescence lifetime is also known to be influenced by the refractive index of the medium and its discontinuities (Lukosz, 1980; Danz et al., 2002). Vallée et al. (2001) studied lifetimes of molecules in thin films at glass/air interface and found shorter mean lifetimes for thicker films, i.e. for situation where the mean molecular distance from the air increases. This agrees with the theoretical prediction that the lifetime of a molecule decreases with increasing distance from the air/polymer interface. The lifetime also depends strongly on the molecular orientation relative to the interface (Danz et al., 2002), as experimentally demonstrated (Macklin et al., 1996; Kreiter et al., 2002). The thin layer of water between the channel surface and the air bubble in the nanochannel devices investigated here constitute a similar system, therefore lifetime changes of the molecules near the water/air interface as observed here would be expected. The thickness of the water layer is estimated to be in the range of nanometers to tens of nanometers, similar to the polymer layer thicknesses in the studies mentioned above. Since the exact thickness of the water layer is not known and multiple interfaces between glass, water and air within the 100 nm deep channel are present, quantitative comparison with theory is not possible at this stage.

FCS measurements are typically performed in a measurement volume located within much larger volume of the sample, so that the diffusion of the molecules through the measurement volume can be considered unrestricted, i.e. unaffected by external boundaries. The diffusion part of the autocorrelation functions is then described by the equation analogous to Eq. (3). If the motion of molecules is restricted by boundaries in the vicinity of the measurement volume, the measured autocorrelation of fluorescence is likely to be affected even when the boundaries lie well outside the measurement volume. Typical examples are FCS in total internal reflection configuration (Starr and Thompson, 2001), where the diffusion is restricted to a half-space, and FCS in micro- and nanochannels (Foquet et al., 2004) and dendrites (Gennerich and Schild, 2000) where the diffusing molecules are confined by the walls. The effect of the

walls is typically modelled as reflective boundary, if binding is not considered. The modified autocorrelation function in such a system reflects the geometrical restrictions on the molecular motion and not changes in the diffusion process itself (diffusion coefficient, (an)isotropy, etc.). A proper consideration of the confinement geometry in the analysis is therefore important in order to avoid misinterpretation of the correlation data, invoking multicomponent or anomalous diffusion, association/dissociation from surfaces, etc.

The effects of confinement on autocorrelation measurements are demonstrated in channels of different width (Fig. 5). We have also demonstrated that the presence of reflective boundary only on one side of the measurement volume is sufficient to affect the measured autocorrelation, as shown in Fig. 6. In some situations it may be practical to use modified illumination schemes for narrow channels, for example to increase the measurement volume size by asymmetrically expanding the excitation beam to cover the whole channel cross-section, leading to effectively 1D diffusion and therefore simplified theoretical description and interpretation.

The confinement effects are likely to play an important role in FCS measurements in cells, where organelles and other cytoplasmatic structures form boundaries and excluded volumes, thus affecting the motion of molecules.

The knowledge of emission characteristics of molecules in submicron fluidic structures could be used to tailor the design of these devices towards better collection efficiencies, as shown by Fouqué et al. on the example of a multilayered mirror used as a microscope slide enhancing the collected fluorescence (Fouqué et al., 2005). On the other hand, the dependence of the fluorescence lifetime on the distance from the interface may interfere with experiments using lifetime changes to monitor various processes, for example conformational changes using resonance energy transfer, on a single molecule level.

## CONCLUSION

The presented results show that FCS and FLIM are useful methods to study the location, motion, and photophysics of fluorescent molecules confined in submicrometer structures. Fluorescence intensity and lifetime imaging indicated that the fluorescence properties of the dye molecules in submicron-depth fluidic structures are modified by the vicinity of interfaces between media with different refractive indices. The FCS measurement confirmed that the measurement geometry (the measurement volume shape together with the space available for diffusing molecules) determines the shape of the fluorescence autocorrelation, and that complex models are needed to describe the autocorrelation if the diffusion of the molecules is restricted by the channel walls located even outside the measurement volume.

## ACKNOWLEDGMENT

M.K. acknowledges funding by Alexander von Humboldt Foundation.

## REFERENCES

- Bacia K, Schwille P. 2003. A dynamic view of cellular processes by in vivo fluorescence auto- and cross-correlation spectroscopy. *Methods* 29:74–85.
- Barnes WL. 1998. Fluorescence near interfaces: The role of photonic mode density. *J Mod Opt* 45:661–699.
- Danz N, Waldhausl R, Brauer A, Kowarschik R. 2002. Dipole lifetime in stratified media. *J Opt Soc Am B* 19:412–419.
- Digman MA, Brown CM, Sengupta P, Wiseman PW, Horwitz AR, Gratton E. 2005. Measuring fast dynamics in solutions and cells with a laser scanning microscope. *Biophys J* 89:1317–1327.
- Dittrich PS, Muller B, Schwille P. 2004. Studying reaction kinetics by simultaneous FRET and cross-correlation analysis in a miniaturized continuous flow reactor. *Phys Chem Chem Phys* 6:4416–4420.
- Dittrich PS, Schwille P. 2002. Spatial two-photon fluorescence cross-correlation spectroscopy for controlling molecular transport in microfluidic structures. *Anal Chem* 74:4472–4479.
- Enderlein J, Ruckstuhl T, Seeger S. 1999. Highly efficient optical detection of surface-generated fluorescence. *Appl Opt* 38:724–732.
- Fouquet M, Korch J, Zipfel WR, Webb WR, Craighead HG. 2004. Focal volume confinement by submicrometer-sized fluidic channels. *Anal Chem* 76:1618–1626.
- Fouqué B, Schaack B, Obeid P, Combe S, Getin S, Barritalut P, Chapon P, Chatelain F. 2005. Multiple wavelength fluorescence enhancement on glass substrates for biochip and cell analyses. *Biosens Bioelectron* 20:2335–2340.
- Gennerich A, Schild D. 2000. Fluorescence correlation spectroscopy in small cytosolic compartments depends critically on the diffusion model used. *Biophys J* 79:3294–3306.
- Kreiter M, Prummer M, Hecht B, Wild UP. 2002. Orientation dependence of fluorescence lifetimes near an interface. *J Chem Phys* 117:9430–9433.
- Krichevsky O, Bonnet G. 2002. Fluorescence correlation spectroscopy: the technique and its applications. *Rep Prog Phys* 65:251–297.
- Kuricheti KK, Buschmann V, Weston KD. 2004. Application of fluorescence correlation spectroscopy for velocity imaging in microfluidic devices. *Appl Spectrosc* 58:1180–1186.
- Lambacher A, Fromherz P. 2002. Luminescence of dye molecules on oxidized silicon and fluorescence interference contrast microscopy of biomembranes. *J Opt Soc Am B* 19:1435–1453.
- Lenne PF, Colombo D, Giovannini H, Rigneault H. 2002. Flow profiles and directionality in microcapillaries measured by fluorescence correlation spectroscopy. *Single Mol* 3:194–200.
- Lukosz W. 1979. Light-emission by magnetic and electric dipoles close to a plane dielectric interface. 3. Radiation-patterns of dipoles with arbitrary orientation. *J Opt Soc Am* 69:1495–1503.
- Lukosz W. 1980. Theory of optical-environment-dependent spontaneous-emission rates for emitters in thin-layers. *Phys Rev B* 22:3030–3038.
- Macklin JJ, Trautman JK, Harris TD, Brus LE. 1996. Imaging and time-resolved spectroscopy of single molecules at an interface. *Science* 272:255–258.
- Petrášek Z, Schwille P. 2007. Single molecules and nanotechnology, Scanning fluorescence correlation spectroscopy. Springer Series in Biophysics, Springer (to appear).
- Rigler R, Elson ES, editors. 2001. Fluorescence correlation spectroscopy. Theory and application, 1st ed. Chemical Physics Series, Springer Verlag, Berlin.
- Schwille P, Haupts U, Maiti S, Webb WW. 1999. Molecular dynamics in living cells observed by fluorescence correlation spectroscopy with one- and two-photon excitation. *Biophys J* 77:2251–2265.
- Starr TE, Thompson NL. 2001. Total internal reflection with fluorescence correlation spectroscopy: Combined surface reaction and solution diffusion. *Biophys J* 80:1575–1584.
- Stavis SM, Edel JB, Li YG, Samiee KT, Luo D, Craighead HG. 2005. Single-molecule mobility and spectral measurements in submicrometer fluidic channels. *J Appl Phys* 98:044903.
- Suhling K, French PMW, Phillips D. 2005. Time-resolved fluorescence microscopy. *Photochem Photobiol Sci* 4:13–22.
- Toptygin D. 2003. Effects of the solvent refractive index and its dispersion on the radiative decay rate and extinction coefficient of a fluorescent solute. *J Fluoresc* 13:201–219.
- Vallée R, Tomczak N, Gersen H, van Dijk EMHP, Garcia-Parajo MF, Vancso GJ, van Hulst NF. 2001. On the role of electromagnetic boundary conditions in single molecule fluorescence lifetime studies of dyes embedded in thin films. *Chem Phys Lett* 348:161–167.

A4

**Precise measurement of diffusion coefficients using scanning fluorescence correlation spectroscopy**

Z. Petrášek and P. Schille

*Biophys. J.* 94:1437–1448, 2008.



## Precise Measurement of Diffusion Coefficients using Scanning Fluorescence Correlation Spectroscopy

Zdeněk Petrášek and Petra Schwille

Biophysics Group, Biotechnologisches Zentrum, Technische Universität Dresden, Dresden, Germany

**ABSTRACT** We have implemented scanning fluorescence correlation spectroscopy (sFCS) for precise determination of diffusion coefficients of fluorescent molecules in solution. The measurement volume where the molecules are excited, and from which the fluorescence is detected, was scanned in a circle with radius comparable to its size at frequencies 0.5–2 kHz. The scan radius  $R$ , determined with high accuracy by careful calibration, provides the spatial measure required for the determination of the diffusion coefficient  $D$ , without the need to know the exact size of the measurement volume. The difficulties in the determination of the measurement volume size have limited the application of standard FCS with fixed measurement volume to relative measurements, where the diffusion coefficient is determined by comparison with a standard. We demonstrate, on examples of several common fluorescent dyes, that sFCS can be used to measure  $D$  with high precision without a need for a standard. The correct value of  $D$  can be determined in the presence of weak photobleaching, and when the measurement volume size is modified, indicating the robustness of the method. The applicability of the presented implementation of sFCS to biological systems is demonstrated on the measurement of the diffusion coefficient of eGFP in the cytoplasm of HeLa cells. With the help of simulations, we find the optimal value of the scan radius  $R$  for the experiment.

### INTRODUCTION

Fluorescence correlation spectroscopy (FCS) was introduced as a method for the measurement of diffusion coefficients and concentrations of fluorescent molecules in dilute solutions (1). Although FCS and its modifications have since been applied to the investigation of a range of phenomena giving rise to fluorescence fluctuations (e.g., molecular photophysics, intramolecular dynamics, conformational changes, intermolecular interactions, etc. (2–4)), characterization of diffusion remains one of its most common applications.

The principle of FCS lies in the quantification of the magnitude and duration of fluorescence fluctuations caused by molecules freely diffusing in and out of the measurement volume. While the magnitude of the fluctuations yields the number of particles in the measurement volume, and the duration of fluctuations the characteristic time the particles take to cross the volume, the geometry of the measurement volume has to be known to convert these quantities to concentration and diffusion coefficient. The complex shape of the diffraction-limited measurement volume, and the difficulty of its accurate parameterization, have been a limiting factor in the determination of absolute diffusion coefficients with FCS.

The measurement volume is most often approximated by a three-dimensional Gaussian with two parameters describing its lateral and axial extent (5). Since these parameters are difficult to determine independently, FCS is usually employed as a comparative method, where the diffusion coefficient of the investigated compound is related to that of a known standard by a comparison of the diffusion times of the

two compounds. However, because of absence of suitable standards (2) and the often encountered difficulty to measure the standard and the investigated sample under the same conditions (e.g., in intracellular applications), alternative methods are sought.

Several FCS variations have been proposed recently to address this problem. Dertinger et al. (6) suggested the use of spatial cross-correlation of fluorescence signals between two overlapping volumes created by two laser beams and fixed at known distance. Jaffiol et al. (7) used a similar configuration, but a single expanded laser beam was used for illumination, and the measurement volumes were defined by two laterally displaced optical fiber apertures. Additionally, thresholding was applied to the fluorescence signal before correlation to enhance the contrast in the resulting cross-correlation function. Blancquaert et al. (8) cross-correlated signals from two volumes of different shapes created by circular and ring pinholes: an inner elongated volume surrounded by an outer annular volume. Ries and Schwille (9) used a line-scanning microscope to measure fluorescence from two lines separated by a defined distance. Cross-correlation of the two signals allows determination of diffusion coefficients of slowly diffusing molecules in biomembranes, or on any flat surface.

Scanning FCS (sFCS) is a common name for a group of FCS methods where the measurement volume is in some way moved relative to the sample (10). It has been implemented for various reasons: to improve the statistical accuracy by measuring the signal from a large number of statistically independent volumes in systems with slow diffusion (11–13); to study binding in immobile samples (14); to avoid photobleaching of slowly diffusing molecules (15); to perform measurements at many locations quasi-simultaneously (16,17); to measure diffusion coefficients over a broad temporal range

Submitted March 13, 2007, and accepted for publication September 14, 2007.

Address reprint requests to Dr. Zdeněk Petrášek, Tel.: 49-(0)351-463-40323; E-mail: zdenek.petrasek@biotec.tu-dresden.de.

Editor: Enrico Gratton.

© 2008 by the Biophysical Society  
0006-3495/08/02/1437/12 \$2.00

doi: 10.1529/biophysj.107.108811

with a standard laser scanning microscope (18); or to measure diffusion, flow, and immobilization simultaneously (19).

We have implemented circular-scanning FCS in a way most similar to that of Skinner et al. (19), but without the position sensitivity. The motivation was to take advantage of the known scan radius  $R$ , and use it as a spatial measure, equivalent to the distance between the measurement volumes in the cross-correlation techniques mentioned above. In this way, determination of the diffusion coefficient is possible without the exact knowledge of the parameters of the measurement volume.

The described implementation of sFCS, rather than being an alternative to the existing sFCS techniques mentioned above, represents a new approach to the measurement of diffusion coefficients providing two significant enhancements over a standard FCS: the calibration of the size of the measurement volume is not necessary, and, consequently, the method becomes robust with respect to disturbances affecting the measurement volume size.

In the following, we describe the procedure to accurately measure the scan radius, and present the results of sFCS measurements on an example of several fluorescence dyes at different scan radii and frequencies. Further, we discuss the choice of the optimal scan radius and frequency, and based on simulations and theoretical considerations, suggest the best values. The lower sensitivity of sFCS to photobleaching, a common limitation in two-photon FCS, compared to FCS with a fixed measurement volume, is demonstrated. The sFCS is shown to be able to detect changes in the size of the measurement volume and yield a correct value of the diffusion coefficient, both in the same measurement, without a need for repeated calibration of the volume size. Finally, it is shown that the technique is capable of measuring diffusion coefficients in living cells without any a priori knowledge about the measurement volume size, and that the sensitivity to the changes in the volume size is also preserved in vivo. An alternative implementation for sFCS is proposed, with less complex illumination optics and a possibility of addition to existing FCS setups based on a two-axis piezo scanner. The sFCS, as implemented in this work, is shown to be a precise and robust technique for the measurement of diffusion coefficients with strong potential for applications in complex heterogeneous systems, such as living cells.

## MATERIALS AND METHODS

### Experimental setup

The measurements were performed on a home-built two-photon laser scanning microscope (10) using a model UPLAPO 60× W3/IR objective (Olympus, Center Valley, PA). The excitation was provided by a tunable Ti:Sapphire laser (Mira 900-F; Coherent, Santa Clara, CA) whose wavelength was chosen depending on the investigated dye: 790 nm (Alexa 488), 820 nm (Alexa 546, fluorescein, rhodamine 6G), or 920 nm (eGFP). The programmable galvanometer scanners steering the beam allow the system to operate in two modes: a conventional imaging laser scanning microscope

mode, and a sFCS mode where the beam is scanned in a circle with a user-defined radius and frequency. The fluorescence, collected by the objective and transmitted through an appropriate emission filter, was detected by an avalanche photodiode (SPCM-CD2801; PerkinElmer, Wellesley, MA). The detected photocount sequence was processed by a SPC-830 module (Becker & Hickl, Berlin, Germany) and stored for further analysis. The SPC-830 module provides timing information of every detected photon with the resolution corresponding to the repetition frequency of the laser (in our case, 13.1 ns).

The scan radii used in this work were in the range 0–1  $\mu\text{m}$ , and the scan frequencies 0.5, 1.0, and 2.0 kHz. Laser excitation intensities between 2 and 5 mW were used in all measurements with the exception of the photobleaching experiments, where up to four times higher intensities were employed. The measurements lasted  $\sim 100$  s.

### Sample

The fluorescent dyes were dissolved in the following solvents: Alexa 546, Alexa 488 (succinimidyl ester; Molecular Probes, Eugene, OR) and rhodamine 6G in water, eGFP (Clontech, Mountain View, CA) and (5(6)-carboxy-)fluorescein (Sigma-Aldrich, St. Louis, MO) in 100 mM phosphate-citrate buffer, pH = 7.5. The solutions at nanomolar concentrations were placed in a 1-mm-deep well with the bottom and the top formed by a #1.5 coverslip, to prevent evaporation of the solvent during the measurement. The measurement volume was positioned at a distance of  $\sim 100$   $\mu\text{m}$  from the coverslip within the well. The experiments were performed at room temperature of  $22.5 \pm 0.5^\circ\text{C}$ .

### Cell culture

HeLa SS6 cells were grown in DMEM including sodium pyruvate (Gibco, Invitrogen, Carlsbad, CA) and 10% Fetal Bovine Serum (Cambrex, East Rutherford, NJ). They were seeded on LabTek chambered cover glasses (Nalge-Nunc, Rochester, NY) 24 h before the transfection with 100,000 cells/ml, leading to 50% confluency on the following day. Transfection of pEGFP-N1 DNA (Clontech) into the cells was mediated by Lipofectamine 2000 (Invitrogen) and followed by a media change after 3 h. The measurements were performed 5–7 h after transfection.

### Theory and data analysis

The profile of the measurement volume, reflecting the two-photon excitation, is approximated by three-dimensional Gaussian function  $W(\mathbf{r})$ ,

$$W(\mathbf{r}) = e^{-\left(\frac{x^2+y^2}{2a^2} + \frac{z^2}{2(wa)^2}\right)}, \quad (1)$$

where  $a$  is a parameter describing the width of the measurement volume in the lateral ( $xy$ ) plane, and  $w$  is the relative extension of the measurement volume along the optical axis. The model autocorrelation function for simple diffusion, when the measurement volume is scanned in a circle of radius  $R$  at a constant frequency  $f$ , is the product of the commonly used diffusion model (5) and an exponential scan factor (13,19):

$$g(\tau) = g_0 \frac{1}{\sqrt{1 + \frac{D\tau}{w^2 a^2}}} \frac{1}{1 + \frac{D\tau}{a^2}} e^{-\frac{R^2 \sin^2(\pi f \tau)}{a^2 + D\tau}}. \quad (2)$$

In standard FCS with a fixed measurement volume the exponential factor is equal to 1 because  $R = 0$ . In this case the autocorrelation  $g(\tau)$  depends on the diffusion coefficient  $D$  and volume size  $a$  via the diffusion time  $\tau_D = a^2/D$ , therefore  $a$  has to be known if  $D$  is to be obtained from the fit (both cannot be determined at the same time). Scanning the measurement volume is mathematically described by multiplying the model function by the exponential scan factor, which effectively decouples  $a$  and  $D$ , making it possible for both

to be obtained from a single fit. Introducing two additional parameters,  $R$  and  $f$ , in the sFCS model does not make the fitting analysis less stable due to too many variable parameters, since both  $R$  and  $f$  can be determined beforehand with sufficient accuracy and then fixed in the fitting process.

The theoretical autocorrelation (Eq. 2) is shown in Fig. 1. The autocorrelation curve (solid line) exhibits oscillations due to the periodic motion of the scanned measurement volume. The upper envelope of the curve is the autocorrelation function corresponding to a fixed measurement volume ( $R = 0$ ). The lower envelope corresponds to a cross-correlation between two fixed volumes positioned at a distance equal to the diameter of the scanned circle.

The insets in Fig. 1 demonstrate decoupling of  $D$  and  $a$ . While in the standard FCS the increase of diffusion coefficient  $D$  produces the same effect on the autocorrelation curve as the decrease of the measurement volume size  $a$ , this is clearly not the case in sFCS. Fig. 1 (inset A) shows that the increase of the diffusion coefficient produces a decrease of correlation at time  $\tau = 1/f$ , but an increase at time  $\tau = 1/(2f)$ , for a suitably chosen scan radius  $R$ . However, the decrease of the measurement volume  $a$  results in decrease of correlation at all times (Fig. 1, inset B). Thus,  $D$  and  $a$  influence the autocorrelation in different ways and can therefore be determined independently at the same time (see also Supplementary Material).

An exponential component describing triplet kinetics has not been included in the model autocorrelation, because the triplet component is usually not observed with two-photon excitation (20–22). All experimental data in this work, where no photobleaching occurs, can be fitted well with the model without a triplet component (Eq. 2).

The fluorescence autocorrelations were calculated off-line from the detected stream of photocounts using the timing information of every photocount. We have applied the multiple- $\tau$  approach (23), with the lag channel width being doubled every  $m = 64$  channels, rather than the more-often-used doubling every eight channels (24). The first  $2m = 128$  channels have a width equal to the temporal resolution of 13.1 ns. The calculation algorithm is similar to that published by Magatti and Ferri (25). Using  $m = 64$  results in finer sampling of the autocorrelation curve needed to resolve the oscillations caused by scanning, and prevents distortions due to the finite

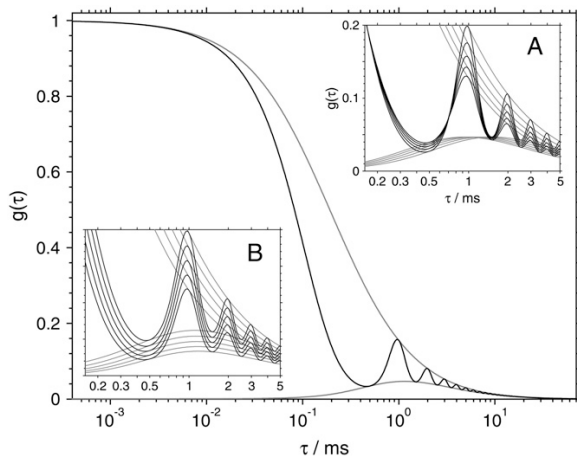


FIGURE 1 The theoretical autocorrelation function (Eq. 2) when scanning the measurement volume at frequency  $f = 1$  kHz along a circular path of radius  $R = 0.38 \mu\text{m}$  (solid line). The upper envelope of the curve (shaded) is the autocorrelation function corresponding to a fixed measurement volume. The lower envelope (shaded) corresponds to a cross-correlation between two fixed volumes positioned at a distance equal to the diameter of the scanned circle. The insets show the variation of the autocorrelation with the diffusion coefficient  $D$  (A), and with the size of the measurement volume  $a$  (B). The other parameters are:  $D = 100 \mu\text{m}^2 \text{s}^{-1}$ ,  $a = 0.14 \mu\text{m}$ , and  $w = 6.5$ .

channel width. This was tested by calculating autocorrelations with  $m = 128, 64, 32, 16$ , and  $8$ , and noting that only the diffusion coefficients obtained with  $m = 8$  and  $16$  were slightly higher than those with  $m > 16$ . The value of  $m$  can be easily increased within the software, if finer sampling of the autocorrelation is required. The experimental autocorrelation curves were analyzed by weighed nonlinear least-squares method with weights estimated from the data, and using a model function described by Eq. 2. The parameters  $D$ ,  $a$ ,  $w$ , and  $g_0$  were optimized in the fit, while the parameters  $R$  and  $f$  were kept fixed at their known values.

## Simulations

The autocorrelation curves were calculated according to Eq. 2 with the time channels of width and spacing identical with the experimental curves. Gaussian noise was added to every channel, with the standard deviation  $\sigma$  similar to that of experimental data. This was estimated from the autocorrelation curves of Alexa 546 as  $\sigma = 7.6 \times 10^{-5} (1/\sqrt{\Delta\tau} + 0.8)$ , where  $\Delta\tau$  is the channel width in milliseconds. The parameters in the simulated curves were:  $D = 100$  and  $300 \mu\text{m}^2 \text{s}^{-1}$ ,  $f = 0.5, 1.0$ , and  $2.0$  kHz,  $R = 0-1 \mu\text{m}$ ,  $g_0 = 1$ ,  $a = 0.14 \mu\text{m}$ , and  $w = 6.5$ . The simulated autocorrelation curves were analyzed in the same way as the experimental data, and the recovered parameters were processed as described in Results.

## RESULTS

### Radius calibration

The determination of the diffusion coefficient using sFCS relies on accurate knowledge of the scan radius  $R$ . The position of the measurement volume within the  $xy$  plane is determined by the driving signal supplied to the galvanometer scanners. The exact relationship between the driving signal and the actual position of the focused laser beam (spatial calibration) was performed by imaging a Ronchi ruling (Edmund Optics, Karlsruhe, Germany) with 600 linepairs per mm, corresponding to a period of  $1.6 \mu\text{m}$ , in reflection mode (Fig. 2 A). Although the image of the lines is not sharp due to the diffraction-limited resolution, the period along the  $x$  direction can be determined with accuracy  $>0.2\%$  from the intensity profile. The intensity profile  $p_x(x)$  averaged over all rows and over the several periods shown in Fig. 2 A is displayed in Fig. 2 B.

This calibration is sufficient in a standard imaging mode of the microscope used, where the scanning frequencies do not exceed  $\sim 100$  Hz. At higher frequencies used in this work (0.5–2 kHz), the scanners are not able to follow the driving signal accurately, resulting in reduced amplitudes and therefore smaller scan radii  $R$  than intended. A dynamic calibration is required to determine the real scan radius  $R$  in such case. This was performed by scanning the beam at a desired frequency  $f$  and nominal radius  $R_n$ , and detecting the signal reflected from the Ronchi ruling. The measured signal was averaged over its period  $1/(2\pi f)$  yielding a temporal profile  $P(t)$ ,  $t \in (0, 1/(2\pi f))$ . The profile  $P(t)$  was then fitted to the equation  $P(t) = ap_x(x(t))$ , where the position  $x(t)$  of the laser focus is described by  $x(t) = x_0 + R \cos(2\pi ft + \varphi_0)$ . The fit parameters were: the scaling factor  $a$ , the spatial offset  $x_0$ , the true scan radius  $R$ , and the initial phase  $\varphi_0$ . In some

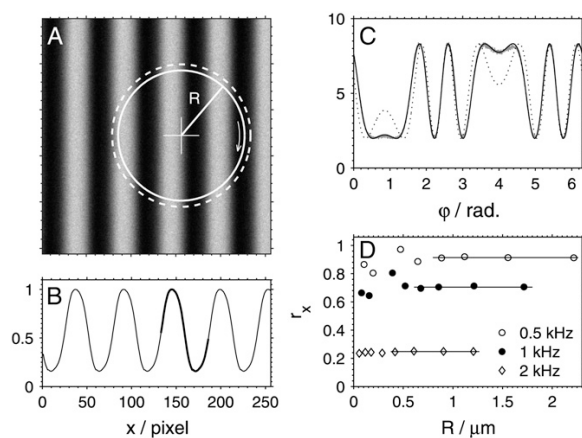


FIGURE 2 Illustration of the calibration of the scan radius  $R$ . (A) Image of the Ronchi ruling with 600 linepairs per mm; image size:  $8 \mu\text{m}$ . The solid circle represents the real scanned path with radius  $R = 2.217 \mu\text{m}$ , the dashed circle is the nominal path ( $R_n = 2.418 \mu\text{m}$ ). (B) The intensity profile  $p_x(x)$  along the  $x$  direction. (C) The experimental temporal profile  $P(\varphi = 2\pi f t)$  measured when scanning along the solid circle drawn in panel A (shaded line), the fit using the spatial profile  $p_x(x)$  shown in panel B (solid line), and the profile that corresponds to the nominal path shown dashed in panel A (dotted line). (D) The radius reduction factors  $r_x$  obtained at different radii  $R$  and frequencies  $f$ ; the solid lines represent the average of the values at four largest radii.

cases the specimen moved slightly along the optical axis ( $z$  direction) between the measurements of the spatial ruling profile  $p_x(x)$  and the temporal profile  $P(t)$ . This was taken into account in the fitting procedure by convoluting  $p_x(x)$  with a Gaussian of width  $\sigma$  (an additional fit parameter; typically 0–4 pixels), thus simulating the blurring due to defocusing. Although this procedure improved the fits, it had negligible effect on the recovered values of  $R$ , indicating that this experimental instability is not critical for the calibration.

An example of the experimental profile  $P(t)$  for  $f = 0.5$  kHz and  $R_n = 2.418 \mu\text{m}$ , and a fit ( $R = 2.217 \mu\text{m}$ ) is shown in Fig. 2 C. Also shown is a profile that would result from motion along a circle with the nominal radius  $R_n$ , if no radius reduction occurred (dashed circle in Fig. 2 A). The large difference between the two profiles for  $R$  and  $R_n$  indicates the high sensitivity of the calibration method.

The frequency-dependent radius reduction factor  $r_x \equiv R/R_n$  was independent of the radius  $R_n$ . However, the precision of its determination was rather low at low radii, mainly because of the small spatial variation of  $p_x(x)$  limited by light diffraction. Therefore, a reduction factor  $r_x$  for every used frequency value was obtained by averaging the values of  $r_x$  for the four largest radii measured (Fig. 2 D).

The dynamic calibration was performed for both  $x$  and  $y$  directions. At the frequency 2 kHz, the highest frequency used, the resulting  $r_x$  and  $r_y$  values varied by 16%, reflecting the fact that the scanned paths are slightly elliptical. This is likely to be caused by mirrors of different sizes being mounted

on the  $x$  and  $y$  scanners, and therefore different resonant frequencies of the two scanners. The difference between  $r_x$  and  $r_y$  at lower frequencies was  $<0.5\%$ . The average  $r$  of the  $r_x$  and  $r_y$  values was used in further data analysis. The values are:  $r = 0.917 \pm 0.005$  at 0.5 kHz,  $r = 0.704 \pm 0.006$  at 1.0 kHz, and  $r = 0.23 \pm 0.02$  at 2.0 kHz.

### Measurements of diffusion coefficients $D$

To determine the diffusion coefficients of Alexa 546, Alexa 488, and eGFP, we measured their fluorescence autocorrelation curves at three scan frequencies (0.5, 1.0, and 2.0 kHz) and a range of scan radii  $R$  between 0 and  $1 \mu\text{m}$ . Fluorescein and rhodamine 6G were measured at 0.5 and 1.0 kHz and radii 1.0 and  $0.7 \mu\text{m}$ . The excitation intensities were chosen to achieve high photon count rate per molecule to maximize the signal/noise ratio (5), but were kept below the limit where photobleaching artifacts appear. The photon count rates per molecule ranged from 1.9 kHz (eGFP) to 6.5 kHz (Alexa 546).

A typical experimental autocorrelation curve with a fit, in this case that of eGFP measured at frequency 1 kHz and radius  $0.385 \mu\text{m}$ , is shown in Fig. 3. Also shown are the upper and lower envelopes, corresponding to the fixed-volume autocorrelation and the cross-correlation between two locations spaced by a distance  $2R$ , respectively. The plot of fit residues indicates the good quality of the fit.

Fig. 4 demonstrates the change of the temporal profile of the fluorescence autocorrelation with varying scan radius  $R$  on the example of several experimental curves of Alexa 546 recorded at 1 kHz. Due to the faster diffusion of Alexa 546 than eGFP (higher diffusion coefficient  $D$ ) the oscillations in the autocorrelation curve are less pronounced than in the

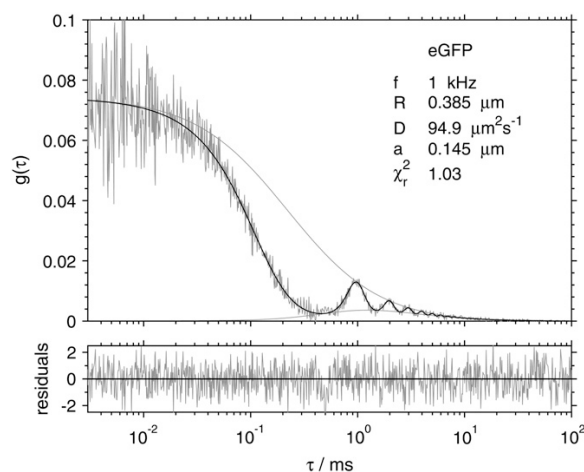


FIGURE 3 Fluorescence autocorrelation of eGFP measured while scanning at frequency 1 kHz with radius  $0.385 \mu\text{m}$ . The fit to Eq. 2 (solid), upper and lower envelopes (shaded), and fit residuals (bottom graph) are shown.

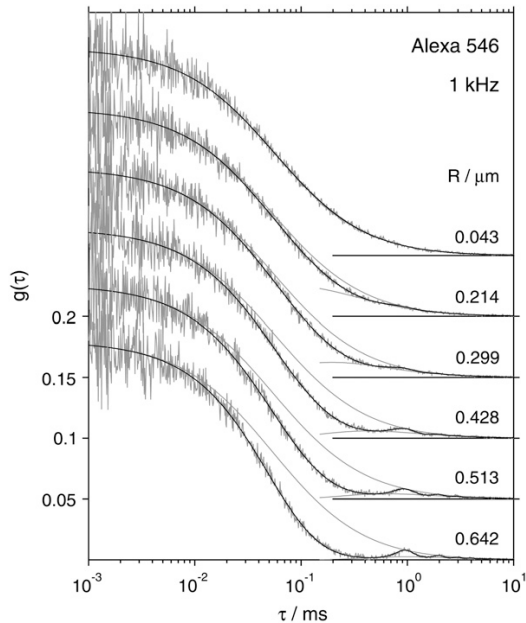


FIGURE 4 Fluorescence autocorrelation curves of Alexa 546 measured at 1 kHz with different radii  $R$ . The fits to Eq. 2 (solid) and the upper and a part of the lower envelopes (shaded) are shown. The curves are offset for clarity. Note that the autocorrelation amplitude is independent of the scan radius  $R$ .

curves of eGFP (Fig. 3). The amplitudes of the autocorrelation curves ( $g(\tau)$  as  $\tau \rightarrow 0$ ) were independent of the scan radius and frequency in all cases, as expected (also demonstrated in Fig. 4).

The autocorrelations were analyzed by fitting them to the model function as expressed by Eq. 2. The fits produced random uncorrelated residues with  $\chi_r^2$  values typically in the range 1.00–1.15. Fig. 5 shows the values of the diffusion coefficients  $D$  and measurement volume sizes  $a$  obtained from the fits of the autocorrelation curves of eGFP measured at three different scan frequencies  $f$  and a range of scan radii  $R$ . We observe, that at small scan radii ( $R \leq 0.2 \mu\text{m}$  for eGFP, and  $R \leq 0.4 \mu\text{m}$  for the Alexa dyes), the spread of the recovered parameters is much larger than at higher scan radii. This is related to the fact that at small radii the parameters  $D$  and  $a$  are strongly correlated, and in the limit of zero scan radius (fixed measurement volume) the autocorrelation is a function of the ratio of the two parameters  $a^2/D$ , as described in Theory and Data Analysis. The change of one parameter can be compensated by an opposite change in the other, and consequently both of them cannot be determined simultaneously. To obtain a more precise value of  $D$  and  $a$ , we averaged the values obtained from the fits at larger radii ( $R > 0.2 \mu\text{m}$  for eGFP, and  $R > 0.4 \mu\text{m}$  for the Alexa dyes) and frequencies 0.5 and 1.0 kHz. The data from the measurements at 2 kHz were excluded from the averaging because of far less accurate determination of the radius reduction factor

$r$  at this high frequency (see Radius Calibration). In the case of fluorescein and rhodamine 6G, we averaged the values obtained at 0.5 and 1.0 kHz separately, because systematically higher  $D$  at higher scan frequencies were obtained: 422 and 450  $\mu\text{m}^2 \text{s}^{-1}$  for fluorescein, and 422 and 430  $\mu\text{m}^2 \text{s}^{-1}$  for rhodamine 6G at 0.5 and 1.0 kHz, respectively.

The final values of the diffusion coefficients  $D$  are summarized in Table 1. The errors, estimated from the standard deviations of the mean, and the errors in the calibration of the scan radius  $R$ , are  $\sim 2\%$ . The difference between the measured diffusion coefficients of Alexa 488 and Alexa 546, for which no literature value is available, is consistent with the difference between their molecular weights ( $M(\text{Alexa 488}) = 643 \text{ g mol}^{-1}$ ,  $M(\text{Alexa 546}) = 1079 \text{ g mol}^{-1}$ ) and the Stokes-Einstein relationship between the molecular size and the diffusion coefficient.

### Choice of optimal scan radius $R$ and frequency $f$

When performing sFCS we are free to select the scan radius  $R$  and the frequency  $f$  within the limits imposed by the hardware. A question remains as to what role the choice of

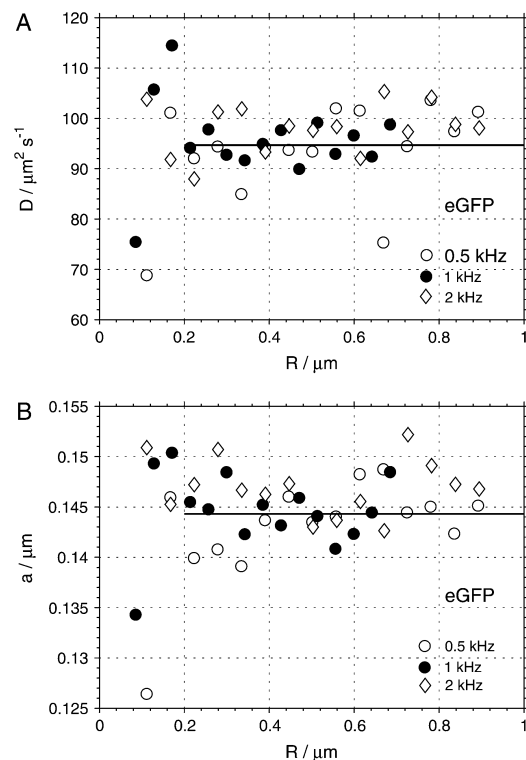


FIGURE 5 Diffusion coefficients  $D$  (A) and measurement volume sizes  $a$  (B) obtained from the fits of the autocorrelation curves of eGFP measured at three different scan frequencies  $f$  and a range of scan radii  $R$ . The lines indicate the mean values calculated as averages over the fit results at frequencies 0.5 and 1 kHz and radii larger than 0.2  $\mu\text{m}$ .

**TABLE 1** The diffusion coefficients  $D$  determined in this work ( $T = 22.5 \pm 0.5^\circ\text{C}$ ) and comparison with literature values

Dye	This work		Literature values	
	$D$ [ $\mu\text{m}^2 \text{s}^{-1}$ ]	$D$ [ $\mu\text{m}^2 \text{s}^{-1}$ ]	$T$ [ $^\circ\text{C}$ ]	Ref.
Alexa 488	435	414	25	(2)
Alexa 546	341	—		
eGFP	95	$93 \pm 4^*$	25	(2,36)
Fluorescein	$436^\dagger$	422–437	25	(37,38)
Rhodamine 6G	$426^\dagger$	$414 \pm 1$	25	(38)

Note that the diffusion coefficients in water solutions are expected to increase with temperature by  $\sim 2\%$  for every degree in the temperature range used, mainly due to decrease of water viscosity with temperature.

\*The value was corrected for the wrong diffusion coefficient of the reference standard used in Schenk et al. (36).

$^\dagger$ Average of the values obtained at frequencies 0.5 and 1.0 kHz.

scan radius and frequency plays in the precision and accuracy of the determined parameters ( $D$ ,  $a$ ), and what the optimal ranges of their values are.

Two conditions have to be fulfilled for the values of  $R$  and  $f$  to be suitable: first, the autocorrelation has to be sufficiently sensitive to changes in the diffusion coefficient, so that the noise on the experimental curve does not result in large spread of the values recovered from the fit; and second, the parameters  $D$  and  $a$  have to be sufficiently uncorrelated, so that  $D$  can be obtained without any additional knowledge of the value of  $a$ . The second condition is clearly not fulfilled in standard FCS with a fixed measurement volume, and decoupling of  $D$  and  $a$  is the reason for introducing scanning into FCS, when this is used for the determination of diffusion coefficients.

To understand how  $R$  and  $f$  influence the values of  $D$  and  $a$  obtained from the fit, we simulated autocorrelation curves by calculating the values in the time channels according to Eq. 2 and adding noise to the individual data points. We then fitted the curves in the same way as the experimental data, and determined the mean (expectation) values and standard deviations of the two parameters,  $D$  and  $a$ , obtained from a fit to a single curve. The simulations were performed for the diffusion coefficients 100 and  $300 \mu\text{m}^2 \text{s}^{-1}$ , the same three values of frequencies used in the experiments (0.5, 1.0, and 2.0 kHz), and a range of scan radii  $R$  between 0 and  $1 \mu\text{m}$ . For every combination of parameters, 1800 curves were simulated and analyzed.

Fig. 6 shows the mean values of diffusion coefficients and their standard deviations  $\sigma_D$ , as obtained from the fits to the simulated data. The standard deviations diverge at low radii, an effect caused by the above-mentioned correlation between  $D$  and  $a$  and the inability to determine both parameters simultaneously at small or zero radii. At a certain radius, a minimum standard deviation is reached, and at larger radii  $\sigma_D$  slightly increases again. At the same time, the mean value of  $D$  exhibits a bias increasing with the scan radius. The optimal value of radius  $R$  with the smallest  $\sigma_D$  and no bias in the diffusion coefficient  $D$  varied with both  $D$  and frequency

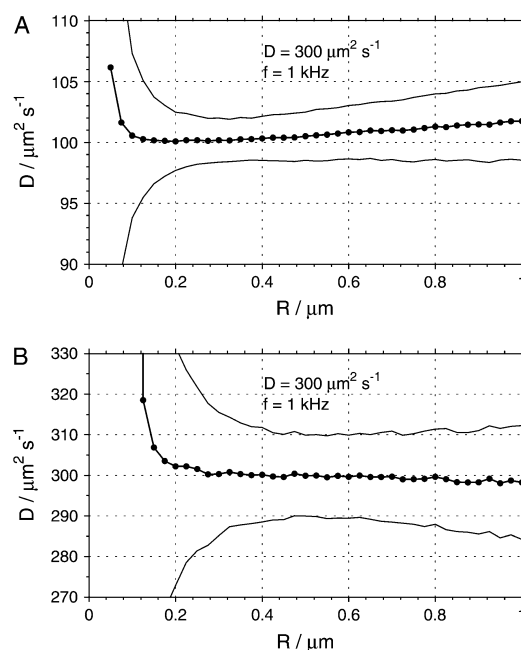


**FIGURE 6** The dependence of the diffusion coefficient  $D$  recovered from the fits of simulated autocorrelation curves on the scan radius  $R$ , displayed for two values of diffusion coefficient:  $100 \mu\text{m}^2 \text{s}^{-1}$  (A) and  $300 \mu\text{m}^2 \text{s}^{-1}$  (B). The thick line corresponds to the mean recovered values of  $D$ , and the thin lines indicate the  $\pm\sigma_D$  widths of the distributions of  $D$  (standard deviation). The optimal scan radii  $R_0$  with no bias in  $D$  and minimum  $\sigma_D$  are  $\sim 0.35 \mu\text{m}$  (A) and  $0.55 \mu\text{m}$  (B). Every data point is a result of analysis of 1800 curves.

$f$ , being larger at larger  $D$  and smaller  $f$ . The standard deviation  $\sigma_D$  at best  $R$  was smaller with smaller diffusion coefficient  $D = 100 \mu\text{m}^2 \text{s}^{-1}$  ( $\sim 2\%$ ) and larger at  $D = 300 \mu\text{m}^2 \text{s}^{-1}$  ( $\sim 3\%$ ), regardless of the frequency  $f$ . Simulations with lower and higher noise level, emulating higher and lower molecular brightness, respectively, provided qualitatively similar results, with the same optimal radius  $R_0$ , and lower standard deviations at lower noise levels and vice versa.

Similar results were obtained for the measurement volume size  $a$ , with the exception that no bias was observed at high radii, and the standard deviations  $\sigma_a$  were smaller than those of  $D$ : 1–2%.

To assess the relevance of the results of the simulations for real experiments, the same analysis should be performed on experimental data. This is impractical, however, due to the prohibitively long times needed to acquire a sufficient amount of data. Therefore, we looked for an alternative way to relate the simulation results to practical experiments.

The fitting algorithm used in the analysis of the autocorrelation curves tries to find a minimum of  $\chi_r^2$  by optimizing the variable parameters of the model function. The depth of the minimum, i.e., how strongly  $\chi_r^2$  changes by varying the fit parameters (or a selected fit parameter) around their

optimal value, determines the stability of the fit with respect to noise, and can therefore be expected to be related to the standard deviation of the parameter in question.

We mapped the  $\chi_r^2$  minimum by calculating  $\chi_r^2$  for a range of  $D$  values centered around the value of  $D$  determined by the fit. The obtained curve was then fitted to a quadratic dependence  $\chi_r^2(D) = \alpha D^2 + \beta D + \gamma$ , with the parameter  $\alpha$  being a measure of the depth of the  $\chi_r^2$  minimum. This calculation can be easily performed on both the simulated and the experimental data, since one curve is sufficient to obtain an estimate of  $\alpha$ .

Fig. 7, A and B, show the dependence of the parameter  $\alpha$  calculated from the simulated decays on the scan radius  $R$  for the same values of diffusion coefficient and frequency as those used in the simulations described above. The data-points were matched to arbitrary smooth curves (lognormal distributions) to facilitate the estimation of the position of the maximum  $\alpha$ . The results show that when the maximum of  $\alpha$  is reached, the radius coincides with the optimal  $R$  value established on the basis of minimum standard deviation of  $D$  (Fig. 6).

The same calculations were performed with the experimental autocorrelation data. Fig. 7 C shows the dependencies  $\chi_r^2(D)$  for Alexa 546 autocorrelations measured at 2 kHz and a range of scan radius values. The  $\alpha$ -values from the fits to these curves are shown in Fig. 7 D, together with a scaled smooth curve corresponding to  $\alpha$ -dependence of simulated data with  $f = 2$  kHz and  $D = 300 \mu\text{m}^2 \text{s}^{-1}$  taken from Fig. 7 B. Clearly, the position of maximal  $\alpha$  for experimental and simulated data coincides, as is the case for all other combinations of frequencies and investigated dyes (not shown).

These findings indicate that the optimal values of scan radius obtained from simulations can be considered applicable for real measurements, despite the idealization of un-

correlated Gaussian noise in the simulated curves (23), and despite the fact that additional disturbances can be present in real experiments. It is therefore possible, in principle, to perform the simulations described above for all relevant combinations of diffusion coefficients, scan frequencies and radii, and to derive from these results the optimal scan radius and frequency for any diffusion coefficient.

Instead, we attempted to obtain a more general semiempirical formula for the optimal scan radius  $R$  from considerations concerning the variations of the autocorrelation curve with the diffusion coefficient. We assume that the measurement of  $D$  will be most precise when the autocorrelation is most sensitive to changes in  $D$ , i.e., when the changes of  $g(\tau)$  with  $D$  are the largest. At the same time we require that the changes of  $g(\tau)$  with  $D$  are distinguishable from the changes caused by variations in  $a$ , to keep the two parameters uncorrelated, as discussed in Theory and Data Analysis, and demonstrated in Fig. 1.

Considering the autocorrelation curves shown in Fig. 1 A, a possible criterion for optimal scan radius  $R_0$  can be formulated: at the optimal scan radius, the changes of  $g(\tau)$  at times  $\tau = 1/(2f)$  and  $\tau = 1/f$  with the diffusion coefficient  $D$  are the largest, but with opposite sign (see Supplementary Material for details). Mathematically, the radius  $R_0$  has to be found where the following maximum is reached:

$$\max \left( \left. \frac{dg(\tau)}{dD} \right|_{\tau=1/(2f)} - \left. \frac{dg(\tau)}{dD} \right|_{\tau=1/f} \right). \quad (3)$$

The minus sign indicates that the changes of  $g(\tau)$  at the two different times occur in opposite directions. A straightforward calculation, simplified by the fact that the second term in Eq. 3 is independent of  $R$ , yields the following formula for  $R_0$ , together with a useful approximation:

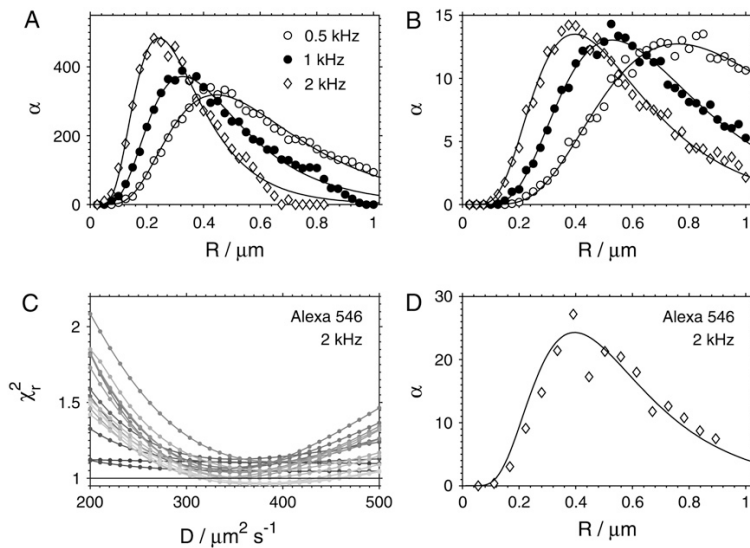


FIGURE 7 Choosing the optimal scan radius  $R$ . (A and B) The parameter  $\alpha$  from the fits  $\chi_r^2(D) = \alpha D^2 + \beta D + \gamma$  obtained from simulated autocorrelation curves at different scan radii  $R$  with diffusion coefficient  $D = 100 \mu\text{m}^2 \text{s}^{-1}$  (A) and  $D = 300 \mu\text{m}^2 \text{s}^{-1}$  (B). (C) The dependence of  $\chi_r^2$  on diffusion coefficient  $D$  for fits of Alexa 546 autocorrelation curves recorded at radii  $R = 0.06\text{--}0.9 \mu\text{m}$  (lighter plots  $\rightarrow$  higher  $R$ ) at frequency  $f = 2$  kHz. (D) The parameter  $\alpha$  obtained from the fits to the curves shown in panel C (diamonds) compared to the curve from simulations with  $D = 300 \mu\text{m}^2 \text{s}^{-1}$  and  $f = 2$  kHz (solid line) as shown in panel B (diamonds).

$$R_0 = \sqrt{\left(2a^2 + \frac{D}{f}\right) \left(1 + \frac{1}{4} \frac{2fa^2 + D}{2fw^2a^2 + D}\right)}, \quad (4)$$

$$\approx \sqrt{2a^2 + \frac{D}{f}} = a \sqrt{2 + \frac{1}{f\tau_D}}. \quad (5)$$

The value of  $R_0$ , as a function of the diffusion coefficient  $D$  for several scan frequencies and assuming  $a = 0.140 \mu\text{m}$ , is displayed in Fig. 8. The  $R_0$  values given by Eq. 4 agree well with the optimal scan radii determined from the simulations, as can be seen from comparison of plots in Fig. 6 with Fig. 8, where the  $R_0$  values obtained from simulations are marked. Equation 4 (or Eq. 5) therefore provides the optimal scan radius at any given frequency. An approximate knowledge of the diffusion coefficient or the diffusion time  $\tau_D$  of the investigated compound is thus required; this can be determined from a preliminary measurement.

Regarding the choice of the best frequency, there is a clear lower limit since, at frequencies that are too low, the correlation decays to values that are too low, before the measurement volume performs one rotation, and the modifications to the autocorrelation curve due to scanning will be lost in noise.

It may appear that using much higher frequencies than those employed in this work would introduce more oscillations in the autocorrelation curve and so increase the sensitivity. However, the oscillations at times much shorter than the diffusion time are determined mainly by the scanning motion and therefore carry little or no information about the diffusion process. It is therefore not clear whether the use of higher scan frequencies would be beneficial.

The data and simulations presented here do not clearly suggest a certain frequency, apart from the fact that 2 kHz is too high due to the slow response of the scanners, this being a problem of instrumental nature. Due to these facts and the

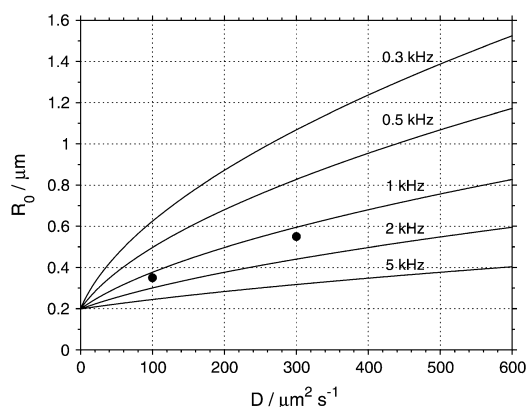


FIGURE 8 The optimal scan radius  $R_0$  determined from Eq. 4, assuming  $a = 0.140 \mu\text{m}$ , plotted for several scan frequencies  $f$ . The points at diffusion coefficients  $100$  and  $300 \mu\text{m}^2 \text{s}^{-1}$  show the optimal scan radius  $R_0$  for the frequency  $1 \text{ kHz}$  obtained from simulations as described in the text, and also shown in Fig. 6.

limited range of useful frequencies available, we have not attempted to search for the optimal frequency value in more detail.

We conclude this section by pointing out that the optimal scan radius  $R$  is such that the loss of correlation, as expressed by the decay of the autocorrelation curve, should be in the same way due to scanning (which is known:  $R, f$ ) and due to diffusion (to be determined:  $D, a$ ). The scanning motion thus acts as an internal reference for the unknown diffusional motion.

### Robustness of sFCS measurements

Since the determination of the diffusion coefficient with sFCS does not require any accurate prior knowledge about the size of the measurement volume  $a$ , it can be expected that the sFCS measurements will be more robust with respect to disturbances and nonidealities affecting the value of  $a$  and thus disqualifying a standard FCS experiment.

It is known that at high excitation intensities, particularly with two-photon excitation, photobleaching of the dye molecules distorts FCS autocorrelation curves and leads to apparently shorter diffusion times  $\tau_D$ , therefore overestimated diffusion coefficients  $D$  (20,26). Scanning the measurement volume, either in a raster (15) or in a circle (19), was shown to alleviate the distortions due to photobleaching.

The same reduction of distortions due to photobleaching is observed in sFCS described here, as shown in Fig. 9. The autocorrelation curves of Alexa 546 were measured with a fixed measurement volume and while scanning at  $1 \text{ kHz}$  and three different scan radii, at a range of excitation intensities. When analyzing the data recorded without scanning, the parameter  $a$  had to be fixed at  $a = 0.138$ , the value determined from previous sFCS measurements. As expected, photobleaching at higher excitation intensities caused the diffusion coefficient obtained from the experiments with a fixed measurement volume to be increasingly overestimated (Fig. 9 A). On the other hand, the diffusion coefficients from the scanning measurements start to deviate from the correct value at higher intensities than in the absence of scanning. This fact is important, since higher excitation intensities can be applied, thus increasing the molecular brightness and therefore the signal/noise ratio. Similar results were obtained for eGFP and Alexa 488.

In situations where there is no possibility to measure the whole intensity series (as shown in Fig. 9 A), but only measurements with limited intensity range are possible, as is often the case in biological applications, we may have no indication whether the value of  $D$  obtained from the fit is affected by photobleaching or not. Scanning FCS provides such an indicator: the measurement volume size  $a$ . As shown in Fig. 9 B, the volume size  $a$  becomes progressively smaller with increasing photobleaching. Since the measurement volume sizes in FCS are usually diffraction-limited, decrease of  $a$  can hardly indicate physically smaller measurement

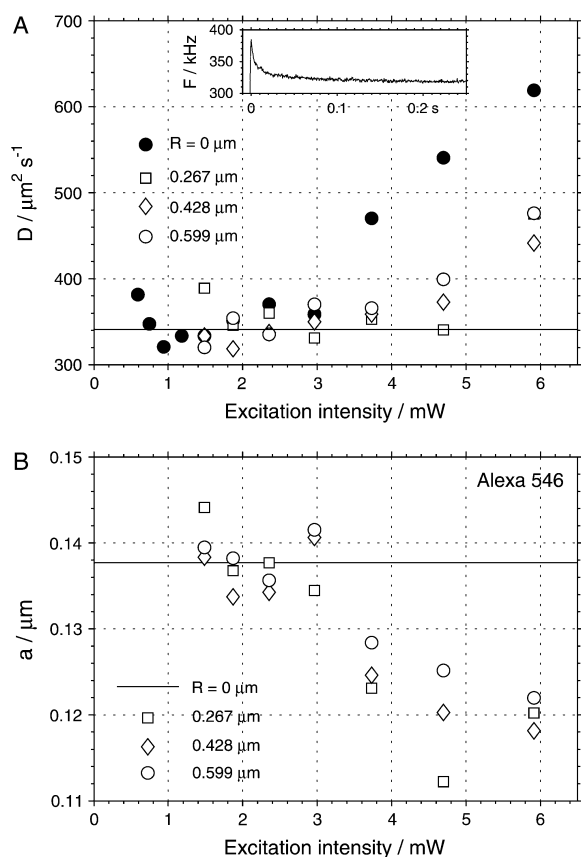


FIGURE 9 The effect of photobleaching on the values of the diffusion coefficient  $D$  (A) and the measurement volume size  $a$  (B) obtained from the fits of the autocorrelation curves of Alexa 546. The results of measurements with fixed measurement volume (solid circles,  $R = 0 \mu\text{m}$ ) and measurements at three different scan radii  $R$  (open symbols) are shown. The solid line in A indicates the diffusion coefficient measured in the absence of photobleaching. The value of  $a$  was fixed to  $0.138 \mu\text{m}$  in the analysis of the data recorded with  $R = 0$  (solid line in B). The scan frequency was 1 kHz. (Inset) Fluorescence decrease due to equilibration between photobleaching and influx of nonbleached molecules to the measurement volume observed upon opening a shutter (excitation power 6 mW, average of 1000 runs).

volumes, but is more likely a manifestation of distortions in the measurement. The unexpectedly low value of  $a$  can therefore be taken as a warning that the recovered diffusion coefficient may not be reliable.

Of course, the quality of the fit remains a universal criterion to reject low-quality data. The autocorrelation curves measured at high bleaching levels did not produce good fits; the  $\chi_r^2$  values reached up to 2.5. In biological applications, the experimental conditions are often far from ideal, and the requirements on  $\chi_r^2$  and randomness of residuals have to be relaxed, making an additional criterion for acceptance/rejection of parameters obtained from analysis extremely useful.

The fact that the effects observed at high powers are indeed due to photobleaching is demonstrated in the inset in Fig. 9 A. The plot shows an initial decrease of fluorescence intensity after the opening of a shutter. We interpret this behavior as an equilibration between photobleaching and influx of nonbleached molecules into the measurement volume. This equilibration occurs on the scale of  $\sim 30$  ms. The triplet state is expected to become populated on a much faster timescale ( $\sim \mu\text{s}$ ), therefore it cannot be the reason for the observations. The stationary concentration of nonbleached molecules in the measurement volume decreases with increasing excitation power, leading to the observed less-than-quadratic dependence of fluorescence (not shown).

Another possible distortion of a FCS measurement is an effective increase of the measurement volume size due to nonideal focusing caused by optical properties of the sample, such as refractive index mismatch or heterogeneity. Such effects are likely to be encountered in biological samples, especially when the measurement is performed deeper within the specimen.

To simulate the increase of the volume size, we decreased the diameter of the excitation beam before entering the scanning unit, thus underfilling the back aperture of the objective and increasing the measurement volume size in the focal plane. The beam diameter was decreased in five steps (five data points in Fig. 10), leading to a progressively larger volume size  $a$ . The increase of the measurement volume was confirmed by a lower fluorescence signal and a lower autocorrelation amplitude due to more molecules being present in the measurement volume.

Fig. 10, A and B, shows the results of the measurements on eGFP in solution performed both with and without scanning. The analysis of the measurements with scanning yields increasing values of  $a$  with a decreasing excitation beam size, without using the information about the beam size in the analysis, as expected. The value of the diffusion coefficient remains independent of the beam size, within the error limits.

To determine the diffusion coefficient from measurements with a fixed measurement volume, the volume size  $a$  has to be known. Ignoring the fact that the volume size  $a$  increases, and using the value of  $a$  from the sFCS measurement with the largest beam size (#1) leads to a progressively smaller apparent diffusion coefficient  $D$ , as shown by solid symbols in Fig. 10 B. Thus, while an incorrect assumption about the size of the measurement volume  $a$  leads to a wrong value of the diffusion coefficient  $D$  in a standard FCS measurement (no scanning), scanning FCS allows us to determine  $D$  without accounting for any changes of the volume size  $a$ .

We have performed similar measurements with varying the beam size in the cytoplasm of HeLa cells expressing eGFP. Scanning FCS measurements allows us to determine the volume size  $a$  and the diffusion coefficient  $D$  independently, from a single measurement, as in the solution studies. Decreasing the excitation beam size yields an increasing volume size  $a$  from the fits to the sFCS data, as with eGFP in

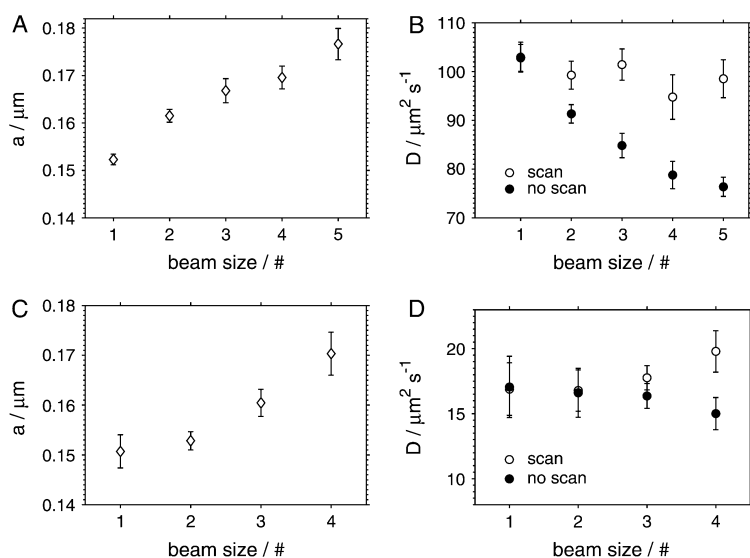


FIGURE 10 The effect of the size of the measurement volume on the parameters obtained from the analysis of eGFP autocorrelations in TRIS buffer (A and B) and in cells (C and D). The measurement volume size was increased by decreasing the beam diameter in five steps (four steps in case of cell measurements), as indicated by the numbers 1–5 on the x axis. The plots A and C show that the increase of the measurement volume can be detected from the fit by the increasing values of the volume parameter  $a$ , both in solution and in the cells. The plots B and D show the diffusion coefficients obtained from sFCS measurements (open circles), and from FCS measurements with a fixed measurement volume (solid circles), where  $a$  was fixed at its minimum value (at beam size #1).

the buffer (Fig. 10 C). FCS measurements without scanning, assuming again the smallest volume size  $a$  (beam size #1), produce smaller apparent diffusion coefficients  $D$  with larger beam sizes (#3 and #4) where the volume size  $a$  deviates significantly from its smallest value (Fig. 10 D). The values of the diffusion coefficient  $D$  obtained with sFCS are in agreement with the literature data (16). The larger relative errors of  $D$  in cells compared to the buffer measurements are caused by the variability of  $D$  among different cells.

These results demonstrate that it is possible to perform in vivo measurements of the diffusion coefficients by sFCS without any knowledge about the size of the measurement volume  $a$ . This method is able to detect uncontrolled changes of  $a$ , and thus prevent an incorrect determination of  $D$ , as would be the case in a standard FCS if assuming a wrong value of  $a$ .

FCS is known to be sensitive to nonidealities other than photobleaching or unaccounted changes of the volume size  $a$ ; for example, optical saturation, the quality of the illuminating laser beam, wrong coverslip thickness, etc. (27,28). We have not attempted to systematically investigate robustness of sFCS to all these effects so far, although such a study will be important for determining the limits of possible applications. We note only that according to our preliminary data, using coverslips of wrong thickness (wrong setting of the correction collar on the microscope objective) results in significantly larger values of  $a$  recovered from the fits to sFCS data (up to 17%), with no apparent effect on the value of  $D$ .

## DISCUSSION AND CONCLUSION

Comparison of the diffusion coefficients measured in this work with the literature data shows a relatively good agree-

ment (Table 1), although the diffusion coefficients of the smaller molecules appear to be systematically biased toward larger values.

The precision of the determination of  $D$  is influenced by both the calibration of the scan radius  $R$  and the noise on the experimental autocorrelation curves. The precision of the radius reduction factor  $r$  determined by calibration is rather high, and is not the limiting factor in our measurements at frequencies 0.5 and 1 kHz. Moreover, we believe that it can be further increased, should the need arise, by elaborating on the calibration procedure described.

The noise on the autocorrelation curves is known to be influenced mainly by the molecular brightness of the investigated fluorochromes (29). Increasing the excitation intensity increases the molecular brightness up to a limit where various artifacts, mainly due to photobleaching and optical saturation, appear (30,31). This limit is considerably lower when two-photon rather than one-photon excitation is used (5,20). We therefore expect that implementing sFCS as described here, with one-photon excitation, would lead to improved signal/noise ratio, and consequently higher precision of the determination of  $D$ . Longer acquisition times also reduce the noise in the data, but extensive measurement periods may not always be practical or possible.

The accuracy of the determination of diffusion coefficient with sFCS, i.e., the presence or absence of bias in the measured value, is considerably more difficult to determine, and can be reliably assessed only by comparison with a known standard. We do not know the reason for larger values of  $D$  obtained in this work compared to the literature values. The results of the simulations indicate that the diffusion coefficients obtained from fits can be biased, if the scan radius is inappropriately chosen, this being an inherent feature of the

fitting algorithm (Fig. 6). However, the deviations predicted by the simulations are too small to explain the differences from the previously published data. Heating in the focus of the objective is also unlikely to be the cause (32).

A small contribution of fast kinetics (triplet) can lead to higher diffusion coefficients if the triplet term is not included in the model function, as confirmed by simulations. For example, 10% contribution of a component with  $\tau_T = 0.003$  ms yields  $D \sim 2\text{--}3\%$  higher. The bias is larger with higher  $\tau_T$  and larger contribution of the exponential component. However, this hypothesis could not be verified, since we could not resolve any triplet contributions in our data, in agreement with previous observations (20–22).

Another potential source of bias is the approximation of the shape of the measurement volume, as expressed by Eq. 1. Although this approximation is accepted as sufficiently good in standard FCS measurements, its limitations have been shown to appear in certain situations (27,33). We assume this to be the most probable explanation for the observed discrepancies. Implementation of a more accurate description of the measurement volume may help clarify this point (34).

The photobleaching measurements described above, and the demonstrated ability of sFCS to yield constant diffusion coefficients and increasing volume sizes upon decreasing the excitation beam diameter, indicate the robustness of sFCS to experimental conditions that directly or effectively influence the value of  $a$ . In a standard FCS, the volume size  $a$  has to be known to correctly determine  $D$ . For example, it has been shown that when measuring diffusion coefficients of molecules in planar membranes, the vertical position of the laser focus determines the size of the measurement area, and if this is not taken into account, wrong values of  $D$  can be obtained (35). Conversely, in sFCS, the recovered value of  $D$  is independent of  $a$ , therefore the volume size  $a$  does not have to be determined independently, as demonstrated here by varying the beam size, or previously with line-scanning FCS on two-dimensional surfaces (9).

The robustness of sFCS is particularly relevant for biological applications, where the samples are often heterogeneous with uncontrollable optical properties. The experiments with cells expressing eGFP show that the essential features of sFCS established in solution measurements are preserved in the *in vivo* experiments: diffusion coefficients can be obtained without any assumptions about the size of the measurement volume  $a$ , and an artificially induced increase of  $a$  (by varying the beam size) can be reliably detected in the fits, without any *a priori* assumptions.

Although we have used the excitation beam diameter to modify the measurement volume size, the volume size in complex samples can increase due to other effects, such as nonideal focusing caused by optical heterogeneity of the sample (refractive index variations).

Since the scan radii are small, typically of a size similar to that of the measurement volume, the presented implementation of sFCS does not require a large homogeneous area

within the sample (for example, cytoplasm) or corrections for background pattern, as in other scanning FCS implementations (18).

We see several advantages of circular sFCS compared to the alternative FCS methods for the measurement of diffusion coefficients mentioned in the Introduction: In sFCS the portions of the scanned circular path are illuminated continuously by the rotating beam, but not simultaneously, which is somewhat equivalent to alternating excitation of overlapping volumes in Dertinger et al. (6). Because of this continuous motion, there is no need for interleaved excitation and consequently, both the excitation and detection parts of the experimental setup are relatively simple. Related to this is the straightforward data processing: the stream of photocounts is simply autocorrelated, and no sorting of photocounts into detection channels (6), or the removing of parts of the data due to the laser beam reaching the end of the scan lines and alignment of scan data (9), is necessary. Furthermore, the calibration of the scan radius is relatively simple and highly accurate, and there is no need for complex measurement volume engineering, as in Blancaquert et al. (8).

On the other hand, the need for moving parts (galvanometer scanners) and illumination optics needed for scanning can be seen as a drawback. We suggest that an experimental configuration considerably less complex than a laser scanning microscope as used here, is adequate for the implementation of sFCS. The scan radii employed in sFCS are  $\sim 1 \mu\text{m}$ , meaning that the angles at which the laser beam has to enter the objective are  $\sim 0.3$  mrad, if the objective focal length of 3 mm is assumed. Then, the scanning mirror can be positioned directly in front of the objective, without any scan or relaying lenses, since the displacement of the beam at the back-objective aperture will be a negligible 0.1 mm, if a realistic distance of 30 cm from the objective is assumed. Thus, a common FCS setup can be converted into sFCS by replacing a mirror with a commercially available two-axis piezo scanner. We are currently developing such a system.

We conclude that scanning FCS, as described here, appears to be a promising variation of FCS tailored for the measurement of diffusion coefficients, be it accurate determination of  $D$  without any *a priori* knowledge about the size of the measurement volume in solutions and *in vitro* experiments, or robust measurements in complex environments, such as living cells and tissues, where possible experimental disturbances affecting the volume size are implicitly taken into account.

## SUPPLEMENTARY MATERIAL

To view all of the supplemental files associated with this article, visit [www.biophysj.org](http://www.biophysj.org).

We thank Eugene P. Petrov for helpful discussions, Karin Crell for the preparation of cell samples, and Jörg Mütze for proofreading the manuscript.

The funding was provided by The International Human Frontier Science Program RGP No. 5/2005, and Europäische Fond für regionale Entwicklung, project No. 4212/06-02.

## REFERENCES

- Magde, D., W. W. Webb, and E. Elson. 1972. Thermodynamic fluctuations in a reacting system—measurement by fluorescence correlation spectroscopy. *Phys. Rev. Lett.* 29:705–708.
- Petrov, E. P., and P. Schwille. 2008. State of the art and novel trends in fluorescence correlation spectroscopy. In *Standardization and Quality Assurance in Fluorescence Measurements: State of the Art and Future Challenges*. U. Resch-Genger, editor. Springer, Berlin, Heidelberg, New York. To appear.
- Bacia, K., and P. Schwille. 2003. A dynamic view of cellular processes by in vivo fluorescence auto- and cross-correlation spectroscopy. *Methods*. 29:74–85.
- Rigler, R., and E. S. Elson, editors. 2001. *Fluorescence Correlation Spectroscopy: Theory and Application*, 1st Ed. Chemical Physics Series. Springer Verlag, Berlin.
- Schwille, P., U. Haupts, S. Maiti, and W. W. Webb. 1999. Molecular dynamics in living cells observed by fluorescence correlation spectroscopy with one- and two-photon excitation. *Biophys. J.* 77:2251–2265.
- Dertinger, T., V. Pacheco, I. von der Hocht, R. Hartmann, I. Gregor, and J. Enderlein. 2007. Two-focus fluorescence correlation spectroscopy: a new tool for accurate and absolute diffusion measurements. *ChemPhysChem*. 8:433–443.
- Jaffiol, R., Y. Blancquaert, A. Delon, and J. Derouard. 2006. Spatial fluorescence cross-correlation spectroscopy. *Appl. Opt.* 45:1225–1235.
- Blancquaert, Y., A. Delon, J. Derouard, and R. Jaffiol. 2006. Spatial fluorescence cross-correlation spectroscopy between core and ring pinholes. *Proc. SPIE*. 6191:61910B.
- Ries, J., and P. Schwille. 2006. Studying slow membrane dynamics with continuous wave scanning fluorescence correlation spectroscopy. *Biophys. J.* 91:1915–1924.
- Petrášek, Z., and P. Schwille. 2008. Scanning fluorescence correlation spectroscopy. In *Single Molecules and Nanotechnology*, Vol. 12. Springer Series in Biophysics. R. Rigler and H. Vogel, editors. Springer, Berlin. 83–105.
- Weissman, M., H. Schindler, and G. Feher. 1976. Determination of molecular-weights by fluctuation spectroscopy—application to DNA. *Proc. Natl. Acad. Sci. USA*. 73:2776–2780.
- Petersen, N. O. 1986. Scanning fluorescence correlation spectroscopy. 1. Theory and simulation of aggregation measurements. *Biophys. J.* 49: 809–815.
- Berland, K. M., P. T. C. So, Y. Chen, W. W. Mantulin, and E. Gratton. 1996. Scanning two-photon fluctuation correlation spectroscopy: particle counting measurements for detection of molecular aggregation. *Biophys. J.* 71:410–420.
- Amediek, A., E. Hausteine, D. Scherfeld, and P. Schwille. 2002. Scanning dual-color cross-correlation analysis for dynamic co-localization studies of immobile molecules. *Single Mol.* 3:201–210.
- Winkler, T., U. Kettling, A. Koltermann, and M. Eigen. 1999. Confocal fluorescence coincidence analysis: an approach to ultra high-throughput screening. *Proc. Natl. Acad. Sci. USA*. 96:1375–1378.
- Ruan, Q. Q., M. A. Cheng, M. Levi, E. Gratton, and W. W. Mantulin. 2004. Spatial-temporal studies of membrane dynamics: scanning fluorescence correlation spectroscopy (SFCS). *Biophys. J.* 87:1260–1267.
- Inoue, M., M. A. Digman, M. Cheng, S. Y. Breusegem, N. Halaihel, V. Sorribas, W. W. Mantulin, E. Gratton, N. P. Barry, and M. Levi. 2004. Partitioning of NaP<sub>i</sub> cotransporter in cholesterol-, sphingomyelin-, and glycosphingolipid-enriched membrane domains modulates NaP<sub>i</sub> protein diffusion, clustering, and activity. *J. Biol. Chem.* 279:49160–49171.
- Digman, M. A., C. M. Brown, P. Sengupta, P. W. Wiseman, A. R. Horwitz, and E. Gratton. 2005. Measuring fast dynamics in solutions and cells with a laser scanning microscope. *Biophys. J.* 89:1317–1327.
- Skinner, J. P., Y. Chen, and J. D. Müller. 2005. Position-sensitive scanning fluorescence correlation spectroscopy. *Biophys. J.* 89:1288–1301.
- Dittrich, P. S., and P. Schwille. 2001. Photobleaching and stabilization of fluorophores used for single-molecule analysis with one- and two-photon excitation. *Appl. Phys. B Lasers Opt.* 73:829–837.
- Eggeling, C., A. Volkmer, and C. A. M. Seidel. 2005. Molecular photobleaching kinetics of rhodamine 6G by one- and two-photon induced confocal fluorescence microscopy. *ChemPhysChem*. 6:791–804.
- Iyer, V., M. J. Rossow, and M. N. Waxham. 2006. Peak two-photon molecular brightness of fluorophores is a robust measure of quantum efficiency and photostability. *J. Opt. Soc. Am. B*. 23:1420–1433.
- Schätzel, K. 1990. Noise on photon correlation data. I. Autocorrelation functions. *Quant. Optics*. 2:287–305.
- Magatti, D., and F. Ferri. 2001. Fast multi- $\tau$  real-time software correlator for dynamic light scattering. *Appl. Opt.* 40:4011–4021.
- Magatti, D., and F. Ferri. 2003. 25 ns software correlator for photon and fluorescence correlation spectroscopy. *Rev. Sci. Instrum.* 74:1135–1144.
- Widengren, J., and R. Rigler. 1996. Mechanisms of photobleaching investigated by fluorescence correlation spectroscopy. *Bioimaging*. 4: 149–157.
- Enderlein, J., I. Gregor, D. Patra, T. Dertinger, and U. B. Kaupp. 2005. Performance of fluorescence correlation spectroscopy for measuring diffusion and concentration. *ChemPhysChem*. 6:2324–2336.
- Enderlein, J., I. Gregor, D. Patra, and J. Fitter. 2004. Art and artifacts of fluorescence correlation spectroscopy. *Curr. Pharm. Biotechnol.* 5: 155–161.
- Koppel, D. E. 1974. Statistical accuracy in fluorescence correlation spectroscopy. *Phys. Rev. A: At., Mol. Opt. Phys.* 10:1938–1945.
- Enderlein, J. 1996. Path integral approach to fluorescence correlation experiments. *Phys. Lett. A*. 221:427–433.
- Nagy, A., J. R. Wu, and K. M. Berland. 2005. Observation volumes and  $\gamma$ -factors in two-photon fluorescence fluctuation spectroscopy. *Biophys. J.* 89:2077–2090.
- Schönle, A., and S. W. Hell. 1998. Heating by absorption in the focus of an objective lens. *Opt. Lett.* 23:325–327.
- Hess, S. T., and W. W. Webb. 2002. Focal volume optics and experimental artifacts in confocal fluorescence correlation spectroscopy. *Biophys. J.* 83:2300–2317.
- Enderlein, J. 2000. Theoretical study of detection of a dipole emitter through an objective with high numerical aperture. *Opt. Lett.* 25: 634–636.
- Benda, A., M. Beneš, V. Mareček, A. Lhotský, W. T. Hermens, and M. Hof. 2003. How to determine diffusion coefficients in planar phospholipid systems by confocal fluorescence correlation spectroscopy. *Langmuir*. 19:4120–4126.
- Schenk, A., S. Ivanchenko, C. Rucker, J. R. Wiedenmann, and G. U. Nienhaus. 2004. Photodynamics of red fluorescent proteins studied by fluorescence correlation spectroscopy. *Biophys. J.* 86:384–394.
- Paul, P. H., M. G. Garguilo, and D. J. Rakestraw. 1998. Imaging of pressure- and electrokinetically driven flows through open capillaries. *Anal. Chem.* 70:2459–2467.
- Culbertson, C. T., S. C. Jacobson, and J. M. Ramsey. 2002. Diffusion coefficient measurements in microfluidic devices. *Talanta*. 56: 365–373.

**A5**

**Circular scanning fluorescence correlation spectroscopy on membranes**

Z. Petrášek, S. Derenko and P. Schwille

*Opt. Express*, 19(25):25006–25021, 2011.



# Circular scanning fluorescence correlation spectroscopy on membranes

Zdeněk Petráček<sup>1,\*</sup>, Susan Derenko<sup>1</sup> and Petra Schwille<sup>1</sup>

<sup>1</sup> Biotechnologisches Zentrum, Technische Universität Dresden, Tatzberg 47/49, 01307 Dresden, Germany

\*[zdenek.petrasek@biotec.tu-dresden.de](mailto:zdenek.petrasek@biotec.tu-dresden.de)

**Abstract:** We discuss circular scanning Fluorescence Correlation Spectroscopy (sFCS) as a simple extension of standard FCS for accurate, robust and fast diffusion measurements on membranes. The implementation is based on a straightforward conversion of a conventional FCS instrument to a sFCS device by mounting a mirror onto a two-axis piezo scanner. The measurement volume is scanned in a circle with sub-micron radius, allowing the determination of diffusion coefficients and concentrations without any a priori knowledge of the size of the detection volume. This is highly important in measurements on two-dimensional surfaces, where the volume size, and therefore the quantitative outcome of the experiment, is determined by the relative position of the surface and the objective focus, a parameter difficult to control in practice. The technique is applied to diffusion measurements on model membrane systems: supported lipid bilayers and giant unilamellar vesicles. We show that the method is insensitive to membrane positioning and to disturbing processes on faster or slower time scales than diffusion, and yields accurate results even for fluctuating or drifting membranes. Its robustness, short measurement times, and small size of the probed area makes this technique particularly attractive for analyzing the properties of membranes and molecules diffusing and interacting within them.

© 2011 Optical Society of America

**OCIS codes:** (180.2520) Fluorescence microscopy; (180.1790) Confocal microscopy; (290.1990) Diffusion; (240.6648) Surface dynamics; (040.3780) Low light level

---

## References and links

1. E. L. Elson and D. Magde, "Fluorescence correlation spectroscopy. I. Conceptual basis and theory," *Biopolymers* **13**, 1–27 (1974).
2. R. Rigler and E. S. Elson, eds., *Fluorescence Correlation Spectroscopy. Theory and Application*, Chemical Physics Series (Springer Verlag, Berlin, 2001), 1st ed.
3. K. Bacia and P. Schwille, "A dynamic view of cellular processes by in vivo fluorescence auto- and cross-correlation spectroscopy," *Methods* **29**, 74–85 (2003).
4. D. Axelrod, D. E. Koppel, J. Schlessinger, E. Elson, and W. W. Webb, "Mobility measurement by analysis of fluorescence photobleaching recovery kinetics," *Biophys. J.* **16**, 1055–1069 (1976).
5. M. J. Saxton and K. Jacobson, "Single-particle tracking: Applications to membrane dynamics," *Annu. Rev. Biophys. Biomol. Struct.* **26**, 373–399 (1997).
6. A. J. García-Sáez and P. Schwille, "Fluorescence correlation spectroscopy for the study of membrane dynamics and protein/lipid interactions," *Methods* **46**, 116–122 (2008).
7. R. Macháň and M. Hof, "Lipid diffusion in planar membranes investigated by fluorescence correlation spectroscopy," *Biochim. Biophys. Acta Biomembr.* **1798**, 1377–1391 (2010).

8. P. Schwille, F. J. Meyer-Almes, and R. Rigler, "Dual-color fluorescence cross-correlation spectroscopy for multicomponent diffusional analysis in solution," *Biophys. J.* **72**, 1878–1886 (1997).
9. K. Bacia, S. A. Kim, and P. Schwille, "Fluorescence cross-correlation spectroscopy in living cells," *Nat. Methods* **3**, 83–89 (2006).
10. J. Enderlein, I. Gregor, D. Patra, and J. Fitter, "Art and artefacts of fluorescence correlation spectroscopy," *Curr. Pharm. Biotechnol.* **5**, 155–161 (2004).
11. S. Milon, R. Hovius, H. Vogel, and T. Wohland, "Factors influencing fluorescence correlation spectroscopy measurements on membranes: simulations and experiments," *Chem. Phys.* **288**, 171–186 (2003).
12. A. Benda, M. Beneš, V. Mareček, A. Lhotský, W. T. Hermens, and M. Hof, "How to determine diffusion coefficients in planar phospholipid systems by confocal fluorescence correlation spectroscopy," *Langmuir* **19**, 4120–4126 (2003).
13. E. Gielen, M. Vandeven, A. Margineanu, P. Dedecker, M. Van der Auweraer, Y. Engelborghs, J. Hofkens, and M. Ameloot, "On the use of z-scan fluorescence correlation experiments on giant unilamellar vesicles," *Chem. Phys. Lett.* **469**, 110–114 (2009).
14. T. Dertinger, V. Pacheco, I. von der Hocht, R. Hartmann, I. Gregor, and J. Enderlein, "Two-focus fluorescence correlation spectroscopy: A new tool for accurate and absolute diffusion measurements," *ChemPhysChem* **8**, 433–443 (2007).
15. Z. Petrášek, C. Hoegge, A. Mashaghi, T. Ohrt, A. A. Hyman, and P. Schwille, "Characterization of protein dynamics in asymmetric cell division by scanning fluorescence correlation spectroscopy," *Biophys. J.* **95**, 5476–5486 (2008).
16. Z. Petrášek, C. Hoegge, A. A. Hyman, and P. Schwille, "Two-photon fluorescence imaging and correlation analysis applied to protein dynamics in *C. elegans* embryo," *Proc. SPIE* **6860**, 68601L (2008).
17. J. Ries, S. Chiantia, and P. Schwille, "Accurate determination of membrane dynamics with line-scan FCS," *Biophys. J.* **96**, 1999–2008 (2009).
18. M. A. Digman, C. M. Brown, P. Sengupta, P. W. Wiseman, A. R. Horwitz, and E. Gratton, "Measuring fast dynamics in solutions and cells with a laser scanning microscope," *Biophys. J.* **89**, 1317–1327 (2005).
19. J. P. Skinner, Y. Chen, and J. D. Müller, "Position-sensitive scanning fluorescence correlation spectroscopy," *Biophys. J.* **89**, 1288–1301 (2005).
20. Z. Petrášek and P. Schwille, "Precise measurement of diffusion coefficients using scanning fluorescence correlation spectroscopy," *Biophys. J.* **94**, 1437–1448 (2008).
21. H. Qian and E. L. Elson, "Analysis of confocal laser-microscope optics for 3-D fluorescence correlation spectroscopy," *Appl. Opt.* **30**, 1185–1195 (1991).
22. S. T. Hess and W. W. Webb, "Focal volume optics and experimental artifacts in confocal fluorescence correlation spectroscopy," *Biophys. J.* **83**, 2300–2317 (2002).
23. M. Born and E. Wolf, *Principles of Optics* (Cambridge University Press, 1999), chap. 8, pp. 484–492, 7th ed.
24. K. M. Berland, P. T. C. So, Y. Chen, W. W. Mantulin, and E. Gratton, "Scanning two-photon fluctuation correlation spectroscopy: Particle counting measurements for detection of molecular aggregation," *Biophys. J.* **71**, 410–420 (1996).
25. J. Widengren, U. Mets, and R. Rigler, "Fluorescence correlation spectroscopy of triplet states in solution: A theoretical and experimental study," *J. Phys. Chem.* **99**, 13368–13379 (1995).
26. S. Chiantia, N. Kahya, and P. Schwille, "Dehydration damage of domain-exhibiting supported bilayers: An AFM study on the protective effects of disaccharides and other stabilizing substances," *Langmuir* **21**, 6317–6323 (2005).
27. D. C. Carrer, E. Kummer, G. Chwastek, S. Chiantia, and P. Schwille, "Asymmetry determines the effects of natural ceramides on model membranes," *Soft Matter* **5**, 3279–3286 (2009).
28. N. Kahya, "Protein-protein and protein-lipid interactions in domain-assembly: Lessons from giant unilamellar vesicles," *Biochim. Acta Biomembr.* **1798**, 1392–1398 (2010).
29. K. Bacia, D. Scherfeld, N. Kahya, and P. Schwille, "Fluorescence correlation spectroscopy relates rafts in model and native membranes," *Biophys. J.* **87**, 1034–1043 (2004).
30. M. Przybylo, J. Sýkora, J. Humpolíčková, A. Benda, A. Zan, and M. Hof, "Lipid diffusion in giant unilamellar vesicles is more than 2 times faster than in supported phospholipid bilayers under identical conditions," *Langmuir* **22**, 9096–9099 (2006).
31. S. Chiantia, J. Ries, N. Kahya, and P. Schwille, "Combined AFM and two-focus SFCS study of raft-exhibiting model membranes," *ChemPhysChem* **7**, 2409–2418 (2006).
32. U. Haupts, S. Maiti, P. Schwille, and W. W. Webb, "Dynamics of fluorescence fluctuations in green fluorescent protein observed by fluorescence correlation spectroscopy," *Proc. Natl. Acad. Sci. U. S. A.* **95**, 13573–13578 (1998).
33. J. Hendrix, C. Flors, P. Dedecker, J. Hofkens, and Y. Engelborghs, "Dark states in monomeric red fluorescent proteins studied by fluorescence correlation and single molecule spectroscopy," *Biophys. J.* **94**, 4103–4113 (2008).
34. J. Widengren and P. Schwille, "Characterization of photoinduced isomerization and back-isomerization of the cyanine dye Cy5 by fluorescence correlation spectroscopy," *J. Phys. Chem. A* **104**, 6416–6428 (2000).
35. K. Bacia and P. Schwille, "Practical guidelines for dual-color fluorescence cross-correlation spectroscopy," *Nat. Methods* **3**, 83–89 (2006).

- ture Protocols **2**, 2842–2856 (2007).
36. E. P. Petrov and P. Schwille, “Fluorescence correlation spectroscopy on undulating membranes,” *Biophys. J.* **88**, 524A–525A (2005).
  37. J. Evans, W. Gratzner, N. Mohandas, K. Parker, and J. Sleep, “Fluctuations of the red blood cell membrane: Relation to mechanical properties and lack of ATP dependence,” *Biophys. J.* **94**, 4134–4144 (2008).
  38. M. B. Schneider, J. T. Jenkins, and W. W. Webb, “Thermal fluctuations of large quasi-spherical bimolecular phospholipid-vesicles,” *Journal De Physique* **45**, 1457–1472 (1984).
  39. Y. Korlann, T. Dertinger, X. Michalet, S. Weiss, and J. Enderlein, “Measuring diffusion with polarization-modulation dual-focus fluorescence correlation spectroscopy,” *Opt. Express* **16**, 14609–14616 (2008).
  40. P. Ferrand, M. Pianta, A. Kress, A. Aillaud, H. Rigneault, and D. Marguet, “A versatile dual spot laser scanning confocal microscopy system for advanced fluorescence correlation spectroscopy analysis in living cell,” *Rev. Sci. Instrum.* **80**, 083702 (2009).
  41. C. Eggeling, C. Ringemann, R. Medda, G. Schwarzmann, K. Sandhoff, S. Polyakova, V. N. Belov, B. Hein, C. von Middendorff, A. Schönle, and S. W. Hell, “Direct observation of the nanoscale dynamics of membrane lipids in a living cell,” *Nature* **457**, 1159–1162 (2009).
- 

## 1. Introduction

The ability to experimentally quantify transport properties and concentrations of molecules on microscopic scales, both in three dimensions and when confined to surfaces, such as cellular membranes, is essential for understanding the details of biological processes on molecular level. The membranes have not only the obvious function of separating different compartments and controlling material exchange between them, but they themselves constitute an environment where biochemical reactions take place. Experimental approaches probing the properties of membranes and molecules interacting with them are therefore of great relevance.

Several optical methods for investigating molecular transport that are readily combined with fluorescence imaging are available: Fluorescence Correlation Spectroscopy (FCS) [1–3], Fluorescence Recovery After Photobleaching (FRAP) [4] and Single Particle Tracking (SPT) [5]. FCS has several advantages over the other methods, most importantly: the measurement is performed within very small (sub- $\mu\text{m}$ ) volume, allowing for high spatial resolution; high temporal resolution, sufficient practically for any biologically relevant molecular transport process; and the ability to determine concentrations by quantifying the magnitude of fluorescence fluctuations without having to rely on the knowledge of molecular brightness. FCS is often applied to the investigation of molecular diffusion in planar membrane systems [6, 7]. Molecular interactions can be monitored by extending FCS to use two excitation and emission channels and two distinct fluorescent labels: Fluorescence Cross-Correlation Spectroscopy (FCCS) [8, 9].

One difficulty in obtaining accurate values of both diffusion coefficients and concentrations with FCS is the need to know the size of the volume in which the measurement takes place. The volume size is usually determined by calibration using a well defined standard sample. However, the differences in the volume size between the calibration and the actual measurement lead to errors [10]. For measurements in bulk (3D), the possible deviations from the calibration value are caused by optical distortions of the diffraction-limited beam. The situation in two dimensions is more complicated: the measurement volume, or rather the area, is defined by the cross-section of the plane with the 3D volume formed by a combined effect of focused laser beam and the confocal pinhole. The relative position of the two defines the size of the volume, therefore the uncertainty about the volume size remains even in the absence of optical distortions [11, 12].

The ideal axial volume position, with the membrane in the objective focal plane, is difficult to adjust experimentally, because of a rather weak dependence of the fluorescence intensity on the axial position of the surface to which the molecules are confined, and also because in practice the position of the maximum of fluorescence intensity does not necessarily coincide with the focal waist [12].

One solution to the positioning problem in membrane experiments is to perform a series of measurements at a range of axial positions and analyze these globally while making an assumption about the shape of the 3D profile of the focused laser beam: the z-scan method [12]. The drawback of this approach is the need to do many measurements, requiring a considerable time, which calls for a high axial stability of the sample on a sub- $\mu\text{m}$  scale. Additionally, even though every single measurement is limited to a plane, the method relies on the assumption of a well-defined volume shape in three dimensions [12, 13].

Another way to deal with the volume problem is to avoid the need for independent volume calibration by employing spatio-temporal correlation techniques. These methods measure and analyze fluorescence correlations between two or more spatially distinct locations, rather than analyzing temporal correlations at a single position. The principle is based on the fact, that the distances between these locations, which can be determined independently of the actual experiment with sufficient accuracy, and are not affected by the optical properties of the sample, provide the required spatial reference scale, as an alternative to the volume size in standard FCS. Examples of these spatio-temporal extensions of FCS include: double-focus FCS [14], scanning FCS (sFCS) with a large circle [15, 16] or a line [17], raster scan FCS (RICS) [18], and small-circle sFCS [19, 20].

Here we present a new simple implementation of small-circle sFCS. It is realized as an easy extension of an existing FCS setup by replacing a mirror with a two-axis piezo scanner, and, contrary to our previous version implemented within a two-photon microscope [20], uses one-photon excitation with the advantages of simpler implementation and better signal-to-noise ratios. The method is applied to diffusion measurements of molecules in model membrane systems: supported lipid bilayers (SLB) and giant unilamellar vesicles (GUV). We show that this type of sFCS on membranes does not suffer from the axial positioning problem, and is highly precise and robust with respect to undesirable effects that may strongly disturb conventional FCS measurements, such as sample drift or membrane thermal fluctuations.

## 2. Theory

The shape of the volume from within which the fluorescence is measured in a FCS experiment is determined by a combination of the illumination and the detection profiles [21, 22]. The light intensity near the focus of a high-NA lens is described by a complex diffraction pattern [23]; the detection efficiency is additionally determined by the confocal pinhole [22]. The combined effect of confinement due to illumination and detection is for the purpose of FCS usually approximated by a three-dimensional Gaussian function [2] or, more accurately, by a function where the illumination component  $W_{\text{ex}}(\mathbf{r})$  has the form of a Gaussian-Lorentzian function [14]:

$$W_{\text{ex}}(\mathbf{r}) = \frac{a_0^2}{a^2(z)} e^{-\frac{x^2+y^2}{2a^2(z)}}, \quad (1)$$

where the lateral volume extent  $a$  depends on the axial distance  $z$  from the focal plane in the following way:

$$a^2(z) = a_0^2 + b^2 z^2, \quad b = \frac{\lambda}{4\pi n a_0}, \quad (2)$$

where  $\lambda$  is the excitation wavelength,  $n$  the refractive index of the medium, and  $a_0$  the volume size in the focal plane. The value of  $a_0$  is determined by the wavelength and the NA of illumination.

When measuring fluorescence of molecules restricted to a horizontal plane, the illuminated area, playing the same role as the measurement volume in 3D, is defined by a cross-section

of the 3D illuminated volume (Eq. (1)) with the plane, and is therefore described by a simple Gaussian function.

Equation (2) forms the basis of the  $z$ -scan method for reliable determination of diffusion coefficients in plane [12]. In this method, the diffusion coefficient  $D$  and  $a_0$  are obtained from a fit to an experimental dependence of the diffusion time  $\tau_D(z) = a^2(z)/D$  on the axial position  $z$  of the membrane within the focus. For this purpose, a series of autocorrelation curves at well defined axial positions has to be measured. The method relies on the validity of Eq. (2), namely the dependence of the volume size  $a$  on  $z$ , and the dependence of the parameter  $b$ , the axial beam divergence near the focus, on the wavelength and  $a_0$ .

In sFCS performed in 2D, we also assume that the cross-section of the laser beam with the plane can be approximated by a Gaussian, however, do not make any assumptions on how the width  $a$  of this Gaussian depends on  $z$  (Eq. (3)):

$$W(x,y) = e^{-\frac{x^2+y^2}{2a^2}}. \quad (3)$$

The uniform motion of the measurement volume in a circle with a radius  $R$  and frequency  $f$  modifies the model fluorescence autocorrelation function for diffusion restricted to two dimensions by an additional exponential factor, yielding [19, 20, 24]:

$$g(\tau) = \frac{1}{cV_{eff}} \frac{1}{1 + \frac{\tau}{\tau_D}} e^{-\frac{R^2 \sin^2(\pi f \tau)}{a^2(1 + \frac{\tau}{\tau_D})}}, \quad (4)$$

where  $V_{eff}$  is the effective measurement volume (area),  $V_{eff} = 4\pi a^2$ , and  $\tau_D$  the diffusion time:

$$\tau_D = a^2/D. \quad (5)$$

The sFCS autocorrelation exhibits periodic modulation due to the circular motion of the volume. The maxima, the minima and the width of the correlation peaks depend on the diffusion coefficient  $D$  and volume size  $a$  in an independent way, making it possible to determine both these parameters from a fit to Eq. (4), as schematically shown in Fig. 1 and described earlier [20].

When the membrane coincides with the objective focal plane (Fig. 1(A), left), the illuminated area is the smallest possible (low  $a$ ), and there is minimal overlap between the focus positions separated by the largest possible distance — the scan circle diameter  $2R$ . When the membrane is moved out of focus, the illuminated area becomes larger (higher  $a$ ) and so does the overlap between two positions separated by  $2R$ . This leads not only to the decrease of the autocorrelation amplitude and an increase in the diffusion time, as in standard FCS, but affects the shape of the autocorrelation in a complex way, for example, the value at the first minimum at  $\tau = 1/(2f)$  increases due to the larger overlap when off focus (Fig. 1(B)). Since these changes, caused by an increase of  $a$ , are different from the changes that would be caused by variations in the diffusion coefficient, the diffusion coefficient and the volume size can be obtained simultaneously from the fit of a single experimental sFCS autocorrelation to Eq. (4), unlike in standard FCS, which yields only their combination in form of the diffusion time  $\tau_D$ .

The uncorrelated character of  $D$  and  $a$  is apparent from the contour plot of  $\chi_r^2$  in the parameter space of  $D$  and  $a$ , constructed by fitting an experimental curve with a model with fixed values of  $D$  and  $a$  (Fig. 1(C)). Not only does the plot exhibit a clear single minimum with respect to  $D$  and  $a$ , but additionally the minimum of  $\chi_r^2$  with respect to  $D$  is practically independent of  $a$  for any fixed value of  $a$  near the absolute minimum, and vice versa, meaning that the two parameters are not correlated.

This is in contrast to standard FCS, where the minimum of the  $\chi_r^2$  plot has a shape of an almost diagonal line, meaning that  $D$  and  $a$  are fully correlated. For every value of  $a$  a value of

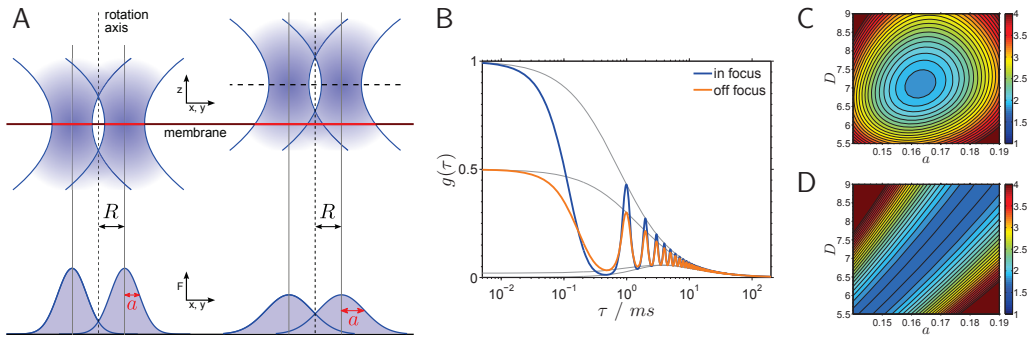


Fig. 1. The principle of circular scanning FCS on a 2D surface (membrane). A: The position of the objective focal plane with respect to the membrane plane affects not only the size  $a$  of the illuminated area on the membrane (the measurement volume  $V_{eff}$ ), but also the volume (area) overlap between any two different beam positions (here shown for the maximum possible distance, the scan circle diameter  $2R$ ). Left: the membrane coincides with the objective focus; Right: the membrane is below the objective focus. B: The axial displacement of the membrane away from the focus influences the autocorrelation in a complex way, changing not only the amplitude  $g(0)$  and the diffusion time  $\tau_D$ , but also affecting the shape of the correlation peaks. The distinct ways of how variations in  $D$  and  $a$  affect the correlation allows the determination of the diffusion coefficient  $D$  and the volume size  $a$  from a single autocorrelation curve. C: The  $\chi_r^2$  map as a function of  $D$  and  $a$  with a single minimum calculated from an experimental sFCS curve, demonstrating that  $D$  and  $a$  are uncorrelated. D: The  $\chi_r^2$  map for a standard FCS curve with a minimum for all values of  $D$  where  $D = a^2/\tau_D$ , showing that  $D$  and  $a$  are fully correlated.

$D$  globally minimizing  $\chi_r^2$  exists, and vice versa, as determined by the combination of the two parameters in the diffusion time  $\tau_D$  (Eq. (5), Fig. 1(D)).

The fact that the fit to sFCS data yields also the size of the illuminated area, parametrized by  $a$ , allows us to calculate the absolute surface concentration  $c$  of the diffusing molecules from the autocorrelation amplitude  $g(0)$ , using Eq. (4):

$$c = \frac{1}{g(0)V_{eff}} = \frac{1}{4\pi a^2 g(0)}. \quad (6)$$

The term accounting for triplet-induced fluctuations [25] was not included in the model, as the characteristic time of these fluctuations ( $< 10 \mu s$ ) is much shorter than the typical diffusion times of lipids and proteins in membranes ( $> 1 ms$ ), and low excitation intensities were used, leading to low population of triplet states.

### 3. Materials and methods

#### 3.1. Experimental setup

The experimental setup is almost identical with a standard FCS instrument (Fig. 2(A)): an expanded collimated laser beam fills the back aperture of the objective and is focused in the objective focal plane. The back-emitted fluorescence is collected and collimated by the same objective, reflected by a dichroic beamsplitter and focused onto an optical fibre, which serves as a confocal pinhole and guides the light to the detector. The scanning capability is achieved by replacing the last fixed mirror before the objective by a two-axis piezo scanner with a mounted circular mirror. Because of the short distance to the objective and small deflection angles, the

beam displacement on the back objective aperture is less than 0.1 mm and no additional relay lenses between the scanner and the objective are needed.

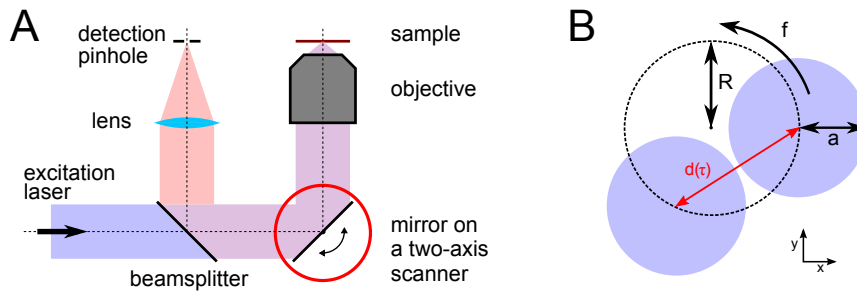


Fig. 2. The experimental setup for scanning FCS. A: The standard FCS setup is modified by mounting the last mirror before the back objective entry onto a two-axis piezo scanner. B: The scanner is used to move the beam uniformly, with a known frequency  $f$ , in a circle of radius  $R$  comparable to the size  $a$  of the focused beam. The distance  $d$  between two focus positions separated by a lag time  $\tau$  varies between 0 and  $2R$ , and is uniquely determined by the relation  $d = 2R \sin(\pi f \tau)$ .

For excitation, a diode laser emitting at 488 nm (Sapphire 488-20, Coherent, Santa Clara, USA) was used. The emitted light was separated from the excitation by a beamsplitter with a reflection edge at 495 nm, and further passed through an emission filter 525/50 nm. The axial position of the objective (Olympus UPLAPO 60 $\times$  W/IR) was controlled by a piezo objective scanner (P-721.10, PhysikInstrumente, Karlsruhe, Germany). The 100  $\mu\text{m}$ -diameter optical fibre end functions as a rather large confocal pinhole, given the overall magnification of 53 $\times$ . The fluorescence was detected with an avalanche photodiode (APD) (SPCM-AQR, PerkinElmer, Waltham, Massachusetts, USA). The raw data (photoncount sequence with temporal resolution of 17 ns) were recorded with a correlator (Flex02-12D, Correlator.com, Bridgewater, USA) for further correlation analysis.

The scanning mirror was not synchronized with the fluorescence detection by the correlator, as synchronization is not necessary for the presented scanning FCS application. This simplifies the technical implementation of the method. Nevertheless, if required, synchronization can be realized by using a commonly available data acquisition card containing analog outputs for scanner control and counter inputs for fluorescence detection.

The two-axis piezo scanner (S-330.2SL, PhysikInstrumente, Karlsruhe, Germany) has a limited, but for our purpose fully sufficient, optical deflection range of 4 mrad. This translates to approx. 7.5  $\mu\text{m}$  and 11  $\mu\text{m}$  within the objective focal plane for the two axes. The factor of approx.  $\sqrt{2}$  follows from the geometry of the optical path, where the beam hits the scanner mirror at 90 $^\circ$ .

For the sFCS application an accurate calibration of the scan radius at the used frequency is very important. At low frequencies, where the scanner follows the driving signal, the calibration was performed by using the light reflected off a Ronchi ruling with 600 line pairs/mm, as described previously for galvano scanners [20]. At scan frequencies reaching and exceeding hundred Hz the scanner does not follow the driving signal exactly, resulting in reduced scan radii. The radius reduction factor was determined by comparing the signal from the accurate internal scanner position sensor at high and low frequencies. The radius reduction factors range from 0.9 at 50 Hz to 0.4 at 200 Hz. For the experiments described here the actual scanning radius  $R$  was 0.385  $\mu\text{m}$ , the frequency  $f$  200 Hz, and the measurement time 100 s.

The scanner was fully controlled via a LabView program. In addition to circular scans, a raster scan mode was programmed, allowing to obtain a small image ( $7.5 \times 11 \mu\text{m}$ ) of the sample and to select a suitable position for the sFCS measurement. For this purpose the signal from the APD was split between a correlator and a counter card (PCI-6602, National Instruments, Austin, Texas, USA) which was synchronized with the scanner and provided the pixel brightness values for the resulting image.

### 3.2. Data analysis

The autocorrelation functions were calculated from the raw data using the multiple-tau algorithm with increased resolution ( $m = 64$ ), as described previously [20]. The data fitting was implemented in Matlab (Natic, USA); the model function was Eq. (4) with an additional offset parameter. The scan radius  $R$  and frequency  $f$  were always kept fixed to the known values, and the remaining parameters,  $D$ ,  $a$ , the autocorrelation amplitude  $g_0$  and an additive offset, were optimized by weighed nonlinear least-squares method (minimizing  $\chi_r^2$ ), with weights estimated from the data.

Non-uniformity of fluorescence along the scanned circle, caused, for example, by immobile bright objects located near one side of the scanned circle, can give rise to additional periodic pattern in the autocorrelation. This feature can be used to identify immobilized particles [19]. In our case these fluctuations were undesirable, and were therefore filtered out by a procedure described before [15]. In the majority of cases the non-uniformity in the data was very weak resulting in negligible difference when the filtering procedure was applied.

### 3.3. Sample preparation

The phospholipid 1,2-dioleoyl-*sn*-glycero-3-phosphocholine (DOPC) was purchased from Avanti Polar Lipids (Alabaster, USA), the dyes 3,3'-dioctadecyloxycarbocyanine perchlorate (DiO) and cholesteryl 4,4-difluoro-5,7-dimethyl-4-bora-3a,4a-diaza-*s*-indacene-3-dodecanoate (Bodipy-Chol) from Molecular Probes (Eugene, USA).

For the preparation of SLBs, chloroform solution of DOPC with  $3 \times 10^{-5}$  fraction of the dye was evaporated in a glass vial; then buffer (10 mM HEPES, 150 mM NaCl, pH=7.4) was added, the mixture was vortexed and sonicated until it became clear, resulting in a solution of small unilamellar vesicles (SUV). A small amount of the SUV solution was pipetted onto freshly cleaved mica attached to a coverslip, and  $\text{CaCl}_2$  at final concentration of 3 mM was added, causing the SUVs to burst. After 30 min. of incubation the solution was gently washed multiple times, resulting in a single bilayer on the mica surface [26].

The GUVs were prepared by the electroformation method on Pt wires [27, 28]. The solution of DOPC in chloroform containing  $5 \times 10^{-5}$  Bodipy-Chol or DiO ( $3 \mu\text{l}$ ) was pipetted onto Pt electrodes in a custom-made teflon chamber and the solvent was left to evaporate. Then the chamber was filled with 150 mM sucrose solution and voltage of 2 V at 10 Hz was applied for 30 min. to form GUVs. The GUVs were gently pipetted into 100 mM glucose solution in an observation chamber. The osmolarity difference tensed the GUVs and minimized the membrane thermal fluctuations; the difference in density of the inner and outer solutions made the GUVs sink to the bottom of the observation chamber. The preparation and measurements were done at the temperature  $22^\circ\text{C}$ .

## 4. Results

### 4.1. Independence on axial positioning

As discussed in the Theory section, the relative positioning of the horizontal membrane and the objective focus defines the measurement volume  $a$  (Fig. 1(A)), and consequently influences

the shape of the measured autocorrelation function (Fig. 1(B)). Nevertheless, the parameters of interest, the diffusion coefficient  $D$  and the concentration  $c$  of the diffusing molecules, should be obtained from the fits independently of the axial membrane position. In order to demonstrate this property of sFCS, we performed measurements on the top pole of a GUV (DOPC with DiO) at different axial membrane positions relative to the laser focus (Fig. 3).

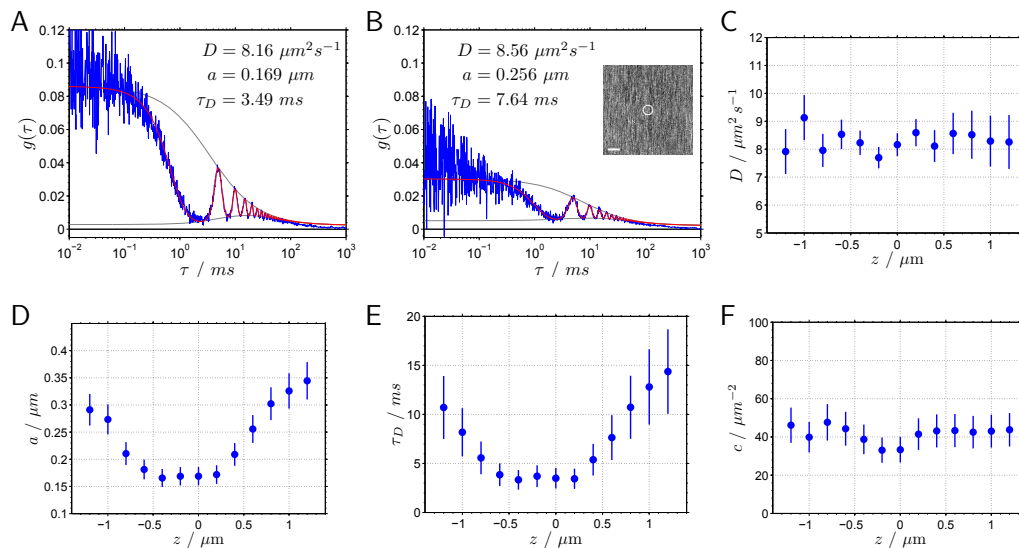


Fig. 3. The dependence of the autocorrelation curves and the fit parameters on the membrane position relative to the focal plane. The measurements with the membrane near the focal plane (A) and away from the focal plane (B) result in clearly different autocorrelations, with the fitting yielding different amplitudes  $g(0)$ , diffusion coefficients  $\tau_D$ , and volume sizes  $a$ , but equal diffusion coefficients  $D$ . A series of measurements at different axial positions results in diffusion coefficient (C) and concentration (F) practically independent of the axial position, and the volume size (D) and diffusion time (E) exhibit a clear minimum when the membrane coincides with the objective focal plane. The inset in B shows the top pole of the GUV with the circular scan path (scale bar  $1 \mu\text{m}$ ). The sample was a GUV prepared with DOPC and DiO.

Figures 3(A) and (B) compare two autocorrelation curves measured at two different axial positions: with the membrane located near the objective focal plane (Fig. 3(A)), and displaced by approx.  $0.6 \mu\text{m}$  away from the objective focus (Fig. 3(B)). As expected, the autocorrelation amplitude  $g(0)$  is lower when out of focus, as the measurement area, therefore also the number of molecules within it, increases. Fitting the data confirms the increase of  $a$  and consequently also of the diffusion time  $\tau_D$ , but, importantly, the diffusion coefficient does not change within the measurement precision.

Figures 3(C–F) summarize the results of a series of measurements at different axial positions where  $z$  varies in the range of  $2.4 \mu\text{m}$ . The diffusion coefficient determined from the fits is practically independent of the axial position within the probed distance of  $\pm 1.2 \mu\text{m}$  from the focal plane. As expected, the volume size  $a$  and the diffusion time  $\tau_D$  exhibit a clear minimum, corresponding to the situation where the objective focal plane and the membrane position coincide.

The concentration calculated with Eq. (6) is also independent of the axial position (Fig. 3(F)), although the precision is lower than in the case of diffusion coefficient. In general, the experi-

ments performed on GUVs and SLBs show that the autocorrelation amplitude is more sensitive to the shape of the measurement volume.

A set of standard FCS measurement analogous to those in Fig. 3 would produce only diffusion times (as in Fig. 3(E)) which cannot be converted to diffusion coefficients without knowing  $a$  for each measurement. The diffusion times vary by a factor of four, which would under an assumption of a constant  $a$  transform into a large variation of  $D$ , also by a factor of four (Eq. (5)). When the axial displacement  $z$  is well controlled, the set of measurements in Fig. 3(E) can be analyzed by the  $z$ -scan method [12]. However, for the  $z$ -scan method to be applicable, a whole series of measurements at different and well defined axial positions is necessary. The major advantage of sFCS is that any single measurement at any axial position provides the diffusion coefficient.

A range of measurements performed on the same GUV or on the same position of SLB exhibited small variations, with standard deviation of  $D$  in a single measurement typically below 5%. However, the variations between different GUVs, or different positions on SLB, were larger, especially in case of SLBs. The diffusion coefficient of Bodipy-Chol in DOPC SLB was found in the range 3.1–4.1  $\mu\text{m}^2\text{s}^{-1}$ , and of DiO in DOPC SLB 1.6–2.1  $\mu\text{m}^2\text{s}^{-1}$ . Bodipy-Chol in GUVs made of DOPC diffused with  $D=7.8\text{--}9.3 \mu\text{m}^2\text{s}^{-1}$ , and DiO with  $D=6.7\text{--}8.5 \mu\text{m}^2\text{s}^{-1}$ . The exact reason for these variations, lying within 20–30%, is not known; a possible explanation for SLBs is the spatial variations of the interaction between the membrane and the support. The obtained values of  $D$  are in general agreement with previous reports [7, 13, 29–31].

In some situations, depending on the intensity of the washing step in the SLB preparation, patches of a second bilayer on the top of the continuous bilayer on mica were observed. The fluorescence intensity of these patches was twice that of the surrounding membrane, and the diffusion coefficient for Bodipy-Chol in DOPC SLB was 5.3–5.8  $\mu\text{m}^2\text{s}^{-1}$ . This value represents an average of  $D$  in both bilayers, and, being closer to the diffusion coefficient in unsupported bilayer (GUV), suggests that the upper bilayer interacts much less with the support than the lower bilayer [30].

#### 4.2. Fitting range

The key parameter obtained from a standard FCS experiment is the diffusion time  $\tau_D$ , the time when the autocorrelation  $g(\tau)$  decreases to approximately one half of its initial value. In order to reliably determine this time from the data, the fitting time interval should be rather broad, covering at least a part of the curve close to its amplitude (short times) and the baseline (long times). This means a time interval at least two orders of magnitude wide.

The situation is different in sFCS, where the relative shapes of the peaks in the correlation function carry information about both the diffusion coefficient and the volume size, and a narrower fitting range is therefore sufficient. We investigated how a fitting range limited to a narrower interval ( $\tau_1, \tau_2$ ) affects the values of the obtained diffusion coefficient (Fig. 4).

A set of 20 measurements on a SLB (DOPC with Bodipy-Chol) was analyzed in a range of intervals where either the initial part of the autocorrelation was excluded: the upper bound was fixed at  $\tau_2 = 30$  ms and the lower bound ranged from 10  $\mu\text{s}$  to 20 ms (Fig. 4(C)), or where the tail of the autocorrelation was ignored: the lower bound was fixed at  $\tau_1 = 10 \mu\text{s}$  and the upper bound was varied from 5 ms to 300 ms (Fig. 4(D)).

In either case, the mean diffusion coefficient  $D$  and its variance are practically independent of both the width and the position of the fitting range. As Fig. 4(C) shows, even when the fitting range is as narrow as two periods of the scanner motion, from 10 ms to 30 ms, the diffusion coefficient and its variance are practically the same as when a much wider part of the autocorrelation is analyzed.

In order to compare the influence of the fitting range in scanning FCS with standard FCS, we

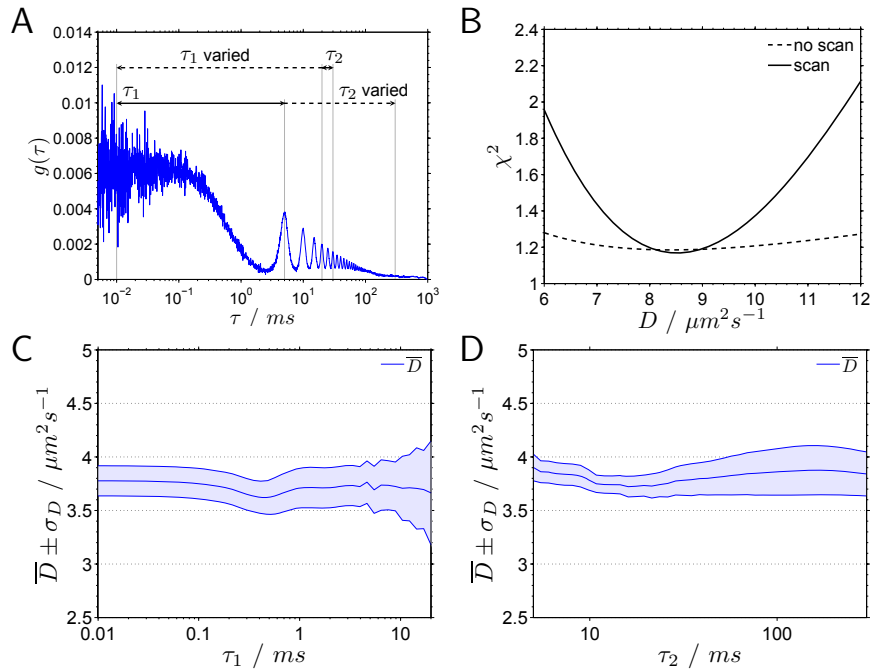


Fig. 4. The recovered diffusion coefficient is independent of the interval  $(\tau_1, \tau_2)$  in which the autocorrelation curve is analyzed. A: The range of intervals in which the data were analyzed had a variable lower bound  $\tau_1$  varying from 10  $\mu\text{s}$  to 20 ms and the upper bound  $\tau_2 = 30$  ms (C), or a fixed lower bound  $\tau_1 = 10$   $\mu\text{s}$  and a variable upper bound varying from 5 ms to 300 ms (D). The mean diffusion coefficient  $\bar{D}$  and its standard deviation  $\sigma_D$  calculated from 20 measurements are practically independent of the fitting range, both when the analysis is limited to either the short (C) or the longer (D) time scales. Sample: DOPC SLB with Bodipy-Chol. B: In circular scanning FCS, even a narrow fitting interval (2.5, 17.5) ms, that is, three scan periods, produces a deep, well defined minimum in  $\chi_r^2$ , sufficiently restricting the diffusion coefficient (solid line). In standard FCS, the same narrow fitting interval leads to a very shallow minimum and is not sufficient to constrain  $D$  (dashed line). Sample: DOPC GUV with Bodipy-Chol.

looked at the depth of the  $\chi_r^2$  minimum with respect to  $D$ . A deeper, more confined minimum of  $\chi_r^2$  means that the fitting result is better defined and less susceptible to noise. Figure 4(B) shows the  $\chi_r^2(D)$  profiles for measurements with and without scanning on a DOPC GUV with Bodipy-Chol. In both cases the fitting range was restricted to three scan periods, from 2.5 ms to 17.5 ms. The sFCS curve was fitted with  $a$  as a free parameter, the standard FCS curve was fitted with  $a$  fixed to 0.165  $\mu\text{m}$ , a value returned from the sFCS fit at  $\chi_r^2$  minimum. While the  $\chi_r^2$  minimum of the sFCS data is well confined, allowing a robust fit, the minimum of the standard FCS data is very shallow, leading to a large spread of  $D$  values.

These results demonstrate an important advantage of circular sFCS over standard FCS: the possibility to restrict the analysis to only a narrow range of correlation times allows us to exclude the parts of the autocorrelation affected by undesirable processes from analysis and still obtain reliable results. For example, one may wish to ignore the early part of the correlation when the effects of the dye photophysics (triplet transitions [25]) or chemical reactions (protonation/deprotonation of fluorescent proteins [32, 33], photoisomerization [34]) become apparent, or simply when the noise at the short lag times is too high. On the other hand, the tail of the

autocorrelation may become affected by slow fluctuations, such as slow sample drifts or slow dye depletion due to photobleaching within a confined region [35]. The restriction of the fitting range in such situations may be preferable to including the processes other than diffusion into the fitting model, and in doing so increasing the number of variable parameters.

In the following section we show two examples of long-range fluctuations that can often be encountered in practice, where sFCS yields correct diffusion coefficients while the standard FCS measurements are difficult to interpret.

#### 4.3. Robustness to slow axial drift

Slow axial drift of the membrane relative to the focal plane during the measurement can lead to two effects: First, the average fluorescence intensity changes as the membrane passes through the center of the measurement volume towards its upper or lower side. This usually becomes apparent in the autocorrelation as additional decay or rise at long times and as an overall offset. Second, the measurement volume  $a$  determined by the cross-section of the membrane and the focal plane continuously changes (Fig. 1(A)), influencing in a corresponding way also the diffusion time and the average number of molecules in the volume.

While the influence of the first effect on the fit results may be eliminated by excluding the long-time part of the autocorrelation from the fit, as shown in the previous section, the change of  $a$  during the measurement influences the autocorrelation at all lag times  $\tau$ , and therefore requires more attention. We note that in standard FCS the change of  $a$  during the measurement renders any previous calibration of  $a$ , if possible at all, invalid, making a subsequent conversion of the diffusion time  $\tau_D$  into the diffusion coefficient  $D$  using Eq. (5) highly inaccurate.

In order to investigate the effects of slow axial drift in sFCS, we first generated autocorrelation curves with the volume size  $a$  varying uniformly in the range  $(a_0, a_0 + \Delta a)$  mimicking the volume change during the drift. Then, we added noise, and fitted the curves to Eq. (4). A series of curves with different  $\Delta a$  was generated. As the smallest value of  $a$  we chose  $0.12 \mu\text{m}$  and the range width  $\Delta a$  was varied from 0, corresponding to a fixed position, to  $0.28 \mu\text{m}$ , representing the largest drift.

The main result of these calculations, summarized in Fig. 5(A), is that the axial drift has a minimal effect on the diffusion coefficient obtained from the fit. The diffusion coefficient increased slightly with  $\Delta a$ , but the deviation from the true value remained below 3%. The single value of the volume size  $a$  obtained from fitting lies not far from the center of the interval  $(a_0, a_0 + \Delta a)$ , as might be expected. The relative concentration  $c$ , calculated from the fitted autocorrelation amplitude  $g(0)$  and  $a$ , also increased with  $\Delta a$ , deviating by 10% from the true value at the largest  $\Delta a$ . The fit quality decreased for broader drift ranges, and the relative deviations of  $D$  and  $c$  depended somewhat on the chosen fitting range, however, not exceeding 6% for  $D$  and 45% for  $c$  in the worst case. While the diffusion coefficient determined with sFCS is minimally sensitive to the axial drift, the concentration is more strongly affected.

The effective diffusion time, calculated from the  $D$  and  $a$  values shown in Fig. 5(A), increases with  $\Delta a$  by a factor of up to three. Analogous calculations without scanning revealed a similar increase of  $\tau_D$ . If a constant  $a$  is assumed, these large variations of  $\tau_D$  with different drift ranges  $\Delta a$  translate into a variations of  $D$  also by a factor of three, a stark contrast to several per cent in sFCS.

In order to experimentally test the robustness of sFCS to axial drift revealed by these calculations, we performed sFCS measurements while moving the SLB (DOPC with Bodipy-Chol) uniformly through the measurement volume. The axial range covered during the measurement time of 100 s was  $\Delta z = 1.8 \mu\text{m}$ . The autocorrelations measured both with and without circular scanning exhibit a large offset (Fig. 5(B)) and do not decay to a constant value at long lag times due to the slow changes in the mean fluorescence caused by the drift in and out of the

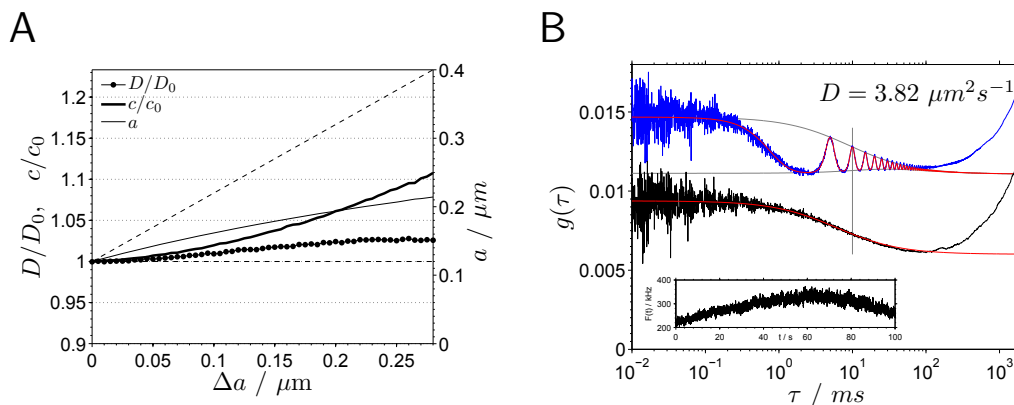


Fig. 5. A slow axial drift has a minimal effect on the sFCS results. A: relative diffusion coefficients  $D/D_0$ , relative concentrations  $c/c_0$ , and volume sizes  $a$  obtained from fits of simulated data; where the actual volume size parameter  $a$  continuously varied in the range  $(0.12, 0.12 + \Delta a) \mu\text{m}$ . The model parameters:  $D = 5 \mu\text{m}^2\text{s}^{-1}$ ,  $a_0 = 0.12 \mu\text{m}$ ,  $f = 200 \text{ Hz}$ ,  $R = 0.4 \mu\text{m}$ . The dashed lines indicate the range of volume sizes  $a$  covered by a given value  $\Delta a$ . B: Experimental autocorrelation curves with (blue) and without (black) circular scanning, where the objective focal plane was moved during the measurement uniformly along the optical axis by  $1.8 \mu\text{m}$ , passing through the membrane. Both curves were fit in the range  $(0.01, 10) \text{ ms}$ . The curve obtained without scanning was shifted down by  $\Delta g(0) = 0.004$  for clarity. The inset shows the fluorescence intensity  $F(t)$  during the measurement.

focal plane (Fig. 5(B), inset). Nevertheless, the fit to the initial part of the sFCS autocorrelation returns the correct diffusion coefficient  $D = 3.8 \mu\text{m}^2\text{s}^{-1}$ . If the value of  $a$  from the sFCS fit is used to calculate the diffusion coefficient from the fit to the standard FCS data, a too high value of  $D = 5.7 \mu\text{m}^2\text{s}^{-1}$  is obtained.

These calculations and experiments show that slow drifts that change the size of the measurement volume, as well as the average fluorescence, on the time scales much slower than diffusion times, practically do not affect the diffusion coefficients obtained from fitting. The sFCS method is therefore robust to slow drifts.

#### 4.4. Robustness to membrane fluctuations

Free-standing membranes in model systems, such as GUVs or flat membranes formed across apertures, as well as cell membranes, can exhibit thermal fluctuations on the time scales approaching those of diffusion [11, 36, 37]. The amplitude and time-scale of these fluctuations depends on the membrane tension, bending rigidity and the parameters of the surrounding medium. The presence of any structures providing support, for example, the cytoskeleton in cells, may efficiently dampen or suppress the membrane fluctuations.

In order to investigate how the fast axial fluctuations affect the sFCS measurements, we used a steady SLB and mimicked the membrane fluctuations by moving the objective axially with respect to the SLB by an objective piezo scanner. The objective scanner was programmed to perform a random walk in a potential centered around the membrane plane. The choice of the axial range within which the objective moved, the average step size and the time per step allowed us to control the amplitude and time-scale of the fluctuations.

Figure 6(A) compares the autocorrelations without and with the axial fluctuations, measured without circular scanning. The axial fluctuations are reflected in the autocorrelation as an ad-

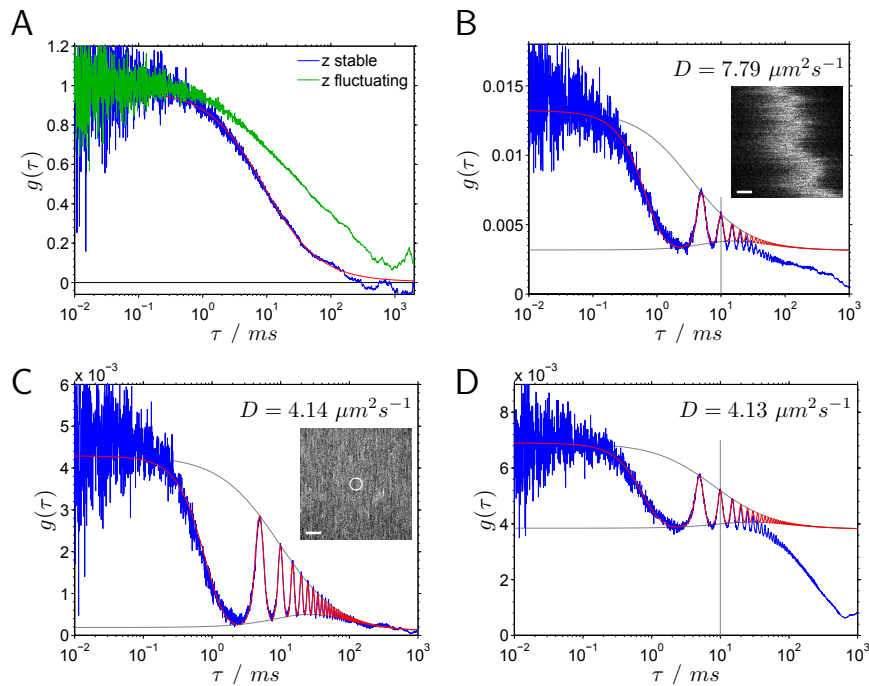


Fig. 6. The effect of membrane fluctuations on the sFCS results. Without circular scanning (A), and in the presence of axial fluctuations the autocorrelation curve (green) deviates significantly from the curve measured in the absence of axial fluctuations (blue), and cannot be described by a simple diffusion model. With circular scanning (C and D), the autocorrelation with axial fluctuations (D) still deviates from that without fluctuations (C), however, a fit of the initial part of the curve in the interval (0.01, 10) ms yields the same diffusion coefficient as obtained when the fluctuations are absent. The inset in C: SLB with the circular scan path. The inset in B: A measurement performed on the top pole of a fluctuating GUV with a fit of the initial part of the curve yields the expected diffusion coefficient (DOPC with DiO). The inset shows the GUV fluctuations (scale bars: 1  $\mu\text{m}$ ).

ditional correlation feature at longer times, making it difficult to fit the data and to reliably determine the diffusion time, and therefore the diffusion coefficient.

Since the axial fluctuations affect the correlation predominantly at longer times, we analyzed the sFCS autocorrelation curves at shorter correlation times, where the interference of the membrane fluctuations is expected to be minimal. Fitting the curves in the range 0.01–10 ms gives identical diffusion coefficients in absence and presence of axial fluctuations, as shown in Fig. 6(C–D). This demonstrates that sFCS is robust to the effects of membrane fluctuations on the correlation experiments.

The condition for this robust property of sFCS is that there is a range of correlation times where the fluctuations due to diffusion dominate, and where the fluctuations due to other effects can be neglected. This is the case of thermal fluctuations in membranes. The fluctuations in GUVs can be decomposed into modes with distinct amplitudes and relaxation times [38]. The mode amplitude and the relaxation time decreases with the mode number, therefore the effect of the thermal fluctuations at short correlation times, corresponding to short relaxation times of membrane fluctuations, is lower.

To test the sFCS performance on a membrane exhibiting thermal fluctuations, we prepared

GUVs that were not tensed by the osmolarity difference of the inside and outside solutions. These GUVs were fluctuating, as shown in the inset of Fig. 6(B), where the objective focus was positioned few  $\mu\text{m}$  below the top pole of the vesicle. The sFCS autocorrelation reflects these fluctuations as an additional correlation decrease in the range of hundred of ms, and an offset. Limiting the fit of the sFCS curve to the lag times below 10 ms yields the correct diffusion coefficient, as it did in the case of the artificially driven objective oscillations described above.

## 5. Discussion and conclusion

The presented circular sFCS applied to membranes is shown to possess two major advantages compared to standard FCS, both particularly important from the point of practical applications. First, the size of the measurement area need not be known for analysis, meaning that the results are not sensitive to the positioning of the membrane with respect to the focus. Second, the method is robust to disturbances occurring on time scales other than diffusion, since the analysis of the autocorrelation can be safely restricted to a narrow interval of correlation times.

The implementation of sFCS in this work is based on a single modification of a basic FCS setup: replacement of a fixed mirror by a mirror mounted on a scanner. A simple upgrade of an existing FCS instrument is therefore straightforward, without an increase in complexity required for other advanced FCS methods exploiting the benefits of spatio-temporal correlation, for example, the use of pulsed excitation or additional light polarization control [14, 39]. The method does not require any synchronization between excitation and detection, therefore the raw data processing is straightforward as in standard FCS. The autocorrelation is directly calculated using existing algorithms, no pre-sorting or aligning of the data, as in line scan methods, is necessary.

Another way to implement circular sFCS is, as shown previously [19, 20, 40], to include the option of a circular scan in an existing confocal laser scanning microscope with FCS capability. This requires only a software modification, as the optical and detection part is identical to a standard FCS, and the galvo scanners typically employed in home-built or commercial confocal scanning microscopes are capable of scanning along the required circular path.

As the technique differs from standard FCS only by addition of the circular motion, the usual performance indicators are not affected. In particular, the molecular brightness, in terms of photon counts per molecule per second, which determines the signal-to-noise ratio, remains the same as without scanning. The necessary measurement times stay in the range from tens of seconds to a few minutes; here 100 s were used for all presented results.

The particular piezo scanner used here is approximately 5 times slower than commonly used galvo scanners [20], with its frequency range limited to several hundreds of Hz. This sets a practical upper limit on the diffusion coefficient that can be measured to around  $100 \mu\text{m}^2\text{s}^{-1}$ . This is fully sufficient for diffusion in phospholipid membranes, or for bulk 3D diffusion of molecules as small as GFP. The range of diffusion coefficients of several hundred  $\mu\text{m}^2\text{s}^{-1}$ , characteristic for smaller molecules in bulk aqueous solution, can be reached with laser scanning microscopes, where the galvo scanners can operate at kHz frequencies.

Since the scanning radius is smaller than  $0.4 \mu\text{m}$ , the measurement is performed within a very small sample area. With the volume size with the parameter  $a$  equal to or larger than  $0.15 \mu\text{m}$ , the detected fluorescence in standard FCS originates predominantly from within a circle of radius  $3a = 0.45 \mu\text{m}$ . With scanning FCS as used here, the probed area is larger only by a factor of approximately 4 (radius of approx.  $0.85 \mu\text{m}$ ). It is therefore not necessary to have a sample with a large flat homogeneous region to scan over as in other sFCS methods, or FRAP experiments. This is important for potential applications on membranes with small domains of different phases or composition, or measurements on cellular surfaces, where it may be difficult to find a large area of horizontal homogeneous membrane. Domains smaller than the laser spot

(lipid rafts) are averaged over in the same way in both standard and scanning FCS. In order to gain access to smaller spatial scales, where the presence of sub-resolution lipid domains could be detected, combination of the presented method with superresolution FCS (STED-FCS [41]) could be considered. This would require reduction of the scanning radius by the same factor by which the measurement volume size is reduced, leading to a scanned area larger than the static measurement volume by a similar factor ( $\sim 4$ ) as in the presented implementation.

An attractive possibility is the direct extension of sFCS to two colour cross-correlation measurements on surfaces, a method that allows the quantification of binding interactions between molecules labeled with different dyes [8, 9]. An important benefit of sFCS would be the knowledge of the size of both measurement volumes  $a_1$  and  $a_2$ , which are in general different due to their dependence on wavelength. Of interest is usually the fraction  $f_2$  of interacting molecules:  $f_2 = c_{12}/(c_2 + c_{12})$ , where  $c_1, c_2, c_{12}$  are the concentrations of species with either of the two or both labels. It can be determined from the experimental ratio of the cross-correlation  $g_{12}(0)$  and autocorrelation  $g_i(0) = 1/(4\pi a_i^2 (c_i + c_{12}))$  amplitudes, taking into account the different sizes  $a_1$  and  $a_2$  of the two concentric areas/volumes (Eq. (7)):

$$\frac{g_{12}(0)}{g_1(0)} = \frac{2a_1^2}{a_1^2 + a_2^2} \frac{c_{12}}{c_2 + c_{12}} \quad (7)$$

The knowledge of  $a_1$  and  $a_2$  would then allow us to avoid the usually made assumption that  $a_1 = a_2$  [35], and to accommodate the different volume sizes in the interpretation of the auto- and cross- correlation amplitudes [8], leading to better quantitative estimates of the interacting fraction of molecules.

The circular sFCS method is also applicable to diffusion measurements in three dimensions, as shown previously with a laser scanning microscope using two-photon excitation [20]. Here, a careful attention must be paid to using an appropriate model for the measurement volume and therefore the autocorrelation function, as the simple 3D gaussian model is not sufficiently accurate to describe the combined effects of excitation beam and detection pinhole in spatio-temporal correlation experiments [14].

The simplicity of the presented method compared to other spatio-temporal fluorescence correlation techniques, and its robustness to various disturbing effects makes it particularly suitable for quantitative characterization of dynamical behaviour and interactions of molecules in membranes and other planar systems.

## Acknowledgements

We would like to thank Jens Ehrig, Christoph Herold and Le Mu for assistance with the sample preparation. This work was supported by the EU (FP7-216027).

## A6

### **Photobleaching in two-photon scanning fluorescence correlation spectroscopy**

Z. Petrášek and P. Schwille

*ChemPhysChem*, 9:147–158, 2008.



DOI: 10.1002/cphc.200700579

# Photobleaching in Two-Photon Scanning Fluorescence Correlation Spectroscopy

Zdeněk Petrášek\* and Petra Schwille<sup>[a]</sup>

Two-photon excitation in fluorescence correlation spectroscopy (FCS) is often preferred to one-photon excitation because of reduced bulk photobleaching and photodamage, and deeper penetration into scattering media, such as thick biological specimens. Two-photon FCS, however, suffers from lower signal-to-noise ratios which are directly related to the lower molecular brightness achieved. We compare standard FCS with a fixed measurement volume with scanning FCS, where the measurement volume is scanned along a circular path. The experimental results show that photobleaching is the dominant cause of the effects observed at the high excitation powers necessary for good signal-to-noise ratios. Theoretical calculations assuming a non-

uniform excitation intensity profile, and using the concept of generalized volume contrast, provide an explanation for the photobleaching effects commonly observed in two-photon FCS at high excitation intensities, without having to assume optical saturation. Scanning alleviates these effects by spreading the photobleaching dose over a larger area, thereby reducing the depletion of fluorescent molecules in the measurement volume. These results, which facilitate understanding of the photobleaching in FCS and of the positive effects of scanning, are particularly important in studies involving the autocorrelation amplitude  $g(0)$ , such as concentration measurements or binding studies using fluorescence cross-correlation between two labeled species.

## Introduction

Fluorescence correlation spectroscopy (FCS) is an optical technique that analyzes fluctuations of the fluorescence signal originating from a small number of molecules within a femtoliter-sized volume, to obtain information about the composition and dynamics of the investigated microscopic system.<sup>[1–3]</sup> In the past decade there has been a large increase in FCS applications in the biological and biochemical sciences, mainly because of its high sensitivity, selectivity, and possibility of minimally invasive measurements within living cells and tissues.<sup>[4–6]</sup>

FCS can be implemented in many ways with respect to the mode of excitation (one- or two-photon), the measurement volume configuration ("open" volume, evanescent field-limited volume, spatially restricted micro- and nanostructures), the number of detection channels (spatially or spectrally separated), and the analysis of the data in terms of auto- or cross-correlation or higher orders of correlation, depending on the system investigated and the information required.<sup>[7,8]</sup> We are concerned with two-photon-excitation FCS applied to a system of molecules diffusing freely without spatial restrictions.

Two-photon excitation in a focus of a high-numerical-aperture (NA) objective results in sufficiently localized excitation due to the quadratic dependence of the excitation probability on the light intensity.<sup>[9]</sup> A direct consequence of this fact is that no pinhole is needed to create a confined measurement volume, as required with one-photon excitation, which results in technically simpler implementation. Other additional advantages with respect to the sample are deeper penetration in the scattering specimen, lower phototoxicity, the possibility to excite two dyes with one wavelength for cross-correlation measurements,<sup>[10–12]</sup> and significantly lower photobleaching outside the focus, thus making longer or multiple measure-

ments in one part of the sample possible.<sup>[13]</sup> However, FCS with two-photon excitation is known to suffer from lower signal-to-noise (S/N) ratios compared to one-photon excitation, an effect usually attributed to stronger photobleaching in the laser focus, and to saturation effects due to high excitation intensities and pulsed excitation.<sup>[14,15]</sup> This fact poses certain limitations on the applicability of two-photon FCS, and is the motivation for this study.

Photobleaching, a severe limiting factor of two-photon excitation, has been investigated in the past, both in relation to two-photon microscopy<sup>[16]</sup> and FCS.<sup>[14,17–19]</sup> It was found to depend on the second, third, or even higher powers of the excitation intensity, depending on the fluorophore, and is likely to be mediated via higher singlet or triplet states leading to the creation of reactive species, as shown by experiments with addition of radical quenchers.<sup>[14]</sup> Photobleaching is reflected in FCS by shortening of diffusion times, change of the autocorrelation amplitude and shape, and decrease of the maximum achievable brightness.<sup>[12,20]</sup> Photobleaching effects on FCS are difficult to quantify. They are thought to appear together with saturation effects, further complicating the theoretical description, although saturation alone is better accessible to theoretical treatment.<sup>[15,21,22]</sup>

[a] Dr. Z. Petrášek, Prof. Dr. P. Schwille  
Biophysics Group, Biotechnologisches Zentrum  
Technische Universität Dresden  
Tatzberg 47-51, 01307 Dresden (Germany)  
Fax: (+49) (0)351 463 40342  
E-mail: zdenek.petrasek@biotec.tu-dresden.de

Supporting information for this article is available on the WWW under <http://www.chemphyschem.org> or from the author.

As all the information about fast-diffusing molecules in FCS is extracted from the fluorescence emitted while the molecule passes through the measurement volume, the S/N ratio is largely determined by the number of photons detected during a typical transit. It has been shown theoretically that the crucial parameter on which S/N ratio in FCS depends is the "molecular brightness"  $\eta$ —the number of photons detected per particle per unit of time.<sup>[23,24]</sup> Higher  $\eta$  values can be achieved by increasing the excitation intensity, but at some point a limit is reached where the data become distorted by bleaching, saturation, and possibly other effects.<sup>[14,20,25]</sup> This limit of maximum achievable brightness for a given fluorophore was shown to be significantly lower with two-photon than one-photon excitation, thus leading to lower S/N ratios. Therefore, it is important to gain deeper understanding of the role of photobleaching in FCS, and to find ways of reducing its negative effects. The reduction of photobleaching is particularly important for cellular applications, where the number of fluorophores available may be low because of low total numbers of investigated molecules or the necessity of weak labeling, and where individual molecules need to be followed for a longer time, for example, due to slow diffusion.

Scanning FCS (sFCS) is a modification of FCS in which the measurement volume is moved relative to the sample, in most cases by moving the excitation beam. It has been implemented in different configurations and used for various reasons, for example, to study slow diffusion<sup>[26–29]</sup> or immobile samples,<sup>[30]</sup> to perform simultaneous measurements at multiple locations or at different temporal scales,<sup>[31,32]</sup> or to measure diffusion, flow, and immobilization simultaneously.<sup>[33]</sup> Reduction of photobleaching effects with scanning has been reported<sup>[33]</sup> and utilized.<sup>[34–36]</sup> Satsoura et al.<sup>[37]</sup> investigated in detail how circular scanning reduces photobleaching in the case of one-photon excitation, by using the approximation of two-dimensional geometry, uniformly illuminated measurement volume, and a point sink model of photobleaching.

Herein, we investigate theoretically how photobleaching affects the autocorrelation amplitude  $g(0)$ . The numerical calculations, which take into account the position-dependent excitation intensity resulting in nonuniform stationary distribution of nonbleached molecules in the measurement area, predict the observed decrease of  $g(0)$  for the more realistic Gaussian–Lorentzian (GL) model of the measurement volume, and provide a qualitative explanation of the temporal profile of the autocorrelation curve distorted by photobleaching. The description utilizes the concept of volume contrast  $\gamma$  generalized by including the distribution of nonbleached molecules. The dimensionless  $\gamma$  is shown to be a parameter suitable for expressing the dependence of the autocorrelation amplitude and molecular brightness on the geometrical factors involved: the shape of the measurement profile and the spatially varying concentration of fluorescent molecules.

Comparison of FCS measurements with fixed measurement volume and volume scanned along a circular path provides evidence that photobleaching is the major factor limiting the performance of two-photon FCS quantified by molecular

brightness, and that optical saturation plays only a secondary role with the fluorophores used.

In accordance with previous reports, scanning is shown to reduce the artifacts due to photobleaching, thus making it possible to reach higher molecular brightness values within the quadratic dependence of fluorescence on the excitation intensity. Scanning alleviates the photobleaching effects by distributing the bleaching dose over a larger area, which is shown to reduce both the molecular depletion and the decrease of the volume contrast. By using scanning it is possible to achieve higher S/N ratios or to reduce the measurement times, both being important factors in *in vitro* screening and intracellular FCS/fluorescence cross-correlation spectroscopy applications, where the auto(cross-)correlation amplitudes are of importance.<sup>[10–12]</sup>

## Theory

FCS analyzes fluctuations of the fluorescence signal  $F(t)$ , which reflect some underlying physical process, typically diffusion, by means of autocorrelation function  $g(\tau)$  defined as [Eq. (1)]:

$$g(\tau) = \frac{\langle F(t)F(t+\tau) \rangle}{\langle F(t) \rangle^2} - 1. \quad (1)$$

The accuracy of measurements is limited by the S/N ratio. Experience and theoretical analysis have shown that the best S/N ratios in FCS are achieved when the amplitudes of fluctuations are large or comparable to the signal itself, which occurs when the number of molecules in the measurement volume is small.<sup>[24]</sup> This requires both low concentrations and small measurement volumes, with their minimum size and the freedom of choice of their shape limited by light diffraction. Another prerequisite for a high S/N ratio is high excitation intensities, often leading to undesired effects commonly attributed to photobleaching and saturation. To understand how photobleaching affects the measured autocorrelation, we investigate in detail the ways in which the geometry of the measurement volume and the nonuniform distribution of nonbleached molecules influence the fluorescence signal  $F(t)$  and its autocorrelation  $g(\tau)$ .

## Illumination, Excitation, and Measurement Profiles

The detected fluorescence  $F(t)$  depends on the concentration of the fluorescent molecules, the excitation efficiency and its spatial distribution across the measurement area, the fluorescence quantum yield of the fluorophore, and the detection efficiency, which is in general also spatially dependent. For the purpose of the calculations below it is common to define several quantities encompassing these factors. Thus, we define illumination profile  $W(\mathbf{r})$  with  $W(0) = 1$  as a dimensionless function describing the spatial distribution of the light intensity in the measurement area. The actual form of  $W(\mathbf{r})$  depends on the way the sample is illuminated (typically by a high-NA objective) and the approximation used,<sup>[38]</sup> and is described in more detail below.

The excitation profile  $E(\mathbf{r})$  is a normalized [ $E(0)=1$ ] function describing the spatial distribution of excitation efficiency. We are concerned with two-photon excitation where the excitation probability depends on the second power of the illumination intensity,  $E(\mathbf{r})=W^2(\mathbf{r})$ . In the case of one-photon excitation, the excitation profile is identical to the illumination profile  $E(\mathbf{r})=W(\mathbf{r})$ . Saturation effects, sometimes encountered at high excitation powers, can be described by a modified excitation profile  $E(\mathbf{r})$ .<sup>[15]</sup>

The spatial dependence of detection efficiency is typically described by a collection efficiency function  $CEF(\mathbf{r})$ . In the confocal detection scheme,  $CEF(\mathbf{r})$  is determined predominantly by the confocal pinhole introducing the desired decrease in detection efficiency in the axial dimension.<sup>[39,40]</sup> This additional spatial restriction of detection is not necessary when two-photon excitation is used, since the excitation alone is already sufficiently confined.<sup>[9]</sup> In the experimental setup used here no detection pinhole was used, and the active area of the detector was considerably larger than the magnified image of the excited volume. Therefore, it can be assumed that  $CEF(\mathbf{r})\equiv 1$ .

Finally, the combination of the excitation profile and the collection efficiency function defines the measurement profile  $S(\mathbf{r})=E(\mathbf{r})CEF(\mathbf{r})$ . In our case, only the excitation profile determines the measurement profile, therefore the relation  $S(\mathbf{r})=W^2(\mathbf{r})$  is used henceforth. The measurement profile includes all the geometrical factors of the measurement arrangement, and in simple words tells us how much fluorescence is detected from a given location  $\mathbf{r}$  (relative to the origin), assuming constant concentration of fluorescent molecules.

All the other, spatially independent factors influencing the fluorescence intensity  $F(t)$  (excitation intensity and detection efficiency considered in the center of the measurement volume, that is at  $\mathbf{r}=0$ , and fluorescence quantum yield) are contained in the molecular brightness  $\eta_0$ . Molecular brightness is the average fluorescence intensity (average number of photons) detected from the center of the measurement area at a constant concentration equal to one molecule per volume unit. A spatially dependent brightness  $\eta(\mathbf{r})$  can be assigned to molecules outside the center of the measurement area:  $\eta(\mathbf{r})=\eta_0S(\mathbf{r})$ .

The fluorescence  $F(t)$  in the definition of the autocorrelation function [Eq. (1)] is a time-dependent fluctuating signal, where the fluctuations are caused by diffusion of individual molecules and by the stochastic nature of light emission. The temporal average of the positions of diffusing molecules results in a stationary concentration of fluorescent molecules  $c(\mathbf{r})$  and stationary fluorescence  $F$  [Eq. (2)]:

$$F = \langle F(t) \rangle = \int \eta_0 S(\mathbf{r}) c(\mathbf{r}) d\mathbf{r} = \int \eta_0 W^2(\mathbf{r}) c(\mathbf{r}) d\mathbf{r} \quad (2)$$

It is natural to define the measurement volume  $V_0$  as [Eq. (3)]:

$$V_0 \equiv \int S(\mathbf{r}) d\mathbf{r} = \int W^2(\mathbf{r}) d\mathbf{r} \quad (3)$$

since in the most common case of constant concentration  $c(\mathbf{r})=c_0$  the fluorescence intensity is equivalent to the intensity

of  $N_0=c_0V_0$  molecules in volume  $V_0$ , each with brightness  $\eta_0$ :  $F=\eta_0c_0V_0$ .

### Models of Measurement Profiles

The illumination and measurement profiles are usually complicated functions due to the diffraction in high-NA objectives, and are therefore often approximated by analytical functions. Two models of illumination (measurement) profiles are commonly used in FCS: 3D Gaussian (3DG) [ $W_G(\mathbf{r})$ ], and GL [ $W_L(\mathbf{r})$ ]. The 3DG model has the following form [Eq. (4)]:

$$W_G(\mathbf{r}) = e^{-\left(\frac{x^2+y^2}{2a^2} + \frac{z^2}{2l\omega^2(z)}\right)} \quad (4)$$

where  $a$  describes the width of the illuminated area in the  $xy$  plane, perpendicular to the optical axis, and  $w$  is a dimensionless factor expressing the extension of the volume along the  $z$  axis ("form factor" or "structure parameter"), typically  $w=3-7$ .

The second model is GL  $W_L(\mathbf{r})$  [Eq. (5)]:

$$W_L(\mathbf{r}) = \frac{1}{\omega^2(z)} e^{-\frac{x^2+y^2}{2a^2\omega^2(z)}} \quad (5)$$

where  $\omega^2(z) = 1 + \left(\frac{z}{a}\right)^2 b^2$ ,  $a$  describes the width of the illuminated area in the  $xy$  plane at  $z=0$ , and  $\omega(z)$  its increase in both directions along the  $z$  axis. The parameter  $b$  depends on  $a$  and on the wavelength  $\lambda/n$  of the excitation light in the sample environment in the following way:  $b=\lambda/(4\pi na)$ .<sup>[15]</sup>

The more commonly used 3DG model leads to a mathematically simple expression for the autocorrelation function, and is characterized by a sharp fall-off in measurement efficiency in the axial direction. The GL model is more appropriate for our pinholeless experimental setup with two-photon excitation, since it more accurately describes the progressively broader lateral extension of the excitation volume with increasing axial distance from the focal plane, and respects the fact that the integrated intensity at every depth  $z$  is constant. This model was shown to provide a sufficiently good description of the excitation profile in comparison with the exact solution of beam propagation.<sup>[15]</sup>

### Autocorrelation Amplitude $g(0)$ and Volume Contrast $\gamma$

Here, we focus our attention on the amplitude of the autocorrelation function, that is, on the value  $g(\tau)$  as  $\tau$  approaches 0, further denoted as  $g(0)$ . In the following, we assume that the only sources of correlation in  $F(t)$  are the fluctuations of the particle number in the measurement volume, and that there are no contributions from other causes, for example, photo-physical processes, such as singlet-triplet transitions. Fluctuations caused by molecules being "trapped" in the triplet state for a relatively long time are commonly observed at moderate or high excitation powers with one-photon excitation,<sup>[25]</sup> but seem to be absent when two-photon excitation is used.<sup>[14,18,41]</sup>

It follows from the definition of  $g(\tau)$  [Eq. (1)] that in the absence of photobleaching the autocorrelation amplitude  $g(0)$  is

equal to [Eq. (6)]:

$$g(0) = \frac{\gamma_0}{c_0 V_0} = \frac{\gamma_0}{N_0} \quad (6)$$

where  $\gamma_0 = \frac{\int S^2(r) dr}{\int S(r) dr}$ , that is, the amplitude is inversely propor-

tional to the number of molecules  $N_0$  in the measurement area. The proportionality constant  $\gamma_0$ , sometimes referred to as "volume contrast",<sup>[19]</sup> is determined by the measurement geometry as expressed by  $S(r)$ , and reflects the confinement, localization, or sharpness of the boundaries of the measurement volume. High values of  $\gamma_0$  (with the maximum of 1) mean well-confined measurement volumes where most molecules contribute to the fluorescence signal with high brightness  $\eta(r)$ . Low values of  $\gamma_0$  reflect the fact that a considerable fraction of the fluorescence signal originates from molecules with low brightness, that is, molecules present at the tails of the measurement profile  $S(r)$ . Autocorrelation amplitudes lowered by weak confinement effects, as expressed by  $\gamma_0$ , result in a lower S/N ratio; therefore, high values of  $\gamma_0$  are desirable in FCS.

Volume contrast  $\gamma_0$  is often combined with the measurement volume  $V_0$  to define the effective measurement volume  $V_{\text{eff}} = V_0/\gamma_0$ . The autocorrelation amplitude is then equal to the inverse of the effective number of molecules  $N_{\text{eff}} = c_0 V_{\text{eff}}$  in the measurement volume. However, for the purpose of investigating the effects of photobleaching, we continue treating the measurement volume and the volume contrast separately.

Using Equations (3) and (6), the measurement volume  $V_0$  and the volume contrast  $\gamma_0$  for the GL and 3DG models are determined:  $V_0(\text{GL}) = \pi^2 a^3/b$ ,  $V_0(\text{3DG}) = \pi^{3/2} a^3 w$ ,  $\gamma_0(\text{GL}) = 3/16 = 0.1875$ , and  $\gamma_0(\text{3DG}) = 2^{-3/2} = 0.3536$ . The volume contrast of the GL profile is approximately two times smaller than that of the 3DG profile. This is a consequence of the slow decrease ( $\approx 1/z^4$ ) and broadening of the GL profile with the distance  $z$  from the focal plane compared with the steep exponential decrease of the more confined 3DG profile.

### Photobleaching

At high excitation intensities, the fluorescent molecules can, due to multiple excitations and interactions with other molecules, undergo photochemical reactions which renders them nonfluorescent, that is, they become irreversibly photobleached. The rate of photobleaching depends on the excitation intensity, and therefore on the immediate position of the molecule in the measurement volume. At a certain time after the beginning of illumination a stationary concentration  $c(r)$  is reached, where the depletion due to photobleaching is compensated by influx of nonbleached molecules due to diffusion. However, this is true only if the diffusion occurs in three dimensions, and if the total sample volume can be considered infinitely large compared to the measurement volume and therefore the supply of nonbleached molecules is infinite. If the diffusion is restricted to two dimensions (e.g. biomembranes), or if the total sample volume is relatively small, no sta-

tionary state is reached and all molecules are finally photobleached.<sup>[19,42,43]</sup>

The temporal development of the concentration of fluorescent (nonbleached) molecules  $c(r,t)$  can be obtained from the diffusion equation with an additional term that describes photobleaching [Eq. (7)]:

$$\frac{\partial c(r,t)}{\partial t} = D\Delta c(r,t) - k_b B(r)c(r,t) \quad (7)$$

where  $D$  is the diffusion coefficient,  $B(r)$  with  $B(0)=1$  is the bleaching profile, that is, the spatial distribution of the bleaching rate, and  $k_b$  is the actual bleaching rate at maximum ( $r=0$ ).

We assume infinite sample volume with unrestricted 3D diffusion, therefore after a certain time a stationary state is reached where the concentration of nonbleached molecules becomes time-independent:  $\frac{\partial c(r,t)}{\partial t} = 0$ ,  $c(r,t) \rightarrow c(r)$ . The stationary concentration  $c(r)$  is then obtained from the modified Equation (7) [Eq. (8)]:

$$\Delta c(r) - k_b B(r)c(r) = 0 \quad (8)$$

where transformation to dimensionless cylindrical coordinates  $r \rightarrow \rho$ ,  $[r=a, \rho(r,z)=(a\rho, a\zeta)]$  is applied. The dimensionless bleaching parameter  $k = k_b a^2/D$  expresses the relative "strength" of bleaching compared to diffusion, and determines the stationary concentration of nonbleached and bleached molecules.

For the purpose of further calculations we define the normalized concentration profile  $c'(\rho) = c(\rho)/c_0$ . The profile  $c'(\rho)$  approaches 1 at infinity and in the absence of photobleaching, and lies between 0 and 1 in other cases. Once the concentration profile  $c'(\rho)$  is known from the solution of Equation (8), the stationary fluorescence  $F$  and the autocorrelation amplitude  $g(0)$  can be determined. Using Equation (2) the fluorescence  $F$  can be written as  $F = \eta_0 c_0 V$ , where  $V$  is defined in analogy to Equation (3) [Eq. (9)]:

$$V = \int c'(\rho) S(\rho) d\rho \quad (9)$$

The fluorescence  $F$ , the measurement volume  $V$ , and the number of molecules  $N = c_0 V$  are smaller in the presence of photobleaching than without photobleaching, where  $c'(\rho) = 1$  and  $V = V_0$ ,  $N = N_0$ . The smaller number of fluorescent molecules  $N$  in the measurement volume may infer that photobleaching always leads to an increase of the autocorrelation amplitude. However, the autocorrelation amplitude  $g(0)$  [Eq. (10)]:

$$g(0) = \frac{\gamma}{c_0 V} = \frac{\gamma}{N} \quad (10)$$

depends also on the volume contrast  $\gamma$  (or the effective volume  $V_{\text{eff}}$ ), which is also affected by photobleaching. The volume contrast is determined from Equations (1) and (10),

where in this case the concentration profile  $c'(\rho)$  becomes a weighting factor in the ensemble averages [Eq. (11)]:

$$\gamma = \frac{\int c'(\rho) S^2(\rho) d\rho}{\int c'(\rho) S(\rho) d\rho} \quad (11)$$

It is not immediately obvious from Equation (11) how  $\gamma$ , and therefore also  $g(0)$ , depends on photobleaching characterized by the bleaching parameter  $k$  and the nonuniform concentration profile  $c'(\rho)$ .

To determine the dependence of  $F$ ,  $\gamma$ , and  $g(0)$  on the photobleaching parameter  $k$ , we have solved Equation (8) numerically for the two considered models, GL and 3DG, and obtained  $c'(\rho)$ .  $F$ ,  $\gamma$ , and  $g(0)$  were then calculated from Equations (9), (11), and (10), respectively, assuming  $\eta_0 = c_0 = 1$ . We presume that the photobleaching rate depends on the third power of the illumination intensity,<sup>[14,18]</sup> and therefore set  $B(\rho) = W^3(\rho)$  in Equation (8). Figure 1 shows plots of the calculated concentration profiles  $c'(\rho)$  and fluorescence profiles  $F(\rho) = \eta_0 c_0 c'(\rho) S(\rho)$  scaled to 1 at their maximum for GL and 3DG models in cylindrical coordinates  $(\rho, \zeta)$  for two values of  $k$ :  $k = 10$  and 100 (see also the figure in the Supporting Information). The initially constant concentration  $c'(\rho)$  decreases with  $k$  in the place of the highest intensity until the fluorescent molecules become depleted. With stronger photobleaching the size of the depleted zone becomes larger. The largest amount of fluorescence is generated from the edges of the depleted zone in which the highest overlap between the measurement and the concentration profiles occurs.

Although this general behavior is common to both investigated models, the fluorescence distributions are significantly different. While in the GL model the points of highest fluorescence intensity are concentrated around the focal plane ( $\zeta = 0$ ) with progressively delocalized fluorescence away from the focal plane, the fluorescence in the 3DG model is rather confined with maxima lying off the focal plane on the vertical axis. Both the measurement volume  $V$  and the volume contrast  $\gamma$  decrease with  $k$  in both models (Figure 2). However, as a consequence of weaker confinement of fluorescence,  $\gamma$  decreases

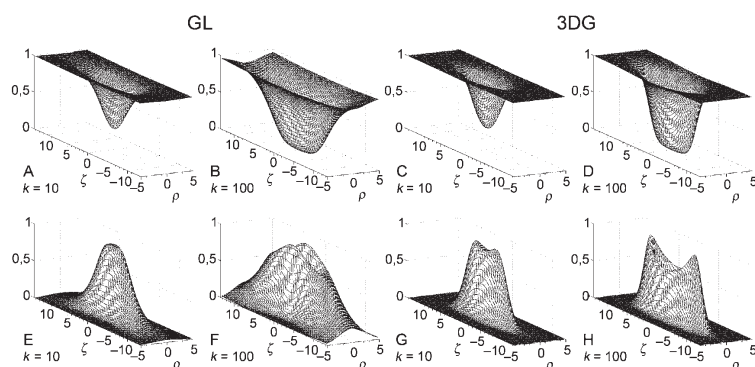


**Figure 1.** Calculated concentration profiles  $c'(\rho)$  (A–D) and fluorescence profiles  $F(\rho) = \eta_0 c_0 c'(\rho) S(\rho)$  scaled to 1 at their maximum (E–H) for GL (A, B, E, F) and 3DG (C, D, G, H) models in normalized cylindrical coordinates  $(\rho, \zeta)$ , for two values of the bleaching parameter  $k = 10$  (A, C, E, G) and 100 (B, D, F, H).

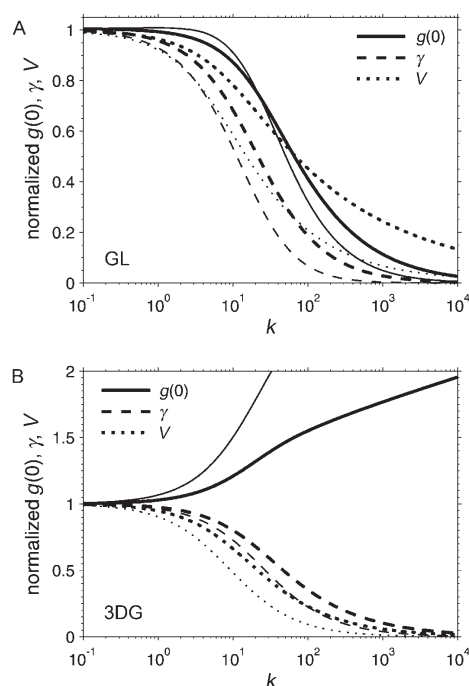


**Figure 2.** Dependence of normalized autocorrelation amplitude  $g(0)$  (—), volume contrast  $\gamma$  (---), and measurement volume  $V$  (.....) on the bleaching parameter  $k$ , obtained from the numerical solution of Equation (8) assuming the GL (A) and 3DG (B) models. The assumed dependence of photobleaching on excitation intensity is cubic:  $B(\rho) = W^3(\rho)$  (thick lines) and quadratic:  $B(\rho) = W^2(\rho)$  (thin lines).

at a higher rate than  $V$  in the GL model, which causes the observable autocorrelation amplitude  $g(0)$  to decrease with the photobleaching parameter  $k$ . The decrease of  $\gamma$  with  $k$  in the 3DG model is weaker than that of  $V$ , which results in the opposite effect—increase of the autocorrelation amplitude  $g(0)$  with  $k$ .

A different dependence of photobleaching rate on illumination intensity does not qualitatively change these results. If second-power dependence of photobleaching is assumed [ $B(\rho) = W^2(\rho)$  in Eq. (8)] instead of third-power dependence, the rates of decrease of  $V$  and  $\gamma$  are modified, but the overall  $g(0)$  behavior remains the same (Figure 2). Similarly, if the values of the parameters  $b$  ranging between 0.1 and 2.0 in the GL model are used, qualitatively very similar dependence of the monitored parameters on  $k$  is obtained, with the only major difference being different scaling with  $k$  (not shown).

Thus, the resulting overall behavior of  $g(0)$  with photobleach-

ing (decrease or increase) depends strongly on the functional form of  $S(\rho)$  but appears to be rather robust with respect to the choice of the actual values of model parameters. Moreover, the decrease of the autocorrelation amplitude  $g(0)$ , known to result from saturation of absorption,<sup>[15]</sup> can also occur as a consequence of photobleaching, and cannot therefore be automatically taken as evidence of the saturation in an FCS experiment.

### Scanning FCS

When the measurement volume is scanned in a circle of radius  $R$  at a constant angular velocity  $\omega_0$ , the autocorrelation function for the 3DG model is the product of the diffusion part and an exponential scan factor [Eq. (12)].<sup>[33]</sup>

$$g(\tau) = \frac{\gamma}{c_0 V} \frac{1}{\sqrt{1 + \frac{\tau}{w^2 \tau_D}}} \frac{1}{1 + \frac{\tau}{\tau_D}} e^{-\frac{2R^2 \sin^2(\omega_0 \tau / 2)}{a^2 (1 + \tau / \tau_D)}} \quad (12)$$

When the scan radius  $R$  is large compared to the measurement volume size  $a$ , and the scan period  $T = 2\pi/\omega_0$  is much larger than the diffusion time  $\tau_D$ , the curvature of the scan path can be neglected and the scan factor can be approximated by a flow factor by taking the limit of  $R \rightarrow \infty$  while keeping the velocity  $v = R\omega_0$  constant [Eq. (13)].<sup>[44]</sup>

$$g(\tau) = \frac{\gamma}{c_0 V} \frac{1}{\sqrt{1 + \frac{\tau}{w^2 \tau_D}}} \frac{1}{1 + \frac{\tau}{\tau_D}} e^{-\frac{v^2 \tau^2}{2a^2 (1 + \tau / \tau_D)}} \quad (13)$$

The scan (flow) factor modulates the pure-diffusion autocorrelation. The loss of correlation with time is caused by both diffusion and the motion of the measurement volume. Which of these two effects dominates the initial part of the autocorrelation is determined by the relation between the diffusion time  $\tau_D$  and the flow time  $\tau_v = \sqrt{2}a/v$ . We are, however, interested in the amplitude of the autocorrelation  $g(0)$  and how it is modified by scanning. This can be inferred from Equation (13). In our case we estimate the value of  $g(0)$  from the experimental data at  $\tau = 3 \times 10^{-4}$  ms; the flow time is  $\tau_v = 4.0$   $\mu$ s at 1000 Hz, and  $\tau_D = 65$   $\mu$ s for Alexa 546. The value of the flow factor in Equation (13) is then  $> 0.99$ , and we can therefore neglect any direct effect of scanning on the experimental values of  $g(0)$ . Although an analytical expression analogous to Equation (13) is not available for the GL model, the direct effect of scanning is expected to be similar, because the size of the measurement volume relative to  $R$  is comparable to that of the 3DG model.

### Experimental Methods

**Experimental Setup:** The fluorescence measurements were performed on a home-built two-photon laser scanning microscope.<sup>[45]</sup> A tunable Ti:sapphire laser (Mira 900-F, Coherent, Santa Clara, USA) was used as the excitation source. The excitation wavelength was set to 820 nm (Alexa 546) or 920 nm (eGFP), and the pulse frequency was 76 MHz. The laser pulse length was 100 fs at 820 nm

and 90 fs at 920 nm before entering the scanning unit. The beam was linearly polarized and expanded by lenses to overfill the back aperture of the objective (Olympus UPLAPO 60 $\times$ W3/IR).

The laser beam was reflected from a dichroic beam splitter (725DCSPXR, AHF, Tübingen, Germany) that separated the excitation and emitted light, and steered by two mirrors mounted on shafts of closed-loop galvanometer scanners (VM2000, GSI Lumonics GmbH, Unterschleißheim, Germany).

The fluorescence was descanned by following the same path as the excitation beam in the opposite direction. After transmission by the beam splitter and the emission filter (HQ600/200M or HQ535/70M, AHF), the fluorescence was focused onto the active area of an avalanche photodiode (APD; SPCM-CD2801, Perkin-Elmer, Wellesley, USA). Descanned detection was used because of the need to focus the emitted light onto the small active area of the APD (diameter 170  $\mu$ m). The final magnification including the scanning optics was 20 $\times$ , therefore the active area of the APD did not act as a confocal pinhole. The scanning optics was built around an inverted IX 71 microscope (Olympus, Tokyo, Japan).

The scanners were controlled by the ADWin Gold system (Jäger GmbH, Lorsch, Germany), a general-purpose microprocessor-controlled unit that generates the voltage waveform driving the scanners and synchronously acquires the signal from the detector. The user interface and the control of the ADWin module and the PIFOC (piezo nanofocusing) device were provided by a program written in the LabView environment (National Instruments, Austin, USA).

Fluorescence autocorrelation curves were obtained by passing the output signal of the APD to a hardware correlator ALV-6000 (ALV GmbH, Langen, Germany). The measurement volume was either fixed in the center of the field of view, or rotated along a circular path with radius  $R = 11.7$   $\mu$ m at frequencies of 10–1000 Hz. The excitation intensities used were in the range 0.4–50 mW. A typical measurement lasted 100 s. The measured autocorrelation curves were corrected for the background signal; the corrections were negligible for all but the lowest excitation intensities.

**Samples:** A solution of Alexa 546 (Molecular Probes, Eugene, USA) in water, or eGFP (Clontech, Mountain View, USA) in phosphate-citrate buffer (pH 7.5) at a concentration in the nanomolar range was placed in a 1-mm-deep well (total sample volume approximately 40  $\mu$ L) with the bottom formed by a #1.5 coverslip, to prevent evaporation of the solvent during the measurements. The measurement volume was positioned at a distance of approximately 100  $\mu$ m from the coverslip within the well.

**Numerical Calculations:** The stationary solution of the modified diffusion equation [Eq. (8)] was found numerically by using the Crank–Nicolson scheme.<sup>[46]</sup> The parameters of the GL and 3DG models needed for numerical calculations were chosen based on previous experiments:  $b = 0.24$  in the GL model, assuming  $a = 0.21$   $\mu$ m,  $\lambda_{\text{ex}} = 850$  nm, and  $n = 1.33$ , and  $w = 4.0$  in the 3DG model;  $a$  is eliminated in numerical calculations by the use of dimensionless coordinates. All calculations were performed with Matlab (The MathWorks, Natick, USA).

### Results

We compared standard FCS (fixed measurement volume) with sFCS autocorrelation curves of Alexa 546 and eGFP solutions measured at a range of excitation intensities (Figure 3). In sFCS experiments, the laser focus was scanned in a circle with its center coinciding with the center of the field of view, and with radius  $R = 11.7$   $\mu$ m and frequency  $f = 300$  Hz, corresponding to a velocity of 22.0  $\mu$ m ms<sup>-1</sup> and a flow time  $\tau_v = 13.5$   $\mu$ s

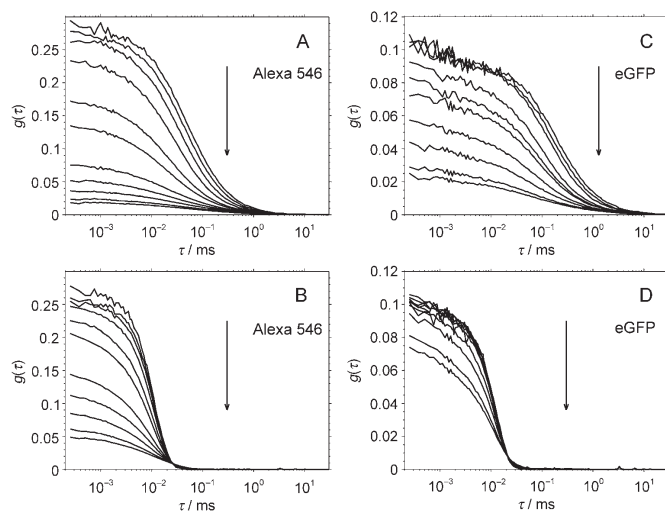


**Figure 3.** Experimental fluorescence autocorrelation curves of Alexa 546 and eGFP measured at different excitation intensities (3.0–30 mW for Alexa 546 and 6.8–46 mW for eGFP). The autocorrelation curves were measured without scanning (A, C) and with scanning (B, D) of the measurement volume in a circle of radius 11.7  $\mu\text{m}$  at a frequency of 300 Hz. Scanning the measurement volume causes the autocorrelation curve to drop sharply at the flow time  $\tau_v = 13.5 \mu\text{s}$  [Eq. (13)] but does not directly affect the autocorrelation amplitude  $g(0)$ . The amplitude is affected indirectly through modification of photobleaching effects. The arrows indicate increasing excitation intensity.

[Eq. (13)]. Since  $\tau_v < \tau_D$ , the information about diffusion in the autocorrelation is significantly suppressed. A small correlation can be observed at integral multiples of the scan period  $T = 1/f$ , when the measurement volume returns to the same position within the sample.

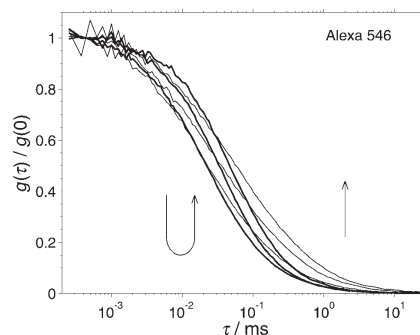
In both FCS and sFCS, the amplitude  $g(0)$  of the fluorescence autocorrelation is constant at low excitation intensities, but starts to decrease with increasing excitation intensity at higher excitation intensity values. In sFCS, however, the decrease appears at higher intensities than with a stationary measurement volume. This reduction, which demonstrates the ability of scanning to reduce the photobleaching effects, is especially pronounced for slower-diffusing eGFP (see also Figure 6 below).

Figure 4 shows several autocorrelation curves of Alexa 546 selected from Figure 3A, normalized to 1 at  $\tau = 0.4 \mu\text{s}$  to emphasize the change of temporal behavior with excitation intensity. At low excitation intensities, the autocorrelation shifts to lower times  $\tau$ , thus resulting in shorter apparent diffusion times  $\tau_D$  when analyzed by a standard 3DG model.<sup>[18,41]</sup> At higher intensities, a longer tail appears and gradually the whole curve shifts back to longer times  $\tau$ . The autocorrelation decrease at the highest intensities is less steep (the curve is “flatter”) than that predicted by the purely diffusional 3DG model. These effects of high excitation intensity on the autocorrelation curves have been observed previously,<sup>[12,15,20,47]</sup> although in some cases an increase of  $g(0)$ ,<sup>[14]</sup> or initial increase followed by decrease of  $g(0)$ ,<sup>[41]</sup> has been reported.

The dependence of the average fluorescence intensity  $F$  on the excitation intensity  $I$  in the autocorrelation measurements described above is shown in Figure 5. At low excitation intensi-

ties the fluorescence increases quadratically with  $I$ , as expected for two-photon excitation. At higher intensities  $I$  the fluorescence dependence is less than quadratic. As with the autocorrelation amplitude  $g(0)$  described above, scanning the measurement volume reduces this known effect of high excitation intensity: the deviation from the quadratic dependence appears at higher intensities  $I$  when the beam is scanned in a circle. Scanning at the radius and frequency used results in an approximately three times higher maximum fluorescence  $F$  being achievable within the quadratic regime than with a stationary measurement volume, for both dyes investigated. Above the quadratic regime, the fluorescence  $F$  is always higher with scanning for a given excitation intensity  $I$ , which means that there are more fluorescent molecules present in the measurement volume.

The inset in Figure 5 shows the fluorescence changes upon starting and stopping the scan. When starting the scan, the excitation beam moves from the center of the field of view onto the circular path where the concentration of nonbleached molecules is higher, which results in a sharp increase of fluorescence. After a few seconds of scanning a new equilibrium concentration of nonbleached molecules is established, with the concentration along the scan



**Figure 4.** Normalized fluorescence autocorrelation functions of Alexa 546 from Figure 3A for six values of excitation intensity: 3.0, 4.5, 7.5, 12, 18, and 30 mW. The curves corresponding to the three lower-intensity values are plotted with thick lines for clarity; the arrows indicate changes in correlation with increasing excitation intensity for corresponding lag times  $\tau$ . Initially, the autocorrelation curves shift to shorter lag times  $\tau$ , which indicates an apparently shorter diffusion time  $\tau_D$  (thick lines); at higher excitation intensities a relative increase of correlation at longer lag times  $\tau$  is observed, accompanied by a shift of the whole curve to longer times, with the curves being “flatter” than those for the standard 3DG model (thin lines).

path being higher than the initial concentration in the center with the fixed beam. This equilibration can be observed as a fast relaxation of fluorescence to a level higher than that before starting the scan. The mean concentration of nonbleached molecules along the circular path is larger than in the case of a stationary measurement volume, because the bleaching dose is now distributed along the perimeter of the

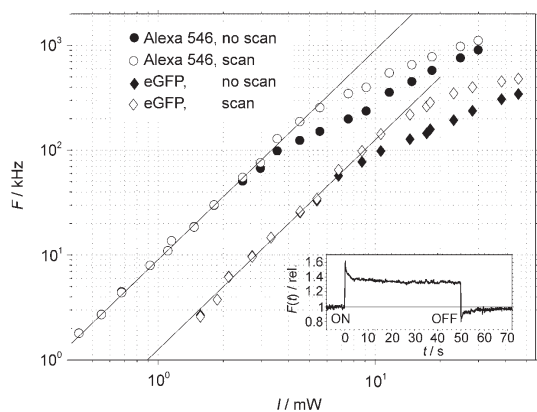


**Figure 5.** Dependence of the fluorescence signal  $F$  on the excitation intensity  $I$  for Alexa 546 (circles) and eGFP (diamonds), without scanning (filled symbols) and with scanning (empty symbols) of the measurement volume. For both dyes, scanning increases the range of excitation intensities  $I$  with quadratic dependence of  $F$  on  $I$ . Above the quadratic regime, the fluorescence  $F$  is always higher with scanning than with a fixed measurement volume. The inset shows the relative changes of fluorescence  $F(t)$  on starting (ON) and stopping (OFF) the scan, with relaxation due to the equilibration between photobleaching and diffusion (Alexa 546, measured at 18 mW).

circular path. Upon stopping the scan, the beam moves back to the center where the molecules are now depleted, followed by the establishment of the same concentration equilibrium as before starting the scan, which results in a return to the same fluorescence level. The fluorescence generated as soon as the beam moves to the center of the scanned circle is lower than that with a fixed beam, presumably because of the molecular depletion over a larger volume (circle diameter) and therefore the absence of fluorescence generated at the edges of the illuminated volume, where the depletion with a fixed beam is lower. These effects upon starting and stopping the scan clearly demonstrate the presence of photobleaching at the high excitation intensities used.

Figure 6 shows the measured dependence of the autocorrelation amplitude  $g(0)$  on the excitation intensity, both without and with scanning, obtained from the autocorrelation curves shown in Figure 3. The dependence of  $g(0)$  on excitation intensity without scanning was fitted to the numerical results described in the Theory section (Figure 2A), assuming the GL model and both second- and third-power dependence of photobleaching on the illumination intensity. Two adjustable parameters were present in each fit: the autocorrelation amplitude  $g(0)$  in the limit of low excitation intensity, and the constants  $\alpha_3$  and  $\alpha_2$  in the relations  $k = \alpha_3 I^3$  and  $k = \alpha_2 I^2$ , which describe the third- and second-power dependence of photobleaching, respectively. The values obtained from the fits are  $\alpha_3 = 0.084 \text{ mW}^{-3}$  and  $\alpha_2 = 0.58 \text{ mW}^{-2}$  for Alexa 546, and  $\alpha_3 = 3.0 \times 10^{-3} \text{ mW}^{-3}$  and  $\alpha_2 = 0.061 \text{ mW}^{-2}$  for eGFP. The plots in Figure 6 indicate that both models describe the decrease of  $g(0)$  reasonably well. The difference between the two models is too small to choose either of them as preferable on the basis of these measurements. The general agreement with the data means, however, that photobleaching as treated in the

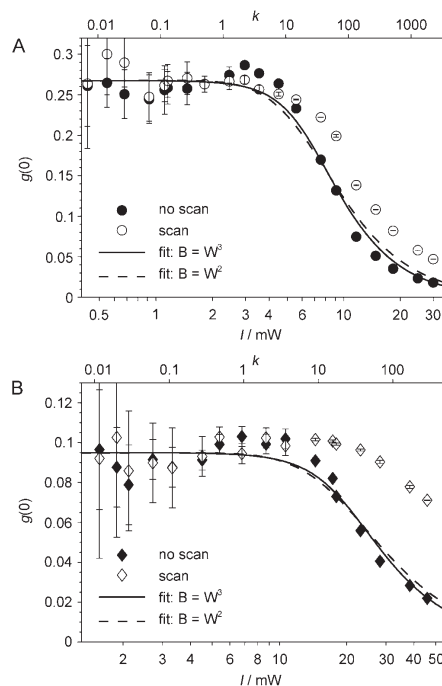


**Figure 6.** Dependence of autocorrelation amplitude  $g(0)$  on the excitation intensity  $I$  without scanning (filled symbols) and with scanning (empty symbols) for Alexa 546 (A) and eGFP (B). The experimental data were fitted to two photobleaching models (see Theory section and Figure 2A) assuming third- [ $B(\rho) = W^3(\rho)$ ] and second-power [ $B(\rho) = W^2(\rho)$ ] dependence of photobleaching on the excitation intensity  $I$ . The  $k$  axes (top) correspond to the model where  $B(\rho) = W^2(\rho)$ . The errors were estimated from the fluctuations in the first few channels of the autocorrelation curves.

Theory section is sufficient to describe the observations in experiments with stationary measurement volume, without the need to consider saturation effects. The lower  $\alpha_3$  and  $\alpha_2$  values of eGFP compared to Alexa 546 mean that eGFP is more photostable in the sense that it can withstand higher excitation intensities. This does not, however, mean that it should produce more fluorescence at these intensities, since this depends also on the two-photon absorption cross section and the fluorescence quantum yield.

Figure 7 shows the dependence of the effective brightness  $\eta^*$  on the excitation power for both Alexa 546 and eGFP. The effective brightness  $\eta^*$  is an experimental parameter determined as the average fluorescence intensity multiplied by the autocorrelation amplitude,  $\eta^* = Fg(0)$ , and is related to the molecular brightness  $\eta_0$  by  $\eta^* = \gamma\eta_0$ , as follows from Equations (2), (9), and (10). Higher effective brightness leads to higher S/N ratios, therefore it is desirable to maximize its value. The results indicate that at low excitation intensities  $I$  the effective brightness follows the expected quadratic dependence on  $I$ , which means that  $\gamma$  is constant. At high excitation intensities, the effective brightness increases more slowly than expected and even reaches a maximum and starts to decrease. This finding can be explained by a decrease of  $\gamma$  due to photobleaching, as predicted in the Theory section (Figure 2A), and can also be af-

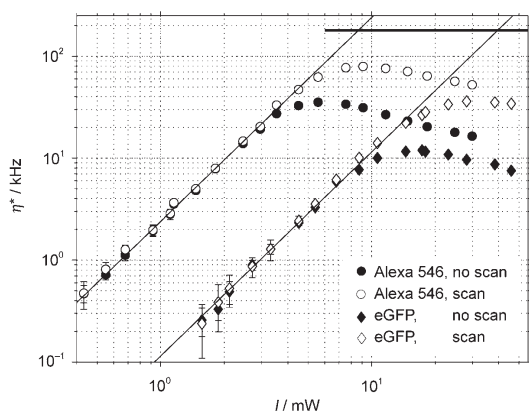


**Figure 7.** Measured dependence of the effective molecular brightness  $\eta^* = Fg(0)$  on the excitation intensity  $I$  for Alexa 546 (circles) and eGFP (diamonds), both without scanning (filled symbols) and with scanning (empty symbols) of the measurement volume. The horizontal line at  $\eta^* = 180$  kHz indicates the effective brightness at which the saturation effects are estimated to start to appear (see Discussion).

ected by a decrease of  $\eta_0$  at the highest intensities due to saturation. As can be seen in Figure 7, scanning the measurement volume increases the maximum value of  $\eta^*$  by approximately two times for Alexa 546 and three times for eGFP. More relevant for practical measurements than the maximum  $\eta^*$  values are the values within the quadratic dependence on excitation intensity. Then, the increase of  $\eta^*$  with scanning is approximately a factor of 2 in both cases. The appearance of a maximum of  $\eta^*$  at certain high excitation intensities has been reported before.<sup>[14,41]</sup> An increase of the maximum values of  $\eta^*$  was achieved previously by using radical quenchers, that is, by reducing photobleaching.<sup>[14]</sup> The fact that the maximum achieved effective brightness  $\eta^*$  of eGFP is lower than that of Alexa 546 means that the yield of bleaching once the molecule is in the excited state is higher for eGFP (ignoring a possible difference in fluorescence quantum yields of the two dyes). That is, the experimentally relevant parameter yield of bleaching/yield of fluorescence at equal fluorescence levels is higher for eGFP than for Alexa 546.

Increasing the scanning frequency can further increase the maximum obtainable brightness  $\eta^*$  and reduce the undesired effects of high excitation intensities. We measured the dependence of the fluorescence signal and autocorrelation parameters on the frequency of scanning at a constant excitation intensity  $I$  near the point where maximum  $\eta^*$  is obtained:  $I = 9.1$  mW for Alexa 546 and  $I = 28$  mW for eGFP. The monitored parameters of fluorescence intensity  $F$ , autocorrelation amplitude  $g(0)$ , and their product, the effective brightness  $\eta^*$ , increase with increasing scanning frequency (Figure 8). The slight decrease of  $F$  at the highest frequencies may be linked to a smaller real diameter of the scanned circle, since the scanners are not able to follow the driving command fully at these high frequencies. The maximum  $\eta^*$  obtained is almost 40 kHz for eGFP and 90 kHz for Alexa 546.

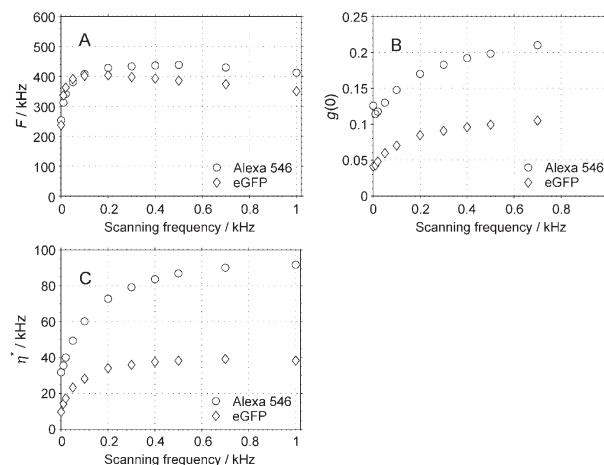


**Figure 8.** Experimental dependence of A) fluorescence intensity  $F$ , B) auto-correlation amplitude  $g(0)$ , and C) effective brightness  $\eta^*$  on the scanning frequency for both Alexa 546 ( $\circ$ ) and eGFP ( $\diamond$ ). The excitation intensities were 9.1 (Alexa 546) and 28 mW (eGFP).

## Discussion

The deviations of fluorescence intensities and autocorrelation functions from the expected behavior commonly observed at high excitation intensities are often explained as a consequence of saturation of the transition between the ground state  $S_0$  and the first excited state  $S_1$  (due to pulsed excitation, finite lifetime of the excited state, or both), and of photobleaching. While saturation has been successfully described theoretically,<sup>[15]</sup> the theoretical treatment of photobleaching is difficult due to the inherent coupling between diffusion and the photobleaching reaction in a system consisting of molecules diffusing in and out of the measurement volume.

The presented results of sFCS show that photobleaching is the principal limiting factor with the experimental configuration and fluorescent dyes used. The following arguments support this conclusion. First of all, scanning with the velocities used here ( $\tau_v \leq 4 \mu\text{s}$ ) would not affect the saturation of the  $S_0 \rightarrow S_1$  transition. The equilibration between the ground and excited states depends on the rates of excitation and  $S_1$  decay, and occurs on a much faster timescale (1–10 ns) than several microseconds, a time for which any location on the circular path of the scanning beam is illuminated.<sup>[25]</sup> The scanning is effectively stationary on the timescale of  $S_0 \rightarrow S_1$  equilibration, and therefore no difference in saturation behavior between scanned and fixed measurement volumes would be expected. The observed differences are therefore of different origin.

The changes of fluorescence intensity  $F$  on starting and stopping the scan and the comparison of  $F$  at the same excitation intensities without and with scanning (Figure 5) clearly indicate variations of the spatially dependent concentration  $c(\mathbf{p})$  of nonbleached molecules. The behavior of  $g(0)$  predicted by numerical calculations using the photobleaching model with the GL illumination profile also agrees with the observations (Figure 6).

The onset of optical saturation can be estimated using the dimensionless saturation parameter  $R_{\text{sat}}^{[15]}$  which describes the reduction of true excitation frequency  $f$  due to pulsed excitation at the laser repetition frequency  $f_0$ :  $f = f_0[1 - \exp(-R_{\text{sat}}^2)]$ . Nagy et al.<sup>[15]</sup> have shown that the saturation effects start to appear at  $R_{\text{sat}} \approx 0.4$ . Taking into account the volume contrast  $\gamma$ , fluorescence quantum yield, and the efficiency of the optical system, we arrive at the corresponding nonsaturated effective brightness  $\approx 180$  kHz. This corresponds to the excitation intensity  $\approx 9$  mW for Alexa 546 and  $\approx 40$  mW for eGFP, as can be read from Figure 7. Thus, the deviations from ideal behavior (decrease of  $g(0)$ , nonlinearity of  $F(I^2)$ , etc.) appear far before the saturation artifacts are expected. For Alexa 546 the data at the six highest excitation intensities are expected to be influenced by saturation, whereas in the case of eGFP all the observed behavior is due to photobleaching. The results of these considerations are in agreement with the known fact that in one-photon FCS much higher molecular brightness values are observed.<sup>[20,18]</sup> 200 kHz and higher, because of weaker photobleaching in the focus.

The calculations of the concentration and fluorescence profiles and  $\gamma$  factors presented in the Theory section show how photobleaching can cause the effects observed in standard two-photon FCS. The two commonly used models of the measurement volume, 3DG and GL, predict very different dependence of the autocorrelation amplitude on photobleaching (Figure 2), and only the GL model agrees with the data (Figure 6).

We have considered two photobleaching models: with quadratic and cubic dependence on the excitation intensity. It has been suggested that photobleaching in two-photon excitation is mediated by triplet states or higher excited singlet states,<sup>[14,17,19,48,49]</sup> which necessitates the absorption of a third photon after the initial two-photon absorption, and therefore leads to a cubic intensity dependence. The actual dependence may be quadratic, as argued by Eggeling et al.,<sup>[49]</sup> since the one-photon transition can be saturated with the high excitation intensities needed for two-photon absorption ( $S_0 \rightarrow S_1$ ). Although the presented experimental data do not allow us to distinguish between the second- and third-power dependence of photobleaching on excitation intensity, they are compatible with both of them.

The effects of photobleaching on the temporal behavior of fluorescence autocorrelation in FCS are usually approximated by multiplying the model autocorrelation function by an additional term with exponential temporal dependence.<sup>[14,15,48,49]</sup> Although the bleaching process itself, in its simplest case, can be described by exponential temporal behavior with the rate constant determined by the excitation intensity, the molecules in FCS experience variable excitation intensities as they move through the measurement volume, and the description by one or two exponential terms is only approximate, and not always sufficient. Although we have limited ourselves to the calculation of the effects of photobleaching on the autocorrelation amplitude  $g(0)$ , the results of the numerical calculation (see Figure 1 and figure in Supporting Information) also offer a qualitative explanation of the observed temporal profile of

fluorescence autocorrelation (Figure 4) in the absence of scanning. Molecules diffusing through the center of the measurement volume are more likely to be photobleached, and therefore contribute to the initial decrease in autocorrelation, and are the cause of the apparently shorter diffusion times observed at moderate excitation intensities [small  $k$  values in Eq. (8)] when the photobleaching effects start to become apparent.<sup>[41]</sup> With strong photobleaching (high values of  $k$ ) the fluorescence is more delocalized (see Figure 1), and the relative contribution to the overall signal from molecules diffusing on the periphery of the measurement volume increases. These molecules are less likely to be photobleached because of lower excitation intensities than in the center. At the same time, they spend more time in the area from which the fluorescence is detected due to the larger extent of this area. Therefore, the molecules at the periphery can cause the relative increase of fluorescence autocorrelation observed at longer times  $\tau$  (see Figure 4). The exact calculation of these effects is complicated because the probability of the molecule being photobleached depends on the trajectory it follows through the measurement volume.<sup>[50]</sup> It is not only the possible complexity of the photobleaching kinetics (photochemistry), but also the coupling with diffusion that complicates the theoretical description.

The description approach used in the Theory section can be applied to experimental configurations where a pinhole is used (for example, by using an optical fiber to lead the fluorescence to the detector), by employing an appropriate collection efficiency function  $CEF(r)$  in the definition of the measurement profile  $S(r)$ . The pinhole is likely to partially suppress the delocalized fluorescence from the periphery of the measurement volume (see Figure 1F and Figure 1B in the Supporting Information), and can therefore affect the trend of change of  $g(0)$  with the bleaching parameter  $k$ , and also the relative increase of correlation observed with strong photobleaching (Figure 4). In the case of one-photon excitation, the excitation profile  $E(r)$  is equal to the illumination profile  $W(r)$ , and an assumption has to be made about the dependence of photobleaching on the excitation intensity. However, care has to be taken when bleaching is directly proportional to excitation [ $B(r) = E(r)$ ], because then photobleaching is not confined to a small volume, the stationary state characterized by  $c'(p)$  may not be reached, and additional approximations need to be used.<sup>[43]</sup>

For the purpose of heuristic understanding, the effects of photobleaching on the autocorrelation can be divided into two parts: the "stationary" effect, whereby the nonconstant concentration profile  $c(p)$  affects the amplitude  $g(0)$  by modifying  $\gamma$  [Eq. (11)] and  $V$  [Eq. 9], and the "dynamic" effect, where the temporal behavior of  $g(\tau)$  changes because the molecules can be photobleached while diffusing through the measurement volume. Scanning has no influence on the dynamic effect—when illuminated, the molecules can still be photobleached. The additional exponential terms, used in the literature to describe photobleaching in FCS, focus on the dynamic effect but omit the stationary part.

On the other hand, scanning alleviates the stationary effect by spreading the bleaching light dose over a larger area—the

scanned circular path as opposed to a fixed measurement volume. This results in reduced depletion of nonbleached molecules described by  $c'(\rho)$ , reduced decrease of  $V$ , and therefore increased fluorescence  $F$  compared to the situation without scanning (Figures 5 and 8A). A second effect of weaker molecular depletion is a reduced decrease of  $\gamma$  [Eq. (11)], manifested experimentally by a higher effective molecular brightness  $\eta^* = \gamma\eta_0$  (Figures 7 and 8C).

The reduction of the depletion of fluorescent molecules by employing circular scanning has been theoretically and experimentally investigated by Satsoura et al.<sup>[37]</sup> Although they considered one-photon excitation and reduced the problem to two dimensions where no stationary state is reached, the principal mechanism of reduction of depletion of fluorescent molecules by scanning remains the same also in our situation. However, their approximation of the finite-sized bleaching profile by a point sink means that the observed changes of effective brightness due to the changes of volume contrast  $\gamma$  cannot be explained by this simplified approach.

In addition to facilitating the understanding of the role of photobleaching in two-photon FCS, sFCS, with its reduction of photobleaching artifacts, is of potentially high practical importance.<sup>[34,35]</sup> Scanning the measurement volume extends the range of excitation intensities within the range of quadratic dependence of fluorescence on excitation (Figure 7), and makes it possible to achieve an effective brightness  $\eta^*$  higher by a factor of approximately 2 for the two investigated fluorescent molecules, which in turn results in a better S/N ratio and the possibility of shorter acquisition times. A higher scanning frequency can further enhance this effect (Figure 8). This is particularly relevant for experiments where the autocorrelation amplitude  $g(0)$  carries the information of interest, such as concentration and cross-correlation measurements, and where the partial loss of diffusion information from the autocorrelation due to scanning is not important. Scanning does not disturb the investigated system more than fixed-volume FCS, and is therefore more acceptable than addition of radical quenchers or other chemical agents known to reduce photobleaching.

Recently, it has been shown that the excitation of molecules only after they have relaxed from their triplet states significantly reduces photobleaching.<sup>[51]</sup> Sufficiently fast scanning could in principle reduce photobleaching in the same way, if any given molecule were excited only for a time shorter than the time  $\tau_t$  needed for the buildup of the triplet state (i.e. if the flow time  $\tau_v \leq \tau_t$  with scanning), and again after having relaxed from the triplet state ( $T > \tau_t$ ). Scanning frequencies approximately one order of magnitude higher than those used here would be necessary to test this possibility.

## Conclusions

We have compared FCS with a fixed measurement volume and sFCS to investigate the role of photobleaching in two-photon FCS. The theoretical calculations and their comparison with experiments provide an explanation of how photobleaching affects the measured autocorrelation curves. The results stress the importance of considering the nonuniform excitation in-

tensity and concentration of nonbleached molecules and the choice of the model function of the measurement volume. The GL model predicts the observed "stationary" effect—the decrease of the autocorrelation amplitude  $g(0)$ —and also provides a qualitative explanation for the temporal distortions of the autocorrelation function ("dynamic" effect). Alternative models assuming a constant concentration of nonbleached molecules lowered by photobleaching are too crude to capture the observed behavior. The results of the calculations together with the sFCS experiments confirm the decisive limiting role of photobleaching in two-photon FCS, with the  $S_0 \rightarrow S_1$  saturation being of minor importance. This conclusion leaves a hope that new, more photobleaching-resistant fluorescent labels could improve the performance of two-photon FCS towards that of its one-photon counterpart.

## Acknowledgements

We thank Markus Burkhardt and Jörg Mütze for helpful discussions. The funding was provided by The International Human Frontier Science Program (HFSP) RGP 5/2005, and the Europäische Fond für regionale Entwicklung (EFRE), project no. 4212/06-02.

**Keywords:** diffusion · fluorescence · fluorescence correlation spectroscopy · photobleaching · photochemistry

- [1] D. Magde, W. W. Webb, E. Elson, *Phys. Rev. Lett.* **1972**, *29*, 705–708.
- [2] E. L. Elson, D. Magde, *Biopolymers* **1974**, *13*, 1–27.
- [3] *Fluorescence Correlation Spectroscopy: Theory and Application*, Chemical Physics Series, 1st ed. (Eds.: R. Rigler, E. S. Elson), Springer, Berlin, **2001**.
- [4] K. Bacia, P. Schwille, *Methods* **2003**, *29*, 74–85.
- [5] S. T. Hess, S. H. Huang, A. A. Heikal, W. W. Webb, *Biochemistry* **2002**, *41*, 697–705.
- [6] V. Vukojevic, A. Pramanik, T. Yakovleva, R. Rigler, L. Terenius, G. Bakalkin, *Cell. Mol. Life Sci.* **2005**, *62*, 535–550.
- [7] N. L. Thompson, A. M. Lieto, N. W. Allen, *Curr. Opin. Struct. Biol.* **2002**, *12*, 634–641.
- [8] E. P. Petrov, P. Schwille *Standardization and Quality Assurance in Fluorescence Measurements: State of the Art and Future Challenges*, Springer Series on Fluorescence, Vol. 5, Springer, Berlin, **2008**, Chap. 23.
- [9] K. M. Berland, P. T. C. So, E. Gratton, *Biophys. J.* **1995**, *68*, 694–701.
- [10] K. G. Heinze, A. Koltermann, P. Schwille, *Proc. Natl. Acad. Sci. USA* **2000**, *97*, 10377–10382.
- [11] S. A. Kim, K. G. Heinze, M. N. Waxham, P. Schwille, *Proc. Natl. Acad. Sci. USA* **2004**, *101*, 105–110.
- [12] S. A. Kim, K. G. Heinze, K. Bacia, M. N. Waxham, P. Schwille, *Biophys. J.* **2005**, *88*, 4319–4336.
- [13] W. R. Zipfel, R. M. Williams, W. W. Webb, *Nat. Biotechnol.* **2003**, *21*, 1369–1376.
- [14] P. S. Dittrich, P. Schwille, *Appl. Phys. B* **2001**, *73*, 829–837.
- [15] A. Nagy, J. R. Wu, K. M. Berland, *Biophys. J.* **2005**, *89*, 2077–2090.
- [16] G. H. Patterson, D. W. Piston, *Biophys. J.* **2000**, *78*, 2159–2162.
- [17] R. Niesner, W. Roth, K. H. Gericke, *ChemPhysChem* **2004**, *5*, 678–687.
- [18] C. Eggeling, A. Volkmer, C. A. M. Seidel, *ChemPhysChem* **2005**, *6*, 791–804.
- [19] J. Mertz, *Eur. Phys. J. D* **1998**, *3*, 53–66.
- [20] P. Schwille, U. Haupts, S. Maiti, W. W. Webb, *Biophys. J.* **1999**, *77*, 2251–2265.
- [21] I. Gregor, D. Patra, J. Enderlein, *ChemPhysChem* **2005**, *6*, 164–170.
- [22] G. Nishimura, M. Kinjo, *Anal. Chem.* **2004**, *76*, 1963–1970.
- [23] D. E. Koppel, *Phys. Rev. A* **1974**, *10*, 1938–1945.
- [24] P. Kask, R. Gunther, P. Axhausen, *Eur. Biophys. J.* **1997**, *25*, 163–169.

- [25] J. Widengren, Ü. Mets, R. Rigler, *J. Phys. Chem.* **1995**, *99*, 13368–13379.
- [26] M. Weissman, H. Schindler, G. Feher, *Proc. Natl. Acad. Sci. USA* **1976**, *73*, 2776–2780.
- [27] N. O. Petersen, *Biophys. J.* **1986**, *49*, 809–815.
- [28] K. M. Berland, P. T. C. So, Y. Chen, W. W. Mantulin, E. Gratton, *Biophys. J.* **1996**, *71*, 410–420.
- [29] J. Ries, P. Schuille, *Biophys. J.* **2006**, *91*, 1915–1924.
- [30] A. Amediek, E. Hausteiner, D. Scherfeld, P. Schuille, *Single Mol.* **2002**, *3*, 201–210.
- [31] Q. Q. Ruan, M. A. Cheng, M. Levi, E. Gratton, W. W. Mantulin, *Biophys. J.* **2004**, *87*, 1260–1267.
- [32] M. A. Digman, C. M. Brown, P. Sengupta, P. W. Wiseman, A. R. Horwitz, E. Gratton, *Biophys. J.* **2005**, *89*, 1317–1327.
- [33] J. P. Skinner, Y. Chen, J. D. Müller, *Biophys. J.* **2005**, *89*, 1288–1301.
- [34] K. G. Heinze, M. Rarbach, M. Jahnz, P. Schuille, *Biophys. J.* **2002**, *83*, 1671–1681.
- [35] T. Winkler, U. Ketting, A. Koltermann, M. Eigen, *Proc. Natl. Acad. Sci. USA* **1999**, *96*, 1375–1378.
- [36] C. Eggeling, P. Kask, D. Winkler, S. Jäger, *Biophys. J.* **2005**, *89*, 605–618.
- [37] D. Satsoura, B. Leber, D. W. Andrews, C. Fradin, *ChemPhysChem* **2007**, *8*, 834–848.
- [38] S. T. Hess, W. W. Webb, *Biophys. J.* **2002**, *83*, 2300–2317.
- [39] H. Qian, E. L. Elson, *Appl. Opt.* **1991**, *30*, 1185–1195.
- [40] J. Enderlein, *Opt. Lett.* **2000**, *25*, 634–636.
- [41] V. Iyer, M. J. Rossow, M. N. Waxham, *J. Opt. Soc. Am. B* **2006**, *23*, 1420–1433.
- [42] J. Widengren, P. Thyberg, *Cytometry Part A* **2005**, *68*, 101–112.
- [43] A. Delon, Y. Usson, J. Derouard, T. Biben, C. Souchier, *J. Fluoresc.* **2004**, *14*, 255–267.
- [44] P. S. Dittrich, P. Schuille, *Anal. Chem.* **2002**, *74*, 4472–4479.
- [45] Z. Petrášek, P. Schuille, *Single Molecules and Nanotechnology, Springer Series in Biophysics, Vol. 12*, Springer, Berlin, **2008**, Chap. 4, pp. 3–104.
- [46] W. P. Press, B. P. Flannery, S. A. Teukolsky, W. T. Vetterling, *Numerical Recipes in C: The Art of Scientific Computing*, Cambridge University Press, Cambridge, **1992**, Chap. 19, pp. 827–857.
- [47] K. Berland, G. Q. Shen, *Appl. Opt.* **2003**, *42*, 5566–5576.
- [48] J. Widengren, R. Rigler, *Bioimaging* **1996**, *4*, 149–157.
- [49] C. Eggeling, J. Widengren, R. Rigler, C. A. M. Seidel, *Anal. Chem.* **1998**, *70*, 2651–2659.
- [50] J. Enderlein, *Phys. Lett. A* **1996**, *221*, 427–433.
- [51] G. Donnert, C. Eggeling, S. W. Hell, *Nat. Methods* **2007**, *4*, 81–86.

---

Received: August 24, 2007

Revised: October 22, 2007

Published online on December 10, 2007

## A7

### **Independence of maximum single molecule fluorescence count rate on the temporal and spectral laser pulse width in two-photon FCS**

J. Mütze, Z. Petrášek and P. Schwille

*J. Fluoresc.*, 17:805–810, 2007.

Related publication:

### **Excitation spectra and brightness optimization of two-photon excited probes**

J. Mütze, V. Iyer, J. J. Macklin, J. Colonell, B. Karsh, Z. Petrášek, P. Schwille,

L. L. Looger, L. D. Lavis, and T. D. Harris

*Biophys. J.*, 102(4):934–944, 2012.



# Independence of Maximum Single Molecule Fluorescence Count Rate on the Temporal and Spectral Laser Pulse Width in Two-Photon FCS

Jörg Mütze · Zdeněk Petrášek · Petra Schuille

Received: 9 March 2007 / Accepted: 17 August 2007 / Published online: 10 October 2007  
© Springer Science + Business Media, LLC 2007

**Abstract** We investigate the fluorescence emission characteristics of standard dye tetramethylrhodamine (TMR) in two-photon fluorescence correlation spectroscopy for different temporal and spectral properties of the femtosecond excitation pulses. After determining the second-order dispersion of our setup, including the microscope objective, a pulse stretcher was employed to control the temporal width at the location of the specimen. As expected, the fluorescence per molecule and therefore the signal-to-noise ratio of an FCS-measurement can be improved at constant average excitation power by altering either the temporal or spectral width of the excitation pulses. We found however, that the maximum achievable molecular brightness is largely independent of the temporal and spectral width in the regime analyzed. This observation confirms the current working hypothesis for two-photon fluorescence correlation spectroscopy that bleaching and saturation, and thus, the inherent properties of the dye system, are the dominant effects limiting the quality of measurements. As a practical consequence, elaborate optimization of temporal and spectral laser pulse width, e.g. by introducing pulse stretchers in the beam path, is less critical than previously expected.

**Keywords** Fluorescence · FCS · Two-photon excitation · Single molecule spectroscopy

## Introduction

Fluorescence correlation spectroscopy (FCS) is a highly sensitive and versatile technique used for the study of dynamics and interactions of individual fluorescently labeled molecules in solution or living cells [1, 2]. Two-photon FCS, where the fluorophore is excited by simultaneous absorption of two photons, provides numerous advantages over conventional FCS, particularly for applications in complex environments such as cells and organisms. It exhibits an intrinsic restriction of the excitation along the optical axis, leading to relatively low scattering background and confinement of the inevitable photobleaching of dye molecules to the focal vicinity [3–5], and thus allows larger penetration depths in biological samples. It moreover offers the possibility to simultaneously excite several spectrally distinct dyes with a single laser wavelength for dual-color cross-correlation measurements [6, 7]. Employing two-photon cross-correlation analysis, it has recently been possible to reveal the complex binding stoichiometry of protein–protein binding reactions in a living cell, demonstration the power of FCS as a method for *in situ* proteomics [8, 9]. The size of the two-photon measurement volume is comparable to conventional FCS without the need for a confocal pinhole. In order to achieve the necessary photon fluxes inside the excitation volume in the sample, it is necessary to employ femtosecond laser pulses with a mean power in the order of a few mW. The main disadvantage of two-photon excitation (TPE) compared to one-photon FCS is the rather low signal-to-noise ratio, usually determined by the detected photon count rate per single molecule per unit time. This signal limitation has so far mainly been attributed to photobleaching and saturation effects [10–12], although detailed reports about the relevance of excitation pulse quality control have so far been lacking. Shorter pulses, which require a broadened

J. Mütze · Z. Petrášek · P. Schuille (✉)  
Biophysics group, Biotechnologisches Zentrum,  
Technische Universität Dresden,  
Tatzberg 47-51,  
01307 Dresden, Germany  
e-mail: pschwil@gwdg.de

spectral profile of the excitation light, are usually considered superior [13, 14], because of their higher efficiency of true two-photon transitions to the first excited state, versus one-photon processes induced by infrared photons that could lead to transitions to higher excited states. On the other hand, saturation might put a limit to the positive effect of pulse shortening already at moderate intensities. It has been demonstrated [6] that the maximum fluorescence emission yield in FCS for common dye systems is crucially dependent on the excitation wavelength, an effect that points to the strong influence of competing transitions to higher excited states, which could in turn be responsible for enhanced photobleaching. This raises the question whether a similar careful optimization as for the wavelength might be required for the pulse width in order to improve the FCS signal. The objective of the present study is thus, to characterize the single molecule signal quality in two-photon FCS with respect to all of these excitation parameters, laser power and wavelength, but also temporal and spectral pulse width for the common fluorophore tetramethylrhodamine (TMR).

## Materials and methods

The temporal analysis of fluorescence intensity fluctuations of molecules passing through an optically defined open observation volume is the key principle of FCS. By recording the auto- and cross-correlation functions  $G(\tau)$  and  $G_x(\tau)$  of the fluorescence intensity fluctuations, it is possible to reveal information on concentrations and kinetic characteristics of different species of labeled molecules. The autocorrelation function (ACF), which is defined as:

$$G(\tau) = \frac{\langle \delta F(t) \delta F(t + \tau) \rangle}{\langle F(t) \rangle^2}, \quad (1)$$

describes the self-similarity of fluorescence fluctuations  $\delta F(t)$  after a lag time  $\tau$ . It contains information on the particle number  $N$  in the effective detection volume ( $N = 1/G(0)$ ) [15], and in the simplest case of freely diffusing molecules with negligible internal dynamics as observed here, its decay is parametrized by the diffusion time  $\tau_D$ , i.e., the characteristic time the molecule spends in the excitation volume, which is dependent on the diffusion coefficient of the molecules and the size of the volume.

One of the key parameters of interest in FCS applications is the number of photons emitted per molecule per second, often termed molecular brightness  $\eta$  [16]. It has been shown that the signal-to-noise ratio and thus, the statistical quality of the FCS data, is directly related to the detected fluorescence count rate per molecule [17, 18]. The molecular brightness  $\eta$  can simply be calculated by dividing the overall fluorescence count rate  $F(t)$  by the number of molecules  $N$  in

the effective measurement volume, where  $N$  can be estimated from the ACF as  $1/G(0)$ .

The time-averaged fluorescence signal for two-photon excitation depends on the square of the excitation intensity  $I_0(t)$  and the temporal width  $\tau_p$  of the excitation pulses [3]:

$$\langle F(t) \rangle \sim \frac{1}{\tau_p} \langle I_0(t) \rangle^2. \quad (2)$$

It follows from this relation, that in the absence of saturation and other limiting effects, the fluorescence yield can be increased either by increasing the mean excitation intensity  $I_0(t)$  or by shortening the duration of the excitation pulses.

Measurements were performed on a home-built two-photon FCS setup [3]. The beam of a mode-locked Titanium:Sapphire laser (Mira 900-F, Coherent, 76 MHz repetition rate) is expanded five times and relayed into an inverted microscope (IX70, Olympus). The laser power is varied using neutral density filters and measured in front of the microscope. After focussing the beam with a high-NA objective (60 $\times$ , 1.2NA IR, water immersion, Olympus), the induced fluorescence is collected by the same objective. The fluorescence emission passes a dichroic beamsplitter and an emission filter and is detected by a fiber-coupled Avalanche Photodiode (PerkinElmer Optoelectronics) with a 100  $\mu\text{m}$  aperture. The temporal width of the femtosecond pulses at the location of the specimen is measured with a commercial autocorrelator (Carpe, APE GmbH). The spectral width is varied by changing the position of an intracavity prism. Sample solutions of TMR (Molecular Probes) with concentrations in the nanomolar range were filled into sealable chambers, assuring a constant sample concentration during the measurements.

## Results

The influence of the excitation power on the autocorrelation curve at a fixed wavelength and pulse width is shown in Fig. 1. The amplitude  $G(0)$  of the correlation curve decreases at high excitation powers (Fig. 1a), indicating an increase in the particle number  $N$  and/or a change in the size of the effective detection volume. This effect has been explained previously as a result of saturation [10, 19]. An effect typical of photobleaching is shown in Fig. 1b, where the normalized correlation functions decay faster at higher powers. The dye molecules are being bleached while diffusing through the detection volume, thus leading to a decrease of the apparent diffusion time. The inset shows that the effective molecular brightness  $\eta$  initially increases nearly quadratically with excitation power, reaches its maximum value of  $\eta_{\text{max}} = 34$  kHz/molecule at 22 mW and slowly decreases at even higher powers.

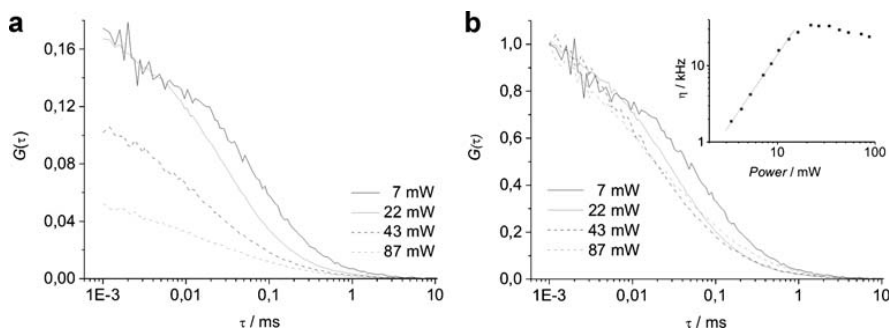


**Fig. 1** The excitation power dependence of the autocorrelation function for a 14 nMol/l solution of TMR ( $\lambda=850$  nm,  $\tau_p=160$  fs). With increasing laser power, both the amplitude  $G(t)$  **a** and the diffusion time **b** decrease. In **(b)** the curves are normalized at  $\tau=1$   $\mu$ s. A change in the shape of the normalized ACF for very high powers

can be observed. The *inset*, plotted at a double logarithmic scale, shows the nearly quadratic dependence of the molecular brightness on the excitation power at low excitation powers up to 15 mW (slope=1.87). At powers above 40 mW,  $\eta$  decreases, which has been attributed to fluorescence saturation and photobleaching [10, 11]

Figure 2 depicts the recorded two-photon spectral dependence of the maximum molecular brightness for different excitation powers but constant pulse width in the accessible range of the Titanium:Sapphire laser between 780 and 930 nm. Measurements were performed at a step size of 10 nm, corresponding to the spectral width of the excitation pulses. For each wavelength,  $\eta$  was recorded at various excitation powers while keeping the spectral and temporal widths of the pulses constant at 10 nm and 160 fs (FWHM), respectively. Uncorrelated background was corrected for as described previously [17, 20] for each individual measurement separately. The spectral variation of the maximum molecular brightness  $\eta_{max}$  dependent on excitation intensity is plotted in Fig. 3. This “maximum- $\eta$ ” excitation spectrum of TMR is qualitatively comparable to the published two-

photon excitation spectrum of a similar dye Rhodamine B [13], indicating that the maximum achievable brightness is obtained by exciting with the wavelength corresponding to the maximum two-photon cross-section. For this reason, the excitation wavelength 850 nm was used for all subsequent measurements.

To control the temporal characteristics of the excitation laser pulses, it is necessary to characterize the pulse broadening by the optical elements in the beam path. Compared to the objective, the induced group velocity dispersion of all other optical elements, such as the beam expander, is negligible. The magnitude of the second order dispersion can be determined from the spectral and temporal pulse widths before entering and after passing the objective. A nearly transform-limited pulse of  $(120\pm 4)$  fs and a spectral width of

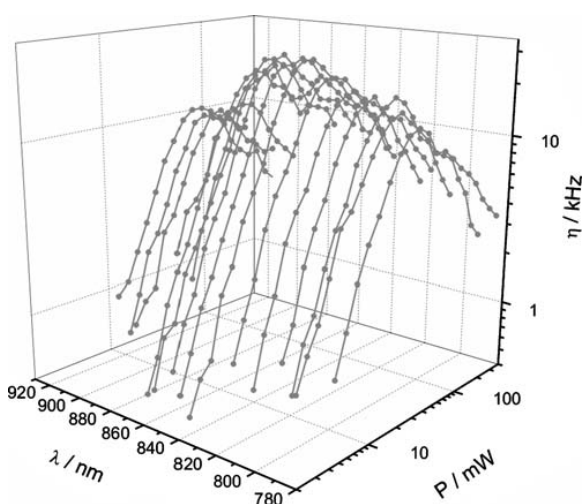


**Fig. 2** Power and wavelength dependence of the molecular brightness in a two-photon FCS measurement for TMR. While the excitation pulse width (160 fs and 10 nm) for each wavelength is kept constant, the excitation power was varied

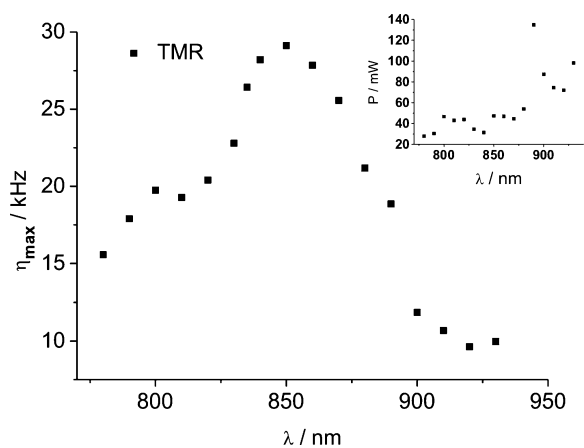


**Fig. 3** Two-photon “maximum- $\eta$ ” excitation spectrum for TMR. The maximum count rate per molecule ( $\eta_{max}$ ) at constant excitation pulse width (160 fs and 10 nm) for each wavelength is displayed. Compared to twice the wavelength of the excitation maximum for one-photon excitation (1,088 nm), the two-photon maximum is shifted to shorter wavelengths. The inset shows the excitation intensities at which the maximum  $\eta$  could be reached

$\Delta\lambda = (10.1 \pm 0.2)$  nm is broadened to  $(161 \pm 4)$  fs by the used objective, yielding a second order dispersion of  $(2,487 \pm 650)$  fs<sup>2</sup>. Comparable values have been obtained by others for similar objectives used in two-photon microscopy [21].

The unwanted pulse broadening in the microscopes objective due to group velocity dispersion was compensated using a method described by Fork et al. [22], which allows the creation of alterable negative group velocity dispersion using a pair of Brewster prisms (made of N-SF10 glass). The objectives dispersion was fully compensated at a total of 16 mm of the prism glass traversed and a prism to prism distance of 64 cm, which corresponds to a theoretical second order dispersion of  $-2,874$  fs<sup>2</sup>. Changing the amount of glass traversed in one of the prisms allowed independent adjustment of the pulse length (Fig. 4).

The inverse proportionality between the fluorescence intensity and the excitation pulse width (Eq. 2) was verified at pulse lengths between 128 and 227 fs (Fig. 5). At the excitation power of 7 mW, a fit to  $a < F(t) > \sim 1/(\tau_p)^\alpha$  dependence for a total of 14 measurements resulted in an average exponent of  $\alpha = 1.03 \pm 0.07$ , in agreement with Eq. 2. At higher excitation powers, the exponent  $\alpha$  decreased notably, indicating severe photobleaching or saturation in the focus of the laser beam.

The power dependencies of the molecular brightness  $\eta$  at constant spectral width ( $\Delta\lambda = 11.4$  nm) for different values of temporal pulse width ( $\tau_p = 128, 159$  and  $227$  fs), and at constant temporal pulse width ( $\tau_p = 213$  fs) for two different values of spectral width ( $\Delta\lambda = 4.9$  and  $12.4$  nm) are depicted in Figs. 6 and 7. At constant spectral width, an increase in brightness  $\eta$  for shorter pulses in the quadratic regime of the

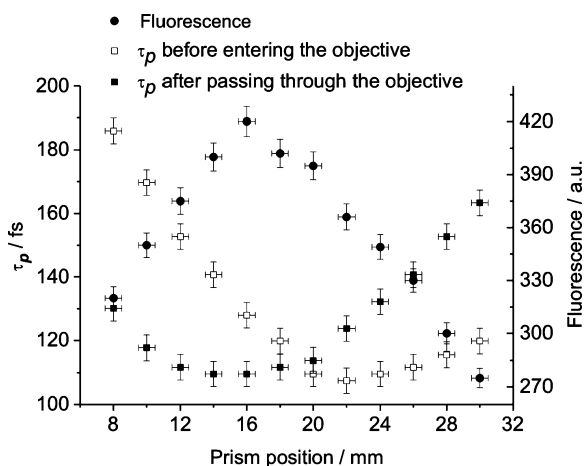


**Fig. 4** Compensation of the group velocity dispersion using two prisms: by changing the amount of prism glass traversed, the amount of induced negative group velocity can be adjusted. In addition to the excitation pulse width before entering and after passing through the objective, the intensity of fluorescence generated in a solution of TMR is shown. The maximum fluorescence intensity coincides with the shortest pulses in the solution (Eq. 2)

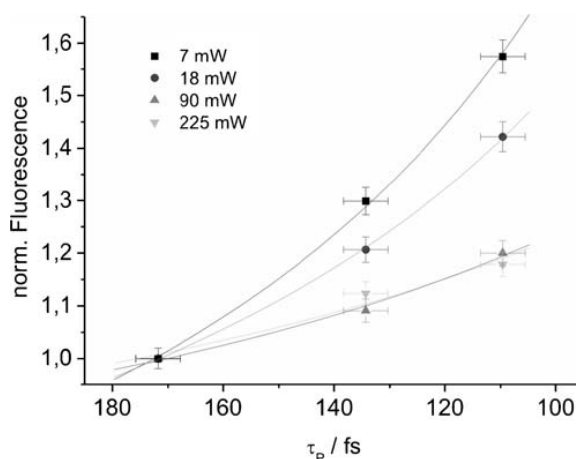


**Fig. 5** Decreasing the pulse width for a 100 nMol/l TMR sample leads to an increase in the normalized fluorescence intensity. Data points were fitted to a  $1/(\tau_p)^\alpha$  dependence resulting in an exponent of  $\alpha = 1.03 \pm 0.07$  for an excitation power of 7 mW, in agreement with Eq. 2. For powers above 7 mW, the fluorescence increase is reduced, indicating the onset of photobleaching or saturation effects in the focus of the laser beam

excitation powers could be observed in agreement with Eq. 2. An average increase in  $\eta$  of 48% (128 fs) and 29% (159 fs) compared to 227 fs was observed. At constant temporal width, the brightness  $\eta$  increased by 40% upon broadening the spectral width from 4.9 to 12.4 nm for excitation powers up to 10 mW (quadratic regime). In both cases, the highest achievable molecular brightness was found to be independent of either  $\tau_p$  or  $\Delta\lambda$ , reaching a maximum value of 35 kHz/molecule. Similarly, the maximum brightness  $\eta$

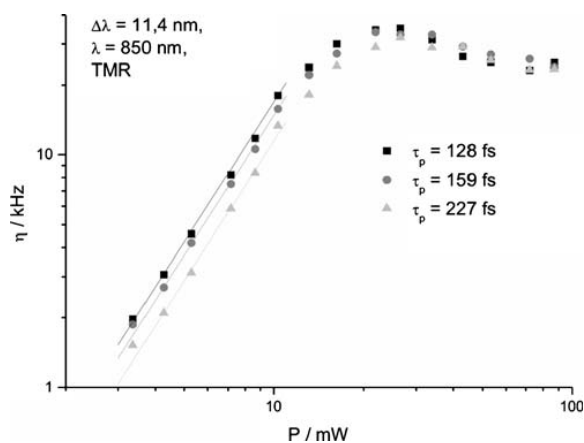


**Fig. 6** Excitation power dependence of the molecular brightness  $\eta$  measured with two-photon FCS for TMR at three different excitation pulse widths. While keeping the spectral width constant at 11.4 nm, the pulse width between 128 and 227 fs using the prism compressor described in the text. An increase in  $\eta$  with shorter  $\tau_p$  (48% for 128 fs and 29% for 159 fs compared to 227 fs) can be observed in the quadratic regime of the excitation power dependence. For comparison, the quadratic slopes are plotted

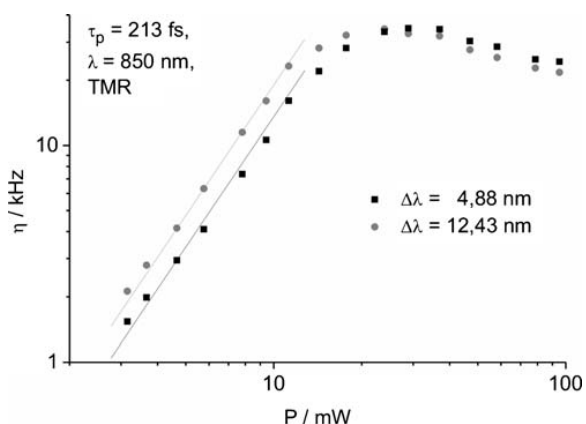


**Fig. 7** Measured excitation power dependence of the molecular brightness  $\eta$  for TMR for two different spectral widths at a constant temporal pulse width of 213 fs. For excitation powers of up to 10 mW, an increase of 40% in  $\eta$  upon extending the spectral width from 4.9 to 12.4 nm could be observed. For comparison, the quadratic slopes are plotted

within the quadratic regime before onset of photobleaching or saturation is independent of  $\tau_p$  or  $\Delta\lambda$ .

## Conclusions

Two-photon pulsed excitation of fluorophores depends, apart from the excitation intensity and wavelength, on the temporal and spectral width of the femtosecond excitation pulses. In FCS, high fluorescence yields, quantified by molecular brightness  $\eta$ , are required for high signal-to-noise ratios. However, high excitation intensities generally needed to achieve high  $\eta$  can cause saturation and/or photobleaching, leading to distortions in autocorrelations curves. We have investigated the effect of the above mentioned parameters influencing two-photon excitation on molecular brightness, with the goal to find their optimal values (i. e. the values leading to the highest molecular brightness before the distortions become apparent) in the range accessible with a commercial infrared femtosecond laser and a relatively simple pre-chirping unit.

The measurements at different excitation wavelengths showed that there clearly is an optimal wavelength at which both the highest maximum molecular brightness  $\eta_{\max}$ , and the highest molecular brightness within the quadratic range can be reached. This is the wavelength of maximum two-photon cross-section, since at constant excitation intensity within the quadratic range, this wavelength yields the highest maximum brightness.

This result also indicates that saturation of the  $S_0$ – $S_1$  transition is not the only factor limiting the maximum molecular brightness  $\eta_{\max}$ . If this was the case, we would expect to reach the same saturation-limited value of

maximum brightness at all excitation wavelengths. Of course, at wavelengths with low two-photon cross-section, higher excitation intensity would be needed to reach this value. We have, however, observed lower maximum brightness values at wavelengths with lower two-photon cross-section. Photobleaching via the population of other excited states is a likely cause, resulting in apparently shorter diffusion times at high excitation intensities (Fig. 1). With the yield of fluorescence and yield of photobleaching both being wavelength- and intensity-dependent, the excitation wavelength 850 nm gives the best ratio of fluorescence yield to photobleaching yield.

Having identified the optimal excitation wavelength, two additional parameters can be relatively easily modified with experimental setups commonly used for two-photon FCS: temporal and spectral pulse width of excitation. Both of them can, in principle, affect excitation and photobleaching efficiencies in the same way as the excitation wavelength, and it is therefore important to check whether an optimization procedure for these parameters is required, as for the wavelength, to obtain best results in FCS, i.e., if a combination of the two can be found where the molecular brightness is maximized.

At very low excitation intensities, the expected inverse proportionality between the fluorescence signal and the temporal width of the excitation pulses is observed. This results in an increase of molecular brightness for shorter temporal width in the quadratic regime, where experiments should be performed in order to minimize errors in the quantification of  $N$  and  $\tau_D$  (Figs. 1, 6 and 7), and also coincides with observations in two-photon microscopy, where linear chirping of the excitation pulses was shown to lead to a reduction in fluorescence signal intensity [23]. However, the highest molecular brightness achievable is independent of the pulse length (Fig. 6) in the regime probed here.

Similar to the temporal width dependence, the molecular brightness exhibits a characteristic spectral width dependence. It is unclear whether this dependence is due to the broader range of accessible excitation wavelengths allowing multiple excitation pathways, or whether it is an effect of different pulse shape [24, 25]. As observed for the temporal pulse width, the spectral pulse width does not affect the maximum achievable brightness.

We conclude, that while there is an optimum excitation wavelength coinciding with the wavelength of maximum two-photon cross-section, the maximum achievable molecular brightness is independent of the temporal and spectral widths of the excitation pulses in the regime analyzed for TMR (similar results were obtained for eGFP, data not shown). This observation indicates that the temporal and spectral pulse widths affect the excitation and photobleaching yields in a similar manner, allowing for no settings with clear improvement of fluorescence to photobleaching yield ratio.

In practice, the total power used to illuminate the sample may be important for reasons other than prevention of saturation or photobleaching, for example, minimizing the phototoxicity and photodamage to biological specimens. Then, in order to minimize possible artifacts and damage to the sample due to intensity-dependent processes, it is desirable to keep the total laser irradiance as low as possible. For a given excitation power, the highest brightness is achieved by minimizing the temporal width and maximizing the spectral width of the excitation pulses. It can therefore be advantageous to implement the presented pre-chirping setup into a two-photon FCS system. In most cases, however, such a careful control and optimization of these pulse parameters is unnecessary, thereby simplifying the experimental setup and performance of two-photon FCS measurements and making them better adaptive for use in biological contexts.

**Acknowledgments** This work was supported by EFRE grant No. 4212/04-02.

## References

- Haustein E, Schwille P (2003) *Methods* 29:153–166
- Bacia K, Kim SA, Schwille P (2006) *Nat Meth* 3:83–89
- Schwille P, Haupts U, Maiti S, Webb WW (1999) *Biophys J* 77:2251–2265
- Denk W, Strickler JH, Webb WW (1990) *Science* 148:73–79
- Berland KM, So PTC, Gratton E (1995) *Biophys J* 68:694–701
- Heinze KG, Koltermann A, Schwille P (2000) *PNAS* 19:10377–10382
- Heinze KG, Jahnz M, Schwille P (2004) *Biophys J* 86:506–516
- Kim SA, Heinze KG, Waxham MN, Schwille P (2004) *PNAS* 101:105–110
- Kim SA, Heinze KG, Bacia K, Waxham MN, Schwille P (2005) *Biophys J* 88:4319–4336
- Berland KM, Shen G (2003) *Appl Opt* 42:5566–5576
- Dittrich PS, Schwille P (2001) *Appl Phys B* 73:829–837
- Eggeling C, Volkmer A, Seidel CAM (2005) *Chem Phys Chem* 6:791–804
- Xu C, Webb WW (1996) *J Opt Soc Am B* 13:481–491
- Niesner R, Roth W, Gerike K-H (2004) *Chem Phys Chem* 5:678–687
- Nagy A, Wu J, Berland KM (2005) *Biophys J* 89:2077–2090
- Iyer V, Rossow MJ, Waxham MN (2006) *J Opt Soc Am B* 23:1420–1433
- Koppel DE (1974) *Phys Rev A* 10:1938–1945
- Kask P, Günther R, Axhausen P (1997) *Eur Biophys J* 25:163–169
- Gregor I, Patra D, Enderlein J (2005) *Chem Phys Chem* 6:164–170
- NL Thompson (1991) *Fluorescence correlation spectroscopy*. In: Lakowicz JR (ed) *Topics in fluorescence spectroscopy*, vol. 1. Plenum Press, pp 337–378
- Guild JB, Xu C, Webb WW (1997) *Appl Opt* 36:397–401
- Fork RL, Martinez OE, Gordon JP (1984) *Opt Lett* 9:150–152
- Wolleschensky R, Feurer T, Sauerbrey R, Simon U (1998) *Appl Phys B* 67:87–94
- Bardeen CJ, Yakovlev V, Squier JA, Wilson KR, Carpenter SD, Weber PM (1999) *J Biomed Opt* 4:362–367
- Pastirk I, Dela Cruz JM, Walowicz KA, Lozovoy VV, Dantus M (2003) *Opt Expr* 11:1695–1701

A8

**Characterization of protein dynamics in asymmetric cell division by scanning fluorescence correlation spectroscopy**

Z. Petrášek, C. Hoegge, A. Mashaghi, T. Ohrt, A. A. Hyman and P. Schwille  
*Biophys. J.*, 95(11):5476–5486, 2008.



## Characterization of Protein Dynamics in Asymmetric Cell Division by Scanning Fluorescence Correlation Spectroscopy

Zdeněk Petrášek,\* Carsten Hoegge,<sup>†</sup> Alireza Mashaghi,<sup>†</sup> Thomas Ohrt,\* Anthony A. Hyman,<sup>†</sup> and Petra Schwillie\*

\*Biophysics Group, Biotechnologisches Zentrum, Technische Universität Dresden, Dresden, Germany; and <sup>†</sup>Max Planck Institute of Molecular Cell Biology and Genetics, Dresden, Germany

**ABSTRACT** The development and differentiation of complex organisms from the single fertilized egg is regulated by a variety of processes that all rely on the distribution and interaction of proteins. Despite the tight regulation of these processes with respect to temporal and spatial protein localization, exact quantification of the underlying parameters, such as concentrations and distribution coefficients, has so far been problematic. Recent experiments suggest that fluorescence correlation spectroscopy on a single molecule level in living cells has great promise in revealing these parameters with high precision. The optically challenging situation in multicellular systems such as embryos can be ameliorated by two-photon excitation, where scattering background and cumulative photobleaching is limited. A more severe problem is posed by the large range of molecular mobilities observed at the same time, as standard FCS relies strongly on the presence of mobility-induced fluctuations. In this study, we overcame the limitations of standard FCS. We analyzed *in vivo* polarity protein PAR-2 from eggs of *Caenorhabditis elegans* by beam-scanning FCS in the cytosol and on the cortex of *C. elegans* before asymmetric cell division. The surprising result is that the distribution of PAR-2 is largely uncoupled from the movement of cytoskeletal components of the cortex. These results call for a more systematic future investigation of the different cortical elements, and show that the FCS technique can contribute to answering these questions, by providing a complementary approach that can reveal insights not obtainable by other techniques.

### INTRODUCTION

Asymmetric division of early embryonic cells is essential for future cell diversity and is preceded by the establishment of cell polarity. A polarization signal leads to distinct concentrations of polarity factors in different cellular domains of the cell.

A good system for studies on polarization and asymmetric cell division is the one-cell *C. elegans* embryo (1–3). Here the first cell division is regulated by PAR proteins, among others (3–5), and requires the motility of the highly dynamic actomyosin cortex (contractions and flows) and the asymmetric localization of PAR proteins (6–8).

The polarization of the fertilized embryo is initiated by an interaction of the centrosome with the cortex (9) and leads to a cortical flow of actomyosin from the posterior toward the anterior part of the cell. This flow is closely connected with the accumulation of PAR-1 and PAR-2 at the posterior, and the restriction of PAR-3, PAR-6, and PKC-3 to the anterior half of the cell.

At a later maintenance phase, the asymmetric redistribution of the PAR proteins back to the whole cortex is prevented by their antagonistic interactions (10). Non-muscle myosin NMY-2, a component of the actomyosin cortex, is required through all phases, and after polarity establishment asymmetrically distributes with a more contractile cortex on the anterior side.

Binding of PAR-1 and PAR-2 to the cortex depends on a functional actomyosin cytoskeleton, as inhibition by cytochalasin B, an actin inhibitor, or downregulation of NMY-2 by RNAi inhibits binding. While direct interaction between PAR-2 and NMY-2 has not been demonstrated, PAR-1 can bind directly to NMY-2 *in vivo*, and PAR-1 localization is dependent on PAR-2 (7,8).

Although several polarity components of the *Caenorhabditis elegans* embryo have been discovered, it remains largely unclear how the asymmetry of the cortex-associated proteins before and during the first division is established and maintained, and how the proteins interact, move, and redistribute within the embryo on the molecular level.

The localization and redistribution of proteins involved in polarity is usually studied by fluorescence microscopy. While this imaging technique reveals the protein distribution and dynamics in living embryo on the second or subsecond timescale, its low temporal resolution does not allow the observation of fast dynamics on the scale of microseconds to milliseconds.

Here we apply standard fluorescence correlation spectroscopy (FCS) to measure the relatively fast diffusion of PAR-2, NMY-2, CDC-37, and a membrane-binding PH domain protein in cytosol. Circular scanning FCS (sFCS) is employed to investigate the considerably slower motion of the two cortex-associated proteins PAR-2 and NMY-2, a task practically impossible with standard FCS.

In FCS, the statistical analysis of the detected fluorescence signal by means of the autocorrelation function reveals important information about the dynamics of the diffusing

Submitted April 10, 2008, and accepted for publication August 26, 2008.

Zdeněk Petrášek and Carsten Hoegge contributed equally to this work.

Address reprint requests to Petra Schwillie, E-mail: petra.schwillie@biotec.tu-dresden.de.

Editor: Alberto Diaspro.

© 2008 by the Biophysical Society  
0006-3495/08/12/5476/11 \$2.00

doi: 10.1529/biophysj.108.135152

species, such as diffusion coefficients and the type of motion (11–13). Scanning FCS, a modification of the standard FCS with the measurement volume being scanned in a controlled fashion across the sample (14), has been introduced to overcome problems with low statistical accuracy in systems with slow diffusion (15,16), to minimize the effects of photobleaching of slowly diffusing molecules, or for other reasons (17–19).

We show that PAR-2 and non-muscle myosin NMY-2 diffuse freely in cytoplasm, with diffusion coefficients lower than expected in aqueous environment, most likely due to collisions with large components of the crowded cytoplasm, formation of larger complexes, or due to transient binding. On the cortex, both proteins exhibit highly dynamic non-uniform distribution. NMY-2 is localized in well-defined patches of the actomyosin cortex that changes its contractility throughout the cell cycle (6). Interestingly, PAR-2 assembles in a less discrete and more dynamic pattern than NMY-2. Scanning FCS autocorrelations of NMY-2 decay at a longer timescale with a sharp falloff, characteristic of directed motion. On contrary, PAR-2 motion is faster and the autocorrelation decay is more gradual, indicating multicomponent diffusive or even subdiffusive behavior.

The presented results show that FCS and sFCS are techniques suitable for the study of protein dynamics in an asymmetric dividing embryo on the temporal scales ranging from microseconds to seconds, and demonstrate that PAR-2 and NMY-2 show largely independent motion on the cortex.

## MATERIALS AND METHODS

### Experimental setup

The experiments were performed on a homebuilt two-photon laser scanning microscope (14,20) using an UPLAPO 60× W3/IR objective (Olympus, Hercules, CA). The excitation was provided by a tunable Ti:Sapphire laser (Mira 900-F, Coherent, Santa Clara, CA) with the wavelength set to 920 nm, and an average power of 5 mW. The laser beam is steered by two galvanometer scanners fully controllable by software, allowing the system to operate in two modes: a conventional imaging laser scanning microscope mode, and an sFCS mode, where the beam is scanned along a circular path with a user-defined radius and frequency. The fluorescence, collected by the objective and transmitted through an appropriate emission filter, is detected by an avalanche photodiode (model No. SPCM-CD2801, PerkinElmer, Wellesley, MA). For correlation measurements, the stream of detected photocounts is either directly autocorrelated with a multiple-tau hardware correlator (ALV-6000, ALV, Langen, Germany), or processed by the SPC-830 module (21) (Becker & Hickl, Berlin, Germany) to obtain timing of every photoncount with resolution 13.1 ns, and stored for further analysis.

The time of a point-FCS measurement at one location was  $10 \times 10$  s. The time of one sFCS measurement was  $\sim 100$  s, corresponding to 30,000 scan orbits at the used frequency of 300 Hz. The scan radii used in this work were in the range 2–9  $\mu\text{m}$ , depending on the size of the flat part of the embryo cortex.

### Biological system

*C. elegans* worms were cultured at 16°C on nematode growth media plates seeded with OP50 bacteria, and shifted to 25°C a day before imaging (22).

GFP::PAR-2 (TH129) (23), GFP::PH-PLC181 (24) and NMY-2::GFP (25) were described before. Briefly, GFP fusion proteins were expressed from stable transgenic worm lines from the pTH-GFP vector under the control of the pie-1 promoter. A transgenic worm line expressing GFP::CDC-37 from the pie-1 promoter (vector pTH-GFP-Gateway, containing the enhanced GFP variant) was produced by microparticle bombardment of unc-119(ed3) worms (26).

The fertilized eggs taken from adult worms were released by slicing animals open with a pair of needles in M9 buffer. Then the eggs were placed on agarose gel spread in a thin layer on a coverslip, and covered with another coverslip. The specimen was turned upside down and observed on an inverted microscope, as described above. The embryos were observed either with objective focus in the equatorial plane (cytoplasm FCS measurements), or with the focus near the coverslip, where the embryo was partially flattened and larger part of the embryo cortex was in focus, thus allowing sFCS measurements.

The sFCS measurements were performed in the maintenance phase after pseudocleavage and before the second cell division. During this time period, the cortex is relaxed after the myosin contractile foci have disassembled, and does not show strong contractile activity as observed in the polarity establishment phase (6). No measurements were performed during pseudocleavage and cytokinesis because of large-scale cortical movements (cell cortex rotation) accompanying cell division. However, more precise specification concerning the phase of the cell cycle was not made, due to the relatively long acquisition time needed ( $\sim 100$  s) and the comparatively short period without large-scale coordinated cortical movements (approximately minutes).

### Data analysis

The fluorescence autocorrelation curves  $g(\tau)$  obtained with the hardware correlator according to the definition

$$g(\tau) = \frac{\langle \delta F(t) \delta F(t + \tau) \rangle}{\langle F(t) \rangle^2} \quad (1)$$

were analyzed using the model of free diffusion in three-dimensional space (12),

$$g(\tau) = \frac{g_0}{\left(1 + \frac{\tau}{\tau_D}\right) \sqrt{1 + \frac{\tau}{w^2 \tau_D}}}, \quad (2)$$

where  $\langle F(t) \rangle$  is the average fluorescence intensity over the whole measurement,  $\delta F(t) \equiv F(t) - \langle F(t) \rangle$ ,  $g_0$  is the amplitude of the autocorrelation function,  $\tau_D = a^2/D$  is the diffusion time,  $a$  is the  $e^{-1/2}$  width of the measurement volume approximated by a Gaussian function ( $a = 0.14 \mu\text{m}$  in our case),  $w$  is the form factor describing the extension of the measurement volume in the axial direction, and  $D$  is the diffusion coefficient. The autocorrelation curves measured on the flattened part of the cell cortex were analyzed by an equivalent model for diffusion in two dimensions, which can be obtained from Eq. 2 by letting  $w \rightarrow \infty$ .

The stream of photocounts recorded during the sFCS measurements was stored and autocorrelated off-line. Since the relevant dynamics occurs on the timescales only 1–2 orders of magnitude shorter than the permissible time of the measurement, the correlation analysis is affected by poor statistical accuracy at long correlation times. For this reason, compensated normalization was chosen in the calculation of the correlations, as it has been shown to provide higher accuracy estimates of the correlations at long correlation times (27). The autocorrelation with compensated normalization is defined in the following way:

$$g(\tau_k) = \frac{\langle (F(t_i)F(t_{i+k}))_i - F_0 F_k \rangle}{F_0^2}, \quad (3)$$

where

$$F_0 = \frac{1}{N-k} \sum_{i=0}^{N-1-k} F(t_i), \quad F_k = \frac{1}{N-k} \sum_{i=k}^{N-1} F(t_i). \quad (4)$$

Scanning the measurement volume introduces periodic oscillations into the autocorrelation curve persisting typically as long as the correlation has a nonzero value. To preserve this periodic pattern, the autocorrelation has to be calculated with sufficiently high resolution even at long correlation times. The common multiple-tau correlation technique does not have sufficient temporal resolution at larger lag times, causing the oscillations to average out. The scanning autocorrelation curves were therefore calculated with linearly spaced channels of constant width (1  $\mu\text{s}$  or 10  $\mu\text{s}$ ). To achieve realistic computation times, the correlation was calculated via Fourier transform of the detected photoncount sequence  $\mathcal{F}(F(t))$  using the following relationship:

$$G(\tau) = \int F(t)F(t + \tau)dt = \mathcal{F}^{-1}(|\mathcal{F}(F(t))|^2). \quad (5)$$

The details on the implementation of the calculation of linear autocorrelation of a long data stream using Fourier transform have been published elsewhere (28).

The long-scale fluorescence fluctuations caused by the global changes of the fluorescence pattern resulted in fluctuations in the tails of the sFCS autocorrelation functions. These fluctuations do not reflect the local dynamics of the fluorescence pattern (fluctuations at any given position along the scanned circle), and were therefore filtered out from the calculated curves by the following procedure. The fluctuating fluorescence signal  $F(t)$  was assumed to consist of the local fluctuating signal  $f(t)$  modulated by a slowly changing global modulation function  $h(t)$ :  $F(t) = f(t)h(t)$ . The function  $h(t)$  was estimated from the measured fluorescence  $F(t)$  by smoothing  $F(t)$  with a bin width of 0.13 s, which corresponds to 39 scan periods. It follows from the above-mentioned definition that the autocorrelation  $g_F(\tau)$  of  $F(t)$  is related to the autocorrelation  $g_f(\tau)$  of  $f(t)$  and the autocorrelation  $g_h(\tau)$  of  $h(t)$  in the following way:

$$g_F(\tau) + 1 = (g_f(\tau) + 1)(g_h(\tau) + 1). \quad (6)$$

The desired autocorrelation  $g_f(\tau)$  was then calculated from Eq. 6 using known  $g_F(\tau)$  and  $g_h(\tau)$ . Since the effective number of measurement locations along the circle is large, this procedure does not affect the resulting temporal autocorrelation profile, as would be the case in a measurement with fixed detection volume. This filtering procedure is demonstrated in Fig. S3 in Supplementary Material, Data S1.

Similarly, average nonuniformity of fluorescence along the scanned circle can produce additional oscillations in the autocorrelation curve, reflecting this nonuniformity. Again, these fluctuations can be filtered out applying Eq. 6, where  $h(t)$  is now the average fluorescence intensity along the scanned circle over the whole measurement, and  $g_h(\tau)$  is the autocorrelation of  $h(t)$  (see Fig. S3 in Data S1). The effect of this procedure is similar to the phase-normalized autocorrelation introduced by Skinner et al. (18) to separate fluctuations due to immobilized particles.

Free diffusion on a two-dimensional surface while scanning the beam with frequency  $\omega$  in a circle of radius  $R$  leads to the following model autocorrelation (16):

$$g(\tau) = \frac{g_0}{1 + \frac{\tau}{\tau_D}} e^{-\frac{R^2 \sin^2(\omega\tau/2)}{a^2(1 + \tau/\tau_D)}}. \quad (7)$$

The preexponential term corresponds to the standard autocorrelation of diffusion process in two dimensions, and the exponential factor describes the periodic modulation due to the scanning motion. The scanning autocorrelation consists of peaks located at correlation times equal to the integer multiples of the scan period  $T$ , that is, at times when the scanning focus returns to the initial position. The peak maxima coincide with the autocorrelation value that would be obtained in the absence of scanning (the preexponential term in Eq. 7). When the scan radius  $R$  is much larger than the size of the measurement volume  $a$ , the correlation between the peaks is practically zero, since the fluorescence at points located far from each other (far compared to  $a$ ) is generally uncorrelated. The width of the peaks forming the autocorrelation increases with the correlation time, as the molecules

diffuse further and further away from their initial position (see Fig. S2 in Data S1). When the molecular motion is much slower than the scanning speed, the shape of the peaks in the autocorrelation function is largely determined by the exponential factor in Eq. 7. Therefore, the exponential factor with an effective width parameter  $a'^2 = a^2(1 + \tau/\tau_D)/R^2$  and an amplitude  $A$  as two fitting parameters were used to fit the peaks of the experimental sFCS autocorrelation functions.

The scanning autocorrelation can be viewed as a part of the full spatiotemporal correlation  $g(x, \tau)$ ; that is, the correlation of fluorescence between two locations spaced by the distance  $x$  at two time points delayed by the time  $\tau$ . This becomes apparent when one realizes that only the values at integral multiples of the scan period are autocorrelations at the same location, while the values at all other times are actually spatial cross correlations between two locations at a distance  $x$ :

$$x = 2R \sin(\omega\tau/2). \quad (8)$$

This equation relates the correlation time  $\tau$  to the spatial correlation coordinate  $x$ , or alternatively, to the phase  $\varphi$  of the circular motion:  $\varphi = \omega\tau$ . Scanning FCS samples the full spatiotemporal correlation at coordinates  $(x, \tau)$  linked by Eq. 8. This sampling is fine enough when the scanning motion is much faster than the relevant timescales determined by the investigated molecular motion. The sFCS autocorrelation can then be displayed as a two-dimensional plot with the axes formed by the  $x$  and  $\tau$  coordinates, and the correlation value color-coded.

The spatiotemporal correlation  $g(x, \tau)$  contains more information than a temporal correlation  $g(\tau)$ , and possibility to measure it experimentally gives a better chance to distinguish between different models of transport. For example, the spatiotemporal correlation of diffusion in two dimensions

$$g(x, \tau) = \frac{g_0}{1 + \frac{\tau}{\tau_D}} e^{-\frac{x^2}{4a^2(1 + \tau/\tau_D)}} \quad (9)$$

exhibits broadening in space with longer correlation times as the molecules diffuse from their initial position. On the other hand, binding to/detachment form a surface,

$$g(x, \tau) = g_0 e^{-k\tau} e^{-\frac{x^2}{4a^2}}, \quad (10)$$

does not show any spatial broadening, since the molecules do not move laterally and disappear fast after detachment from the surface. Although these two models already show different dependence of the autocorrelation  $g(\tau)$  on the correlation time, the additional differences in spatial correlation, accessible experimentally with sFCS, can help to better discriminate between alternative models (see Fig. S1 in Data S1 for several models of spatiotemporal correlation).

## RESULTS

### Diffusion in cytoplasm

The PAR-2 and NMY-2 proteins are known to localize in cytoplasm and in different parts of the embryo cortex, depending on the phase of the cell cycle (29). Whereas PAR-2 localizes almost exclusively on the posterior cortex after polarity establishment, NMY-2 localizes predominantly on the anterior cortex, while being less contractile on the posterior (Fig. 1, A and B). However, posterior localization of PAR-2 depends on NMY-2 (7). Therefore, an interesting question is whether PAR-2 can bind to the cortex directly by association with NMY-2. We tested this hypothesis by studying the dynamics of both proteins in the cytosol and on the cortex by FCS.

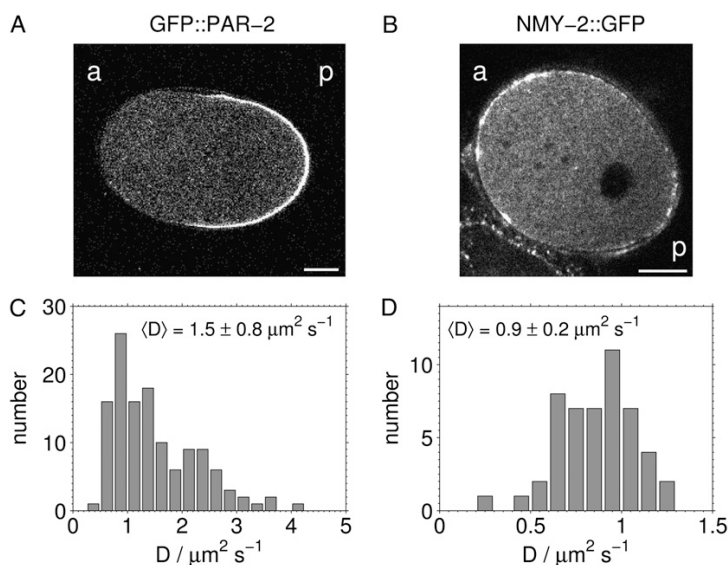


FIGURE 1 Diffusion coefficients of GFP::PAR-2 (A and C) and NMY-2::GFP (B and D) in the cytosol. The measurement volume was positioned into different parts of the cytosol, while focused into the midplane of the embryo (A and B), and the measured autocorrelation curves were fitted to Eq. 2. The distributions of the obtained diffusion coefficients  $D$  are shown in panels C (GFP::PAR-2) and D (NMY-2::GFP). (Scale bar, 10  $\mu\text{m}$ . *a*, anterior; *p*, posterior.)

We have employed two-photon FCS with the measurement volume positioned in a fixed location within the cytoplasm to measure the mobility of GFP::PAR-2 and NMY-2::GFP. The measurement volume was positioned away from the pronuclei; the movement of the pronuclei did not influence the measured protein dynamics because it occurs on a much longer timescale. The autocorrelation curves were analyzed using the model of diffusion in three dimensions (Eq. 2). The distributions of the obtained diffusion coefficients are shown in Fig. 1 C (GFP::PAR-2) and Fig. 1 D (NMY-2::GFP). The mean values of the diffusion coefficients determined from the measured distributions are shown in Table 1, with the errors indicating the widths of the distributions. The differences in the distributions of the diffusion coefficients of the two proteins indicate that PAR-2 and NMY-2 in the cytosol do not diffuse as a part of a common complex. The possibility to use Eq. 2 to describe the measured autocorrelations indicates predominantly diffusive behavior of the two proteins in cytoplasm.

For comparison, we performed analogous FCS measurements on two other proteins in cytosol: GFP::CDC-37 and GFP::PH. CDC-37, a protein of similar size to PAR-2 (Table 1), is required for polarity establishment and mutual exclu-

sion of anterior and posterior PAR proteins (30). It is uniformly distributed in both anterior and posterior halves of the embryo and does not localize on the cortex. The PH domain, a small protein domain derived from mammalian PLC1 $\delta$ 1, is known to bind to PIP<sub>2</sub> lipid present in the plasma membrane, and therefore serves as a membrane marker (24,31). Embryos expressing GFP::PH display very bright fluorescence on the plasma membrane and weaker fluorescence in the cytosol, permitting standard FCS measurements in both. The measured diffusion coefficients of both proteins again exhibit broadened distributions. The mean values together with the standard deviations indicating the distribution widths are shown in Table 1.

In addition to cytosolic diffusion, it was possible to measure standard FCS autocorrelations of the GFP::PH on the membrane, by focusing onto the flattened bottom part of the embryo as described below, and thus preventing the movement of the membrane out of focus. The diffusion of the GFP::PH on the membrane is  $\sim 1$  order-of-magnitude slower than in the cytosol (Table 1). The relatively fast diffusion of all the investigated proteins in cytosol and the PH domain on the membrane (compared to PAR-2 and NMY-2 dynamics on the cortex; see below) means that no distortions due to photobleaching occur.

TABLE 1 Diffusion coefficients determined with FCS

Protein	Location	M/kDa	$D/\mu\text{m}^2 \text{s}^{-1}$
NMY-2	Cytosol	257	$0.9 \pm 0.2$
PAR-2	Cytosol	96	$1.5 \pm 0.8$
CDC-37	Cytosol	69	$4.8 \pm 1.3$
PH	Cytosol	47	$8.1 \pm 2.0$
PH	Membrane	47	$1.1 \pm 0.3$

The error indicates the width of the distribution of  $D$ . The molecular mass  $M$  is inclusive the GFP label.

### Scanning FCS on the cortex

Attempts to perform standard FCS measurements on PAR-2 and NMY-2 localized on the cortex by positioning the measurement volume on the cortex when focused in the embryo midplane (Fig. 1, A and B) did not provide satisfactory results. The main reason was the motion of the embryo caused by its development, on the timescale of  $\sim 100$  s needed for the

measurement. Motion of the cortex as a whole out of the measurement volume cannot be separated from the slow motion of molecules within the cortex, thereby compromising the results.

Another problem with measurements with fixed volume is the low statistical accuracy due to the very slow motion of the molecules on the cortex: during the maximum realistic measurement time, limited by the development of the embryo, insufficient number of molecules passes through the measurement volume, resulting in low accuracy of the averaging procedure. Additionally, photobleaching can occur during the long residence time in the measurement volume.

To overcome these problems, we have used circle sFCS, where the measurement volume is moved along a circular path with a known radius and frequency (16,18). The objective was focused near the coverslip onto the flattened bottom part of the embryo. In this way, the largest possible part of the cortex was simultaneously present in focus. The radius was chosen as large as possible so that the whole scanning path lied within the focused part of the cortex (Fig. 2, *A* and *B*). Longer scan path means that information from effectively more independent volumes is averaged, implying better statistical accuracy. The data obtained in this way represents an average over the scanned path, and it is therefore implicitly assumed that the typical dynamics are the same at all probed locations.

The fluorescence intensity trace was recorded with the SPC-830 module and its autocorrelation was calculated off-line as described in Materials and Methods. Typical autocorrelation curves of GFP::PAR-2 and NMY-2::GFP are shown in Fig. 3, *A* and *B*, respectively. The peaks on the blue curves at times  $nT$ , where  $T$  is the scan period  $T = 1/300$  s, correspond to the autocorrelation at the same location after  $n$

rotations of the measurement volume. The shapes of the peaks (not discernible in the figure) were fitted to the model as expressed by Eq. 7, and the fitted amplitude of every peak is marked as a black dot in the plots in Fig. 3, *A* and *B*. An example of fits to several selected peaks of a GFP::PAR-2 autocorrelation function is shown in Fig. S2 in [Data S1](#). The curve formed by the amplitudes of all peaks then represents the loss of correlation of the fluorescence pattern on the cortex, and reflects the temporal redistribution of this pattern, in a similar way as an ordinary FCS curve reflects the passage of molecules through the measurement volume.

The typical decay of autocorrelation of GFP::PAR-2 was found to differ from that of NMY-2::GFP, as shown in Fig. 4, where several normalized autocorrelation curves (formed by peak maxima as described above) of each protein are plotted. The autocorrelation of GFP::PAR-2 decays over a broad temporal range and cannot be described by simple diffusion with one component (see Fig. 5). Its extended shape suggests multicomponent or anomalous diffusion. The autocorrelation decay of NMY-2::GFP is steeper than the autocorrelation of a two-dimensional diffusional process, possibly indicating contribution of translational motion, which alone leads to a steep  $\exp(-(\tau/\tau_f)^2)$  temporal dependence (32). The motion of NMY-2::GFP on the cortex is slower than GFP::PAR-2, as can be seen by comparison of the curves in Fig. 4. Surprisingly, the dynamics of NMY-2::GFP as characterized by the autocorrelation curves was found to be similar in both anterior and posterior parts of the cell, independently of the higher fluorescence intensity in the anterior part.

The distribution of both the proteins on the cortex was nonuniform, with rapidly changing pattern (Fig. 2, *A* and *B*). The sizes of the features in both cases were near or below the

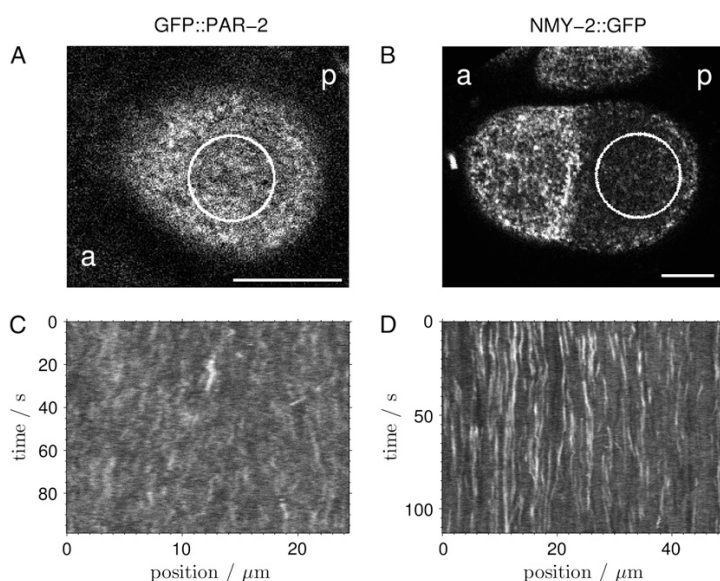


FIGURE 2 Nonuniform fluorescence pattern of GFP::PAR-2 (*A* and *C*) and NMY-2::GFP (*B* and *D*) on the cortex. The objective was focused near the coverslip onto the flattened part of the embryo. The circles in panels *A* and *B* indicate the scan path for sFCS measurements. (*C* and *D*) The fluctuating fluorescence intensity recorded in the sFCS measurement is displayed in a two-dimensional plot, where the horizontal axis corresponds to one revolution (scan period  $T$ ), and the vertical axis to subsequent revolutions during the course of measurement (from *top* to *bottom*). The columns in the plot then show the fluorescence fluctuations at individual positions along the scanned circle. (*C*) GFP::PAR-2, (*D*) NMY-2::GFP. (Scale bar, 10  $\mu\text{m}$ . *a*, anterior; *p*, posterior.)

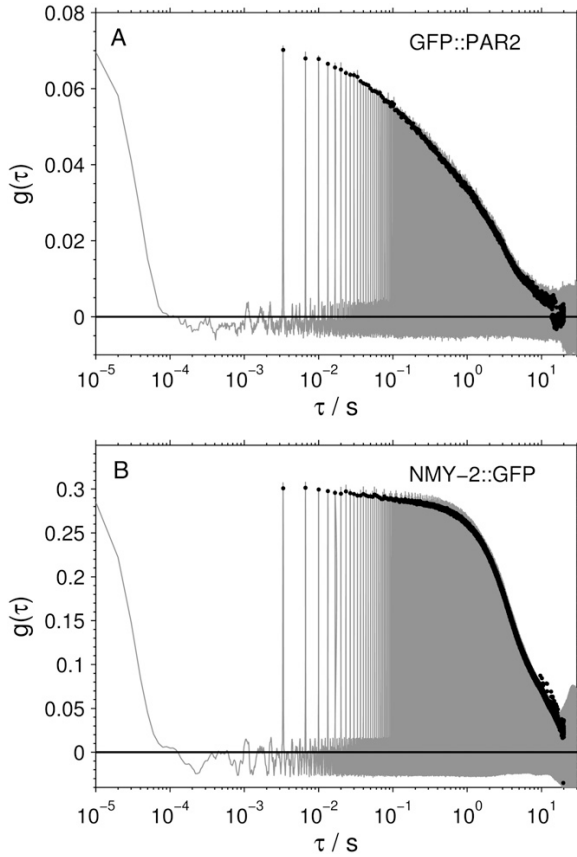


FIGURE 3 The experimental fluorescence autocorrelations from sFCS measurements (shaded). The amplitudes of the peaks obtained from fits to Eq. 7 are indicated by solid dots. (A) GFP::PAR-2, (B) NMY-2::GFP.

optical resolution. The autocorrelation curves describe also the motion and the dynamics of this pattern rather than only the dynamics of individual independently moving molecules. The pattern of NMY-2::GFP consists of bright spots with size comparable to or below the resolution limit (6), whose movement appears to be to some extent coordinated and partially directional (nondiffusive). This can be seen in Fig. 2 D, where the fluorescence intensity from sFCS measurements is plotted in a two-dimensional plot in such a way that each line corresponds to one revolution, the horizontal axis corresponds to points along the circle, and the measurement time increases from the top to the bottom. The inclined vertical traces originate from bright spots crossing the scanned circle at a certain angle. Parallel traces belong to spots moving in the same direction and indicate therefore coordinated motion. The fluorescence distribution of GFP::PAR-2 on the cortex is also found to be nonhomogeneous and highly dynamic. However, it appears to be much less concentrated into discrete spots and its motion is less coordinated (Fig. 2 C).

The character of motion of fluorescently labeled molecules is reflected by spatiotemporal correlation  $g(\tau, x)$ . Therefore,

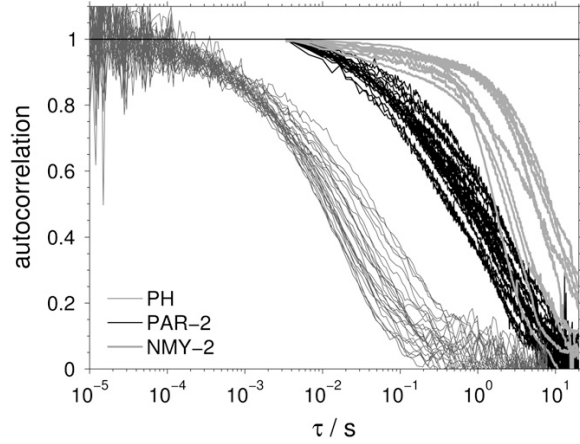


FIGURE 4 Comparison of sFCS autocorrelations of GFP::PAR-2 (black) and NMY-2::GFP (thick gray) on the cortex and FCS autocorrelations of GFP::PH (thin gray) on the membrane from measurements in several embryos. The sFCS autocorrelations are formed by the fitted amplitudes of the peaks as shown in Fig. 3.

the sFCS correlation data were displayed as functions of the correlation coordinates  $(\tau, x)$ , as described in Materials and Methods (Figs. 6 and 7). Both PAR-2 and NMY-2 exhibit spatial broadening of the correlations with increasing correlation time  $\tau$ , as can be better seen in Figs. 6 B and 7 B, where the correlations are normalized at every time  $\tau$  to a maximum. The broadening appears at shorter times in case of PAR-2

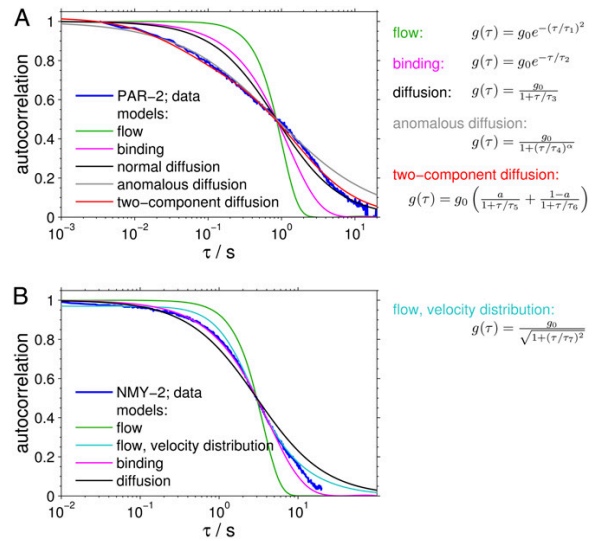


FIGURE 5 Comparison of a typical sFCS autocorrelation (blue) of GFP::PAR-2 (A) and NMY-2::GFP (B) with several simple models of transport: uniform flow (green), binding/dissociation (magenta), normal diffusion (black), anomalous diffusion (gray), normal two-component diffusion (red), and flow with a Gaussian distribution of speeds, centered at  $v = 0: p(v) \sim \exp(-v^2/(2\sigma_v^2))$  (cyan). The parameters  $\tau_i$  are the characteristic time constants of the relevant process.

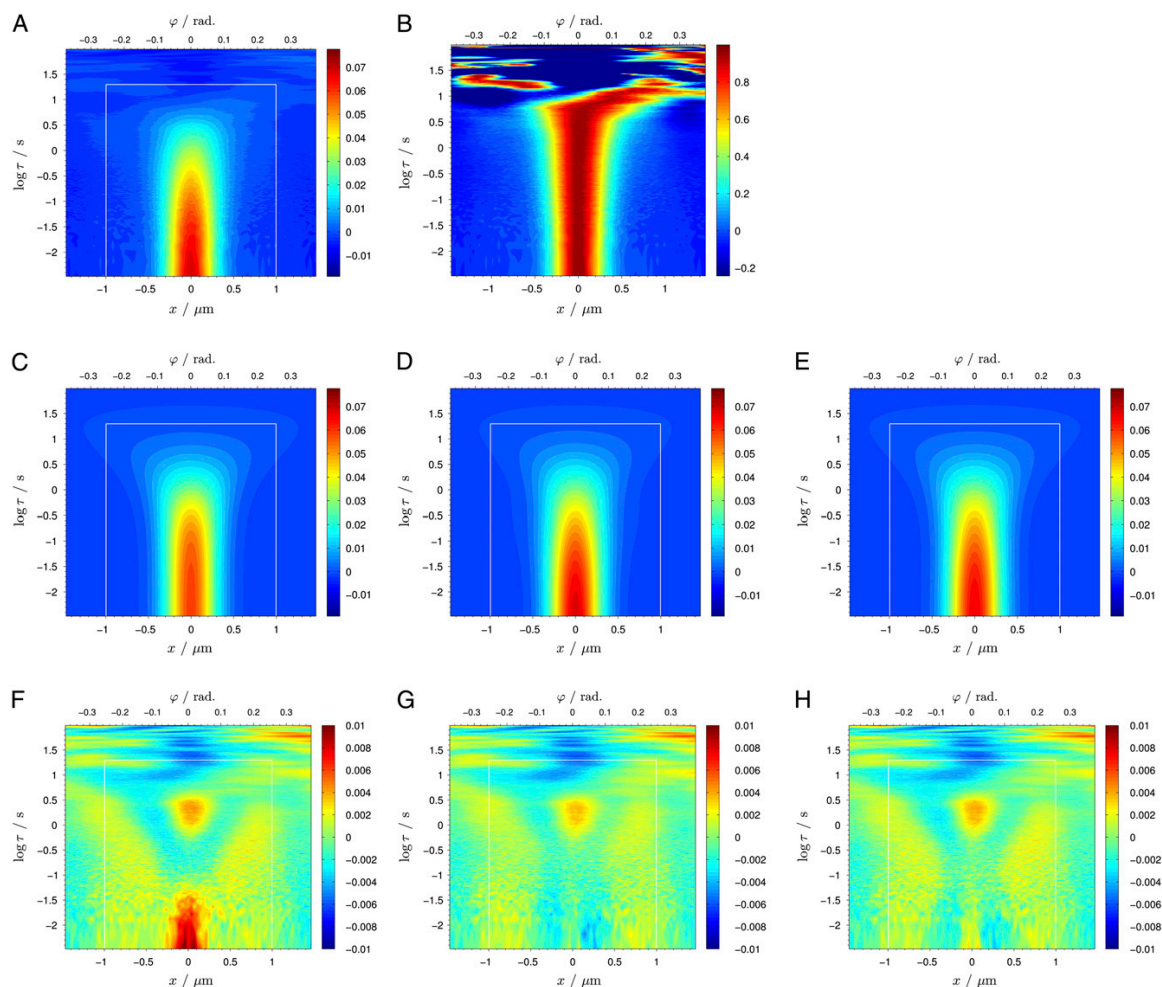


FIGURE 6 sFCS autocorrelation of GFP::PAR-2 displayed in spatiotemporal representation, and fits to three different models. The value  $x$  is the spatial and  $\tau$  the temporal correlation coordinate. (A) The spatiotemporal autocorrelation. (B) The spatiotemporal autocorrelation normalized to the maximum at each  $\tau$  value to emphasize the spatial broadening. (C and F) Fit to a one-component diffusion model and the residuals of the fit ( $\chi^2 = 4.61 \times 10^{-6}$ ). The white rectangle denotes the fitting range. (D and G) Fit to a two-component diffusion model and the fit residuals ( $\chi^2 = 3.99 \times 10^{-6}$ ). (E and H) Fit to a model with one diffusion and one binding/dissociation components, and the fit residuals ( $\chi^2 = 4.37 \times 10^{-6}$ ). The correlation coordinate  $x$  (corresponding to the distance along the scanned circle) can be equivalently expressed by the scan phase  $\varphi$ , or by the time from the peak maximum  $\tau$ . These three coordinates are related to each other in the following way:  $x = 2R \sin(\omega\tau/2)$ ,  $\varphi = \omega\tau$ .

than NMY-2, which is consistent with the shorter correlation times, implying faster motion. The normalized correlations also show that the time  $\tau \sim 10$  s represents a practical accuracy limit in these measurements, beyond which the data are dominated by noise. The PAR-2 correlation was fitted to three models: one-component diffusion, two-component diffusion, and one-component diffusion with one binding/dissociation component, using an appropriate linear combination of Eqs. 9 and 10 (Fig. 6, C–H). As expected from observations made above (Fig. 4), the one-component diffusion model does not describe the data well. Out of the two models with two components, two-component diffusion leads to a better fit with the data than one diffusion and one

binding component, as judged by the residual plots and the values of  $\chi^2$  (Fig. 6, G and H). No fitting of NMY-2 spatiotemporal correlation was attempted, because the spatial features start to appear at correlation times too close to the accuracy limit (Fig. 7 B).

## DISCUSSION

### Scanning FCS on the cortex

The presented results of the sFCS measurements demonstrate that this technique is capable of capturing the dynamics, which is too slow for conventional FCS. By scanning along a

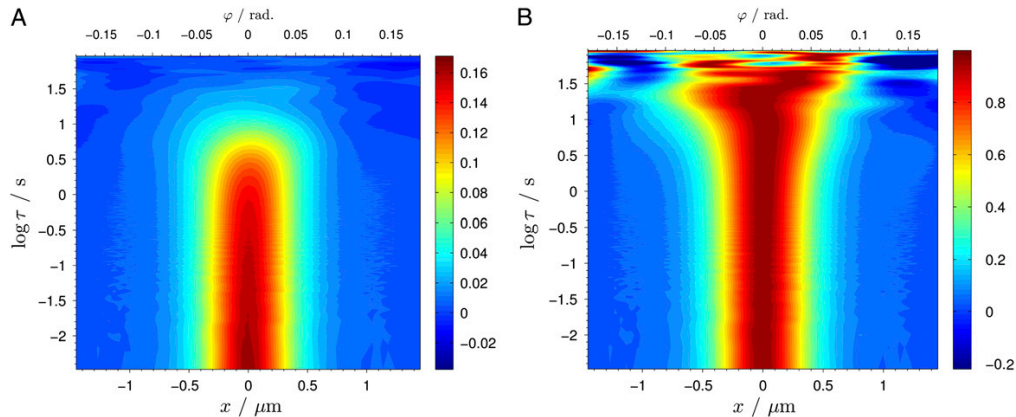


FIGURE 7 sFCS autocorrelation of NMY-2::GFP displayed in spatiotemporal representation. (A) The spatiotemporal autocorrelation. (B) The spatiotemporal autocorrelation normalized to the maximum at each  $\tau$ .

circle, multiple locations are probed pseudo-simultaneously, and sufficient averaging can be achieved in a time shorter by one-to-two orders of magnitude than the time necessary for a measurement with a fixed detection volume. Furthermore, no photobleaching of slowly moving molecules was observed (Fig. 2, C and D), which can be attributed to the fact that each location along the circular path is illuminated for only a small fraction of the scan period  $T$ .

The sFCS correlations represent information averaged along the scanned circle. To see whether there are any statistically significant variations in dynamics at different points, we divided the raw data and calculated autocorrelations at individual locations along the circle (see Fig. S4 in Data S1). The individual curves are strongly affected by poor statistics (which is one of the reasons for averaging over a larger area); however, within the limits of this accuracy, the dynamics are comparable at all points along the circle.

The comparison of the sFCS autocorrelation curves (Fig. 4) of GFP::PAR-2 and NMY-2::GFP shows that the dynamics of both proteins on the cortex are clearly distinct from each other. While the motion of GFP::PAR-2 is faster and has a rather diffusive or subdiffusive character, the motion of NMY-2::GFP is slower and the sharp falloff of the autocorrelation indicates contribution of directed flow. Fig. 5 B shows by comparison with several models that the NMY-2::GFP autocorrelation decay is steeper than that of diffusion, but more gradual than flow with uniform speed. A reasonable assumption of distribution of flow velocities results in an autocorrelation curve with a slope close to the experimental data, as demonstrated on the example of Gaussian velocity distribution  $p(v) \sim \exp(-v^2/(2\sigma_v^2))$ . Although the binding model matches the data well, the observed lateral motion of myosin clusters is not compatible with this model.

The partially coordinated flow of myosin might be related to the deformation of the actin cortex to which the bright spots of NMY-2::GFP are thought to be linked. The different falloff times of the NMY-2::GFP autocorrelation curves are

likely to be caused by natural variations in cortical motion in any given experiment. The cortical flow speed during polarity establishment has been previously determined as  $\sim 4 \mu\text{m min}^{-1}$  (5) with maximum value of  $7.7 \mu\text{m min}^{-1}$  (6), which translates into equivalent flow times  $\tau_f$  of the correlation curves of 4.1 s or 2.1 s, respectively. This value is comparable to the characteristic decay times of the NMY-2 sFCS autocorrelations (Fig. 4), suggesting that the myosin moves with similar velocities at both polarity establishment and maintenance phases. During the polarity establishment phase the myosin patches move all in the same direction, resulting in a net cortex flow, while in the later phases the motion is directionally uncorrelated, preventing appearance of any large-scale flows, and being observable only as a reorganization of the punctuate fluorescence pattern.

The decay of the sFCS autocorrelation of PAR-2 is more gradual than the loss of autocorrelation due to the following simple transport processes: uniform flow, binding/dissociation, and normal diffusion, as shown in Fig. 5 A. Combination of binding with diffusion or flow cannot result in an autocorrelation that is flatter than in any of these processes alone. The PAR-2 autocorrelation decay can be better described by the model of anomalous diffusion with a time-stretching parameter  $\alpha$ . Even better match with the experimental data can be achieved by considering contribution of two (or more) motion components, each with its own type of transport and time constant, as demonstrated by two-component diffusion in Fig. 5 A. The fits to the spatiotemporal correlation (Fig. 6) also favor a two-component diffusion model over a model with one-component diffusion and one binding/dissociation component. The multicomponent diffusion model is consistent with the presence of slow bright clusters (Fig. 2 C) and faster smaller complexes or individual molecules. The gradual autocorrelation decay, broadening of sFCS autocorrelation peaks with increasing lag time, and the dynamics of bright patches as seen in Fig. 2 C all suggest presence of diffusional motion within the cortex. This does not, however, exclude the

possibility of minor contribution of binding kinetics to one or more components of motion, with diffusion still being the dominant transport mechanism.

The differences in the dynamics between PAR-2 and NMY-2 proteins inferred from the autocorrelation data show that although there might be minor fractions that bind each other, the proteins move within the cortex mostly independently.

The faster motion of PAR-2 relative to that of NMY-2, which is assumed to reflect the cortex dynamics, and the presence of a clearly detectable pattern (Fig. 2 A), raises the question of the role of the membrane present above the cortex in the localization of PAR-2. Although the dynamics of PAR-2 on the cortex are slower than those of the PH domain on the membrane, the localization of PAR-2 with components of the membrane cannot be excluded. The existence of a PAR-2 pattern implies reduced molecular mobility, and the autocorrelations measured with sFCS are likely to be dominated by the dynamics of the bright PAR-2 pattern rather than the dynamics of individually diffusing PAR-2 molecules, therefore leading to a slower-decaying autocorrelation. It is not clear whether the bright pattern dynamics represents motion of bright clusters containing many GFP-labeled PAR-2 molecules, or whether the observed dynamics is a net effect of simultaneous growth and disassembly of otherwise static clusters (or combination of the two phenomena). Developing a model of fluorescence autocorrelation and spatiotemporal correlation resulting from the latter mechanism might help to discriminate between the two processes.

The measured mean diffusion coefficient of the PH domain on the membrane ( $1.1 \mu\text{m}^2 \text{s}^{-1}$ ) is comparable with that of fluorescent lipid analogs in plasma membranes of rat basophilic leukemia cells ( $0.8\text{--}0.9 \mu\text{m}^2 \text{s}^{-1}$ ) and human embryonic kidney cells ( $1.4 \mu\text{m}^2 \text{s}^{-1}$ ) (33), suggesting free diffusion of GFP::PH bound to PIP<sub>2</sub> in the membrane.

Cheeks et al. (5) used fluorescence recovery after photobleaching (FRAP) to show that photobleached PAR-2 on cortex completely recovers on the scale of tens of seconds. Their FRAP results are limited by the time resolution of 2 s, and do not permit further characterization of the type of the recovery process. With scanning FCS, we could access shorter timescales down to the millisecond range, and identify the presence of more components of motion. The two-component diffusion can be furthermore linked to the observed heterogeneous highly dynamic PAR-2 cortex pattern, not reported previously. Scanning FCS has the advantage of higher temporal resolution over FRAP, thus forming a bridge between the FRAP technique applicable on the timescales of seconds and longer, and a standard FCS operating at millisecond scales and shorter. Representing the sFCS data in terms of spatiotemporal correlation further increases the information obtainable with sFCS.

Other fluorescence correlation techniques could in principle be applied to study the dynamics of the cortex-localized proteins. For example, spatiotemporal image correlation

spectroscopy has been used to produce a map of flows from a sequence of images (34). Our preliminary results with spatiotemporal image correlation revealed limitations on the spatial and temporal resolution imposed by the high transport speeds and the available fluorescence signal in our data (28). Scanning FCS currently appears to be the optimal approach for the studied problem on the way between point- and image-correlation techniques.

Another technique for studying dynamics is particle tracking, which, however, requires identification of the features to be tracked. While this may be successful for NMY-2, it would be hardly possible for PAR-2 with our data, where the brighter fluorescent areas cannot be unambiguously identified and separated from their surroundings in subsequent image frames due to low contrast and imaging rate and high noise. This is likely to be the case also for some other PAR proteins. To reliably compare dynamics of two or more proteins, it would be, however, preferable that the data are obtained using the same technique. We see a possible alternative to tracking in a certain combination of tracking and correlation techniques, where the image features need not be identified, but their displacement from one image frame to another is determined by correlation, in a way similar to image registration techniques commonly used, for example, in medical imaging. The feasibility of this approach applied to a comparatively noisy fluorescence microscopy images remains to be tested.

### Diffusion in cytoplasm

The dynamics of the investigated GFP-labeled proteins in the cytosol can be reasonably well described by free diffusion. The observed spread of diffusion times is mainly due to the presence of long-time fluctuations in the fluorescence intensity, which affect the autocorrelation curves at long times and limit the accuracy of the fits to the simple diffusion model. The measured diffusion coefficients therefore reflect the fastest component of the motion of the proteins in the cytoplasm.

Although the solvent viscosity of cytoplasm, as measured by rotational mobility (i.e., microviscosity), is known to be similar to that of water, the translational diffusion of probes of various sizes indicates considerably higher and additionally size-dependent apparent viscosity. This effect has been explained by heterogeneity and crowding of the cytoplasm, where collisions with large structures and reversible binding lead to effectively lower diffusion coefficient and stronger dependence of the diffusion coefficient on the particle size, than that predicted by the Stokes-Einstein relationship (35,36).

The measured diffusion coefficients of the investigated proteins in cytosol are all significantly smaller than the diffusion coefficient of free GFP in buffer ( $87 \mu\text{m}^2 \text{s}^{-1}$ ) (37): the fastest GFP::PH is  $\sim 11\times$  slower, and the slowest NMY-2::GFP  $\sim 100\times$  slower. Purified GFP-labeled proteins were not available to perform direct comparison with their diffusion in a buffer. The simplifying assumption of a cube

root dependence of the diffusion coefficient on the molecular mass predicts only 1.5–2× smaller diffusion coefficient of the individual protein molecules in buffer compared to GFP. These results indicate the role of cytoplasmic crowding on the motion of the investigated proteins.

Although PAR-2 and CDC-37 are of similar size, PAR-2 diffusion is approximately three times slower, indicating possible localization in a larger complex or self-association. Similarly, the low diffusion coefficient of NMY-2 may be a consequence of association with other cytoplasmic components and homodimerization. The possible involvement of PAR-2 and NMY-2 in large protein complexes could be linked to the mechanism by which they become localized to the cortex.

## CONCLUSION

We have shown that FCS and sFCS can be used to study the dynamics of fluorescently labeled molecules on both short and long timescales even in such a complex and dynamic system as a polarized embryo that will divide asymmetrically, by overcoming the limitations of low statistical accuracy and photobleaching. Although cortex localization of PAR-2 depends on the presence of NMY-2 (8), our data indicate that PAR-2 is not recruited to the cortex by binding to posterior localized NMY-2 patches. By using circular sFCS, we could show that PAR-2 dynamics are faster than NMY-2, and further that PAR-2 distribution in the cortex is not uniform but heterogeneous, with a highly dynamic pattern distinct from that of NMY-2. It is therefore more likely that NMY-2 changes the properties of the cortex in a way that PAR-2 can associate with it, and presence of PAR-2 on the cortex might be inhibitory for NMY-2 contractility.

Circular sFCS, with its single-molecule sensitivity and full utilization of the fluorescence signal, provides information about the molecular dynamics and the type of motion, which is too slow for standard FCS, and not resolvable with imaging. Furthermore, sFCS provides information on spatial correlation in addition to temporal correlation, facilitating better characterization of transport processes in living organisms and discrimination between different models on basis of their spatiotemporal correlation.

Measurement along a perimeter of a relatively large circle overcomes two significant limitations encountered in FCS when applied to slowly moving molecules: photobleaching accompanied by depletion of fluorescent molecules in the fixed measurement area, and statistical noise due to the insufficient number of molecules crossing the measurement volume during the measurement. In comparison to imaging, higher temporal resolution, determined by the scanning frequency, is achieved with sFCS. Furthermore, by using two-photon excitation one additionally benefits from the possibility of long measurement times without disturbing the embryo development.

Future sFCS studies on other polarity proteins, along with fluorescence microscopy and RNAi experiments, will con-

tribute to a better understanding of asymmetric cell division in *C. elegans* and in other systems.

## SUPPLEMENTARY MATERIAL

To view all of the supplemental files associated with this article, visit [www.biophysj.org](http://www.biophysj.org).

We thank Carrie Cowan and Nathan Goehring for stimulating discussions.

C.H. was supported by an Ernst Schering Foundation Postdoctoral fellowship. Funding was provided by The International Human Frontier Science Program grant No. RGP 5-2005, and Europäische Fond für Regionale Entwicklung project No. 4212-06-02.

## REFERENCES

1. Cowan, C. R., and A. A. Hyman. 2004. Asymmetric cell division in *C. elegans*: cortical polarity and spindle positioning. *Annu. Rev. Cell Dev. Biol.* 20:427–453.
2. Schneider, S. Q., and B. Bowerman. 2003. Cell polarity and the cytoskeleton in the *Caenorhabditis elegans* zygote. *Annu. Rev. Genet.* 37:221–249.
3. Nance, J. 2005. PAR proteins and the establishment of cell polarity during *C. elegans* development. *Bioessays.* 27:126–135.
4. Munro, E. M. 2006. PAR proteins and the cytoskeleton: a marriage of equals. *Curr. Opin. Cell Biol.* 18:86–94.
5. Cheeks, R. J., J. C. Canman, W. N. Gabriel, N. Meyer, S. Strome, and B. Goldstein. 2004. *C. elegans* PAR proteins function by mobilizing and stabilizing asymmetrically localized protein complexes. *Curr. Biol.* 14:851–862.
6. Munro, E., J. Nance, and J. R. Priess. 2004. Cortical flows powered by asymmetrical contraction transport PAR proteins to establish and maintain anterior-posterior polarity in the early *C. elegans* embryo. *Dev. Cell.* 7:413–424.
7. Guo, S., and K. J. Kemphues. 1996. A non-muscle myosin required for embryonic polarity in *Caenorhabditis elegans*. *Nature.* 382:455–458.
8. Boyd, L., S. Guo, D. Levitan, D. T. Stinchcomb, and K. J. Kemphues. 1996. PAR-2 is asymmetrically distributed and promotes association of P granules and PAR-1 with the cortex in *C. elegans* embryos. *Development.* 122:3075–3084.
9. Cowan, C. R., and A. A. Hyman. 2004. Centrosomes direct cell polarity independently of microtubule assembly in *C. elegans* embryos. *Nature.* 431:92–96.
10. Cuenca, A. A., A. Schetter, D. Aceto, K. Kemphues, and G. Seydoux. 2003. Polarization of the *C. elegans* zygote proceeds via distinct establishment and maintenance phases. *Development.* 130:1255–1265.
11. Rigler, R., and E. S. Elson, editors. 2001. *Fluorescence Correlation Spectroscopy, 1st Ed. Theory and Application*, Chemical Physics Series. Springer Verlag, Berlin.
12. Bacia, K., and P. Schwille. 2003. A dynamic view of cellular processes by in vivo fluorescence auto- and cross-correlation spectroscopy. *Methods.* 29:74–85.
13. Petrov, E. P., and P. Schwille. 2008. *Standardization and Quality Assurance in Fluorescence Measurements II: Bioanalytical and Biomedical Applications*, Vol. 6, Springer Series on Fluorescence. Springer, Berlin, Heidelberg, New York.
14. Petrášek, Z., and P. Schwille. 2008. *Single Molecules and Nanotechnology*, Vol. 12, Springer Series in Biophysics. Springer, Berlin, Heidelberg, New York.
15. Petersen, N. O. 1986. Scanning fluorescence correlation spectroscopy. 1. Theory and simulation of aggregation measurements. *Biophys. J.* 49:809–815.

16. Berland, K. M., P. T. C. So, Y. Chen, W. W. Mantulin, and E. Gratton. 1996. Scanning two-photon fluctuation correlation spectroscopy: particle counting measurements for detection of molecular aggregation. *Biophys. J.* 71:410–420.
17. Amediek, A., E. Hausteine, D. Scherfeld, and P. Schwille. 2002. Scanning dual-color cross-correlation analysis for dynamic co-localization studies of immobile molecules. *Single Mol.* 3:201–210.
18. Skinner, J. P., Y. Chen, and J. D. Müller. 2005. Position-sensitive scanning fluorescence correlation spectroscopy. *Biophys. J.* 89:1288–1301.
19. Digman, M. A., C. M. Brown, P. Sengupta, P. W. Wiseman, A. R. Horwitz, and E. Gratton. 2005. Measuring fast dynamics in solutions and cells with a laser scanning microscope. *Biophys. J.* 89:1317–1327.
20. Petrášek, Z., M. Krishnan, I. Mönch, and P. Schwille. 2007. Simultaneous two-photon fluorescence correlation spectroscopy and lifetime imaging of dye molecules in submicrometer fluidic structures. *Microsc. Res. Tech.* 70:459–466.
21. Becker, W., A. Bergmann, E. Hausteine, Z. Petrášek, P. Schwille, C. Biskup, L. Kelbauskas, K. Benndorf, N. Klöcker, T. Anhut, I. Riemann, and K. König. 2006. Fluorescence lifetime images and correlation spectra obtained by multidimensional time-correlated single photon counting. *Microsc. Res. Tech.* 69:186–195.
22. Brenner, S. 1974. Genetics of *Caenorhabditis elegans*. *Genetics*. 77:71–94.
23. Schonegg, S., A. T. Constantinescu, C. Hoegge, and A. A. Hyman. 2007. The  $\rho$ GTPase-activating proteins RGA-3 and RGA-4 are required to set the initial size of PAR domains in *Caenorhabditis elegans* one-cell embryos. *Proc. Natl. Acad. Sci. USA*. 104:14976–14981.
24. Audhya, A., F. Hyndman, I. X. McLeod, A. S. Maddox, J. R. Yates, A. Desai, and K. Oegema. 2005. A complex containing the Sm protein CAR-1 and the RNA helicase CGH-1 is required for embryonic cytokinesis in *Caenorhabditis elegans*. *J. Cell Biol.* 171:267–279.
25. Nance, J., E. M. Munro, and J. R. Priess. 2003. *C. elegans* PAR-3 and PAR-6 are required for apicobasal asymmetries associated with cell adhesion and gastrulation. *Development*. 130:5339–5350.
26. Praitis, V., E. Casey, D. Collar, and J. Austin. 2001. Creation of low-copy integrated transgenic lines in *Caenorhabditis elegans*. *Genetics*. 157:1217–1226.
27. Kojro, Z. 1991. Normalization and statistical noise level in the normalized autocorrelation function. Compensated normalization. *J. Phys. Math. Gen.* 24:L225–L229.
28. Petrášek, Z., C. Hoegge, A. A. Hyman, and P. Schwille. 2008. Two-photon fluorescence imaging and correlation analysis applied to protein dynamics in *C. elegans* embryo. *Proc. SPIE*. 6860:68601L.
29. Cowan, C. R., and A. A. Hyman. 2007. Acto-myosin reorganization and PAR polarity in *C. elegans*. *Development*. 134:1035–1043.
30. Beers, M., and K. Kemphues. 2006. Depletion of the co-chaperone CDC-37 reveals two modes of PAR-6 cortical association in *C. elegans* embryos. *Development*. 133:3745–3754.
31. Hurley, J. H., and T. Meyer. 2001. Subcellular targeting by membrane lipids. *Curr. Opin. Cell Biol.* 13:146–152.
32. Palmer, A. G., and N. L. Thompson. 1987. Theory of sample translation in fluorescence correlation spectroscopy. *Biophys. J.* 51:339–343.
33. Bacia, K., D. Scherfeld, N. Kahya, and P. Schwille. 2004. Fluorescence correlation spectroscopy relates rafts in model and native membranes. *Biophys. J.* 87:1034–1043.
34. Brown, C. M., B. Hebert, D. L. Kolin, J. Zareno, L. Whitmore, A. R. Horwitz, and P. W. Wiseman. 2006. Probing the integrin-actin linkage using high-resolution protein velocity mapping. *J. Cell Sci.* 119:5204–5214.
35. Luby-Phelps, K. 2000. Cytoarchitecture and physical properties of cytoplasm: volume, viscosity, diffusion, intracellular surface area. *Int. Rev. Cytol.* 192:189–221.
36. Verkman, A. S. 2002. Solute and macromolecule diffusion in cellular aqueous compartments. *Trends Biochem. Sci.* 27:27–33.
37. Swaminathan, R., C. P. Hoang, and A. S. Verkman. 1997. Photobleaching recovery and anisotropy decay of green fluorescent protein GFP-S65T in solution and cells: cytoplasmic viscosity probed by green fluorescent protein translational and rotational diffusion. *Biophys. J.* 72:1900–1907.



## 9 Erklärung

Hiermit erkläre ich, dass die vorliegende Habilitationsschrift von mir selbst und ohne andere als die darin angegebenen Hilfsmittel angefertigt wurde. Die wörtlich oder inhaltlich übernommene Stellen wurden als solche gekennzeichnet.

Ein früheres Habilitationsgesuch an einer anderen Hochschule ist nicht erfolgt.

Ein an die Fakultät zu übersendendes Führungszeugnis nach §30 Abs. 5 Bundeszentralregistergesetz wurde bei der zuständigen Meldebehörde beantragt.

Die in der Habilitationsschrift enthaltenen Veröffentlichungen, wurden von mir zu einem entscheidenden Teil geplant, experimentell durchgeführt und geschrieben, mit folgenden Ausnahmen: die im Artikel A3 eingesetzten Nanokanal-Strukturen wurden von M. Krishnan angefertigt; der Experimentaufbau im Artikel A5 wurde unter meiner Betreuung von S. Derenko konstruiert; die Daten im Artikel A7 wurden von J. Mütze unter meiner Betreuung aufgenommen und analysiert, und der Artikel zusammen mit ihm geschrieben; und die Arbeiten im Artikel A8 wurden zum gleichen Teil zusammen mit C. Hoege durchgeführt.

Zdeněk Petrášek

